Wind and temperature in a glacierised Himalayan valley, and their controlling mechanisms

Emily Ruth Potter

British Antarctic Survey
and Scott Polar Research Institute, University of Cambridge

This dissertation is submitted for the degree of
Doctor of Philosophy

Wolfson College

April 2019

Declaration

This thesis is the result of my own work and includes nothing which is the outcome of work done in collaboration except as declared in the Preface and specified in the text. It is not substantially the same as any that I have submitted, or, is being concurrently submitted for a degree or diploma or other qualification at the University of Cambridge or any other University or similar institution except as declared in the Preface and specified in the text. I further state that no substantial part of my thesis has already been submitted, or, is being concurrently submitted for any such degree, diploma or other qualification at the University of Cambridge or any other University or similar institution except as declared in the Preface and specified in the text. It does not exceed 225 pages.

Emily Ruth Potter
April 2019

Wind and temperature in a glacierised Himalayan valley, and their controlling mechanisms

Emily Ruth Potter

The Hindu-Kush Karakoram Himalaya (HKKH) contains the third largest quantity of snow and ice in the world, after the Polar Regions. Meltwater from this snow and ice feeds many of the major rivers in Asia, which ultimately provide water for 1.9 billion people. Due to its complex and rugged terrain, as well as a scarcity of in-situ measurements and fine-scale numerical modelling studies, important factors influencing melt and precipitation, such as the local valley wind regimes and the lapse rates of near-surface temperatures, are poorly understood in the HKKH. This thesis aims to improve understanding of the valley wind regime and temperature lapse rate for the glacierised Dudh Koshi River Basin in the Nepalese Himalaya, which includes the Khumbu Glacier, by utilising results from a high-resolution atmospheric model and measurements from a field campaign.

First, the mechanisms controlling the local wind regime in the Dudh Koshi Valley are investigated, by running the Weather Research and Forecasting (WRF) model at 1 km horizontal resolution for one month in the summer and one month in the winter. The WRF model output is found to well represent the diurnal cycle of the wind when compared to existing in-situ observations, which is characterised by strong up-valley near-surface winds during the day and weak (predominantly up-valley) winds at night in both months. A momentum budget analysis reveals that the predominant physical drivers of the near-surface wind acceleration are the pressure gradient, advection and turbulent vertical mixing, which are extremely spatially variable over the valley. The results also show that the local wind regime and its drivers are strongly affected by the presence of glaciers, which act to weaken the up-valley flow.

Second, as the Khumbu Glacier is largely debris-covered (along with many glaciers in the HKKH), a new debris-cover category is added into the WRF model. This enhancement is found to improve the model representation of near-surface temperature, relative humidity, wind speed and radiation, in comparison to the default category of clean-ice glaciers. The addition of the new debris-cover category, and the resulting change in near-surface tempera-

ture and wind speed are found to have consequent effects on water vapour, hydrometeors and ultimately snow cover.

Third, to investigate the temperature lapse rate, a series of temperature sensors was installed throughout the Dudh Koshi Valley and over the Khumbu Glacier for 18 days during the pre-monsoon season in 2017, and the entire monsoon season. Lapse rates are found to vary considerably, both diurnally and over the pre-monsoon and monsoon periods. Temperature budget analysis based on output from the WRF model reveals that (both off-glacier and on the debris-covered glacier) the near-surface temperature during the day is warmed by turbulent vertical mixing and cooled by advection. Furthermore, at night a relationship is identified between strong downslope winds on the glacier and shallow lapse rates, due to warming from advection and cooling from turbulent vertical mixing. In addition, in the monsoon season there is a substantial contribution from latent cooling during the day.

This is the first work to provide a full momentum and temperature budget analysis for a valley in the HKKH region. It is hoped that the advances made in this thesis may ultimately help inform developments to weather and climate models over the region, including highlighting the need for debris-covered glaciers to be represented in atmospheric models.

Acknowledgements

First and foremost, I would like to thank my supervisors, Andrew Orr and Ian Willis, who have guided me through this PhD with encouragement and enthusiasm. It has been a real pleasure to work with them for the past years, and I have enjoyed my PhD more than I ever imagined. They were instrumental in suggesting initial ideas for this PhD, and have patiently guided me through the preparation of this thesis.

Secondly, I would like to thank the staff and students, both past and present, at the British Antarctic Survey (BAS). BAS has been an incredible place to work, and I have felt welcomed and supported throughout my time here. Many of them have helped a great deal with this project. A huge thanks to everyone in the Atmosphere, Ice and Climate team for all their support. In particular, John King provided scientific advice and guidance throughout this PhD. Pranab Deb helped with initial python coding and WRF setup when I first arrived. Alison Ming helped with many mathematical queries, particularly the momentum budget and the statistics used in this thesis. Tony Phillips has provided exceptional help with coding, data storage and general computing issues over the years. Daniel Bannister provided considerable help with the WRF modelling, including changing the WRF model land cover for me, as well as providing support and encouragement. Elena Field in the BAS mapping department provided advice on map-making.

A huge thanks to my fellow students at BAS (not least for the weekly cake), who have provided friendship, support and practical help from day one. In particular, thanks to Amy King, Ella Gilbert, Mike McCarthy (who compiled the previous studies of debris-covered glacier properties, used in Chapter 4), Tom Hudson and Rebecca Vignols. My particular thanks goes to Christine McKenna, who has helped with maths, coding (in particular providing the original code for the bootstrap method used in this thesis), meteorology and countless other questions over the years, and has been my conference buddy at many conferences and meetings.

Thirdly, many colleagues from outside of BAS helped to get this project off the ground. Patrick Wagnon was extremely generous in sharing the observational data included in Chapters 3 and 4 in this thesis. Pierre Chevallier collated the Ev-K2-CNR data, used in Chapter 3, with permission from Elisa Vuillermoz and Franco Salerno, who were instrumental in its collection. Amongst others, Francesca Pellicciotti, Emily Collier and Walter Immerzeel have provided advice and interesting conversation over the years.

The fieldwork aspect of this project was a truly incredible opportunity for me, and also a very steep learning curve. It would not have been successful without the considerable help which I received. At BAS, Tracy Moffat-Griffin, Thomas Lachlan-Cope, Zachary Smith, Hamish Pritchard and in particular Steve Colwell helped hugely with the preparation and instrument setup in Cambridge. Thanks also to Adam Copeland and the geography department at Cambridge University, as well as the operations team at BAS for the loan of much of the meteorological equipment.

The fieldwork would not have been possible without the EverDrill team, who allowed me to join their fieldwork campaign. Duncan Quincey helped with the initial fieldwork concepts and setup, along with suggestions for the construction of the temperature stations and much help in the field, and put me in touch with Scott Watson, who lent most of the temperature sensors. Bryn Hubbard provided advice on cloud monitoring during the fieldwork. Tenzing Sherpa negotiated and helped with the setup of the temperature stations. Evan Miles had many scientific suggestions, and also collected the temperature stations in October so that I could leave them over the monsoon period. He also provided the digital elevation model to calculate the station elevations. Katie Miles also collected the sensors in October, as well as patiently coating radiation shields with me in the field in May. The fieldwork was supported by Himalayan Research Expeditions, and particular thanks goes to Mahesh Magar for guiding and navigating on the glacier, and for helping with much of the station setup, as well as providing advice on ice-cliff melting and glacier movement when the stations were left over the monsoon season. I cannot thank the EverDrill team enough. It was incredibly motivating to be able to see the places I was studying, and they gave me an amazing first experience of fieldwork.

This PhD has been generously funded through a National Environmental Research Council studentship. The fieldwork was additionally funded by the Royal Geographical Society, the Royal Meteorological Society and the Mount Everest Foundation. Wolfson College,

Cambridge University provided funds for a trip to the American Geophysical Union annual meeting through a travel grant, and the Polar Climate and Predictions team at BAS also provided additional funding.

More personally, thank you to my partner John, who has loved and supported me over the last three years, and smoothed my journey to the end of this PhD. Finally, thank you to my family, especially my grandma Jane for reminding me that there is more to life than work, my sisters Katie and Phoebe, and most of all my parents Jane and Gavin, who have supported, encouraged and advised me through the last few years, as they have through all my endeavours.

Table of contents

List of figures

List of tables

Nomenclature

Roman Symbols

F_Θ	Forcing from horizontal and numerical diffusion, and model physics in the potential temperature budget
F_U	Forcing from Coriolis, curvature, horizontal and numerical diffusion, and model physics in the zonal direction
F_V	Forcing from Coriolis, curvature, horizontal and numerical diffusion, and model physics in the meridional direction
N	Brunt-Väisälä frequency
p	Air pressure
p_{dh}	Hydrostatic pressure of the dry atmosphere
p_{dht}	Hydrostatic pressure of the dry atmosphere at the top of the model
q_c	Mixing ratio of cloud
q_v	Mixing ratio of water vapour
R	Pearson moment correlation coefficient
U	Mass coupled zonal velocity
u	Zonal velocity
V	Mass coupled meridional velocity
v	Meridional velocity
W	Mass coupled vertical velocity

w Vertical velocity

$\mathbf{V}$ Mass coupled velocity (U,V,W)

$\mathbf{v}$ Velocity (u,v,w)

Δz Thickness of vertical level in the WRF model

Greek Symbols

α Inverse density of moist air

α_d Inverse density of dry air

η Vertical coordinate used by WRF

Θ Mass coupled potential temperature

θ Potential temperature

μ_d Mass of dry air in the column

ρ Air density

ϕ Geopotential

Acronyms / Abbreviations

AWS Automatic Weather Station

CAM Community Atmosphere Model

CN Changri Nup

D1 to D4 Nested WRF model domains (D4 being the inner domain)

DEM Digital Elevation Model

ERA-Interim ECMWF (European Centre for Medium-Range Weather Forecasts) Re-Analysis

Ev-K2-CNR Everest-K2-National Research Council

GLIMS Global Land Ice Measurements from Space

GLOF Glacier Lake Outburst Flood

GPS Global Positioning System

HKKH Hindu-Kush Karakoram Himalaya

LR Lapse rate (near-surface temperature lapse rate)

LT Nepali local time (UTC+5:45 hr)

LW radiation Longwave radiation

m asl meters above sea level

ML Mera La

MM5 Fifth-generation Pennsylvania State University–National Center for Atmospheric Research Mesoscale Model

MN Mera-Naulek

MS Mera Summit

NA Not Applicable (data unavailable)

Na Namche

Noah-MP Noah multi-physics

Ph Pheriche

Py Pyramid

RCP Representative Concentration Pathway

RGI Randolph Glacier Inventory

RH Relative Humidity

RK3 Third-order Runge-Kutta

RMSE Root mean square error

SRTM Shuttle Radar Topography Mission

SW radiation Shortwave radiation

TG1 to TG10 On-glacier stations in fieldwork campaign

TV1 to TV9 Off-glacier stations in fieldwork campaign

USGS United States Geological Survey

UTC Coordinated Universal Time

WPS WRF preprocessing system

WRF model Weather Research and Forecasting model

Chapter 1

Introduction

1.1 Motivation

Approximately 1.9 billion people in Asia depend on water from major rivers that originate from the Hindu-Kush Karakoram Himalaya (HKKH) region, including the Indus, Ganges and Brahmaputra rivers. Spring and summer melting of the snowpacks and glaciers in the region provide a vital feed to these rivers (Immerzeel et al., 2010; Pritchard, 2017; Wester et al., 2019). Most of the glaciers in the HKKH are shrinking due to climate change (Bolch et al., 2012; Kraaijenbrink et al., 2017), affecting the water resources available for domestic consumption and industry, for example agriculture and hydro-electric power, especially in times of drought (Pritchard, 2017).

The extreme mountainous topography, and the complex interactions between air flow and orography in the HKKH, have a major impact on the meteorological processes taking place in this region (Ueno et al., 2001; Yasunari, 1976). This often leads to substantial small-scale variability in basic variables such as temperature, wind and precipitation, all of which affect snowfall, glacier accumulation, snow melt and glacier melt. As such, understanding the local atmospheric processes in the HKKH is key to understanding the behaviour of the glacio-hydro-meteorological system. However, due to limited in-situ data and a lack of model studies at fine spatial scales, the local atmospheric processes that influence the accumulation and melting of snow and ice are poorly understood. In addition, the unique topography and climatology of the HKKH makes it difficult to interpret the results from much more well-studied mountain ranges, such as the Alps (Gobiet et al., 2014), to this one.

There are three meteorological phenomena that are of particular importance in the HKKH, but have been under-researched. These are the valley wind circulations, the near-surface temperature lapse rates and the effect of the land surface on meteorological variables. These three phenomena form the basis of this thesis, and are outlined in more detail in the following paragraphs.

The first phenomenon investigated is the valley wind circulation, and its characteristic diurnal cycle. This flow system transports moisture and clouds up valleys, influences the spatial and temporal characteristics of near-surface air temperature, and affects blowing snow and the transport of pollutants (Bollasina et al., 2002; Egger et al., 2002; Immerzeel et al., 2014; Karki et al., 2017; Orr et al., 2017; Shea et al., 2015a; Tartari et al., 1998). As such, an improved understanding of the wind dynamics in valleys in the HKKH region will increase understanding of the glacio-hydro-meteorological system. In addition, subsequent improved representation of local circulations in atmospheric models will result in better predictions of important meteorological variables such as temperature, humidity, radiation and precipitation, which are required as inputs to glacio-hydrological models (Widmann et al., 2017).

The characteristic diurnal cycles of valley wind regimes have been relatively well documented in the HKKH. These studies have mostly been observational, and limited to point based studies of winds (Inoue, 1976; Ohata et al., 1981; Shea et al., 2015b; Ueno et al., 2001, 2008). A few have been modelling based, and therefore able to analyse the wind patterns more generally (Collier and Immerzeel, 2015; Karki et al., 2017; Song et al., 2007; Sun et al., 2018; Zängl et al., 2001; Zou et al., 2008). However, only a handful of the modelling studies have investigated some of the mechanisms driving the local wind circulations (Bonekamp et al., 2018; Sun et al., 2018; Zängl et al., 2001), making it difficult to generalise the results. These latter studies have mostly focussed on the effects of the pressure gradient on the winds. The pressure gradient is, generally, the main driver of the wind, caused by differential heating patterns at different spatial scales. Further research is needed to properly clarify the role of the pressure gradient, as well as the influence of other physical forces driving the wind acceleration in the valleys of the HKKH.

A second important meteorological phenomenon in the HKKH is the near-surface temperature lapse rate, and its relationship to other meteorological variables. Due to the lack of in-situ meteorological observations at high altitudes in the HKKH, glacio-hydrological models often extrapolate from available measurements at lower altitudes, using fixed lapse rates,

to determine the temperature distribution at higher elevations. However, where they have been measured, lapse rates in the HKKH vary considerably both temporally and spatially, and therefore it is difficult to infer lapse rates from one region in the HKKH to another, or take the lapse rate from one season and use it in others (Immerzeel et al., 2014; Thayyen and Dimri, 2014, 2018). Additionally, due to the unique climate and size of the HKKH, lapse rates cannot be inferred from other mountain ranges (Thayyen et al., 2005b).

A few studies have analysed near-surface temperature variation in the Dudh Koshi Valley, in the Nepalese Himalaya, although these have used only a handful of observational locations (Shea et al., 2015b; Yang et al., 2017). There has been significant work recently in examining lapse rates and air temperature variability in the Langtang valley, also in the Nepalese Himalaya, using a large observational dataset (Heynen et al., 2016; Immerzeel et al., 2014; Steiner and Pellicciotti, 2016). There is, therefore, a need for more comprehensive studies of near-surface temperature lapse rates in valleys other than Langtang. In addition, Heynen et al. (2016) point to the need for a study which specifically investigates the impact of wind on lapse rates, as has been examined in other mountain ranges such as the Alps (Shaw et al., 2016), but never for the HKKH region.

A third important phenomenon to study in the context of weather and climate of the HKKH is land surface type, as this has a substantial impact on the near-surface meteorological variables (Bonekamp et al., 2018; Collier et al., 2015; Ma et al., 2013). Further work on understanding its effects is needed, in particular to determine the effects of snowpacks and glaciers on the local valley wind regime (Yang et al., 2017). In addition, the substantial effects of glacier debris-cover on the near-surface meteorological variables has been recognised in recent years (Brock et al., 2010; Collier et al., 2015; Steiner and Pellicciotti, 2016). This is particularly critical as the proportion of debris-cover on glaciers in the HKKH is set to increase with future glacier melt (Scherler et al., 2018). However, there has been only one attempt so far to include debris-cover in an atmospheric model, in a study using a coupled atmosphere-glacier model (Collier et al., 2015, 2014). Although coupled models are extremely useful for modelling glacier-atmosphere feedbacks, they are computationally expensive to run. As such, there is a need for a simple land surface classification for debris-covered glaciers in atmosphere-only models. This can then be used to further examine the effects of debris cover on atmospheric variables.

1.2 Thesis objectives and overview

The overarching aim of this thesis is to investigate the local wind circulation and temperature lapse rates in a Himalayan valley, with a particular focus on the mechanisms controlling them, and the effects of changing land cover, particularly the role of debris-covered glaciers. The Dudh Koshi Valley, which includes the Khumbu Glacier, is picked as a case study.

It is hoped that this work will improve understanding of the atmospheric controls on glacier melt in the region, leading to more accurate predictions of glacier mass balance with future climate change. The investigation into the effects of changing land cover on near-surface meteorology will give an indication of how regional climate in Himalayan valleys may change in the future, in response to glacier melt and increased debris cover on the glaciers.

Based on the discussion above, this thesis has three main aims:

1. To establish the patterns of the local wind regime and the dominant mechanisms controlling it.
2. To identify temperature lapse rates, the controls on this temperature variation, and the ways in which lapse rates vary in relation to other meteorological variables.
3. To investigate the effects of glaciers (particularly the difference between clean-ice glaciers and debris-covered glaciers) on wind variability and temperature lapse rates, and the subsequent effects on other meteorological variables.

This thesis consists of six chapters. The present chapter sets out the motivation for the study and briefly describes the three main aims of this thesis.

Chapter 2 expands on the motivation given in this chapter. It gives an in-depth review of scientific progress to date, and explores the open questions remaining.

The first thesis aim is addressed in Chapter 3. The Weather Research and Forecasting (WRF) model is run at high resolution for the months of July 2013 and January 2014, to identify the variation in wind speed and direction over the Dudh Koshi Valley. The WRF model is validated using observations of near-surface wind (as well as air temperature). To investigate the dynamical drivers of the local valley winds, a detailed momentum budget

analysis of output from the WRF model is performed to determine the magnitude of each of the drivers of the near-surface wind, their variation over the valley, and their diurnal cycle. Vertical profiles of the wind and its drivers are also examined.

The second thesis aim is addressed in Chapter 5, which analyses the results of a field campaign that I undertook in May 2017, to investigate the temperature lapse rates in the Dudh Koshi Valley and over the Khumbu Glacier. The WRF model is run for the same periods as the fieldwork campaign. Causal mechanisms of lapse rate variation are identified from analysis of the observational data are further investigated using the WRF model, by analysing the results of a potential temperature budget from the WRF model output.

The third thesis aim is split over Chapters 3, 4 and 5. The effects of the glaciers on the near-surface wind are investigated in Chapter 3 by rerunning the WRF model with all the permanent snow and ice removed. In Chapter 4, a new debris-covered glacier land surface category is added to the WRF model, and a case study is conducted to demonstrate the improvement in the model compared to using the default clean-ice glacier category or bare ground, by comparison with available measurements. In addition, Chapter 4 examines the impact of this new land surface category on the wind, temperature, and several other meteorological variables. A more detailed analysis of the effects of glacier debris cover on near-surface temperature in the WRF model is presented in Chapter 5.

Lastly, Chapter 6 summarises the findings of the previous chapters, and puts the results into the context of previous studies. In addition, it assesses the extent to which the preceding chapters have answered the three main thesis aims, and suggests avenues for future work.

Chapter 2

Literature review

2.1 The Hindu-Kush Karakoram Himalaya

The HKKH region contains the greatest quantity of snow and ice outside of the Polar Regions (Wester et al., 2019). It covers the Himalaya in the southeast, and the Hindu Kush, Karakoram, Pamir Alai, Kunlun Shan and Tian Shan to the northwest. It stretches over 2000 km, from Kyrgyzstan and Tajikistan in the west, through to India, Nepal, China and Bhutan in the east. These mountains contain 90,000 glaciers, the highest concentration in the world (RGI Consortium, 2015). Ten major rivers in Asia have their headwaters in the HKKH, including the Indus, Ganges and Brahmaputra (Fig. 2.1) (Wester et al., 2019). In the spring and summer, meltwater from the glaciers and snowfields feeds these rivers (Bookhagen and Burbank, 2010). Glaciers can store precipitation as ice for decades or even centuries, which makes them a particularly important source of water in times of drought (National Research Council, 2012; Pritchard, 2017).

2.1.1 Large-scale climate in the HKKH

There are two distinct large-scale climatic regimes influencing the HKKH region, the Indian summer monsoon and winter westerly disturbances (Bookhagen and Burbank, 2006; Wester et al., 2019). The Indian summer monsoon is the predominant large-scale driver of precipitation over the Himalaya, in the eastern areas of the HKKH. In the central Himalayan region, approximately 80 % of precipitation falls during the Indian summer monsoon (Bookhagen and Burbank, 2010). The monsoon season typically lasts from June/July to September/October, with length and onset dates varying by location (Government of Nepal, 2019; Singh and

Fig. 2.1 The HKKH region, and the 10 major rivers that originate in the HKKH. Figure taken from Wester et al. (2019).

Ranade, 2010).

By contrast, in the westerly regions of the HKKH, the majority of precipitation falls during the winter months. The precipitation often falls as part of large-scale synoptic events known as the westerly disturbances (Wester et al., 2019). These storms are associated with variations in the subtropical westerly jet stream (Dimri et al., 2015; Madhura et al., 2015). The air temperature also varies considerably over HKKH region, due to both the large-scale regimes, as well as the different humidities, altitudes and latitudes of the regions (Wester et al., 2019).

2.1.2 Regional-scale climate in the HKKH

In addition to the large-scale climatic variations discussed above, the extreme topography in the HKKH induces variations in climatic variables at a regional scale. For example, within the Indus River Basin, Hasson et al. (2014) found substantial differences between nine sub-basins in the snow line elevation, which varied from 3200 m asl to 4600 m asl. This indicates that air temperature varies considerably between sub-basins, even at the same elevation.

In the Himalaya, topography has also been found to considerably affect precipitation, causing it to fall in two distinct bands at different elevations, one to the south of the lesser Himalaya, and the other band, which is discontinuous, to the south of the greater Himalaya (Bookhagen and Burbank, 2006). Most of the precipitation falls to the south of the highest topography (as the monsoon approaches from the south of the Himalaya), leading to a strong south-to-north gradient in precipitation (Bookhagen and Burbank, 2006, 2010). There is also a substantial difference in precipitation amounts between the eastern and western areas of the Himalaya, with much higher amounts in the eastern areas (Bookhagen and Burbank, 2010).

2.1.3 Regional climate modelling in the HKKH

The variation in climatic variables across the HKKH discussed above highlights the need for regional modelling studies to fully understand the meteorological processes taking place in the region. Very few high-resolution modelling studies have been carried out in this region.

In the few regional climate modelling studies focussed on the HKKH, model spatial resolution is found to be important for accurate representation of meteorological variables (Bonekamp et al., 2018; Collier and Immerzeel, 2015; Karki et al., 2017). Precipitation and temperature in Himalayan valleys is found to be most accurately represented using a convection-permitting model of at least 1 km resolution (Collier et al., 2015; Karki et al., 2017). Even higher resolutions, of 500 m, have been found to further improve modelled precipitation, wind and temperature (Bonekamp et al., 2018).

Accurate representation of the surface land cover is also important in this region, especially for correct representation of precipitation in the monsoon season (Bonekamp et al., 2018), and to model the correct surface temperature, wind speed and surface fluxes (Collier et al., 2015). In addition, semi-idealised studies have suggested that the glacier cover and valley shape have a significant impact on winds in valleys (Ma et al., 2013; Zängl et al., 2001). These studies will be discussed further in Section 2.2.4.

Lastly, model setup can have a significant impact on the model performance. For example, spinup time can affect modelled precipitation (Bonekamp et al., 2018). Choice of microphysics also has a big effect on modelled precipitation and radiation reaching the surface, with double-moment schemes leading to more accurate precipitation representation than single-moment schemes (Orr et al., 2017).

2.1.4 Climate change in the HKKH

Most of the glaciers and snowpacks in the HKKH have retreated in the past decades (Yao et al., 2012). Along with other high-elevations regions globally, the HKKH is particularly sensitive to climate change from increased greenhouse gasses (Kraaijenbrink et al., 2017; Pepin et al., 2015). In addition, the HKKH region is subject to climate change from black carbon (from cooking stoves) and other aerosols which are transported to the HKKH from the cities in Asia (Duan et al., 2006; Ramanathan and Carmichael, 2008; Wester et al., 2019). It is thought that in the Himalaya, the effects of black carbon emissions on heating in the troposphere maybe equally large to those of atmospheric carbon dioxide (Ramanathan and Carmichael, 2008). In addition, black carbon landing on snowpacks and glaciers in the HKKH increases their albedo, which can lead to further melt (Jacobi et al., 2015; Ménégoz et al., 2014). The rapid decline in the snowpacks and glaciers is predicted to continue in the future (Kraaijenbrink et al., 2017; Shrestha and Aryal, 2011). Warmer temperatures increase snow and ice melt, and also cause more rain, rather than snow, at higher altitudes, decreasing accumulation and further increasing melt (Wester et al., 2019). Large-scale precipitation patterns that influence the HKKH region, such as the Indian summer monsoon, have also been affected by climate change (Loo et al., 2015; Turner and Annamalai, 2012). Rainfall from the monsoon is generally expected to increase in the future, but there may also be a delay in the onset of the monsoon, and increased inter-annual variability (Loo et al., 2015; Turner and Annamalai, 2012).

Temperature change in the HKKH

Analysis of the global land-surface air temperature dataset LSAT-V1.1, based on in situ measurements, suggests that from 1901-2014 the surface temperature of the HKKH has increased by an average of 0.104 °C per decade, although the largest temperature changes have occurred since the 1970s (Ren et al., 2017). There have also been shifts in the diurnal cycle over the HKKH, with the minimum (nightime) temperatures increasing more than the maximum (daytime) temperatures (Ren et al., 2017). In the eastern parts of the HKKH, it has been found that, in general, warming is enhanced at higher elevations (National Research Council, 2012; You et al., 2017). In addition to the average increases in temperature, the number of extreme warm events (in the top 10th percentile) has increased and the number of extreme cold events (in the bottom 10th percentile) has decreased, especially over eastern regions of the HKKH (Sun et al., 2017).

Kulkarni et al. (2013) used a regional climate model at 50 km spatial resolution to predict temperature changes in the western, central, and eastern regions of the HKKH. Despite differences between the regions, all three show a warming trend when analysed up to the end of the 21st century. If the target of limiting global warming to 1.5 °C by the end of the century is met, Kraaijenbrink et al. (2017) predict an average warming of 2.1 °C in HKKH (which varies spatially, from a warming of 1.9 °C in the eastern HKKH to a warming of 2.3 °C in the Hindu Kush). Analysis of region climate models from the Coordinated Regional climate Downscaling Experiment (CORDEX) predicts warming of 2 °C to 3 °C under the RCP4.5 scenario, and a warming of 3 °C to 6 °C under RCP8.5 by the end of the century in the central Himalayan region (Sanjay et al., 2017).

Precipitation change in the HKKH

The considerable variability of precipitation in the HKKH makes it difficult to determine trends in precipitation over the whole region. Palazzi et al. (2013) investigate changes in precipitation in the Hindu-Kush Karakoram (to the west) and Himalaya (to the east), using a variety of satellite data, in situ measurements, reanalysis and a global climate model. Some of the observational datasets suggest that there has been a slight decreasing trend in summer precipitation from 1950-2010 in the Himalayan region. Using in situ weather stations, Ren et al. (2017) find a slight decrease in precipitation since the beginning of the 20th century over the entire HKKH region, but a substantial increase since 1980 (although this latter increase may be influenced by an increase in the number of observations). Analysis of a dataset based on station data over the whole HKKH shows an increase in intense precipitation over much of the region between 1961 and 2012, both in amount and number of days (Zhan et al., 2017).

Predicting future changes in precipitation is also difficult due to the different controls on that precipitation, which vary both spatially and temporally. Historically, global climate models struggle to represent rainfall from the Indian monsoon, with many models under-representing rainfall during the monsoon season (Menon et al., 2013). Models which under-represent precipitation typically also fail to capture the spatial distribution of the rainfall, and in general the onset of the monsoon is late in many global climate models (Menon et al., 2013; Sperber et al., 2013). However in general, the summer monsoon precipitation is predicted to increase by the end of the century (Kulkarni et al., 2013; Sanjay et al., 2017). Kulkarni et al. (2013) suggest that precipitation could increase by 20-40 % by the end of the century, compared with the end of the last century, while Sanjay et al. (2017) predict that under RCP8.5, summer monsoon precipitation will increase by 22 % by the end of the

century over the south-eastern Himalaya. There is a disagreement between models on the precipitation change over other parts of HKKH (Sanjay et al., 2017). In general over the HKKH, extreme wet events are predicted to increase under future global warming (Guo-Yu and Shrestha, 2017; Palazzi et al., 2013). In some areas, such as the Koshi River Basin in the Eastern HKKH, both extreme dry and extreme wet events are likely to become more common in the future (Rajbhandari et al., 2017).

Glacier change in the HKKH

Glaciers in HKKH are generally losing mass at rates comparable to those in other parts the world (National Research Council, 2012). Estimates vary, but the glaciers in the HKKH are thought to be lowering at an average rate of between $0.18\,\mathrm{m\,y^{-1}}$ and $0.38\,\mathrm{m\,y^{-1}}$ (Brun et al., 2017; Kääb et al., 2012). However within the HKKH region there is a large variability in elevation loss, with some glaciers in the western HKKH showing only a small reduction or even an increase in elevation, while some in the Central and Eastern Himalaya are decreasing in elevation at rates of over $0.6\,\mathrm{m\,y^{-1}}$ (Kääb et al., 2012). If the global temperature warming is limited to 1.5 °C, Kraaijenbrink et al. (2017) predict a 36 % decrease in the total amount of ice in HKKH by the end of the century. Higher global warming scenarios may see over 50 % of ice disappear (Wester et al., 2019). Immerzeel et al. (2013) note that one of the greatest difficulties in predicting the future water supply in the HKKH region is the large spatial and temporal differences in both glacier melt and precipitation across the HKKH.

2.1.5 Hydrological change in the HKKH

Drought and river shortages

Overall, it is possible that a future increase in rainfall could combat the loss of meltwater from the snowfields and glaciers in the Himalaya, however a change in the temporal or spatial distribution of water in the rivers, even in a small area, could have a big effect on those living downstream (Immerzeel et al., 2013). It is thought that periods of drought may increase with future climate change (Eriksson et al., 2009; Xu et al., 2009). It is difficult to calculate the exact contribution of glacier meltwater to rivers in HKKH, and it varies considerably in different regions and at different times of the year (Barnett et al., 2005; Kaser et al., 2010; Pritchard, 2017; Schaner et al., 2012).

In general, meltwater has a much smaller contribution to the large rivers in the central and eastern HKKH (including the Himalaya) compared to the western HKKH, due to the

high levels of monsoon rainfall at lower elevations in the eastern regions (Kaser et al., 2010; Pritchard, 2017). Bookhagen and Burbank (2010) suggest that snowmelt accounts for about 20 % of river flow in the eastern and central Himalaya, but individual river catchments vary considerably. In the Ganges River Basin (which covers much of the Himalaya), Immerzeel et al. (2010) calculated that 10 % of downstream discharge is due to snow and glacier melt, of which 40 % is from glaciers.

Approximately 240 million people live in the mountainous areas of the HKKH (Wester et al., 2019). These communities may be more vulnerable to changes in the water supply than those at lower elevations (Wahid et al., 2014). Meltwater can provide a large contribution to the smaller, tributary rivers that these communities rely on, sometimes providing over 50 % of the river discharge for at least one month per year (Kaser et al., 2010; Schaner et al., 2012). If the quantity or timing of the precipitation or snow and ice melt changes, it could have serious consequences for these populations (Bookhagen and Burbank, 2010). As the glaciers shrink, initially the runoff to the rivers will remain stable or possibly increase, but in a few decades the supply of water could decrease dramatically and suddenly (Barnett et al., 2005; Laghari et al., 2012).

Uses of water in the HKKH

There are a number of risks from changing water patterns facing industries in the HKKH. The predominant industry in Nepal, for example, is agriculture, which is highly dependent on water supply from rivers (Shrestha and Aryal, 2011). Further west in the Indus River Basin, almost all of the water is extracted to irrigate crops for the 237 million people who live there (Laghari et al., 2012). In addition to agriculture, hydroelectric power provides a large proportion of the electricity in HKKH, and is set to expand rapidly in the near future (National Research Council, 2012; Zarfl et al., 2015).

Glacier lake outburst floods

For the populations living close to the glaciers in the mountains, Glacier Lake Outburst Floods (GLOFs) are a significant natural hazard (National Research Council, 2012). GLOFs usually occur when a glacier retreats, leaving a gap between the terminus of the glacier and the moraine. The moraine forms a dam, behind which a glacier lake is formed from the glacier meltwater. It is also possible for the lake to be dammed by the glacier itself. When one of these glacier lakes drains suddenly, it causes flooding. GLOFs can be devastating

to communities living downstream and destroy hydroelectric power stations (Shrestha and Aryal, 2011), and glacier lakes in Nepal are growing particularly rapidly (National Research Council, 2012). In addition, melting glaciers can leave steep slopes exposed and susceptible to landslides (Dadson and Church, 2005).

2.2 Local valley circulations

2.2.1 Importance of valley winds

Understanding the local valley wind regimes in the HKKH is key to better understanding the drivers of the glacio-hydro-meteorological system. There are a number of ways in which winds in the valleys affect other meteorological variables, as well as glacier melt. Although the monsoon is the main driver of precipitation in Himalayan valleys, the local valley wind regimes also affect precipitation by transporting moisture and clouds up the slopes and valleys during the day, especially at high altitudes (Bollasina et al., 2002; Egger et al., 2002; Karki et al., 2017; Orr et al., 2017; Shea et al., 2015b; Tartari et al., 1998). It has been found that, whilst the monsoon drives most of the heaviest precipitation, much of the light, daily precipitation is affected by convection due to the diurnal cycle in winds in valleys, and these local effects are particularly important at high altitudes (Tartari et al., 1998). Shea et al. (2015b) observed that the valley circulations drive patterns of cloud, pushing the clouds which form at low altitudes to higher altitudes during the day, affecting the radiation reaching the snow and ice, and therefore glacier melt. Winds also affect the temperatures in Himalayan valleys (Immerzeel et al., 2014). A large uncertainty in glacier modelling is the effect of the wind on the snowfall patterns and redistribution of snow in the valley (Wagnon et al., 2013). In addition, black carbon blown to the glaciers from lower down the valley can affect glacier melt rates (Bonasoni et al., 2012; Xu et al., 2009). Thus, the local wind regime plays an important role, ultimately, in glacier accumulation, ablation, and therefore mass balance.

2.2.2 Diurnal valley wind systems

Two important thermal wind mechanisms that occur in valleys worldwide are those that cause slope winds and valley winds (Whiteman, 2000; Zardi and Whiteman, 2013). Both mechanisms are the result of forcing from differential heating in the valley, which causes a pressure gradient and therefore wind acceleration. Slope winds blow upslope during the day and downslope at night. They are caused by the heating (cooling) of the ground during the day (night), leading to a local horizontal pressure difference between the air at the slope

surface and at the same altitude away from the slope. Valley winds blow along the valley axis, up-valley during the day and down-valley at night. They are formed by the unequal heating of the air in the valley or between the valley and the wider surroundings, also leading to a pressure difference. I will refer collectively to the winds on the slopes and in the valleys, including these two mechanisms, as the local valley wind regime. These two mechanisms are illustrated in Fig. 2.2. Two other wind mechanisms can occur around valleys and mountains, cross-valley winds and mountain to plain winds (Whiteman, 2000). If one wall of the valley is heated more than the other, a cross-wind can develop due to the temperature (and therefore pressure) difference. In addition, there can be pressure differences between air over a mountain and air at the same elevation away from the mountain, leading to a larger-scale wind, known as the mountain to plain wind. The latter two mechanisms will not be discussed in this thesis (cross-valley winds are generally weaker than valley and slope winds (Whiteman, 2000)).

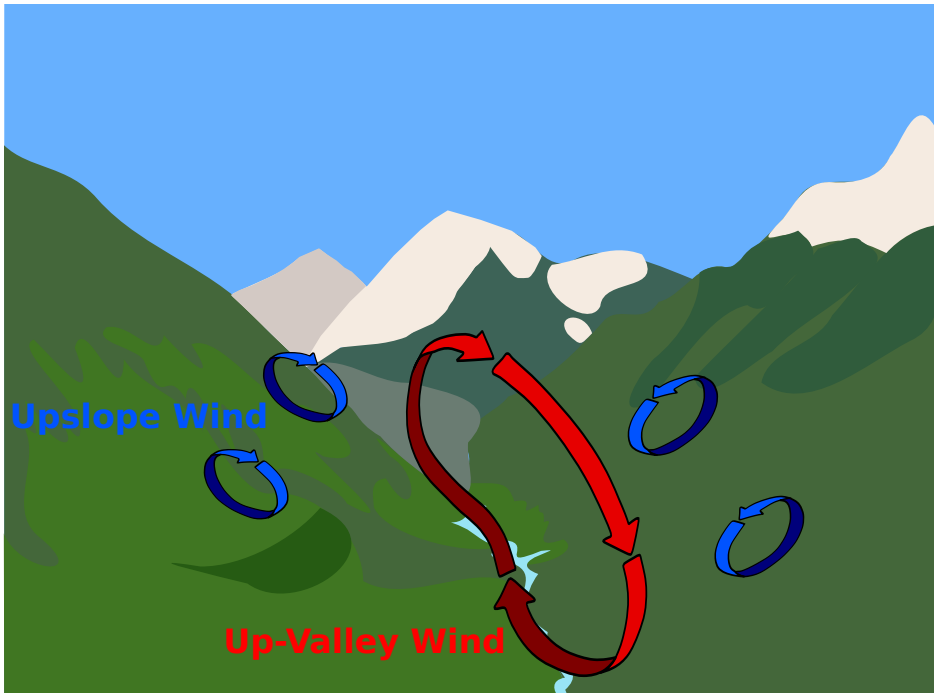

Fig. 2.2 Illustration of the local valley wind regime during the day. Wind travels up-valley and upslope near the surface during the day, with a return flow higher in the atmosphere.

There have been a number of idealised studies in recent years which examine the mechanisms controlling the valley and slope winds. In general, deeper, narrower valleys lead to stronger up-valley winds (Wagner et al., 2015a). This is due to narrower valleys with

comparatively smaller volumes having a larger temperature difference with the surrounding air, and therefore stronger up-valley winds (Wagner et al., 2015a,b). Steeper valleys also lead to stronger up-valley winds, due to both the smaller valley volume increasing the valley heating, and the steeper valley floor increasing the slope wind up the valley (Wagner et al., 2015b). Valleys with tributaries are more complex, and tributaries can affect the flux of air into and out of the valley (O'Steen, 2000).

There are many factors affecting the local valley wind regime. It has been observed that the local valley wind regime occurs most strongly on clear days in the summer, when the diurnal temperature difference is at its greatest (Lugauer and Winkler, 2005; Zardi and Whiteman, 2013). In general, synoptic winds can affect the local valley wind regime, especially in shallower valleys (Lang et al., 2015), but in the steep Nepalese Himalaya the variability within each day is thought to be dominated by the local circulations (Yasunari, 1976).

Lastly, surface cover is known to have a big effect on the local valley winds, especially the presence of ice, which restricts the surface temperature to 0 °C (Oerlemans and Grisogono, 2002; Zardi and Whiteman, 2013). If the air in the valley is above 0 °C, this can cause 'glacier winds' which are a shallow layer of katabatic wind during the day. The effects of valley surface will be discussed more fully in the context of Himalayan valleys in Sections 2.2.4 and 2.4.2.

2.2.3 Momentum budgets

Along with the idealised studies discussed above, momentum budgets are sometimes used to illuminate the most important mechanisms in various aspects of thermal wind regimes, in both idealised and real setups. Momentum budgets compare the magnitude of the terms in the fundamental equations driving a climate model. On a large scale, Van den Broeke et al. (2002) and van Angelen et al. (2011) analysed the dynamical terms in the momentum budget over the Antarctic Ice Sheet and the Greenland Ice Sheet, respectively. They both analysed the large-scale climatology of the katabatic winds on the ice sheets. Renfrew (2004) also used a momentum budget approach to investigate the dynamical mechanisms on an idealised slope representative of Antarctica or Greenland, and found that advection and the buoyancy force were dominant in the wind acceleration, but that the relative sizes of these forces varied considerably by location. On a smaller scale, Lehner and Whiteman (2014)

used a momentum budget analysis with the WRF model to determine the dominant role of the pressure gradient in forming a cross-valley circulation in a crater.

2.2.4 Mechanisms controlling wind in Himalayan valleys

The scarcity of weather stations and detailed modelling studies in the HKKH region means that there are still considerable uncertainties surrounding our understanding of the local valley wind regime. The presence of a local wind regime has been previously documented in valleys in this region (Inoue, 1976; Ohata et al., 1981; Shea et al., 2015b; Ueno et al., 2001, 2008; Yang et al., 2017; Zängl et al., 2001). However, few studies have investigated the forces driving the local wind regime. Sun et al. (2018) found that horizontal pressure gradients are crucial in the formation of the wind in the Arun Valley, Nepal (Fig. 2.3). Zängl et al. (2001) conducted a number of studies using real and idealised topography representing the large Kali Gandaki Valley, Nepalese Himalaya, to investigate the diurnal wind circulation (Fig. 2.3). As well as the pressure difference caused by the low pressure over the Tibetan Plateau, they found that the topography of the valley and the moisture in the air substantially affect the valley winds. For example, the more complex topography of the real simulation had slower downslope winds than the smoother idealised topography. Research is needed into the magnitude of the pressure gradient force, as well as the influence of other physical forces driving the wind acceleration, such as advection, the rotation (Coriolis effect) and curvature of the Earth, diffusion and turbulent vertical mixing.

Effects of snow and ice on the valley wind

As mentioned in Section 2.2.2, glaciers and snow cover can alter the local valley wind regime. This has been observed in the Dudh Koshi Valley, the focus of this thesis (Fig. 2.3), where an association between wind direction and snowfall events has been observed (Ohata et al., 1981). Glaciers can also cause anomalous local valley wind regimes in some valleys in the HKKH. For example, the Rongbuk Valley is characterised by a down-valley flow in the afternoon (Song et al., 2007; Zou et al., 2008). This was initially attributed to the glacier coverage causing glacier winds (Cai et al., 2007), however using a regional model to remove the glaciers from the valley, Ma et al. (2013) found that it was a combination of the glaciers and the local wind regime that caused the unusual flow. The Rongbuk and Dudh Koshi Valleys differ significantly in aspect, size and glacier coverage (Fig. 2.3). As such, the effects of the glaciers should also be examined in the Dudh Koshi Valley.

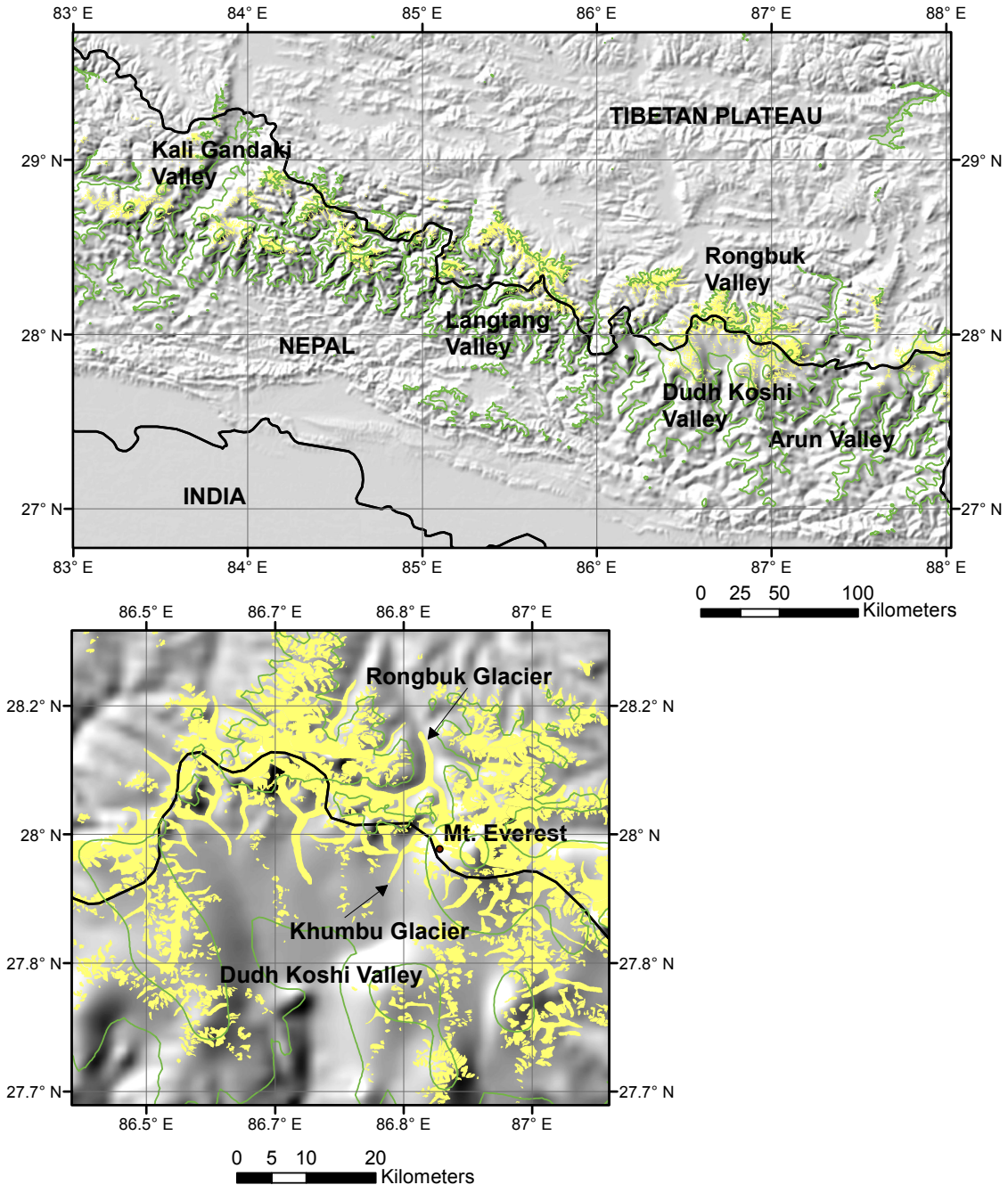

Fig. 2.3 Map showing part of the Nepalese Himalaya and the Tibetan Plateau, including some of the river valleys (top). The glacierised region (shown in yellow) of the Dudh Koshi and Rongbuk valleys is also shown (bottom), as well as the location of Mt. Everest.

2.3 Near-surface temperature variation

2.3.1 Importance of near-surface temperature lapse rates

Near-surface air temperature is an essential input for glacier modelling (Petersen et al., 2013). Glaciers are often in locations which are difficult to access, which necessitates an approximation of the temperature at a high elevation, often from a lower elevation weather station. As such, understanding how the near-surface air temperature varies with elevation is of vital importance to accurate glacier modelling. The most commonly used relationship to describe temperature variation with elevation is a linear lapse rate. Often, the term 'lapse rate' refers to the change in temperature with altitude above a point on the earth, i.e. the environmental lapse rate. However for the remainder of this thesis, the near-surface temperature lapse rate, i.e. the variation with near-surface air temperature as you move up in elevation, will be referred to as the lapse rate. This definition of lapse rate depends on the path chosen to measure it up the mountain, for example the lapse rate going up the southern side of the mountain, and the lapse rate going up the northern side of the mountain, are likely to differ due to differential heating by the sun. This definition of lapse rate has also be used by Steiner and Pellicciotti (2016).

Over Yala Glacier, in the Nepalese Himalaya, changing the lapse rate had a much larger impact on glacier melt than changing the gradient of precipitation. The lapse rate determines the equilibrium line altitude, and a change of under 250 m in the equilibrium line altitude caused a maximum difference in melt of 400 % in certain months (Immerzeel et al., 2014). On Vestari-Hagafellsjökull, in Iceland, a difference in lapse rate of 1 $^{\circ}$C km^{-1} led to a 600 mm water equivalent difference in melt over four months in the summer (Hodgkins et al., 2012).

Often, the environmental lapse rate (i.e. how the temperature varies with altitude away from the ground), is taken for such approximations (often assumed to be 6.5 $^{\circ}$C km^{-1}) (Arnold et al., 2006; Nolin et al., 2010). However numerous studies have reported that the near-surface temperature lapse rate is lower than the environmental lapse rate (Heynen et al., 2016; Minder et al., 2010; Wang et al., 2018; Yang et al., 2017).

2.3.2 Variability of near-surface temperature lapse rates

Various studies have looked at the variation in lapse rates, and near-surface air temperature more generally, including the relationship between lapse rate and other meteorological variables, and the dependence of the lapse rate on topography.

Seasonal variation in lapse rates is of particular importance. On a large scale, analysis of 20 years' worth of temperature measurements in Nepal found the steepest lapse rates in the pre-monsoon season (followed by the post-monsoon season) and the shallowest in winter (followed by the monsoon season), and also suggested that warmer temperatures and drier conditions are associated with steeper lapse rates (Kattel et al., 2013). Over the southern slopes of the eastern Himalaya in Bhutan, shallow lapse rates were found in the monsoon season, associated with increased latent heating at high elevations and decreased sensible heat at lower elevations (Kattel et al., 2018). However, Wang et al. (2018) found substantial spatial variation in lapse rates over the Tibetan Plateau, analysed over a 4 year period. While the western and north-eastern areas showed steeper lapse rates in the warmer months, the opposite was found in the south-eastern areas. Over the Koshi basin (which includes the Dudh Koshi River Basin), in Nepal, Salerno et al. (2015) found lapse rates of $-6.5\,^{\circ}\mathrm{C\,km^{-1}}$ in the pre-monsoon season and $-5.7\,^{\circ}\mathrm{C\,km^{-1}}$ in the monsoon and post-monsoon seasons. This finding of similar lapse rates in the very humid monsoon season and the much drier post-monsoon suggests that the changes in humidity is not the only factor affecting lapse rates in this region. Both Salerno et al. (2015) and Kattel et al. (2013) suggest that the shallower lapse rates in the post-monsoon/winter seasons may be due to radiative cooling, but this has not been directly tested.

On a smaller scale, Yang et al. (2017) examined data from five stations over an elevation range from 2660 m asl to 5600 m asl over a four year period in the Dudh Koshi River Basin (Fig. 2.3). They found lapse rates were shallowest in winter, followed by the monsoon season (although when only data from the lower elevations stations were evaluated, the shallowest lapse rates were during the monsoon). They found substantially steeper lapse rates at the lower three stations compared to those derived from all five stations during the non-monsoon seasons. Yang et al. (2017) found shallower lapse rates in the Dudh Koshi Valley (over four years) compared to those found by Salerno et al. (2015) over the entire Koshi River Basin (over 20 years).

There have been a number of studies analysing lapse rates in the Langtang Valley, in the Nepalese Himalaya (Fig. 2.3). An early study analysing data from just three weather stations suggests that the near-surface air temperature is more variable over debris-covered ice than over clean-ice glaciers (Fujita and Sakai, 2000). Surprisingly, Fujita and Sakai (2000) found steeper lapse rates in more humid conditions, as well as steeper lapse rates when the air temperature overall was warmer, and the wind speeds lower (however each lapse rate was derived from just two stations). They suggest that the increased precipitation during periods of increased humidity could lead to more evaporation from the surface, and therefore latent cooling, which would be transported to the air temperature at 2 m through turbulent mixing.

Heynen et al. (2016) analysed data from up to 27 temperature sensors over a 2.75-year period in the Langtang Valley, following a previous study using a smaller spatial and temporal dataset in the same valley (Immerzeel et al., 2014) (Fig. 2.3). In smaller studies, it is possible that measurements from one station might substantially influence the lapse rate calculations. However Heynen et al. (2016) did not find substantially different lapse rates using the full 27 stations when compared to a smaller subset of stations. There is consistency between the years, but strong seasonal and diurnal variation in lapse rates (Heynen et al., 2016). They found the steepest lapse rates in the pre-monsoon, between $-6.0\,^{\circ}\mathrm{C\,km^{-1}}$ and $-6.4\,^{\circ}\mathrm{C\,km^{-1}}$, and shallowest lapse rates in the monsoon season of $-4.5\,^{\circ}\mathrm{C\,km^{-1}}$ to $-4.2\,^{\circ}\mathrm{C\,km^{-1}}$. However they did not find the shallow lapse rates in the winter that Yang et al. (2017) and Kattel et al. (2013) reported. Heynen et al. (2016) attribute the shallow monsoon lapse rates to latent heat release and increased cloud cover, which reduced temperature variation both along the valley, and between the day and night. The diurnal cycle in lapse rates shows the shallowest lapse rates in the early morning in all seasons (Heynen et al., 2016). Variability was also found between sensors at the same elevations across the valley. To my knowledge, the studies by Heynen et al. (2016) and Immerzeel et al. (2014), in the Langtang Valley, are the only studies analysing a high concentration of temperature data measurements off-glacier in a Himalayan valley. Heynen et al. (2016) point to a need for further understanding of the mechanisms affecting temperature variation, especially during the pre-monsoon.

Overall, Yadav et al. (2018) summarise a number of studies reporting lapse rates in the Himalaya, including those discussed above. There is a very large range in lapse rates, both within and between different studies. The seasonal variation is clear. Many studies find the pre-monsoon season to have steeper lapse rates than the monsoon season (Kattel et al., 2015; Pratap et al., 2013; Thayyen and Dimri, 2014; Thayyen et al., 2005a; Yadav et al.,

2018). However this did not necessarily hold true over debris-covered glaciers (Steiner and Pellicciotti, 2016), and there was no clear consensus for the other seasons.

2.3.3 Mechanisms of near-surface temperature variation in unglacierized valleys

A few studies have used idealised models to further understand the processes affecting near-surface air temperature over homogeneous land surfaces. There is still debate as to the effects of local valley circulations on daytime heat transfer. In general, there is agreement that in the morning, the near-surface air is heated through turbulent mixing, via the sensible heat flux from the ground (Schmidli, 2013; Serafin and Zardi, 2010). This heat is then transported away from the surface by advection, which is entrained back into the core of the valley by the reverse flow at higher elevation (Schmidli, 2013; Serafin and Zardi, 2010). However some heat may be transported away from the valley by advection (Schmidli, 2013). There is still some question as to whether this has a net heating or cooling effect on the valley, however the near-surface mechanisms by which turbulent mixing heats the near-surface air during the day, and advection cools the near-surface air, are well understood in dry, idealised valleys (Schmidli, 2013; Serafin and Zardi, 2010). The idealised studies discussed above have not included the effects of moisture or heterogeneous land surfaces, and it is thought that these additions could alter the results (Schmidli, 2013; Serafin and Zardi, 2010).

2.3.4 Near-surface temperature variation over clean-ice glaciers

Numerous studies have examined the influence of clean-ice glaciers and ice sheets on lapse rates, finding that over clean ice, near-surface lapse rates are generally shallower than the environmental lapse rate (Gardner et al., 2009; Hodgkins et al., 2012; Marshall et al., 2007). This is thought to be due, at least partly, to the effects of katabatic glacier winds.

Greuell and Böhm (1998) proposed a model of 2 m air temperature over a glacier, based on the katabatic wind flowing down a melting alpine glacier. The model only accounts for the effects of sensible heat exchange (by turbulent vertical mixing) and the movement of the parcel of air down the slope, i.e. it assumes radiative processes to be negligible, and assumes a dry atmosphere. As the parcel of air (with temperature greater than 0 °C, as is necessary for the glacier to be melting) moves down the slope due to the katabatic wind,

the potential temperature drops due to sensible heat exchange with the glacier surface. The model proposed by Greuell and Böhm (1998) is in a Lagrangian framework, i.e. it models the potential temperature following a parcel of air. Transferred into an Eulerian framework (as used in this thesis), this implies that advection is having a heating effect, as the parcels of air upwind have greater potential temperature than the parcels of wind downwind.

The Greuell and Böhm model has been tested in various studies (Ayala et al., 2015; Carturan et al., 2015; Petersen et al., 2013). Models based on the Greuell and Böhm (1998) method tend to produce the best results when there is a well-developed katabatic boundary layer (Carturan et al., 2015; Petersen et al., 2013). Ayala et al. (2015) found warming over the glacier tongue, thought to be due to advection or entrainment of warm air. Overall, the development of a katabatic boundary layer has been found to have a substantial effect on the lapse rates over clean-ice glaciers, with shallower lapse rates during periods of stronger katabatic winds, often eclipsing the effects of elevation (Petersen and Pellicciotti, 2011; Shea and Moore, 2010).

2.3.5 Near-surface temperature variation over debris-covered glaciers

There have been few studies examining temperature distribution over debris-covered glaciers. Debris-covered glaciers tend to have a small elevation range (Anderson and Anderson, 2016), making it difficult to measure lapse rates. As mentioned in Section 2.2.2, over clean ice glaciers, the surface temperature is restricted to a maximum of 0 °C (as above 0 °C the glacier surface starts to melt). If the air above the ground is warmer than 0 °C, the temperature (and therefore pressure) gradient can lead to katabatic winds. Unlike over clean-ice glaciers, katabatic winds do not generally form over debris-covered areas of a glacier. When the air temperature is above freezing during the day, the temperature of the debris cover is likely to heat up to or above the temperature of the air, and therefore the katabatic winds cannot form due to the lack of a 0 °C boundary with the glacier (Brock et al., 2010).

A few studies have looked at the variation in lapse rate on the debris-covered Miage Glacier, Italy, where there are steep lapse rates over the debris cover (Brock et al., 2010; Shaw et al., 2016). The lapse rate is steeper when there is less cloud, and generally steeper for high wind speeds, which are also associated with warmer temperatures. Up-glacier winds were associated with shallower lapse rates than down-glacier winds (Shaw et al., 2016). There is

thought to be a correlation between debris surface temperatures and air temperature at 2 m in low wind conditions, due to the large turbulent heating contribution to air temperature at 2 m (Foster et al., 2012). Thicker debris cover (which is generally at lower elevations on the glacier) tends to have a higher surface temperature (Brock et al., 2010; Nicholson and Benn, 2013), which could contribute to the steep lapse rates.

To my knowledge, there have only been two investigations of near-surface air temperature above a debris-covered glacier using more than a few sensors. One is the study on Miage Glacier discussed above, by Shaw et al. (2016). The other, Steiner and Pellicciotti (2016), examines air temperature variability over the Lirung Glacier, in the Langtang catchment of the Nepalese Himalaya (Fig. 2.3), over the same period as the corresponding study of off-glacier lapse rates by Heynen et al. (2016) discussed in Section 2.3.2. Steiner and Pellicciotti (2016) found that air temperature over the debris-covered area on Lirung glacier was higher than would be predicted using the lapse rate for the valley. They attribute this to the debris cover being drier than the surrounding area, and therefore warmer during the day. This effect was found to be greater during the day than at night, and greater during the pre- and post-monsoon seasons than the winter and monsoon seasons. At night, the lapse rate over the glacier could be described using a linear fit, however during the day it was not possible to ascertain a lapse rate for the debris-covered portion of the glacier (due to the small elevation range of approximately 200 m and the differential warming of the debris during the day).

2.4 Surface properties and model representation of debris-covered glaciers

2.4.1 Surface properties of debris-covered glaciers

There have been various attempts to measure the surface characteristics of debris-covered glaciers around the world. Debris-covered glaciers are found from the Nepalese Himalaya (Inoue and Yoshida, 1980; Kayastha et al., 2000; Lejeune et al., 2013; Nicholson and Benn, 2013; Quincey et al., 2017; Takeuchi et al., 2000), to the high-latitude glaciers in Svalbard (Nicholson and Benn, 2006), to ice-covered volcanoes in Chile (Brock et al., 2007), and even the McMurdo Ice Shelf, Antarctica (Glasser et al., 2006). As such, the debris properties vary considerably from place to place.

Various surface properties have been measured on debris-covered glaciers, which are relevant for the fluxes affecting near-surface air temperature and wind. Albedo varies considerably over debris-covered glaciers, from under 0.1 to over 0.9 when snow-covered (Brock et al., 2010; Inoue and Yoshida, 1980; Nicholson and Benn, 2013). However over Himalayan glaciers most studies suggest it is approximately 0.2 (when not snow covered) (Inoue and Yoshida, 1980; Kayastha et al., 2000; Lejeune et al., 2013; Nicholson and Benn, 2013; Takeuchi et al., 2000).

Surface roughness length is another variable which varies considerably over debris-covered glaciers. Both debris thickness and debris particle size can vary hugely over very small spatial scales (Inoue and Yoshida, 1980; McCarthy et al., 2017). On one glacier in Nepal, surface roughness lengths have been calculated from 0.005 m to 0.5 m (with median values from 0.03 m to 0.05 m) (Miles et al., 2017). Another recent study found roughness lengths to vary from 0.006 m to 0.043 m on a single glacier in Nepal (Rounce et al., 2015).

Rounce et al. (2015) found a similarly large range in thermal conductivity of debris cover over a single glacier, from 0.42 $\mathrm{W\,m^{-1}\,K^{-1}}$ to 2.28 $\mathrm{W\,m^{-1}\,K^{-1}}$. Lastly, emissivity is rarely measured in observational campaigns, and is often assumed to be 1 (Brock et al., 2007; Reid et al., 2012). Where it is reported it shows less variation than other variables, around 0.94 to 0.95 (Brock et al., 2010; Nicholson and Benn, 2006).

2.4.2 Debris cover in atmospheric modelling

To my knowledge, there has only been one attempt to include a representation of debris-covered glaciers in an atmospheric model (Collier et al., 2015). This has been introduced as part of a coupled atmosphere-glacier model (first developed using a clean-ice representation only, by Collier et al. (2013)), using the WRF model for the atmosphere modelling. As such, the surface fluxes are provided by the glacier model (Collier et al., 2014), and the debris thickness is needed as a model input, as the debris is split into multiple layers. The model has been tested over the Karakoram, and compared against a clean-ice version of the model (Collier et al., 2015).

The addition of debris cover to the model has a large impact on near-surface meteorological variables (Collier et al., 2015). The near-surface temperature lapse rate is shallower over the debris-covered glacier than in the corresponding clean-ice model, by over 1 $^{\circ}\mathrm{C\,km^{-1}}$.

There is a decrease in wind speed due to the addition of debris cover (due to the increase in surface roughness), and the winds over debris-covered ice are up-glacier during the day, in comparison to the clean-ice version of the model, which has katabatic winds throughout the day and night. Lastly, there is a large increase in the planetary boundary layer height, which reaches 1.4 km over debris-cover, as opposed to approximately 200 m over clean ice.

2.5 Study region

The Dudh Koshi River Basin is in the eastern Nepalese Himalaya, along the southern slopes of Mt Everest (Fig. 2.4) and includes the Khumbu region. The altitude ranges from a few hundred metres above sea level (m asl) to the top of Mt Everest at 8848 m asl (Fig. 2.4). In the lower regions, the valley is forested, turning to bare rock with glaciers across the higher altitude areas (Magnani et al., 2018). Approximately 25 % of the glacierised area is debris-covered (Salerno et al., 2017; Shea et al., 2015a). There are strong seasonal and diurnal cycles of temperature, wind and precipitation, as discussed further below.

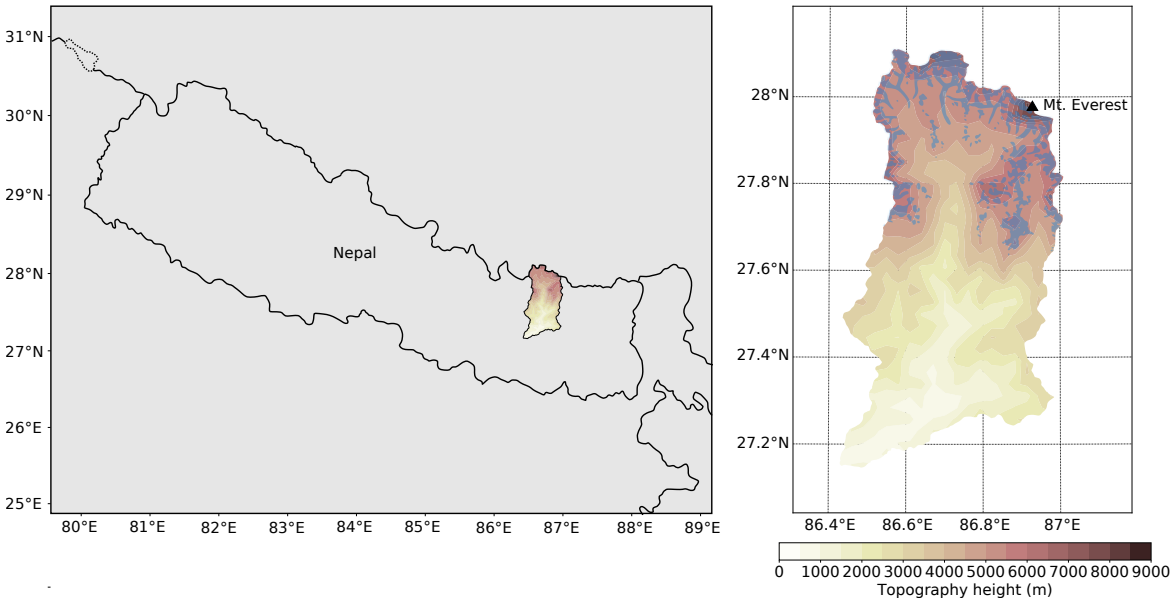

Fig. 2.4 The location of the Dudh Koshi River Basin in Nepal (left) and the topographic height from the WRF model (shaded contours) of the Dudh Koshi River Basin (right). The glacierised region is shown in blue shading, and the location of Mt. Everest is marked as a black triangle. The glacier outline is taken from the Randolph Glacier Inventory (RGI Consortium, 2015).

The warmest temperatures occur during the monsoon season, and the coldest in the winter months (Wagnon et al., 2013; Yang et al., 2017). There is a diurnal cycle in temperature throughout the year, however the amplitude of the diurnal cycle is reduced during the monsoon season, due to the increased cloud cover (Inoue, 1976; Ohata et al., 1981; Yang et al., 2017).

The local wind regime is characterised by up-valley winds during the day throughout the year, with weak up-valley winds at night during the monsoon season and some evidence of down-valley winds at night in the winter (Inoue, 1976; Ohata et al., 1981; Shea et al., 2015b; Ueno et al., 2001; Yang et al., 2017). Peak wind speeds tend to be in the early afternoon (Ohata et al., 1981). In the monsoon season the winds are generally light, and dominated by the valley circulations (Tartari et al., 1998; Ueno et al., 2001). The nighttime down-valley wind seen in a classic diurnal circulation have not been recorded during the monsoon (Inoue and Yoshida, 1980; Ohata et al., 1981; Ueno et al., 2001). This is thought to be due to latent heat release due to the increased cloud cover in the monsoon season (Ohata et al., 1981). In the winter, the influence of the subtropical jet stream can lead to wind speeds which exceed $35\,\mathrm{m\,s^{-1}}$ (Tartari et al., 1998). The local valley wind regime drives cloud patterns, pushing the clouds which form at low altitudes to higher altitudes during the day (Shea et al., 2015b).

Most of the precipitation falls during the monsoon season, with about 80 % of the annual precipitation falling during these months (Tartari et al., 1998; Wagnon et al., 2013). Precipitation decreases with altitude after about 2500 m asl (Salerno et al., 2015), although may be uniform at higher elevations (Barry, 2008; Tartari et al., 1998; Yang et al., 2017). During the monsoon season, oscillations in the anticyclone over Tibet cause a periodic cycle in the strength of the monsoon (Yasunari, 1976). This leads to heavy precipitation every ten days or so from the synoptic-scale monsoon, with regular local, lighter showers caused by valley circulations (Barry, 2008). In general, precipitation at lower elevations is thought to be caused by the large-scale monsoon rains, whereas at higher elevations the precipitation is more strongly affected by the daily convective precipitation caused by the valley winds (Bollasina et al., 2002; Tartari et al., 1998; Yasunari and Inoue, 1978).

2.6 Relevance of previous work for key thesis aims

Due to the variability in climate and glacier characteristics in the HKKH region, it is difficult to generalise from one region to another (National Research Council, 2012). In order to make

realistic parameterisations in large-scale climate models, better understanding of the regional scale processes in the valleys of the HKKH is needed. Although few regional modelling studies have been conducted in the Himalaya, those that have been conducted suggest that, at a high spatial resolution, regional modelling can be a useful tool to investigate meteorological processes in glacierised valleys in the HKKH. This thesis will build on the results of the studies discussed above. In particular, it will build on the regional climate modelling studies outlined in Section 2.1.3, by taking the recommendations for high spatial resolution, and following the suggestions for physics options.

2.6.1 Relevance of previous work on valley wind regimes

Section 2.2 highlights the importance of understanding local valley wind regimes in valleys in the HKKH. Local valley winds are known to affect temperature, precipitation and the movement of snow and pollutants. This makes understanding these winds crucial, ultimately, for understanding changes to glacier mass balance. In addition, parametrisations of local valley wind regimes are needed for large-scale climate models.

The theoretical principles of local valley wind systems are understood, with changes in pressure causing winds within the valleys. However there are still questions remaining about how real topographies and atmospheric conditions affect these winds. In the HKKH, diurnal valley winds have been observed, often through a few point-based observations. There is a need for further studies on the local wind regimes over entire valleys, and especially into the mechanisms controlling these winds.

Momentum budget analysis has been usefully employed to analyse the mechanisms forcing various thermal wind regimes, including large-scale katabatic winds and small-scale winds in craters. Chapter 3 will apply a momentum budget analysis to determine the forces affecting the acceleration of the local wind regime in the Dudh Koshi Valley. To my knowledge, this analysis has never been used previously to investigate the wind in a valley in the HKKH.

2.6.2 Relevance of previous work on near-surface temperature lapse rates

Section 2.3.1 highlights the importance of understanding variability in near-surface temperature lapse rates for accurate glacier modelling. There is considerable variation in lapse rates, both spatially and temporally. For example, lapse rate steepness varies by season, but this seasonality is different for different areas of the Himalaya and the Tibetan Plateau (Wang et al., 2018; Yadav et al., 2018). As such, further study is needed of lapse rates at a valley scale. The idealised studies discussed in Section 2.3.3 suggest that understanding the different contributions of the potential temperature budget is useful to fully understand the near-surface temperature variation.

Although there have been various attempts to model lapse rates over clean-ice glaciers (Ayala et al., 2015; Carturan et al., 2015; Greuell and Böhm, 1998; Petersen et al., 2013), there has been very little work on characterising the temperature variation over debris-covered glaciers (Shaw et al., 2016; Steiner and Pellicciotti, 2016). This motivates the second thesis aim, to understand the temperature variation in the Dudh Koshi Valley and over the Khumbu Glacier, and to use a temperature budget analysis to determine the controls on this temperature variation. These are addressed in Chapter 5.

2.6.3 Relevance of previous work on the effects of glaciers on meteorology

Section 2.2.4 highlights the important role that snow and ice can play in forming the local winds in valleys in the HKKH. The direct effects of snow and ice have only been investigated through one modelling study in the Karakoram, in a valley very different to the Dudh Koshi Valley. Chapter 3 will build on these results by conducting a sensitivity experiment to examine the role of glaciers in the formation of the local valley wind regime in the Dudh Koshi Valley. As discussed in Section 2.1.4, the glaciers in the HKKH are losing mass at a considerable rate. As such, understanding how this mass loss may affect the local wind regime is crucial for correct future predictions of meteorological variables.

Section 2.4.1 provides a summary of the measured surface properties of debris-covered glaciers, which will be used as a basis for the new debris cover addition to the WRF model in Chapter 4. Section 2.4.1 demonstrates the difficulties with using single values to represent surface properties of debris-covered glaciers, which are extremely heterogeneous. However,

the inclusion of debris cover in an atmosphere-glacier model by Collier et al. (2015) caused considerable changes to the near-surface meteorology. Although the variation in parameters such as albedo and surface roughness across debris-covered glaciers is large, it is not as large as the differences between debris-covered and clean-ice glaciers. Whilst the model introduced by Collier et al. (2015) is a powerful tool for measuring feedbacks between the glacier and the atmosphere, coupled models can be slow to run, and the discussion above points to a need for a simple and non-costly surface representation of debris-covered glaciers to be added to atmospheric models. This addition will be the focus of Chapter 4, which will also examine the effects of adding the debris-covered glacier category on the surface and near-surface meteorological variables, and validate it by comparison with measurements. The effects of the new debris cover addition, and particularly the effect on the near-surface temperature, will be further analysed in Chapter 5.

Chapter 3

Dynamical drivers of the local wind regime in a Himalayan valley

Wind in valleys in the Himalaya drives moisture and clouds up-valley, and also affects temperature. As such, understanding the local valley wind regimes is vital for future predictions of the glacio-hydro-meteorological system. This chapter uses the WRF regional climate model at a spatial resolution of 1 km to investigate the forces driving the local valley wind regime in a river basin in the Nepalese Himalaya, during July 2013 and January 2014. The model is compared against in situ observations, and the diurnal cycle of the wind is analysed. A momentum budget analysis of the model output is analysed to determine the drivers of the valley wind regime. Lastly, the glaciers in the model are removed, to analyse the impact of the glaciers on the local valley winds. This chapter forms the basis of the paper Potter et al. (2018), and many of the figures and much of the text is reproduced from that manuscript.

3.1 Model, observations and methods

The WRF model version 3.8.1 (Skamarock et al., 2008) was used to run a regional climate simulation over the Dudh Koshi River Basin, which includes the Khumbu region. Two month-long runs were conducted, for July 2013 and January 2014 (hereafter referred to as the 'summer' and 'winter' runs respectively). The near-surface air temperature and wind speed and direction from the model was then compared to observations.

3.1.1 Atmospheric model description

Previous high-resolution atmospheric modelling studies in the Nepalese Himalaya suggest that a horizontal resolution of around 1 km is necessary to accurately represent valley winds (Collier and Immerzeel, 2015; Karki et al., 2017; Orr et al., 2017). This is therefore selected as the resolution of the innermost domain, which is nested within three other domains at resolutions of 27, 9 and 3 km (Fig. 3.1 (a)). It is noted that a 1 km grid resolution is only just high enough to resolve the glaciers, and a higher resolution could lead to more accurate representation of the topography, glacier mask, and the atmospheric processes taking place. However, due to computational limitations, it was not possible to run the WRF model at a resolution higher than 1 km. Although it can limit the interaction between small- and large-scale flow in the outer domains, one-way nesting is used for consistency with the glacier removal experiments. The model has 50 vertical levels from the surface to 50 hPa, with around seven levels located in the lowest kilometre.

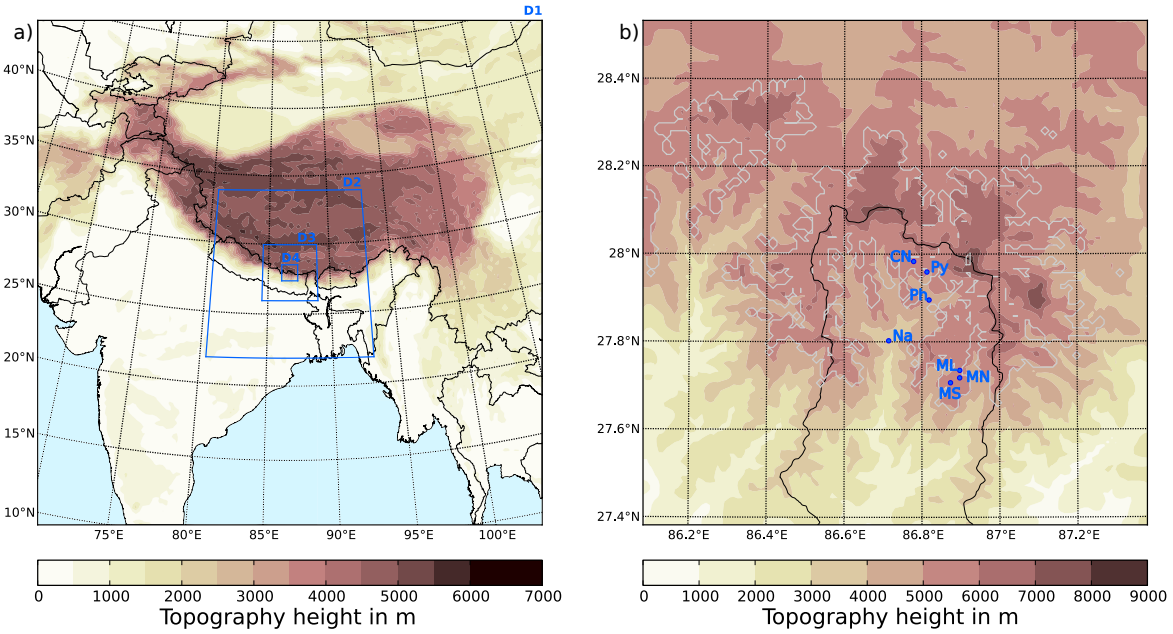

Fig. 3.1 The geographical extent of the four WRF model domains (labelled D1 to D4) and the topographic height of the outer domain (m; shading) (a).The innermost 1 km domain (D4) showing the topographic height (m; shading) (b), the watershed outline of the Dudh Koshi River Basin (solid black line), the extent of the permanent snow and ice in the model (solid grey line), and the location of the automatic weather stations used in this study at Namche (Na), Pheriche (Ph), Pyramd (Py), Mera-Naulek (MN), Mera La (ML), Changri Nup (CN) and Mera Summit (MS) (blue filled circles).

The default U.S. Geological Survey (USGS) WRF topography in the innermost domain has been replaced with 90 m resolution topography from the Shuttle Radar Topography Mission (SRTM) (Jarvis et al., 2008), as the USGS topography is not always fully accurate (Karki et al., 2017). This adjustment was made by Daniel Bannister, a postdoctoral research associate at the British Antarctic Survey. Both the USGS topography in the outer domains and the SRTM topography in the inner domain are interpolated to the model grid using a combination of three methods, a grid-cell average, a bi-linear interpolation of the nearest four source points, and an average of the nearest four source points. A small (5 km by 4 km) patch of smoothing is applied over Mt. Everest in the innermost domain, to improve model efficiency. This allowed the model time step in the inner domain to be increased from 1 s to $3.\dot{3}$ s.

The WRF model uses various datasets as input into the physics schemes used by the model. Two of these are the soil type dataset (variable `ISLTYP` in WRF) which determines the properties of the underlying soil (clay, water, sand, land-ice etc), and the landuse dataset (variable `LU_INDEX` in WRF) which determines the surface properties of the land (grassland, urban and built-up land, tundra, snow or ice etc). The permanent snow and ice (representing glaciers in the model) is poorly represented in the default (USGS) landuse dataset over the Hindu-Kush Karakoram Himalaya (Collier and Immerzeel, 2015; Orr et al., 2017), and so is adjusted in the innermost two domains to match the state-of-the-art Randolph Glacier Inventory (RGI) (RGI Consortium, 2015). This provides the most accurate worldwide glacier outlines available, and is supplemental to the Global Land Ice Measurements from Space (GLIMS) project. The adjustment to the WRF model landuse was also made by Daniel Bannister. In addition, in the underlying soil type 'land ice' is coarsely represented in the WRF model setup (due to the resolution of the underlying input dataset), so is altered to be consistent with the surface landuse 'permanent snow and ice', by changing the soil type to 'land ice' everywhere that the surface landuse is 'permanent snow and ice'. In the default WRF landuse types used in this chapter, debris cover is not represented in the model. This will be addressed in Chapter 4.

Most of the physics and dynamics options have been chosen following those used in Collier and Immerzeel (2015), who selected the physics schemes based on two short test simulations in a catchment in the Nepalese Himalaya, in the winter and summer. However the microphysics scheme has been chosen following the results and recommendations of Orr et al. (2017), who analysed a selection of both single and double moment microphysics

Table 3.1 Details of the WRF model setup

Domains and forcing data	
Number of domains	4
Horizontal grid resolution	27 km, 9 km, 3 km, 1 km
Number of vertical levels	50
Model top	50 hPa
Topography data	Domains 1, 2 & 3: U.S. Geological Survey 30 s; domain 4: Shuttle Radar Topography Mission (Jarvis et al., 2008) with a 5 km by 4 km patch of smoothing over Mt. Everest
Land surface and snow and ice data	Domains 1 & 2: U.S. Geological Survey 30 s; domains 3 & 4: U.S. Geological Survey 30 s, adjusted using the Randolph Glacier Inventory (RGI Consortium, 2015)
Forcing data	ERA-Interim (Dee et al., 2011)
Spin-up period	14 days
Physics schemes	
Microphysics	Morrison double-moment (Morrison et al., 2009)
Radiation	CAM scheme (Collins et al., 2004)
Surface layer	Revised MM5 (Jiménez et al., 2012)
Land surface	Noah-MP (multi-physics) (Niu et al., 2011)
Planetary boundary layer	Mellor-Yamada Nakanishi and Niino level 2.5 (Nakanishi and Niino, 2004)
Cumulus	Domains 1 & 2: Kain-Fritsch (Ma and Tan, 2009); domains 3 & 4: none
Slope-dependent radiation	on
Shadowing of neighbouring grid cells	on
Dynamics	
Diffusion	Calculated in real space
Eddy diffusion coefficient	Diagnosed from horizontal diffusion
Short-wave numerical noise filter	On
Top of model damping	Rayleigh damping in top 5000 m of model
Time off-centring for vertical sound waves	Set to 1

schemes over the same catchment as Collier and Immerzeel (2015), and found that the double moment Morrison scheme performed best. The model is initialised and forced by ERA-Interim data at the boundaries every six hours (Dee et al., 2011) and the spinnup period is 14 days. This was chosen after checking the speed of stabilisation of soil properties such as soil moisture content and soil temperature, which suggested that over a week was needed for stabilisation. Soil moisture is initialised and input every six hours by the WRF Preprocessing System (WPS), which calculates the soil moisture from the volumetric soil water (at four soil layers) given in the ERA-Interim data. Soil temperature is similarly interpolated from the soil temperature given at four soil layers in ERA-Interim. For full model details, see Table 3.1. Although not explicitly tested, it is assumed that the WRF model represents the mean wind and temperature over each month at least as well as the ERA-Interim data used to force the model.

Table 3.2 Details of the AWSs. The latitude, longitude and elevation of each station is shown. In addition the surface type of the AWS is shown, along with the height at which the air temperature and wind speed and direction are measured, and the percentage of missing data for each variable and each month. Lastly, the data provider is shown.

Name	Latitude (°N)	Longitude (°E)	Height (m asl)	Surface type	Temperature measured height (cm) (% missing in July, January)	Wind measured height (cm) (% missing in July, January)	Data provided by
Namche	27.8023	86.7146	3570	off-glacier	200 (0, 54)	500 (0, 53.90)	Ev-K2-CNR
Pheriche	27.8954	86.8188	4260	off-glacier	200 (0.13, 0)	500 (0.13, 0)	Ev-K2-CNR
Pyramid	27.9592	86.8133	5035	off-glacier	200 (43.68, 0.13)	500 (42.61, 0)	Ev-K2-CNR
Mera La	27.7347	86.8977	5350	off-glacier	235 (NA, 0)	285 (speed: NA , 0, direction: NA, 0.40)	glacioclim
Mera-Naulek	27.7177	86.8974	5360	clean-ice glacier	141 (0.13, 0)	195 (speed: 7.39, 0, direction: 0, 0.13)	glacioclim
Changri Nup	27.9832	86.7791	5363	debris-covered glacier	152 (22.72, NA)	204 (speed: 24.46, NA, direction: 22.72, NA)	glacioclim
Mera Summit	27.7065	86.8737	6352	clean-ice glacier	165 (NA, 0)	320 (speed: NA, 0, direction: NA, 0.54)	glacioclim

3.1.2 Observational data

Model results are compared against data from seven Automatic Weather Stations (AWSs) that are available for the valley. Their locations can be seen in Fig. 3.1. Of these, four of the AWSs, at Namche, Pheriche, Pyramid and Mera-Naulek, have data for both July 2013 and January 2014. In addition, there is data from Changri Nup for July 2013 and Mera La and Mera Summit for January 2014. For full details for the AWSs see Table 3.2. The data for Namche, Pheriche and Pyramid were provided by the Ev-K2-CNR group, and the details provided in Table 3.2 came from http://geonetwork.evk2cnr.org. The sensors for the wind measurements were supplied by LSI-Lastem (Italy). Yang et al. (2017) has further details of their locations and instrumentation. The data at Mera La, Mera-Naulek, Changri Nup and Mera Summit came from the glacioclim group (Université Grenoble Alpes) and the information shown in Table 3.2 for these stations comes from https://glacioclim.osug.fr/spip.php?article75. Shea et al. (2015b) has further details of the location and instrumentation of these AWSs. Instantaneous hourly measurements of wind speed and direction are used for this analysis.

3.1.3 Momentum budget

The dynamics in the WRF model are based on the moist flux-form nonhydrostatic Euler equations (Skamarock et al., 2008). The horizontal momentum components of these equations are:

$$\partial_t U = -\nabla \cdot \mathbf{V}u - (\mu_d \alpha \partial_x p + (\alpha/\alpha_d)\partial_\eta p \partial_x \phi) + F_U \tag{3.1}$$

$$\partial_t V = -\nabla \cdot \mathbf{V}v - (\mu_d \alpha \partial_y p + (\alpha/\alpha_d)\partial_\eta p \partial_y \phi) + F_V \tag{3.2}$$

Here $\mu_d(x,y)$ is the mass of dry air in the column and p is the pressure. The coupled wind velocity $\mathbf{V} = (U,V,W) = \mu_d \mathbf{v}$, where U and V are the mass coupled zonal and meridional velocities and W is the mass coupled vertical velocity, and $\mathbf{v} = (u,v,w)$ is the uncoupled velocity. The vertical coordinate used by WRF is given by $\eta = (p_{dh} - p_{dht})/\mu_d$ where p_{dh} is the hydrostatic pressure of the dry atmosphere and p_{dht} represents this value at the top of the model. ϕ is the geopotential and $\nabla\cdot$ is the divergence. The inverse density of dry air is given by α_d, with $\alpha = \alpha_d(1+q_v+q_c...)^{-1}$ where q_v, q_c are the mixing ratios of vapour and cloud, respectively. The ∂_* sign denotes partial differentiation with respect to subscript *. See Skamarock et al. (2008) for further details.

In Eq. 3.1 the zonal wind component of the mass coupled acceleration at a fixed point in space is represented by $\partial_t U$. The advection term is given by $-\nabla \cdot \mathbf{V}u$. The forcing term F_U represents acceleration due to the effects of Coriolis and curvature, horizontal and numerical diffusion and the contribution from model physics, which here arises from sub-grid scale turbulent vertical mixing, hereafter referred to as turbulent vertical mixing. The term $-(\mu_d \alpha \partial_x p + (\alpha/\alpha_d)\partial_\eta p \partial_x \phi)$ represents the pressure gradient force. The effects of damping at the top of the model have been ignored as these only affect the winds in the stratosphere (not shown). Eq. 3.2 is analogous to Eq. 3.1, but for the meridional wind component. The advection, Coriolis, curvature, horizontal diffusion, numerical diffusion, turbulent vertical mixing and pressure gradient terms were extracted from the WRF model using code adapted from Moisseeva (2014) and following the method suggested by Lehner (2012). Full details of the code extraction can be found in Appendix B.

The pressure gradient is predominantly caused by gradients in potential temperature, and its effects close to the ground are highly dependent on topography (Moisseeva and Steyn, 2014; Skamarock et al., 2008). It is driven by two scales of temperature variations, both synoptic-scale temperature differences and the local temperature differences which contribute to slope and valley winds. Advection is related to the horizontal and vertical differences in wind velocity, and represents, therefore, the influence of the surrounding wind on the wind at the point being measured. Turbulent vertical mixing acts throughout the atmospheric column (Skamarock et al., 2008). Numerical diffusion is a non-physical parameter, which is added

for model stability, necessary over the complex topography. Numerical diffusion acts to dampen poorly resolved features with wavelengths of twice the horizontal resolution (i.e. 2 km in this set up), and has an effect on both momentum and potential temperature (Knievel et al., 2007). In the following analysis, all forces have been divided by the mass of dry air in the column, and are therefore represented as the components of (uncoupled) acceleration (i.e. $\partial_t u$, $\partial_t v$).

3.1.4 Methods

The July 2013 and January 2014 periods were chosen due to data availability of the observation measurements, however these months are found to be broadly representative of recent climatology in the region when compared with previous studies. This suggests that these results can be considered representative of the region in recent years.

Wagnon et al. (2013) analysed the 2 m air temperature at Namche, Pheriche and Pyramid between 2003 and 2012. The approximate average temperatures in July for that study (and corresponding averages from the July 2013 observations used in this study) were 11 (10.8) °C, 8 (7.8) °C and 4 (4.1) °C at Namche, Pheriche and Pyramid respectively. The equivalent values for January in the Wagnon et al. (2013) study (and the January 2014 in this study) are -1 (0.2) °C, -6 (-6.1) °C, -8 (-7.8) °C. As such, the temperature in July 2013 and January 2014 is representative of the temperatures for July and January between 2003 and 2012.

In addition, Yang et al. (2017) analysed the diurnal cycle in the wind at the same stations between 2007 and 2011, and found that the average minimum (maximum) meridional wind velocity for the full monsoon season was approximately $0.5\,(3.5)$ m s^{-1}, $1\,(6)$ m s^{-1} and $0.8\,(3.6)$ m s^{-1} at Namche, Pheriche and Pyramid, respectively. The observations from July 2013 used in this study have approximate average minimum (maximum) wind speeds of $0.5\,(3.9)$ m s^{-1}, $1\,(4)$ m s^{-1} and $0.9\,(4)$ m s^{-1} at Namche, Pheriche and Pyramid respectively (Fig. 3.3 (b), (d) and (f)). This indicates that the wind speed in July 2013 is broadly similar to the wind speed in this region between 2007 and 2011. Equivalent values from Yang et al. (2017) were not available for the winter months.

To compare the model outputs to the AWS measurements, the model hourly air temperature at 2 m, and model hourly wind velocity at 10 m at the nearest grid point to the AWS

location is selected, where the 'grid point' is in the centre of the grid box for temperature, and staggered for the meridional and zonal winds (Skamarock et al., 2008) (note the 2 m and 10 m heights were chosen as these heights can be outputted directly from the WRF model). The use of the nearest model grid point to the observations was compared to a linear interpolation to the AWS location, but there was little difference between the nearest point and linear interpolation (not shown). The model temperature at 2 m is adjusted to account for the difference between the model elevation and actual AWS elevation, using the average air temperature at 2 m lapse rate calculated over the entire model domain at each time step. The average lapse rate at each time step is calculated by taking the slope of a linear regression between air temperature at 2 m and elevation, as illustrated in Fig. 3.2. No attempt is made to adjust the air temperature from the measurement height to 2 m (all the air temperature measurements are taken from between 1.41 m and 2.35 m; Table 3.2).

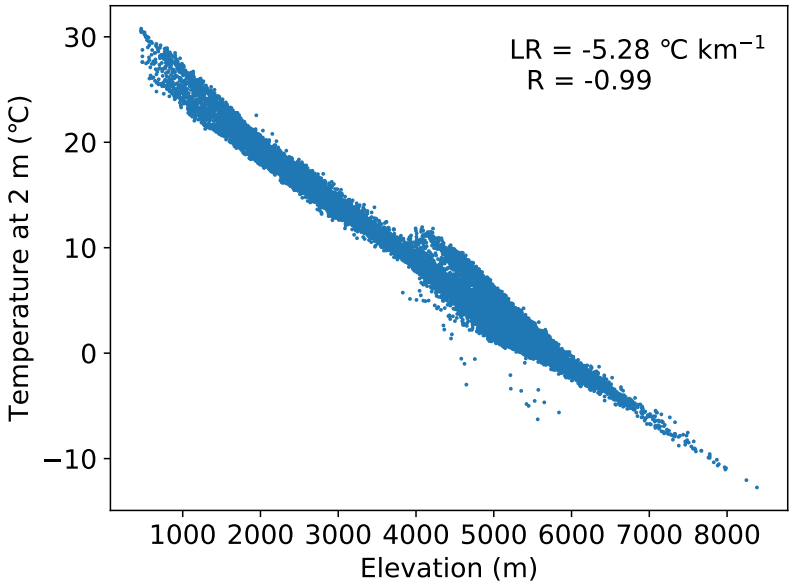

Fig. 3.2 The linear regression between air temperature at 2 m and elevation, taken from every point in the inner model domain at one time step. The lapse rate (LR), and the correlation coefficient (R) are also shown.

The observational wind data, however, are adjusted to a height of 10 m by assuming conditions of neutral stability and using a logarithmic profile, as suggested in Whiteman (2000). This calculation requires an estimate of the surface roughness length (z_0) of the terrain, which is assumed to be 0.25 m high grass in the summer with $z_0 = 0.04$ m (Oke, 2002) at the Namche, Pheriche and Pyramid sites, which are off-glacier. By contrast, the

Changri Nup station is on debris-covered ice, so the roughness length in the summer is taken as $z_0 = 0.02$ m, from Quincey et al. (2017). Mera Naulek is on clean ice, but is often snow-covered, so the roughness length is taken as is taken as that for snow, $z_0 = 0.001$ m (Oke, 2002). All stations are assumed to be snow covered during January 2014, with $z_0 = 0.001$ m (Oke, 2002). All results are in local time (LT) (UTC+5:45 hr), and only the results of the Dudh Koshi River Basin, in the innermost 1 km domain, are analysed. The assumption of neutral stability may introduce errors into the results, however the adjustment only slightly changes the observed wind speeds. For example the unadjusted maximum daily wind speed at Pheriche is approximately $4\,\mathrm{m\,s^{-1}}$, and the adjusted wind speed is just over $4\,\mathrm{m\,s^{-1}}$.

To investigate the effects of glacier cover on the local valley wind, the model runs are repeated but with all permanent snow and ice (referred to as the glacierised region; Fig. 3.1) removed by changing the landuse (variable `LU_INDEX` in the WRF model, as mentioned above) to barren ground, and the underlying soil type (variable `ISLTYP` in the WRF model, as mentioned above) from land ice to rock. No other aspects of the model are changed, and snow can still fall during the run. The experiments with the glacierised region removed will be referred to as the 'perturbation experiments'.

To test for statistical significance in the change in the wind velocity when the glacierised region is removed from the model, a paired two-tailed Student's t-test was conducted at each point in the inner model domain, with autocorrelation taken into account. A paired bootstrap method (von Storch and Zwiers, 1999) was also employed to test for significance. This produced a very similar result to the t-test, but to be conservative only the data points which were significant in both tests are shown as significant in the results. For the full details of the statistical methods used, see Appendix A.

Two attempts were made to split the pressure gradient into local and synoptic scales. In the first method, similar to that used by Moisseeva (2014), the pressure gradient is linearly interpolated from WRF model levels to a height of 300 hPa at each model point, to represent the synoptic pressure gradient. The local pressure gradient is found by taking the difference between the pressure gradient at the lowest model level and the synoptic pressure gradient. This worked well in the summer run, where the pressure gradient varies very little above the atmospheric boundary layer. However it was not suitable for use in the winter run, where the pressure gradient varies considerably at higher altitudes. Second, the model was run at a resolution of 60 km, to determine the large-scale pressure gradient. This resolution is

similar to the reanalysis forcing data resolution. However this large-scale pressure gradient was found to be very noisy, and still affected by topography, so not thought to be suitable to represent the synoptic scale pressure gradient. Due to the issues with both methods, the pressure gradient has not been split in any of the figures in this chapter.

3.2 Results

3.2.1 Summer run

Model Validation and wind characteristics

The 10 m wind is compared between the model and observations, to validate the model and ensure that the model is producing the right wind characteristics. In addition, due to the importance of temperature in forming the local pressure gradient, the model monthly averaged 2 m air temperature is compared to the observations at each of the five sites to validate the model.

The model represents the off-glacier stations (Namche, Pheriche and Pyramid) well for temperature (Fig. 3.3 (a), (c) and (e)), with root mean square errors (RMSEs) of 1.18, 1.17 and 1.33 °C, respectively. At all three stations there is a strong diurnal cycle with peak temperatures around midday. At Namche and Pheriche (Fig 3.3 (a) and (c) respectively), the model has peak temperature approximately two hours after the observations record peak temperature.

At the on-glacier stations (Mera-Naulek and Changri Nup) the model represents the 2 m air temperature less well (Fig. 3.3 (g) and (i)), with RMSEs of 1.59 and 3.05 °C, respectively. At Mera-Naulek the model shows a weak but consistent diurnal cycle, with temperatures during the day approximately 2 °C higher than at night. Between 18:00 and 06:00 LT, the model matches the observations well. At midday, the model is about 1 °C too cold. The observations show peak temperatures at sunrise (and a second, smaller peak at sunset). This is likely to be an error in the observations. The cause of this error is unknown, but one possible reason could be from overheating due to ventilation inefficiency in the morning (and evening).

At Changri Nup (Fig. 3.3 (i)), the AWS is on debris-covered ice, but there is no debris-cover representation in the model. The model shows a weak diurnal cycle in 2 m air temperature with an amplitude of around 2 °C, whereas the debris cover in the observations has the effect of increasing the daytime temperature to 7 °C to 8 °C above the nighttime temperature. There is a gap in the night-time observations at Changri Nup, making it difficult to determine how accurately the model is representing the 2 m air temperature during this period, but it appears to match well for the few nighttime observations available (from about 22:00 to 02:00). The lack of debris cover in the model is addressed in Chapter 4. At all five stations,

in both the model and observations, there is very little variability in the diurnal cycle in temperature over the month, i.e. the standard deviation of the air temperature at 2 m for each hour is much smaller than the magnitude of the diurnal cycle (Fig. 3.3 (a), (c), (e), (g) and (i)).

At Namche and Pheriche, the 10 m wind speed and direction is well represented by the model (Fig. 3.3 (b) and (d) and Fig. 3.4 (a), (b), (c) and (d)), as evidenced by the low RMSE values for wind speed of 1.32 and 1.5 m s $^{-1}$ respectively. However, the daytime wind speed is underestimated at both Namche and Pheriche, and also occurs later in the model than in the observations at Namche. Wind speeds are approximately 4 m s^{-1} during the day and 1 m s^{-1} at night at both locations (Fig. 3.3 (b) and (d)). The observed wind direction during the day is south-south-easterly at both Namche and Pheriche (Fig. 3.4 (a) and (c)) and the model is a slightly too easterly (southerly) at Namche (Pheriche). Both Namche and Pheriche are located on the valley floor, which is likely to account for the directional consistency in the observed winds and the generally good agreement between the observations and model at these locations (Fig. 3.1). At night the wind is weaker and less directionally consistent compared to daytime, but still mostly from a south-south-easterly direction (Fig. 3.4 (b) and (d)).

For the stations located at higher elevations near the peaks of the mountains, the model is less accurate at representing the observed winds. Note that there is a large proportion of observational data missing at Pyramid (over 42%, Table 3.2), which makes a reliable analysis of the model skill difficult at this station. Although all model output is shown in Fig. 3.3, only hours where there are observations are used to calculate the RMSE. Compared to the available data, the model fails to capture the maximum wind speed in the diurnal cycle at Pyramid (Fig. 3.3 (f)). The model represents the wind direction relatively well during the day at Pyramid, where the wind is predominantly from the south-south-west, but it fails to capture the night-time wind direction (Fig. 3.4 (e) and (f)).

At Mera-Naulek the modelled winds are both more variable and generally stronger than the observed winds (Fig. 3.3 (h)). This stems from the model predicting several synoptic (multi-day) wind events that are not seen in the observations (Fig. 3.5). No distinct diurnal cycle is seen in wind strength in either the model or observations. At Changri Nup (Fig. 3.3 (j)) a highly variable diurnal cycle is seen in the observations which is not captured by the model, although the model does roughly capture the magnitude of the wind speed over the month. The wind direction is highly varied during the day and night at Changri Nup, in both

the model and the observations (Fig. 3.4 (i) and (j)).

These high-elevation stations, especially at Mera-Naulek and Changri Nup, are not governed by the local valley winds, as is evident in the lack of strong diurnal cycle in both the model and observations (Fig. 3.3 (h) and (j)). The lack of strong prevailing wind at these stations makes it difficult for the model to accurately capture the exact speed and direction of the wind. The lack of prevailing wind is seen both in this study, and in previous studies analysing these stations (Shea et al., 2015b). In addition, small topographic features (such as which side of a ridge a weather station or model grid point is) could have a considerable impact on both the model and observed wind. These small topographic features are not resolved by the model, and therefore neither is the subsequent wind field. As the stations at Pyramid, Mera-Naulek and Changri Nup are not representative of the local valley winds, the momentum budget components at Namche and Pheriche (where both the model and observations show a clear diurnal cycle, indicative of valley winds) are likely to be more representative of the valley and slope wind mechanisms.

Figure 3.6 shows the model 10 m wind over the Dudh Koshi River Basin. Along the valley floor, there is a clear diurnal cycle in the 10 m wind during the summer, with strong up-valley winds during the daytime (averaged between 06:00-18:00 LT), and much weaker but still up-valley winds during the nighttime (averaged between 19:00-05:00 LT) (Fig. 3.6). The upslope winds are damped over the high-elevation glacierised regions of the valley during the day (Fig. 3.6 (a)). The downslope nighttime winds that appear in a classic valley circulation (Whiteman, 2000; Zardi and Whiteman, 2013) are not apparent in either the model or observations in this study for July 2013 (Figs 3.6 and 3.4). This agrees with other studies in the Khumbu region of the Nepalese Himalaya, where nighttime downslope winds are not found in the monsoon season (Ohata et al., 1981; Ueno et al., 2001).

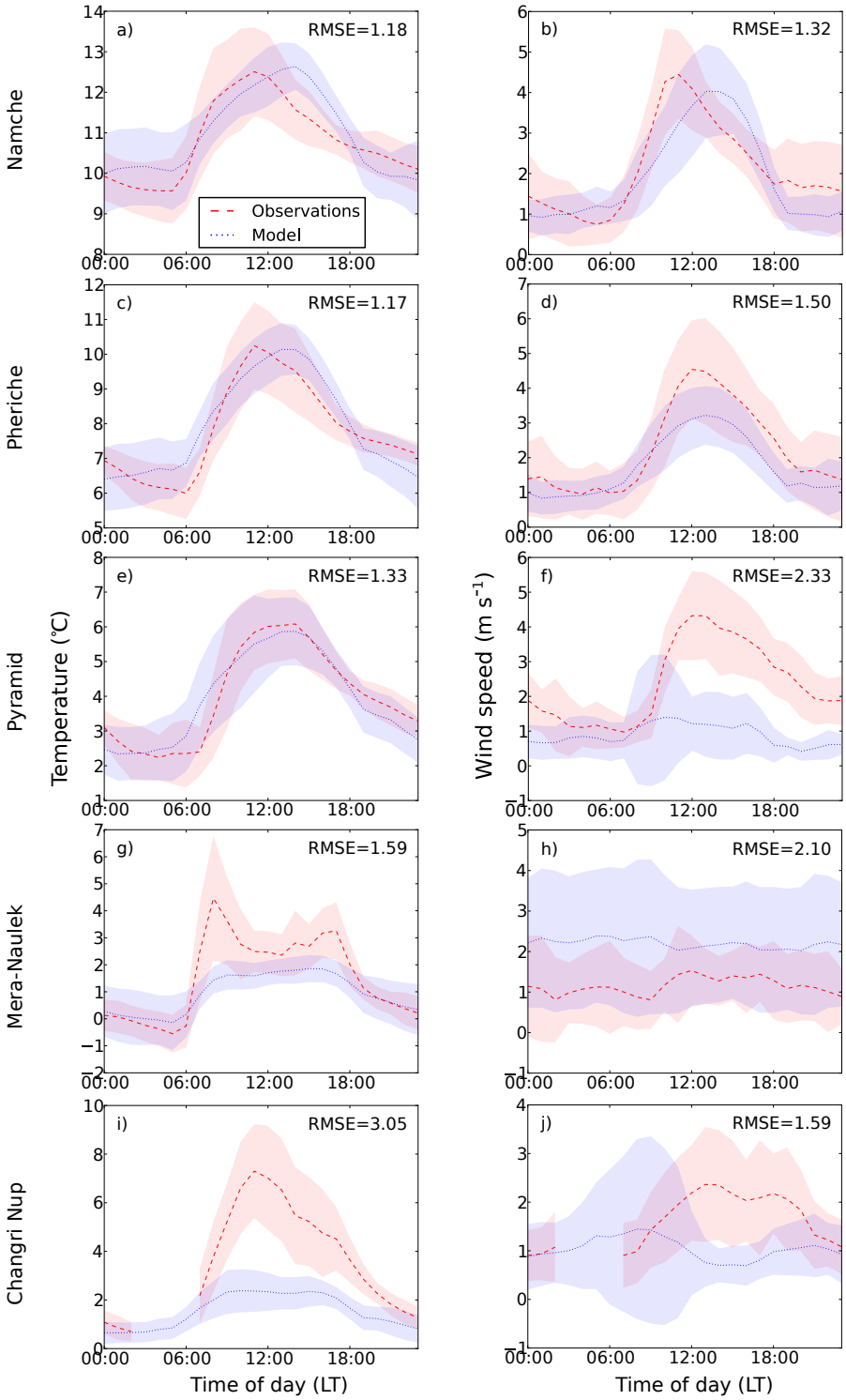

Fig. 3.3 The average diurnal air temperature at 2 m (°C; a) and wind speed at 10 m ($m\,s^{-1}$; b) for July 2013 in the model (blue) and observations (red) at Namche. Panels (c-d), (e-f), (g-h) and (i-j) are as (a-b), but for Pheriche, Pyramid, Mera-Naulek and Changri Nup, respectively. Shading represents one standard deviation from the mean, and the root mean square error (RMSE) is also shown.

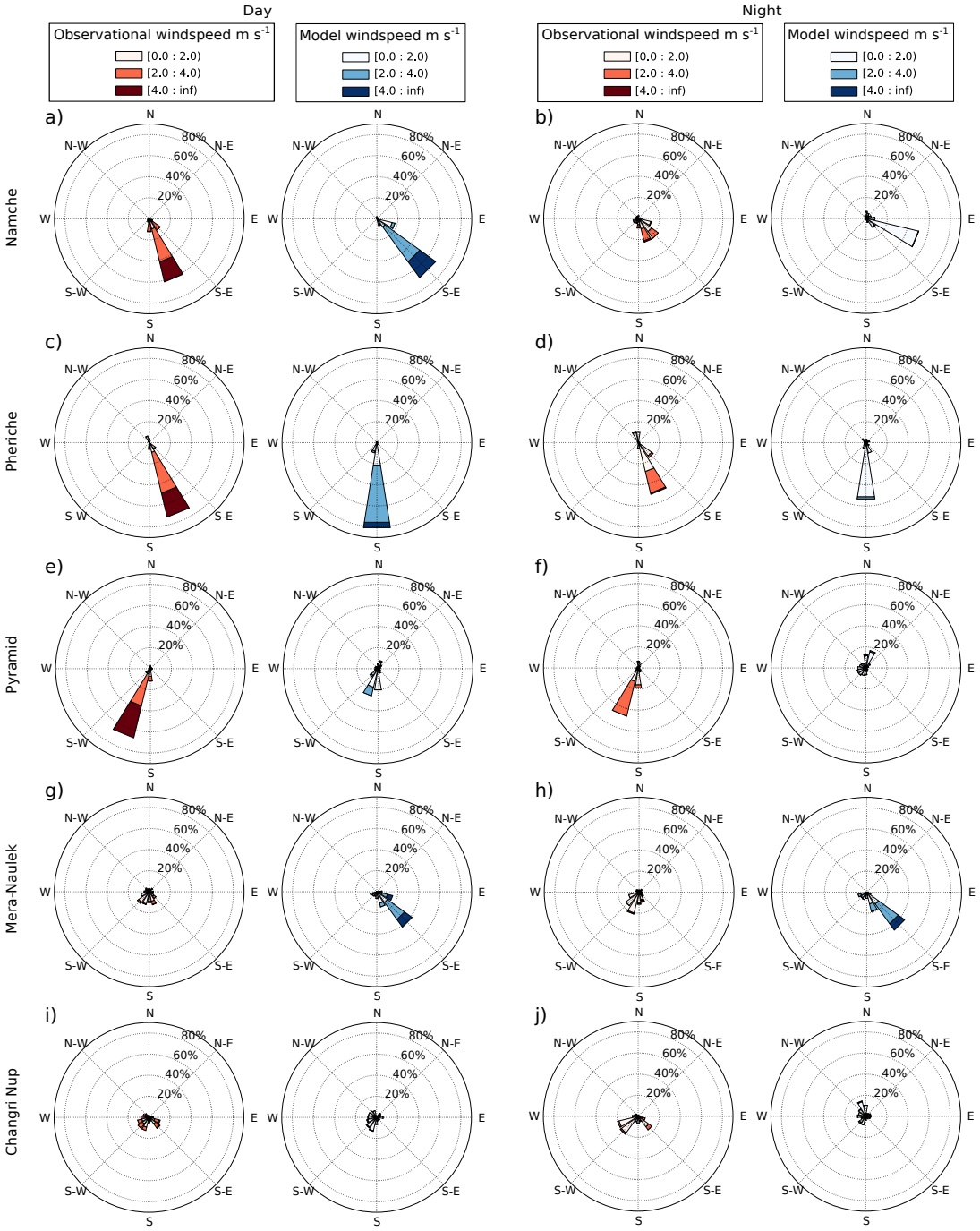

Fig. 3.4 Windroses showing the average wind speed and direction at 10 m during the day (06:00-18:00 LT; a) and night (19:00-05:00 LT; b) for July 2013 in the observations (red, left) and model (blue, right) at Namche. Panels (c-d), (e-f), (g-h) and (i-j) are as (a-b), but for Pheriche, Pyramid, Mera-Naulek and Changri Nup, respectively.

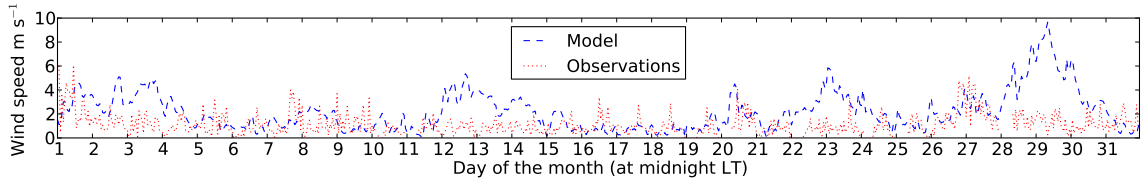

Fig. 3.5 The wind speed at 10 m in the model (blue) and observations (red) at Mera-Naulek for the month of July 2013.

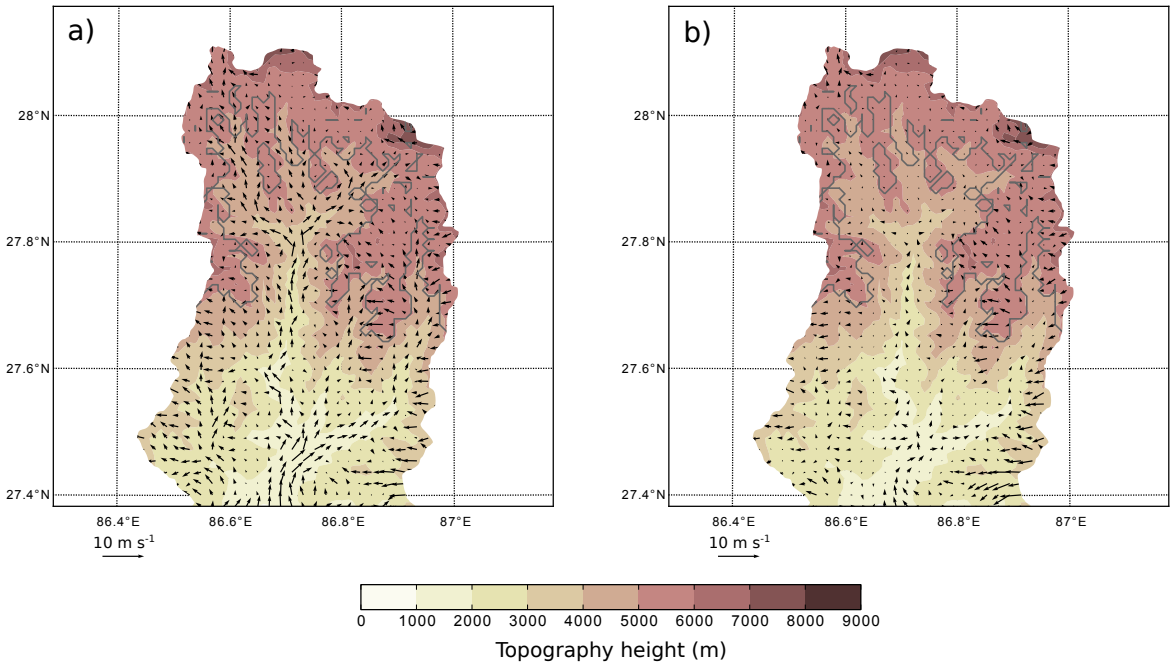

Fig. 3.6 The average daytime (06:00-18:00 LT; a) and nighttime (19:00-05:00 LT; b) model winds at 10 m (m s^{-1}; vectors) for July 2013 for the Dudh Koshi River Basin. Wind vectors are displayed at every second model grid point (every 2 km) for clarity. Also shown are the model topographic height (m; shading) and the extent of the permanent snow and ice in the model (solid grey line).

Momentum budget

As discussed, only Namche and Pheriche are located at the bottom of the valley and display a clear diurnal cycle in both the observation and model wind speeds, representing the local valley wind regime. As such, the detailed momentum budget analysis will be restricted to these two sites.

Based on the momentum budget analysis shown in Fig. 3.7 (c), (d), (g) and (h), the main drivers of near-surface wind acceleration at Namche and Pheriche (taken from the lowest model level, approximately 25 m above ground) are from the pressure gradient, advection, turbulent vertical mixing and numerical diffusion. There is a clear diurnal cycle in these acceleration components. The momentum budget components generally offset each other; often this occurs between the pressure gradient and one or more of the other forces. Despite Namche and Pheriche both having a relatively strong southerly (mainly up-valley) wind component during the day (Fig. 3.7 (a) and (b)), considerable differences exist in their respective acceleration components. At Namche, the southerly wind acceleration in the morning and deceleration in the afternoon is caused by a positive advection component offset by a negative pressure gradient, whereas at Pheriche it is caused by positive advection and pressure gradient, dampened by turbulent vertical mixing and numerical diffusion (Fig. 3.7 (c) and (d)). The pattern in the acceleration components at Namche is due to the southerly wind being blocked by a hill just to the north of its location (Fig. 3.8), leading to a strong negative horizontal velocity gradient and therefore a positive advection term and negative pressure gradient term during the day. In the zonal flow there is also little variability in the diurnal cycle of the wind velocity and the acceleration components over the month. The diurnal cycle in the wind is much weaker in the zonal direction than in the meridional direction, as expected from the predominantly along-valley wind flow. Differences in the acceleration components between Namche and Pheriche are also apparent in the zonal direction (Fig. 3.7 (g) and (h)).

The dominance of the pressure gradient, advection, turbulent vertical mixing and numerical diffusion is seen over the entire Dudh Koshi River Basin (Fig. 3.9). The acceleration causing the up-valley daytime winds seen in Fig. 3.6 is predominantly caused by these four terms. As would be expected from previous studies of valley circulations (Zardi and Whiteman, 2013), the largest component of acceleration comes from the pressure gradient term. This is followed by numerical diffusion (despite it having only a small effect on the wind at Namche and Pheriche (Fig. 3.7)), and then advection and turbulent vertical mixing

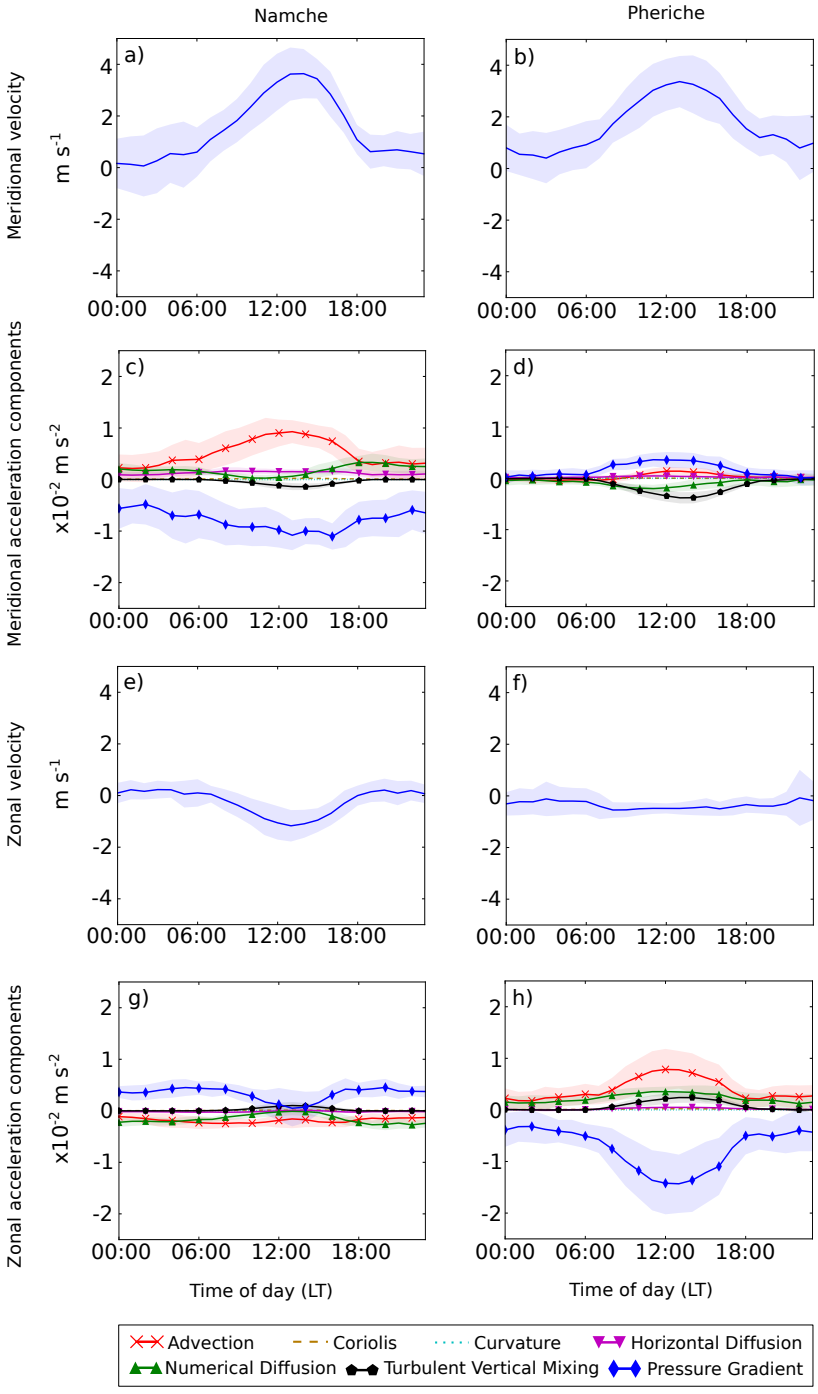

Fig. 3.7 The average diurnal cycle for July 2013 of the meridional wind component (m s^{-1}) at Namche (a) and Pheriche (b) for the summer model run, and the associated acceleration terms (m s^{-2}) at Namche (c) and Pheriche (d), taken from the lowest model vertical level. Panels (e-h) are as (a-d), but for the zonal wind component and acceleration terms. Shading indicates one standard deviation from the mean.

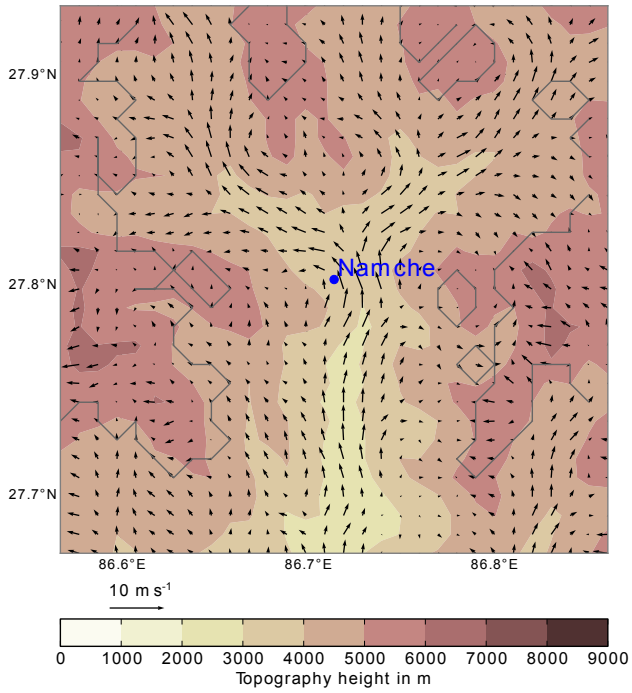

Fig. 3.8 The average daytime (06:00-18:00 LT) model winds at 10 m (m s^{-1}; vectors) for July 2013 around Namche. Also shown are the model topographic height (m; shading) and the extent of the permanent snow and ice in the model (solid grey line).

during the day. At night, the pressure gradient, numerical diffusion and advection terms are the largest.

The acceleration components are extremely variable over the river basin (Figs 3.10 to 3.12). Due to this noise, it is difficult to draw solid conclusions from the distribution of the acceleration components. The variation may be due to the complex underlying topography. Some possible spatial patterns in the acceleration components are described below.

The pressure gradient generally drives the wind up-valley south to north and upslope to the west and east over the non-glacierised areas of the valley during the day (Fig. 3.10 (a) and (b)). The pressure gradient has a strong diurnal cycle in the valley over the non-glacierised areas, but a less clear cycle over glacierised areas (Fig. 3.10). The effect of the glaciers on the pressure gradient is analysed further in Section 3.2.3.

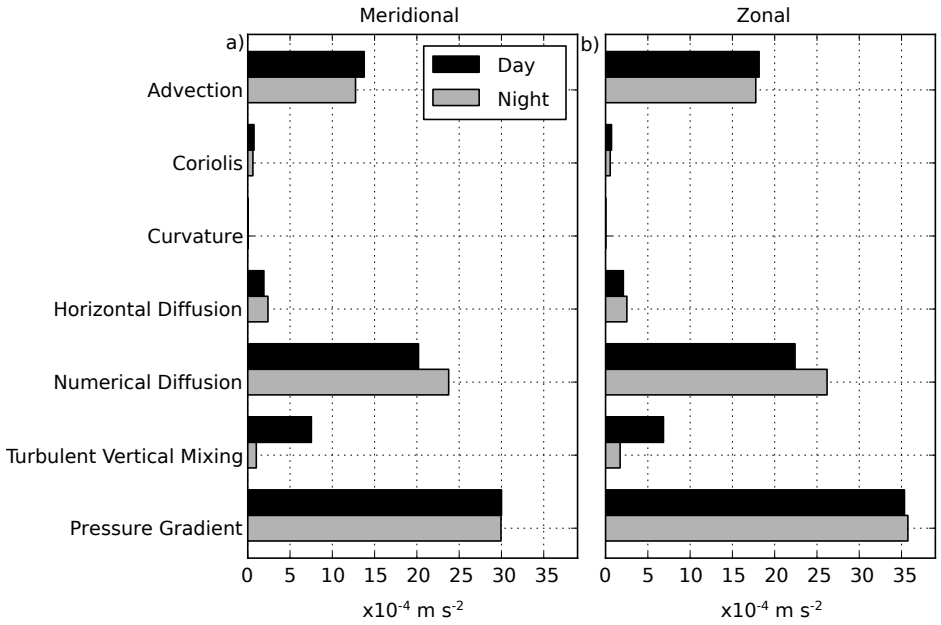

Fig. 3.9 The valley averaged absolute contributions of each momentum budget component term to the wind acceleration (m s^{-2}) at the lowest model level for July 2013. The components are shown in the meridional (a) and zonal (b) directions averaged over the day (06:00-18:00 LT; black bars) and night (19:00-05:00 LT; grey bars).

Numerical diffusion acts both positively and negatively in both the meridional and zonal directions, with no discernible pattern over the river basin (not shown).

Advection is highly spatially variable. There is a larger contribution from advection along the valley bottom (Fig. 3.11), due to the stronger winds along the bottom of the valley (Fig. 3.6). There is also a larger contribution from advection at the edges of the river basin (on the north side in the meridional direction and the western and eastern edges in the zonal direction) which is likely due to larger horizontal velocity gradients across the mountain ridges. There is a reduction in the advection along the bottom of the valley at night, as would be expected due the decrease in the valley winds, but little change at the mountain ridges as the wind here is not predominantly caused by the valley wind regime, therefore does not show a strong diurnal cycle, as discussed previously.

As discussed previously, over the entire region, the turbulent vertical mixing has a small contribution to the wind acceleration compared to the pressure gradient (Fig. 3.9), but as seen at Pheriche, it can have an important contribution in some areas (Fig. 3.7 (d)). It shows the clearest spatial patterns and diurnal cycle over the valley (Fig. 3.12). There is a mostly

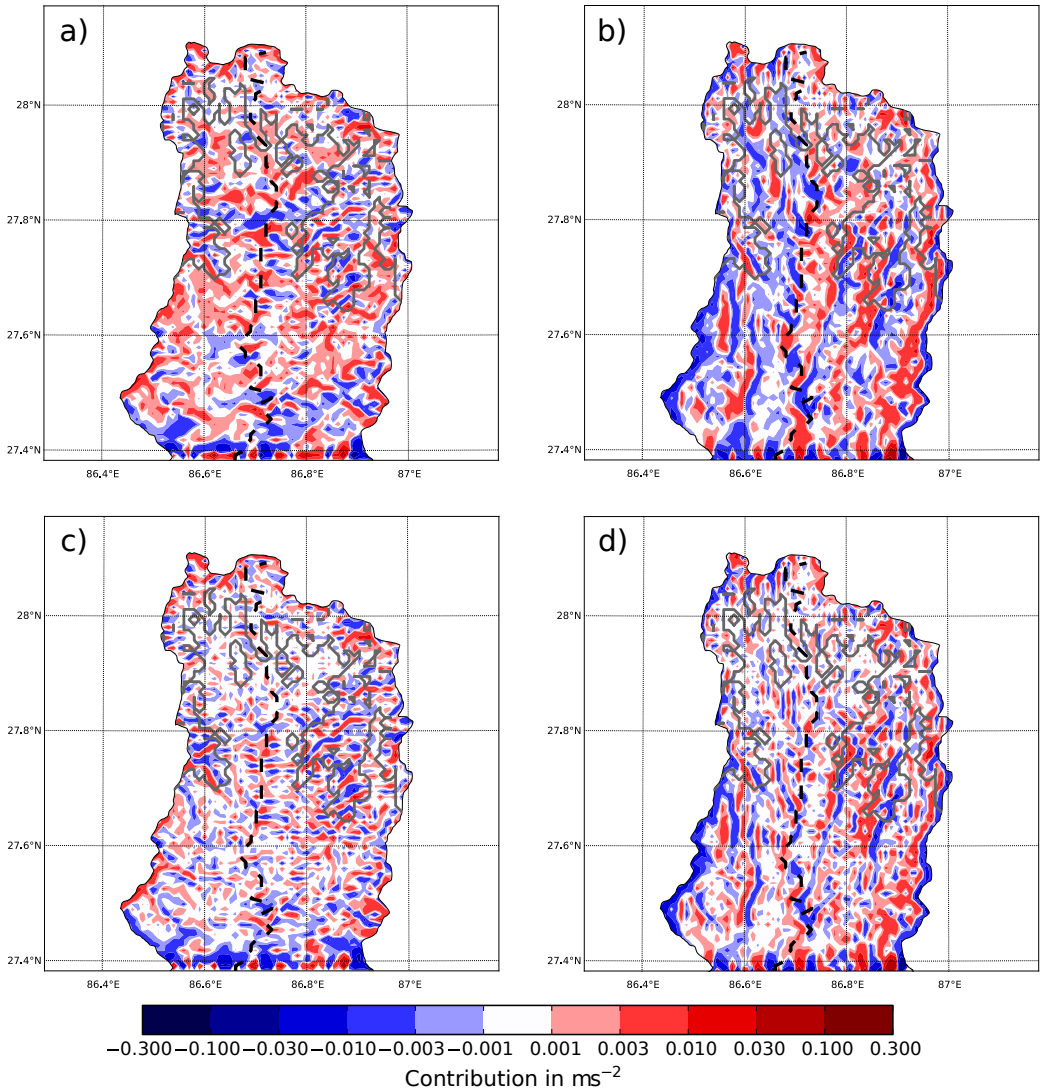

Fig. 3.10 The pressure gradient contribution to the momentum budget (shading; m s^{-2}) in the meridional and zonal direction ((a) and (b) respectively) from the lowest model level averaged over July 2013 during the day. Panels (c-d) are as (a-b), but for nighttime. Note the non-linear colour scale. The extent of the permanent snow and ice in the model is also shown (solid grey line), and the bottom of the valley is marked by a black dashed line.

negative meridional acceleration from this component over non-glacierised areas during the day (Fig. 3.12 (a)), countering the mostly southerly direction of flow (Fig. 3.6), and similarly this term acts to dampen the upslope wind (westerly to the east of the valley, easterly to the west of the valley) in the zonal direction during the day (Fig. 3.12 (b) and Fig. 3.6). Over glacierised areas and over the whole basin at night there is very little contribution from turbulent vertical mixing (Fig. 3.12 (c) and (d), and Fig. 3.9), as turbulent vertical mixing is strongly affected by the surface sensible heat flux (Lehner, 2012), and therefore the heating

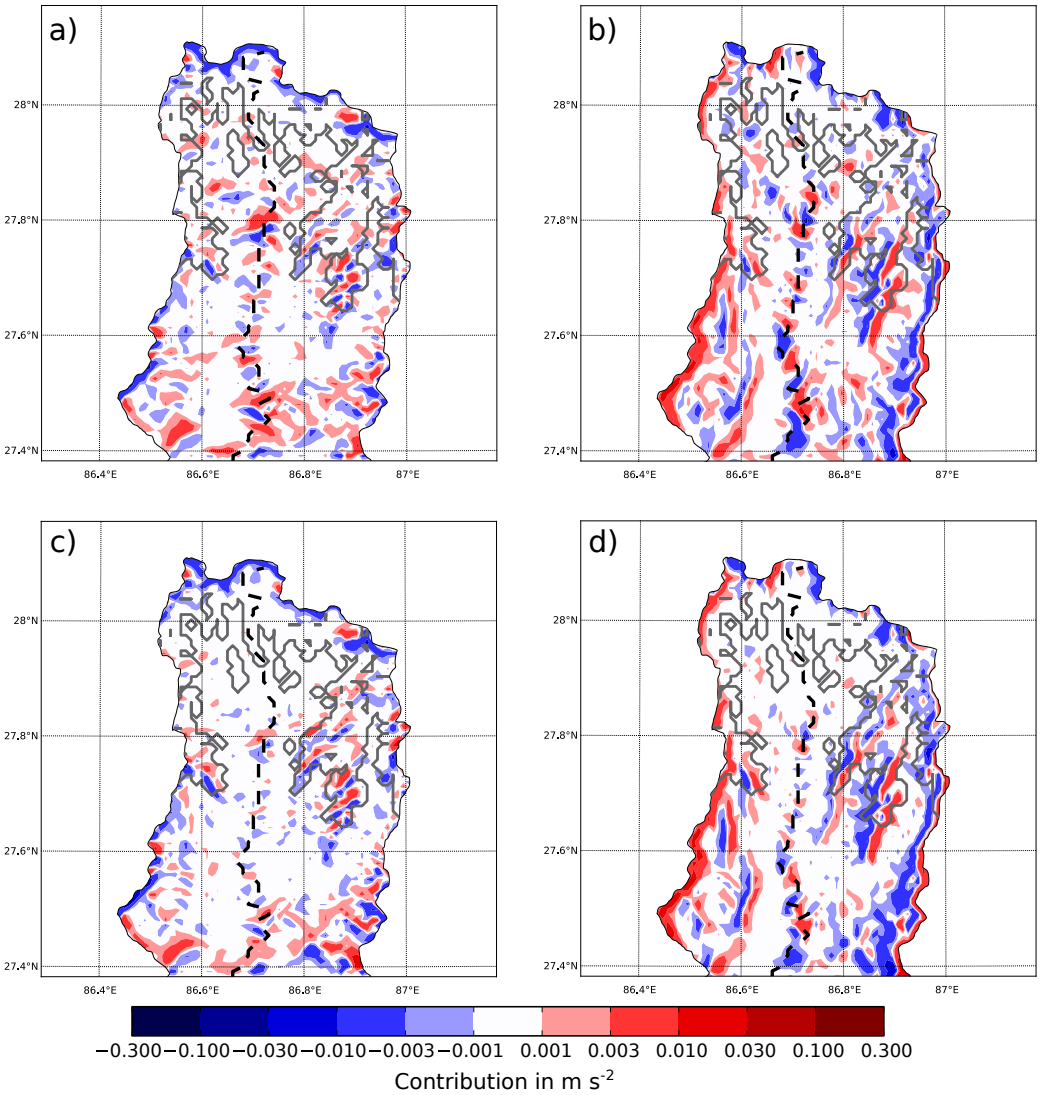

Fig. 3.11 As for Fig. 3.10, but for advection.

of the ground.

Figure 3.13 examines the vertical distribution of the meridional and zonal wind components and the associated momentum budget terms at Namche, Pheriche, as well as the average for the whole valley, during the day. Analogous results during nighttime were similar in pattern to the daytime results away from the surface, though smaller in magnitude, and so are not shown. The results show that at Namche and Pheriche the advection, pressure gradient and numerical diffusion components are the dominant drivers of the horizontal wind acceleration (excluding near the surface) up to 5000 m into the atmosphere in both the

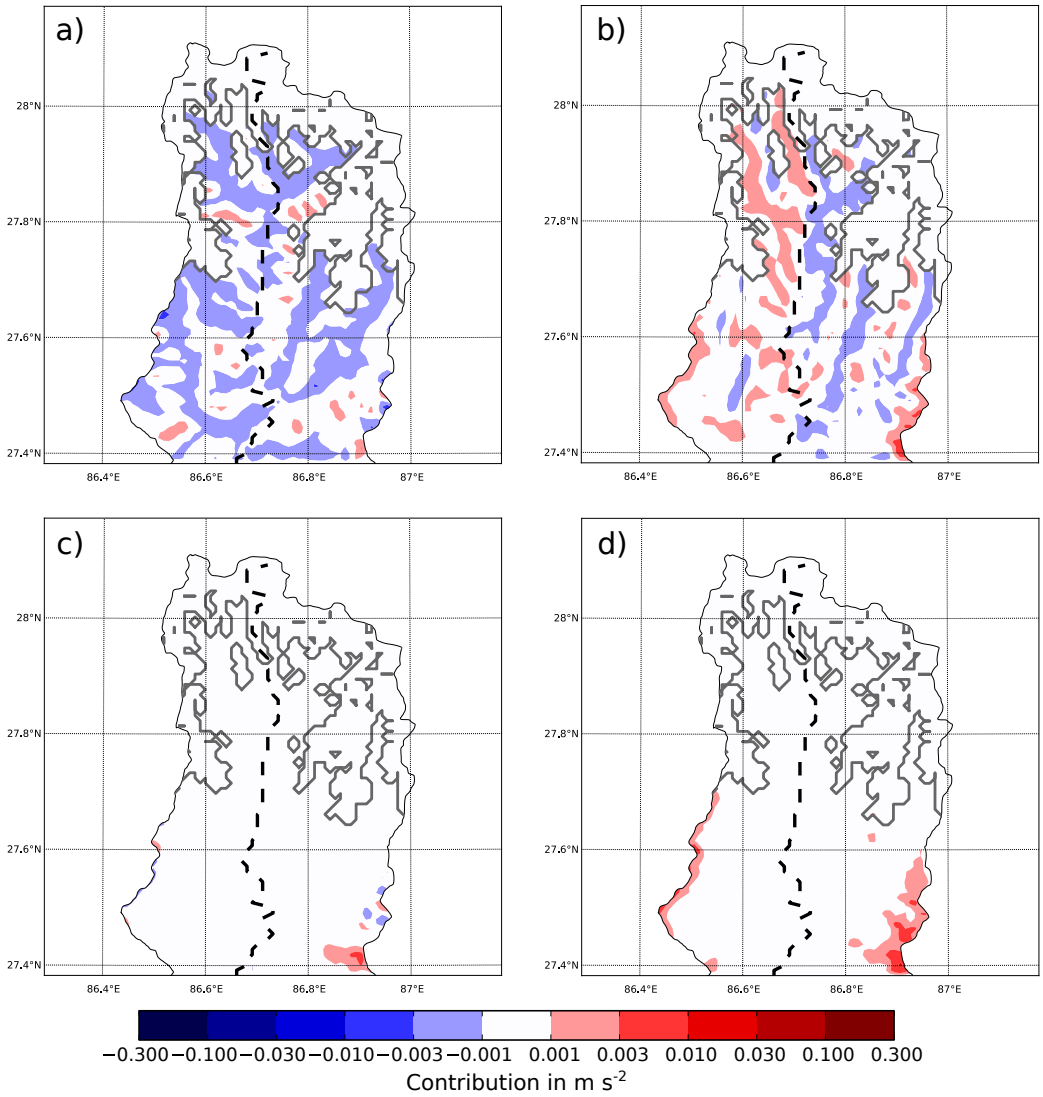

Fig. 3.12 As for Fig. 3.10, but for turbulent vertical mixing.

meridional and zonal directions (Fig. 3.13 (d), (e), (j) and (k)).

At Namche there is a low-level jet structure in the meridional wind component, with a maximum velocity at about 300 m above the ground (Fig. 3.13 (a)), which is predominantly accelerated by a positive advection component offset by a negative pressure gradient (Fig. 3.13 (d)). This pattern of advection offset by pressure gradient continues to almost 2000 m above the ground at Namche, above which there is a cross-over point where the pressure gradient and advection terms switch signs.

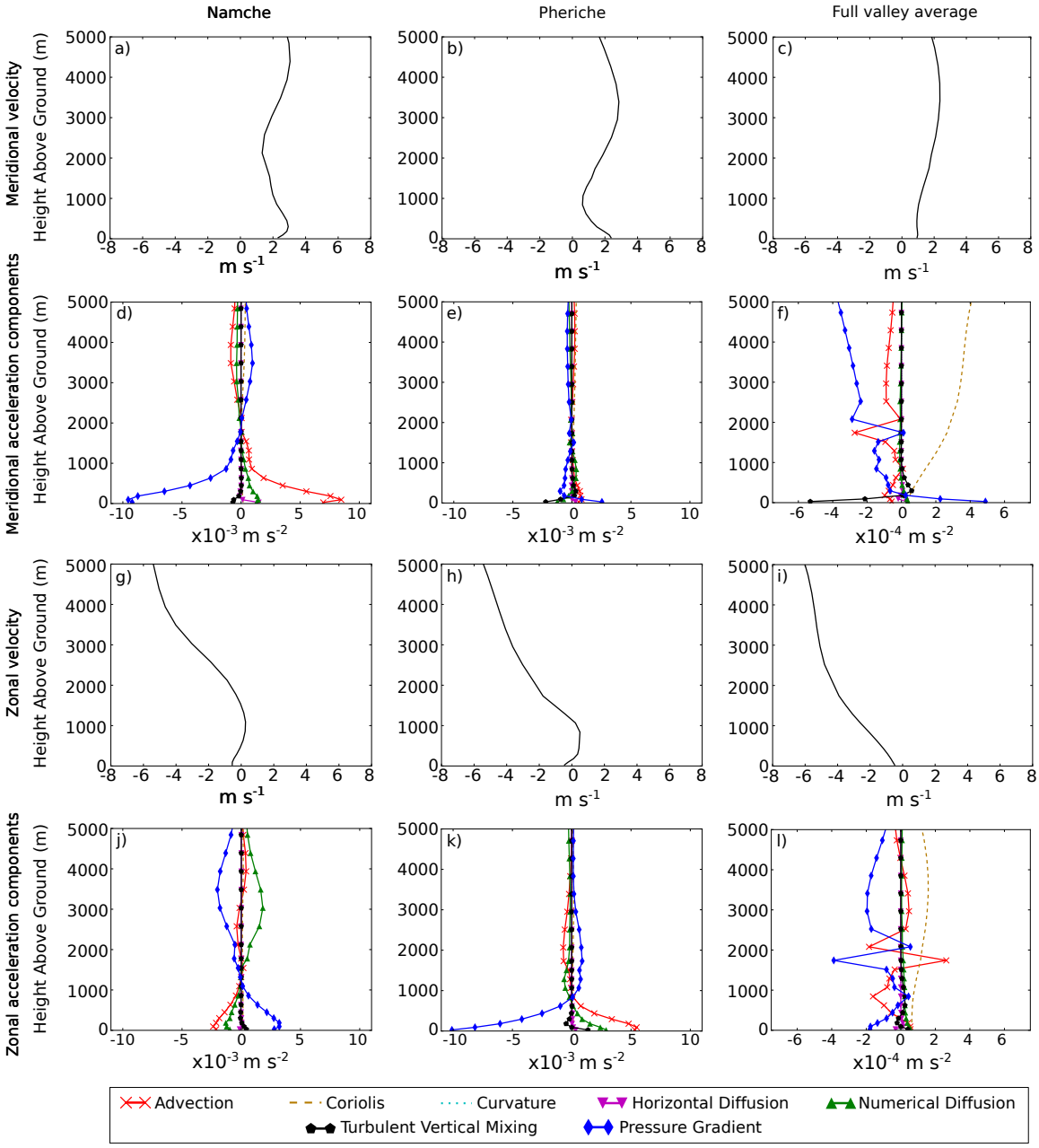

Fig. 3.13 The average daytime (06:00-18:00 LT) vertical distribution of the model meridional wind component (m s^{-1}) at Namche (a), Pheriche (b), and averaged over the entire valley (c) for July 2013. Panels (d-f) show the associated acceleration terms (m s^{-2}) at Namche, Pheriche and the valley average respectively. Panels (g-l) are as (a-f), but for the zonal wind component and associated acceleration terms. Note the change in scale in panels (f) and (l). The valley average has been taken over the area shown in Fig. 3.6, beginning from 27.43°N to avoid boundary issues.

At Pheriche the maximum meridional velocity is near the surface (Fig. 3.13 (b)), but here the positive pressure gradient term is offset by negative numerical diffusion and turbulent vertical mixing terms, which switch sign at about 200 m (Fig. 3.13 (e)). There is another switch at about 1500 m. As Pheriche is approximately 700 m higher than Namche, the 1500-2000 m cross-over points represent similar altitudes at both sites, and, as such, indicate a change in forcing from inside the valley to the free atmosphere. The pressure gradient (and advection) term is much larger below this cross-over point than above it, particularly in the meridional direction at Namche and the zonal direction at Pheriche. This suggests that the near-surface pressure gradient examined in Fig. 3.7 and Fig. 3.10 is caused by local pressure gradients rather than synoptic pressure gradients in the summer run. The dominance of the local pressure gradient over the synoptic pressure gradient was confirmed by splitting the pressure gradient into its local and synoptic components, following the method used by Moisseeva and Steyn (2014) (not shown).

Despite being less than 10 km apart, the vertical profiles at Namche and Pheriche show different patterns of acceleration components, as discussed. Figure 3.14 shows the vertical velocity at Namche and Pheriche, up to 5000 m into the atmosphere, over the full month (Fig. 3.14 (a) and (b) respectively). Near the ground, the diurnal cycle in vertical velocity is clear, with positive vertical velocity during the day at both stations. However from about 1000 m to 2500 m above the ground, there is a consistent negative vertical velocity at Namche, and a mostly-consistent positive vertical velocity at Pheriche. This subsequently effects the terms of the momentum budget above the ground. This suggests that there is a small-scale standing wave pattern over both stations. One theory is that these standing waves may be caused by trapped orographic gravity waves (e.g. Alexander et al. (2017)). Trapped orographic gravity waves are gravity waves which are prevented from propagating upwards due to a stable layer in the atmosphere (Alexander et al., 2017). In this case, they may be due to the background wind speed in the zonal direction increasing with height, as is evident in Fig. 3.13 (g), (h) and (i). The Scorer parameter is also examined (Fig. 3.15). The scorer parameter describes a ratio between the Brunt-Väisälä frequency, which measures the stability of the atmosphere, and the wind speed. This parameter can be approximated by $\sqrt{\frac{N^2}{U^2}}$, where N is the Brunt-Väisälä frequency and U is the horizontal wind speed, as described by Orr et al. (2015). A sudden decrease in the Scorer parameter in the atmosphere, as is clear at both Namche and Pheriche (Fig. 3.15) indicates that, if orographic gravity waves are present, they may be trapped (Jackson et al., 2013). Trapped gravity waves would explain a consistent vertical velocity at the two stations. The stationary features may also be due to the relatively

consistent (in direction) flow near the surface flowing over the complex topography.

When averaged over the entire valley, the momentum budget components approach a quasi-geostrophic balance between the Coriolis term and the pressure gradient term, although there is still a small contribution from the advection term (Fig. 3.13 (f) and (l)).

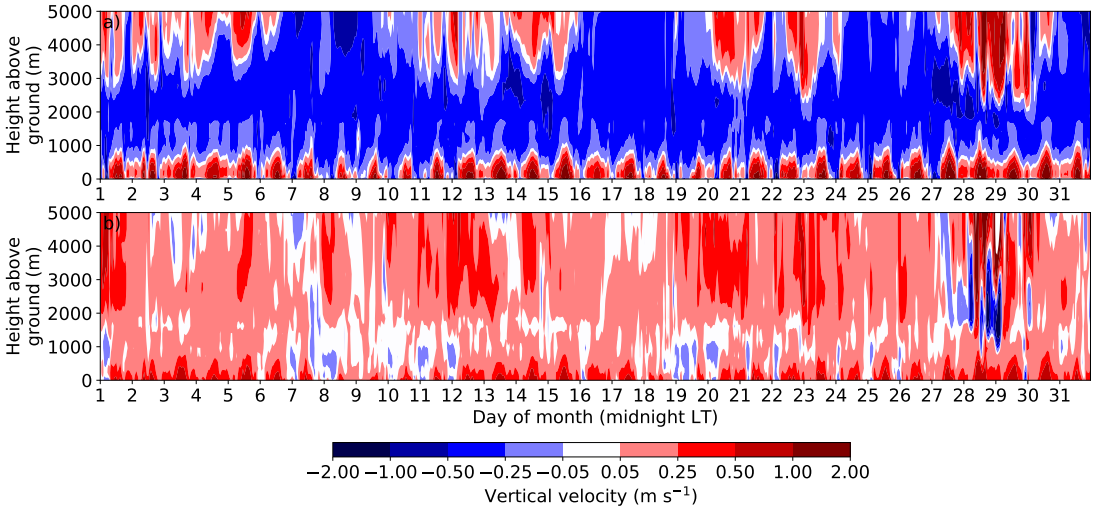

Fig. 3.14 The vertical velocity, at Namche (a) and Pheriche (b), from the ground to 5000 m above the ground.

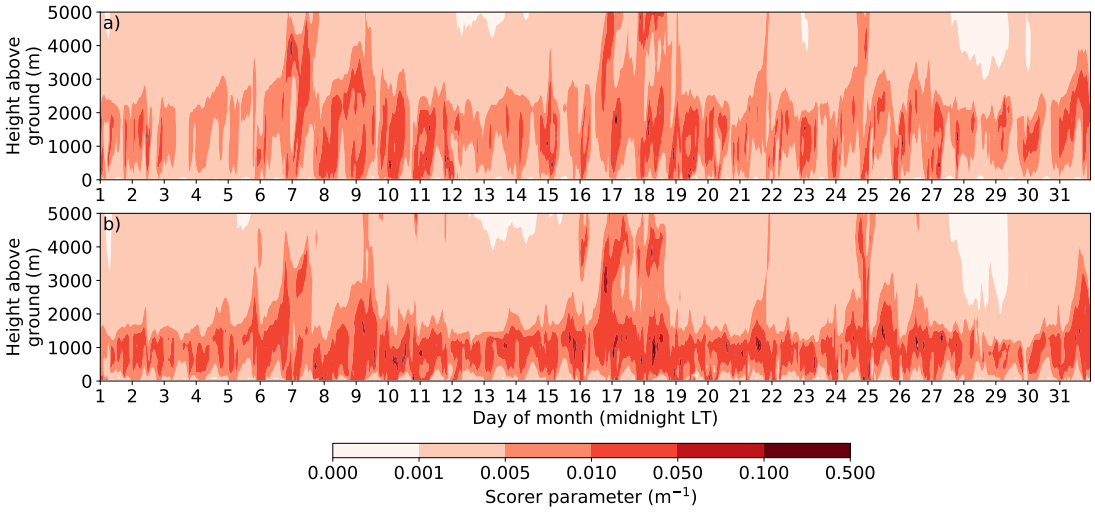

Fig. 3.15 The Scorer parameter (approximated by $\sqrt{\frac{N^2}{U^2}}$, where N is the Brunt-Väisälä frequency and U is the horizontal wind speed, at Namche (a) and Pheriche (b), from the ground to 5000 m above the ground.

3.2.2 Winter run

Model Validation and wind characteristics

The winter run does not represent the 2 m air temperature at the off-glacier stations as well as the summer run (Fig. 3.16 cf Fig. 3.3), with RMSEs of 1.94, 3.23 and 3.04 °C at Namche, Pheriche and Pyramid respectively. Near-surface air temperature is best represented at Namche (Fig. 3.16 (a)) (although it is noted that over half of the observational data is missing for this month at Namche (Table 3.2)). At Pheriche the model roughly captures the peak temperature but has a warm bias of about 2 °C at night (Fig. 3.16 (c)). At Pyramid the amplitude of the diurnal cycle is captured but the model has a cold bias of approximately 2 °C throughout the day and night (Fig. 3.16 (e)). There is also a systematic cold bias in the model throughout the day and night at Mera La (Fig. 3.16 (g)), however at this location the model landuse type is glacier, whereas Mera La is an off-glacier station, which is probably the reason for the bias at this station.

The cold bias in the model is also apparent at the on-glacier stations (Mera-Naulek and Mera Summit). Note that a cold bias in WRF over high-elevations in the winter has also been found by Karki et al. (2017). In addition the model overestimates of the amplitude of the diurnal cycle at Mera-Naulek and Mera Summit (Fig. 3.16 (i) and (k)), with the observations showing an increase in temperature from night to day of approximately 2 °C at both sites, and an increase of 4 °C and 3 °C in the model output at Mera-Naulek and Mera Summit respectively. There is more variation in the diurnal cycle of 2 m air temperature in the winter run than the summer run, which is caused by multi-day synoptic temperature variations in the winter run which are not seen in the summer run. These large-scale variations are well captured by the model at all locations (Fig. 3.17).

Similarly to in the summer run, the model represents the wind speed and direction relatively well in winter at Namche and Pheriche, with an RMSE for wind speed of 1.15 and 1.82 $\mathrm{m\,s^{-1}}$ respectively (Fig. 3.16 (b) and (d)). Namche has the best match for wind speed, but the model has a slight easterly bias (Fig. 3.18 (a) and (b)). At Pheriche, the model and observed winds both come from the south and south-south-west direction (Fig. 3.18 (c)) during the day, however the model fails to capture the amplitude of the diurnal cycle, overestimating the nighttime wind speed by 1 $\mathrm{m\ s^{-1}}$ and underestimating the maximum daytime wind (Fig. 3.16 (d)).

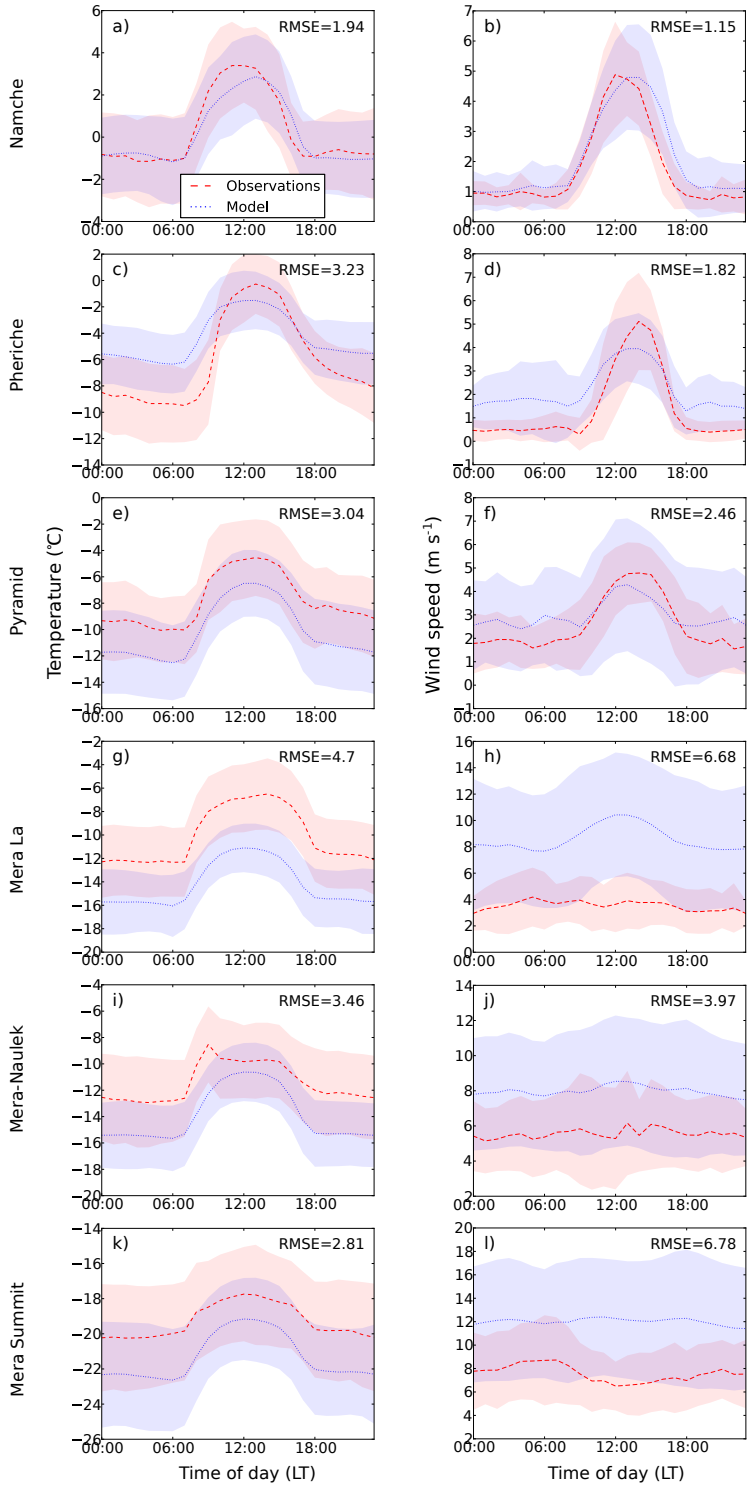

Fig. 3.16 As in Fig. 3.3, but for January 2014. Panels (a-b), (c-d), (e-f), (g-h), (i-j) and (k-l), are for Namche, Pheriche, Pyramid, Mera La, Mera-Naulek and Mera Summit, respectively.

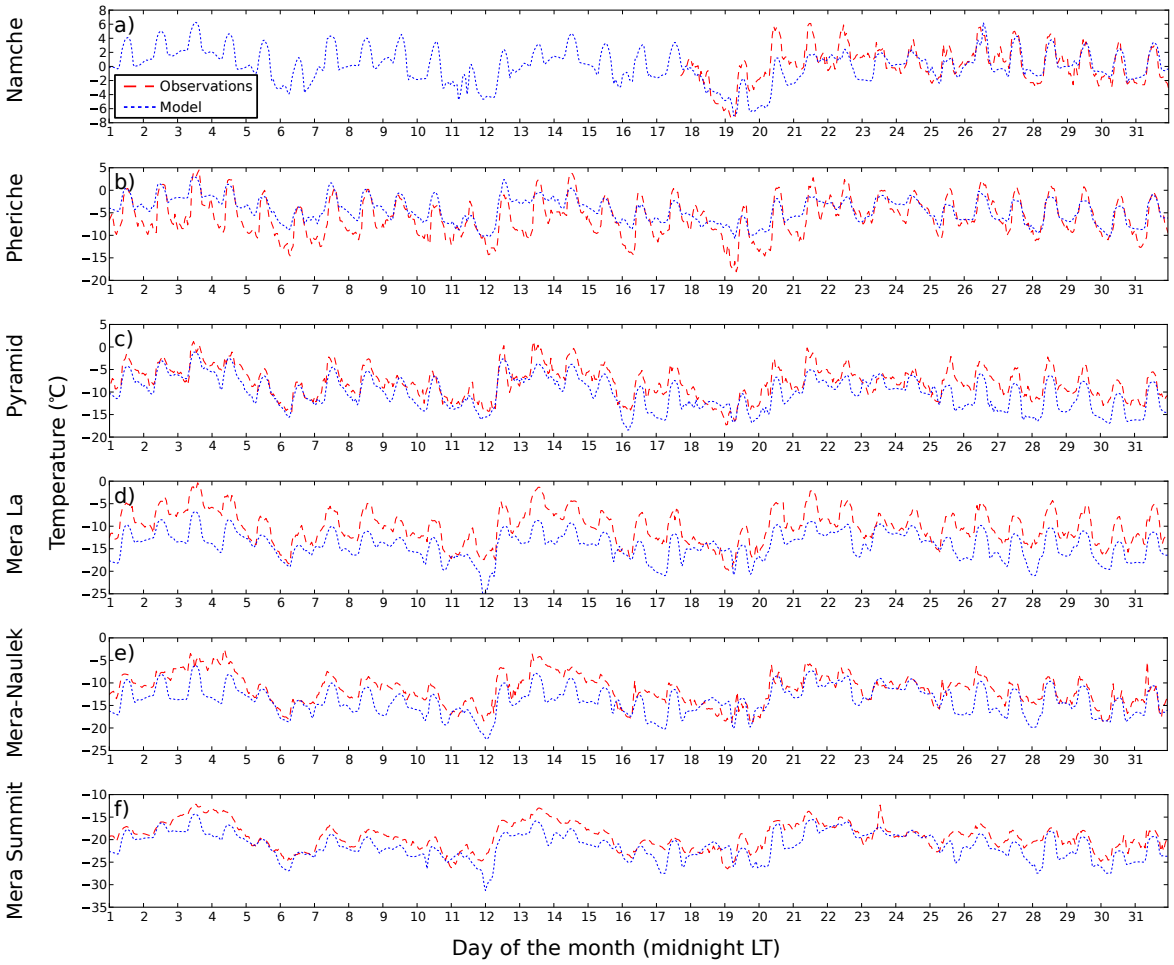

Fig. 3.17 The January 2014 air temperature at 2 m in the model (blue) and observations (red). Panels (a-f) are for Namche, Pheriche, Pyramid, Mera La, Mera-Naulek and Mera Summit, respectively.

The model somewhat captures a diurnal cycle in the wind at Pyramid in the winter, but there is more variation in the model wind speed than in the observations (Fig. 3.16 (f)). At the high-altitude stations of Mera La, Mera-Naulek and Mera Summit, the model overestimates the wind speed at 10 m throughout the month, by about 4 m s $^{-1}$ on average at Mera La and Mera Summit, and 2 m s $^{-1}$ at Mera-Naulek (Fig. 3.16 (h), (j) and (l)). Figures 3.18 (g-l) demonstrate that this is due to a very strong westerly wind in the model (which is less directionally consistent in observations), so either the model is overestimating the effects of the winter westerlies, or the model topography is not accurately sheltering the wind at these sites.

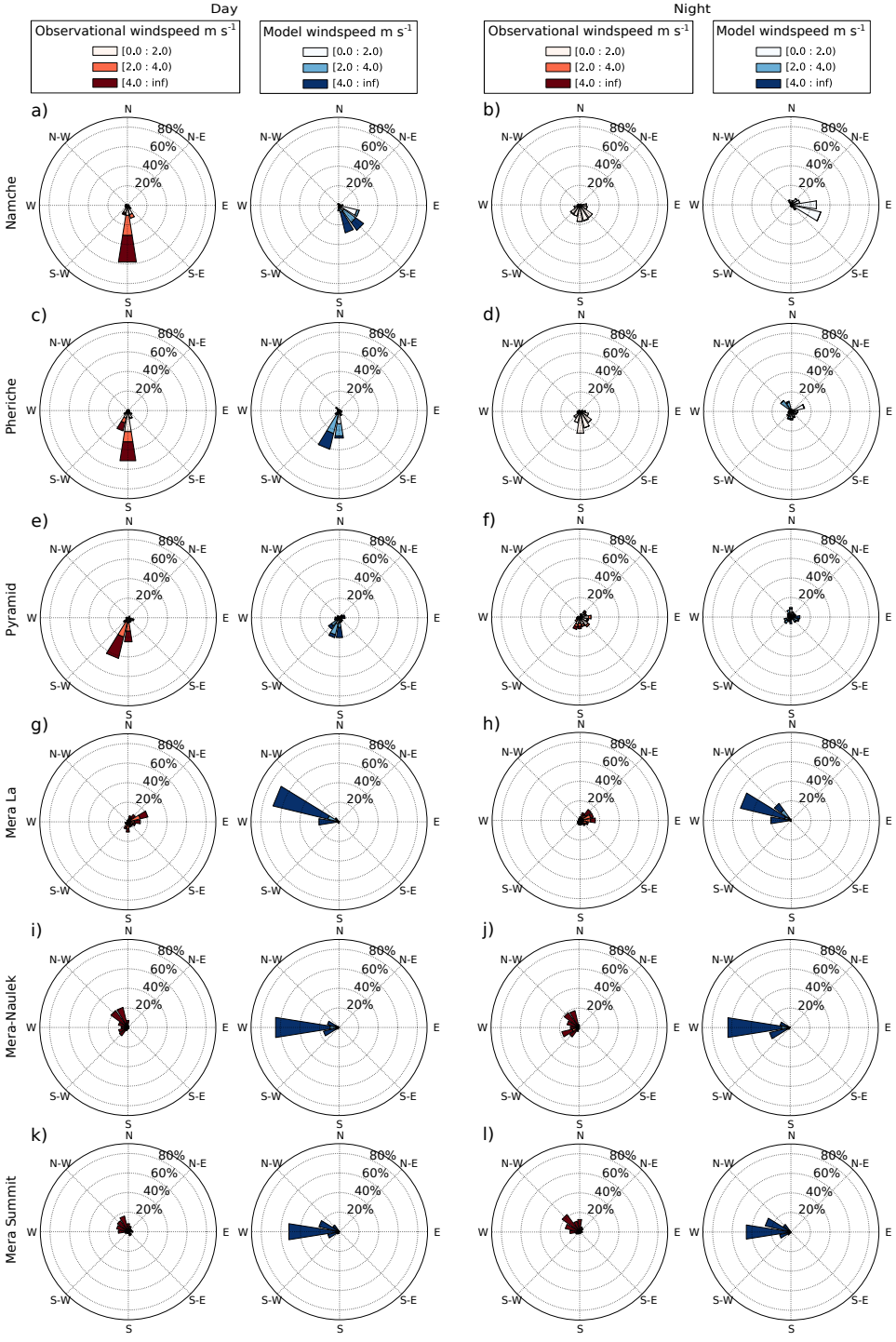

Fig. 3.18 As for Fig. 3.4, but for January 2014. Daytime is taken as 07:00-17:00 LT in the winter run. Panels (a-b), (c-d), (e-f), (g-h), (i-j) and (k-l), are for Namche, Pheriche, Pyramid, Mera La, Mera-Naulek and Mera Summit, respectively.

Figure 3.19 shows that over the entire valley, along the valley floor, the pattern in the near-surface winds in the model output in the winter run is similar to that in the summer run; up-valley winds during the day and the wind weakening at night. However at high elevations the winter pattern is different to that of the summer, with strong westerly winds throughout the day and night (Fig. 3.19). Additionally, in the summer run the up-valley winds continue up to (or just over) the permanent snow and ice outline during the day in the north of the valley (Fig. 3.6 (a)). However in the winter run, the up-valley winds dampen before the glaciers, and in this region, just below the glacier outline, there are the downslope nighttime winds of a classic diurnal circulation (Fig. 3.19 (a) and (b)).

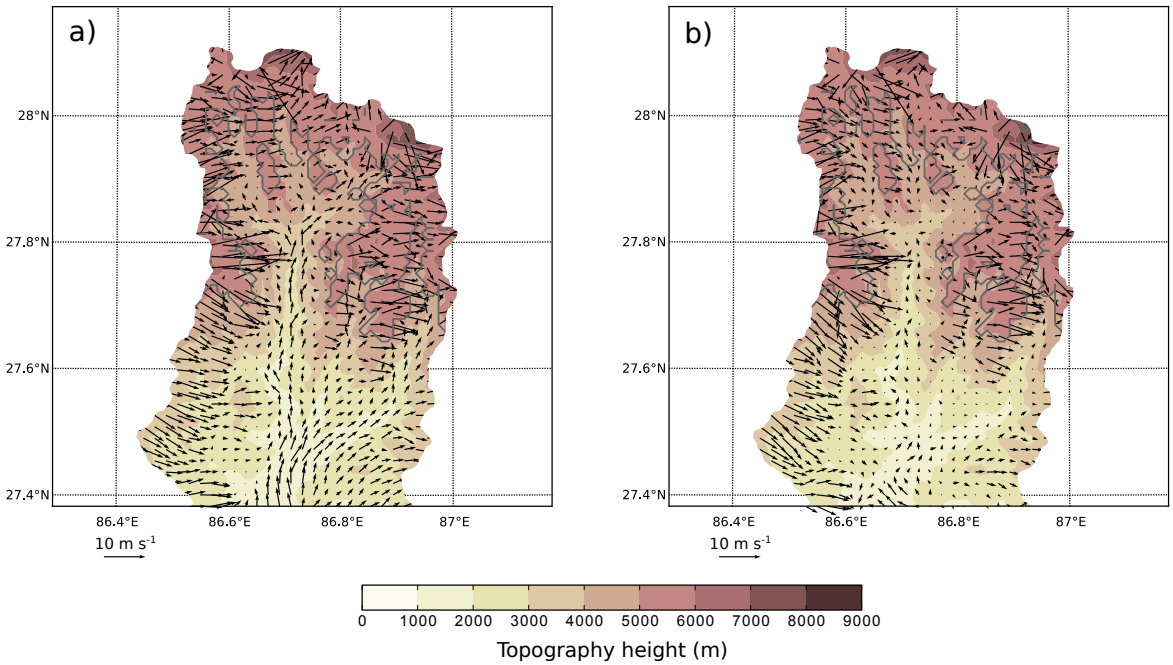

Fig. 3.19 As for Fig. 3.6, but for January 2014. Daytime is taken as 07:00-17:00 LT in the winter run.

Momentum budget

Momentum budget analysis for the winter run is restricted to Namche and Pheriche, just as it is in the summer run. As discussed, there is a similarity in the winds along the valley floor between the winter and summer runs (Fig. 3.19 cf. Fig. 3.6). This similarity is also seen in the wind velocities and acceleration components at Namche and Pheriche (Fig. 3.7 cf 3.20). In the meridional direction at both locations there is a clear diurnal cycle in the winds with stronger winds during the day, and much weaker winds at night in the winter run (Fig. 3.20 (a) and (b)), of broadly similar wind velocities compared with the summer run. In the zonal direction, there is a much weaker diurnal cycle, again similarly to the summer run (Fig. 3.20 (e) and (f)). In addition, the patterns in the acceleration components are similar at Namche and Pheriche in the winter to those seen in the summer (Fig. 3.20 (c), (d), (g) and (h)). However, the diurnal cycle in both the wind speeds and the acceleration components is slightly more variable over the month in the winter run (Fig 3.20) compared to the summer run (Fig 3.7).

Over the entire valley, every component of the near-surface acceleration is larger in the winter run than in the summer run, in both the meridional and zonal directions (Fig. 3.21 cf. Fig. 3.9). Just as in the summer run, the pressure gradient is still the largest term in the acceleration of the near-surface winds. The advection term surpasses the numerical diffusion term to become the second biggest term, but the pressure gradient, advection, numerical diffusion and turbulent vertical mixing terms remain the largest terms during the day.

Maps of the pressure gradient, advection and turbulent mixing terms for the winter run show similar patterns to those in the summer run (Figs. 3.10 to 3.12) and are therefore not shown. Along the valley floor, all three terms show a comparable pattern to those seen in the summer run. The pressure gradient and advection terms also show a similar pattern at high elevations, however at these high elevations the size of both terms is increased. The turbulent vertical mixing term has an additional negative contribution in the zonal direction at high elevations, which is seen in both the day and night and which acts to dampen the westerly wind flow at these high elevations.

The most noticeable difference in the vertical distribution of the acceleration components in the winter run compared to the summer run is the increase in wind speed at high altitudes, especially in the zonal direction, where wind speeds reach above 40 m s^{-1} (Fig. 3.22 (g-i), cf. Fig. 3.13 (g-i)), demonstrating the influence of the winter westerlies. The

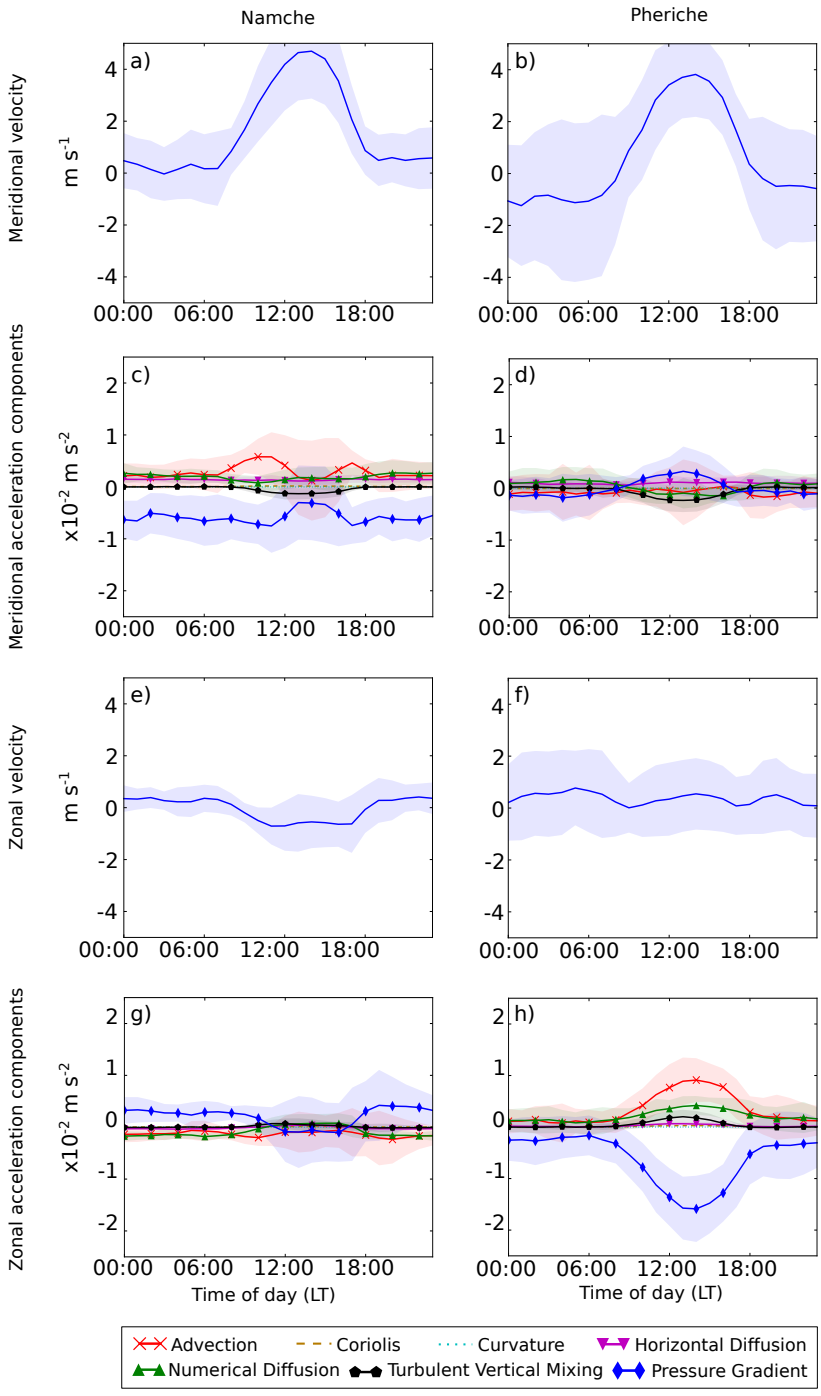

Fig. 3.20 As for Fig. 3.7, but for January 2014.

drivers in the wind acceleration at Namche and Pheriche are also larger at high altitudes away from the surface in the winter run than the summer run, but the pressure gradient, advection, numerical diffusion and Coriolis terms remain the largest terms (Fig. 3.22 (d), (e), (j) and (k) cf 3.13 (d), (e), (j) and (k)). There is a larger contribution (and a switch in

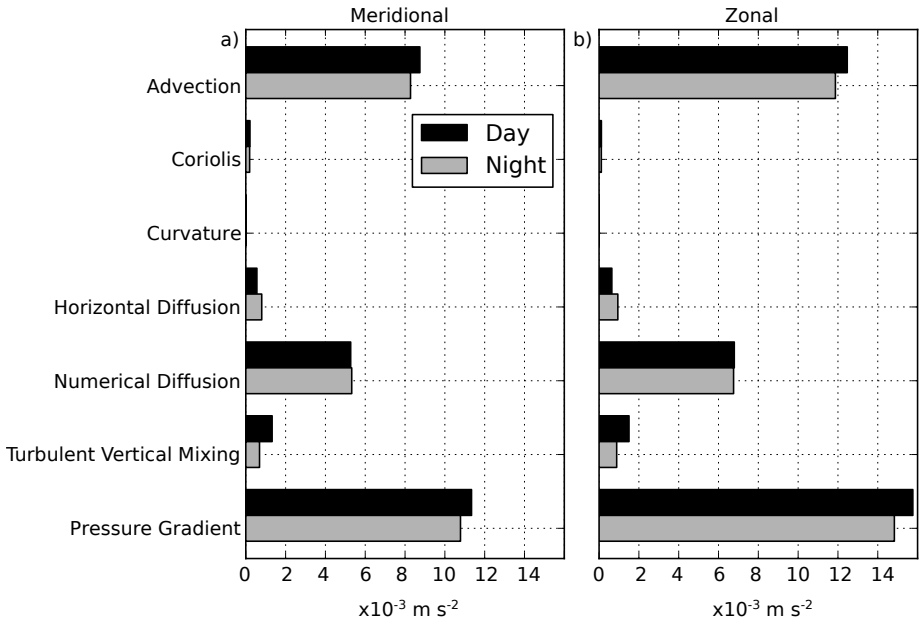

Fig. 3.21 As for Fig. 3.9, but for January 2014. Note the change of scale. Daytime is taken as 07:00-17:00 LT in the winter run.

sign) from the Coriolis acceleration in the meridional direction in the winter run compared to the summer run. This is due to the switch in direction and increase in zonal wind at high altitudes. Due to the increase in the magnitude of the drivers at high altitudes, and the variability of the pressure gradient throughout the atmospheric column, it is not possible to determine whether the near-surface pressure gradient is predominantly locally or synoptically forced in the winter. However the cross-over point in the acceleration components at around 1000 m above the surface at Namche and Pheriche indicates a difference in the mechanisms driving the winds in the valley compared to the free atmosphere (Fig. 3.22 (d), (e), (j) and (k)).

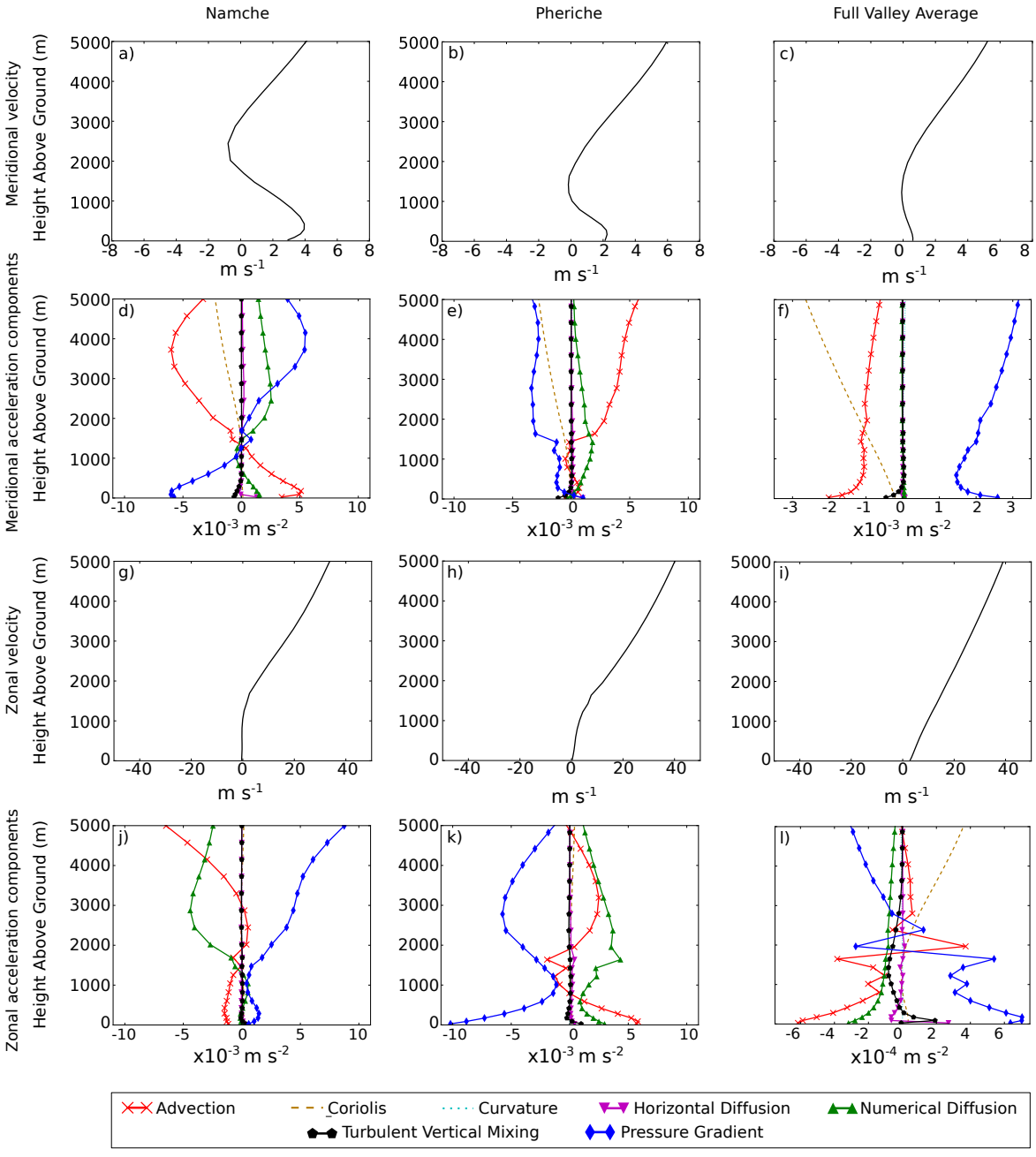

Fig. 3.22 As for Fig. 3.13, but for January 2014. Note the change of scale in the zonal velocity and panels (f) and (l). Daytime is taken as 07:00-17:00 LT in the winter run.

3.2.3 Removal of glacierised region

Figure 3.6 and maps of each of the acceleration terms (Fig 3.10, Fig 3.11 and Fig 3.12) indicate that the wind and the drivers of the wind acceleration are extremely variable over the valley, and also influenced by the presence of permanent snow and ice. In this section the role of glacier coverage is investigated by repeating the summer and winter runs discussed above, but with all the permanent snow and ice removed in the model. These repeated runs are referred to as the perturbation experiments.

Changes to the local valley winds

In the summer run, the daytime up-valley winds are weaker over the glaciers (Fig. 3.6 (a)). However in the summer perturbation experiment, the daytime up-valley winds continue to the top of the river basin (Fig. 3.23 (a)), with stronger wind velocity in the summer perturbation compared to the summer run. This demonstrates that the winds are currently being damped by the glaciers, rather than, for example, by the increasing topographical gradient. There is no consistent difference seen in the winds between the winter run and the winter perturbation experiment (not shown). This is probably because the winds over the glacierised regions are much stronger in the winter run (Fig. 3.19), suggesting that the synoptic influence dominates over the valley winds at high elevations in the winter run. As such, only the summer run and perturbation experiment will be analysed further.

Momentum budget

For both the summer run and the summer perturbation experiment, the pressure gradient generally accelerates the wind up-valley during the day (Fig. 3.24 (a)). Over the non-glacierised areas of the valley, there is a strong diurnal cycle in the pressure gradient, with a large southerly (up-valley) acceleration from the pressure gradient during the day and a small northerly (down-valley) acceleration at night. Over the currently glacierised areas of the valley, the diurnal cycle is considerably smaller in the summer run, and shows only a small decrease in the southerly acceleration at night (Fig 3.24 (a)). In the summer perturbation experiment, there is a substantial increase in the pressure gradient up-valley acceleration over the currently glacierised areas compared to the summer run (Fig. 3.24 (a)).

The turbulent vertical mixing term dampens the winds during the day over currently non-glacierised regions in the summer run and the summer perturbation experiment (Fig. 3.24 (b)). Over the currently glacierised areas during the day in the summer run, and over

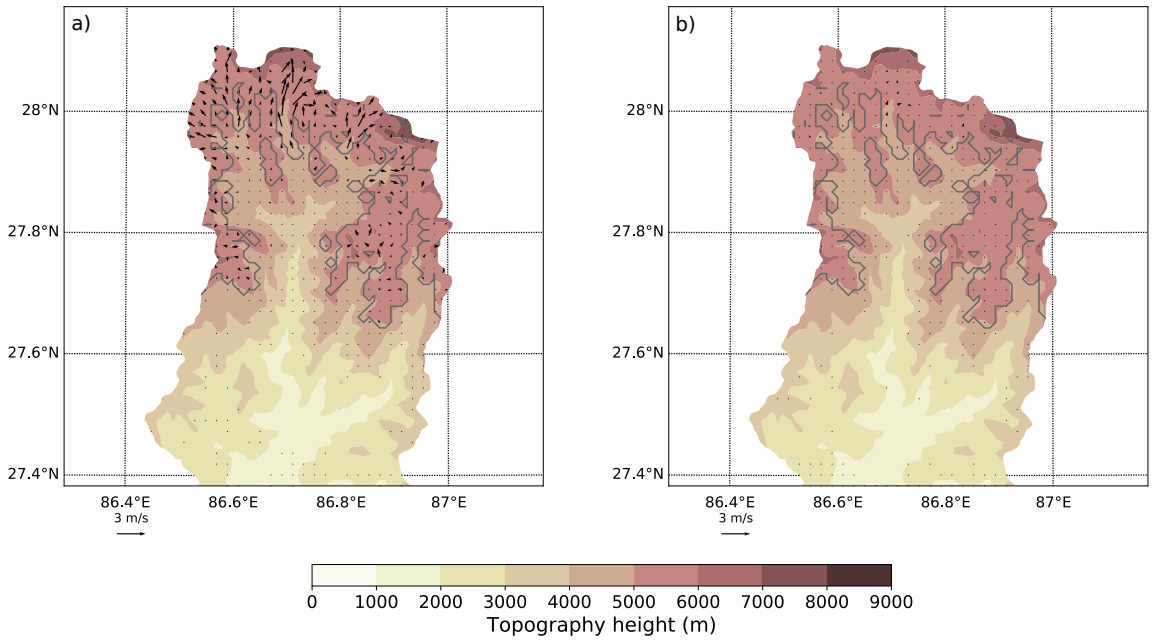

Fig. 3.23 As for Fig. 3.6, but for the difference in the winds at 10 m between the summer perturbation experiment and the summer run (perturbation experiment minus summer run). Only vectors which show a significant difference in either the meridional or zonal velocities are shown. Note the change in scale compared to Fig. 3.6.

the whole basin at night in both the summer run and summer perturbation experiment, there is very little contribution from turbulent vertical mixing (Fig. 3.24 (b)). In the summer perturbation experiment, there is an increased northerly acceleration (dampening) of the up-valley meridional wind from turbulent vertical mixing over the areas where the glaciers have been removed during the day. In the summer perturbation experiment, the increase in the up-valley acceleration from the pressure gradient is larger than the dampening from the turbulent vertical mixing, leading to the increase in winds seen in Fig. 3.23. The other drivers do not show a substantial change in the summer perturbation experiment compared to the summer run when averaged over the currently glacierised area.

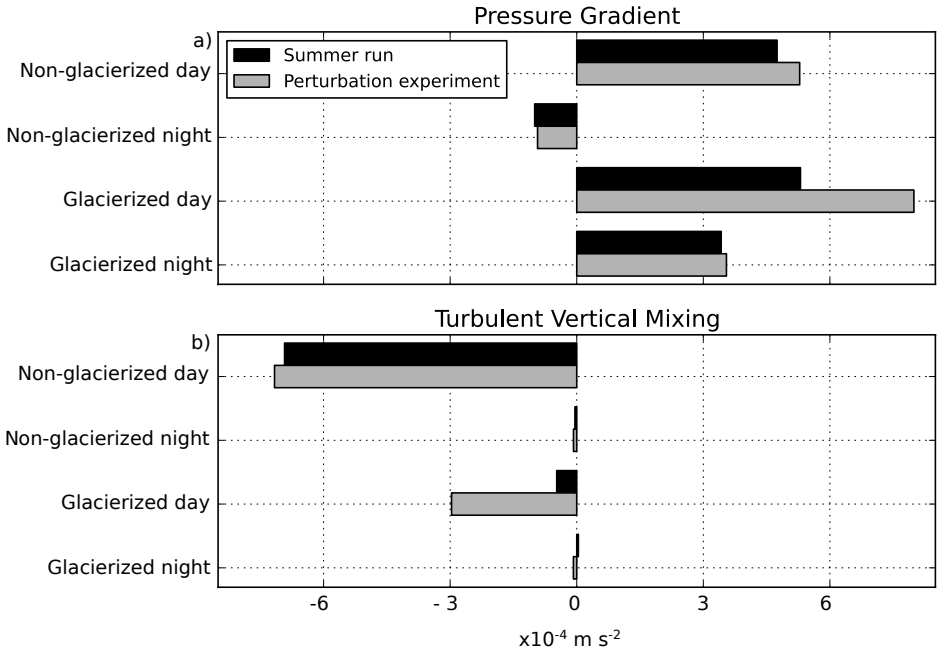

Fig. 3.24 The meridional acceleration component of the pressure gradient (a) and the turbulent vertical mixing (b) terms, averaged over the glacierised and non-glacierised regions of the valley for the day (06:00-18:00 LT) and night (19:00-05:00 LT) for July 2013. The valley average has been taken over the area shown in Fig. 3.6, for the glacierised and non-glacierised regions (bounded by the grey line), beginning from 27.43°N to avoid boundary issues. The summer run is shown in black and the summer perturbation experiment is shown in grey. A positive value indicates a south to north acceleration (mostly up-valley) over the region.

3.3 Discussion and conclusions

In this chapter, the WRF model was run at 1 km resolution over the Dudh Koshi River Basin for July 2013 and January 2014, and compared to seven AWSs varying in location from the valley floor to the mountain peaks. The model accurately represents the near-surface air temperature and wind speed and direction at two AWSs located in the valley, but is less accurate at predicting temperature and wind at the mountain peaks. In the summer there is a clear diurnal cycle in the near-surface winds over the non-glacierised areas of the valley, with strong up-valley winds during the day and weak up-valley winds at night, confirming previous findings (Inoue, 1976; Ohata et al., 1981; Shea et al., 2015b; Ueno et al., 2001; Yang et al., 2017). In the winter, the winds at lower elevations in the valley show a similar pattern to those in the summer, however at high elevations there is an influence from the synoptic-scale winter westerly winds. Previous work has suggested that in winter, a classic local wind regime is seen in this valley, with downslope winds in the nighttime (Yang et al., 2017). This study finds that this is only true of the wind just below the glacier margins, and does not hold further down the valley where weak up-valley nighttime winds dominate. The model wind in this study shows nighttime downslope winds just below the glacier margin in winter, which agrees with the findings of Bollasina et al. (2002), who found weak downslope winds during winter at night at the Pyramid station, which is located just on the glacier margin. This study partially supports the findings of Ueno et al. (2008), who found very weak nighttime winds in winter at lower elevations of the valley, but the results of this chapter are not consistent with their finding of nighttime downslope winds at Pheriche in the winter of January 2003. It is possible that this is due to inter-annual variability in the wind, which could be due to differences in snow extent.

Using a momentum budget analysis of the WRF model output, this chapter shows that the dominant drivers of the near-surface horizontal wind acceleration in the summer are the pressure gradient, advection, turbulent vertical mixing, and the non-physical numerical diffusion term. These drivers also show a clear diurnal cycle. Although the interplay between the terms is complex, typically the pressure gradient term dominates. Examining the vertical distribution of the pressure gradient suggests that in the summer the near-surface pressure gradient is caused mostly by local rather than synoptic pressure gradients. The drivers of near-surface wind acceleration are extremely variable over the valley, and also affected by the presence of glaciers. When the glaciers are removed from the model in the summer, there is an increase in the pressure gradient which causes the up-valley winds to continue

to the top of the valley, although the winds are partially damped by an increase in northerly acceleration from turbulent vertical mixing. The change in the winds confirms the theory proposed by Yang et al. (2017), that the glaciers in the valley are the cause of the retardation of the northward winds in the valley.

Compared to the summer, the magnitude of all the acceleration components increases in the winter, particularly at high altitudes, and there is a less clear diurnal cycle in the wind and the dynamical drivers near the surface. The influence of the winter westerlies is seen in the model at high altitudes at Namche and Pheriche.

In both the summer and the winter runs, the vertical components of the momentum budget switch sign (or drop to zero) at approximately 1500-2000 m above the ground, suggesting that there is a distinction between the drivers of the local wind acceleration inside the valley and in the free atmosphere. A standing wave pattern affects the vertical distribution of acceleration terms at Namche and Pheriche. However when the momentum budget components are averaged over the valley, they approach a quasi-geostrophic balance at upper levels of the atmosphere.

Dynamical downscaling has been shown to improve representation of meteorological variables, such as wind and temperature, when compared with larger-scale reanalysis (Heikkilä et al., 2011; Soares et al., 2012). This chapter demonstrates that the WRF model can be used to accurately represent regional-scale climate processes, such as the valley wind regime. In addition, it highlights the usefulness of dynamical downscaling for sensitivity experiments, such as the removal of the glaciers in the Dudh Koshi Valley, and for improving understanding of the mechanisms controlling the valley wind regime.

The high spatial variability of the wind acceleration components and the dominance of the pressure gradient both result from the impact of the tremendously complex terrain that characterises the Dudh Koshi River Basin as well as the wider HKKH region, which requires modelling with a resolution of around 1 km in order to realise accurate output (Collier and Immerzeel, 2015; Karki et al., 2017; Orr et al., 2017; Zängl et al., 2001). The importance of the local pressure gradient and turbulent vertical mixing additionally suggests that the accurate representation of the land surface type and surface exchange is crucial to compute correct heat and moisture fluxes, necessary to produce accurate results in the near-surface wind field. This requires accurate representation of the input land cover field, and particularly

the glacier coverage. If the glaciers continue to melt in this region due to climate change, we are likely to see summer daytime up-valley winds continuing further up the valley due to the increase in the pressure gradient. This increase in up-valley winds is likely to affect other meteorological variables, potentially causing changes to cloud cover at a regional scale, and thus affecting incoming radiation and precipitation.

Chapter 4

Adding debris cover to the WRF model

Approximately 25 % of the glacierised area of the Dudh Koshi River Basin is debris covered (Salerno et al., 2017; Shea et al., 2015a). Debris cover has been shown to have a substantial impact on near-surface meteorological variables and the surface energy balance terms (Collier et al., 2015). However debris cover is not included in the standard WRF land cover categories, and has only been included, previously, as part of a sophisticated coupled atmosphere-glacier model (Collier et al., 2015). As such, there is a need for a simple representation of debris cover in atmospheric models. This chapter introduces a new debris-covered glacier land cover category for the WRF model. The model is tested in a pilot study, using the meteorological observations from the Changri Nup AWS introduced in Chapter 3, and the model results are compared to output computed using two of the standard WRF land cover categories, clean-ice and bare ground (used in Chapter 3 in the 'summer run' and 'summer perturbation experiment', respectively). Lastly, the effect of the new debris-covered glacier land cover category on near-surface meteorological variables is compared to results computed using the original clean-ice category over the Dudh Koshi River Basin.

4.1 Model and methods

4.1.1 WRF land cover categories

The WRF model consists of two distinct software programmes. The WRF preprocessing system (WPS), and the WRF model itself. The WPS software creates the initial and boundary conditions used by the WRF model. These include the static data, which uses the USGS dataset (Loveland et al., 2000) to create the 'landuse index' (WRF variable LU_INDEX), giving 24 land cover categories. Other variables, such as the dominant soil category at the

top and bottom of the soil layers, the fraction of vegetation each month and the annual mean soil temperature are also created by WPS. The WRF model then takes the processed static data and assigns values to the land cover categories through a series of tables. Different land surface models (the physics schemes in WRF which, along with the surface layer schemes, determine the heat and moisture fluxes at the surface) in the WRF model use different combinations of the tables, all of which have the extension .TBL. One such table is LANDUSE.TBL, which is used by all land surface models and gives basic properties, such as albedo and surface roughness, of each of the 24 land cover categories in LU_INDEX, for both summer and winter. In addition, the table VEGPARM.TBL contains details of the vegetation parameters for the 24 land cover categories. Values from VEGPARM.TBL will overwrite those in LANDUSE.TBL, where they involve the same parameters (e.g. surface roughness). The table MPTABLE.TBL contains more details of the vegetation for the 24 land cover categories in LU_INDEX, such as leaf area and stomatal resistance. The surface layer schemes also use the tables to calculate frictional velocities (Skamarock et al., 2008). For full details of these tables and variables, see Appendix C. As well as the tables giving values for each of the 24 land cover categories, SOILPARM.TBL provides values (such as soil conductivity and soil porosity) for the 19 underlying soil categories described by the WRF variable ISLTYP. This has not been altered in this section, as the underlying soil category for the debris-covered glacier category is left as 'land ice'.

As such, there were two stages to adding debris cover to the WRF model:

1. Create a debris mask to input as a land cover category in WPS.
2. Add the values for debris cover to the various tables in WRF used by the land surface model.

4.1.2 Methods

Defining the debris cover mask

As discussed in Section 3.1.1, the default 'snow or ice' (called 'clean-ice' throughout this thesis) category defined in LU_INDEX has been altered to match the Randolph Glacier Index (RGI) outline (RGI Consortium, 2015). An approximation for the debris-covered areas of the glaciers is obtained as follows. A satellite image taken from band 4 of Landsat 8, from April 2017, was used to distinguish the clean-ice area (from the debris-covered area and the off-glacier areas) by extracting colours brighter than a certain threshold value (chosen by

eye). This clean-ice area was then cropped using the RGI outline (to remove any 'bright' areas of the domain that were not on the glaciers), leaving only the clean-ice area within the full glacierised area. The clean-ice area was then superimposed on the existing 30 s resolution USGS 24 land cover categories (including the updated RGI glacier outline) to split the original glacierised area, such that any ice in the original glacierised area but not in the clean-ice area is defined to be debris-covered ice. The new land cover categories are input into WPS. A land cover category that is not present in any of the domains (herbaceous tundra) was replaced by the new debris-covered glacier land cover category. Daniel Bannister (a postdoctoral researcher at the British Antarctic Survey) added the new debris-covered glacier land cover category to the USGS dataset and transformed the dataset into a format readable by WPS. The debris cover mask is only created for the inner model domain. The original and resulting new LU_INDEX categories are shown in Fig. 4.1.

In order to validate the 2 m air temperature over the debris covered part of the Khumbu Glacier in Chapter 5, the debris cover mask over the Khumbu Glacier is manually adjusted so that the land cover categories where the measurements are taken match those observed in the field. This involved changing nine grid points in total, four from shrubland or mixed shrubland to debris-covered glacier, four from debris-covered glacier to barren, and one from mixed shrubland to barren.

Adding the debris cover properties

As mentioned above, there are three tables in the WRF model which describe the land cover parameters, and one which describes the underlying soil type. SOILPARM.TBL represents the underlying soil type, and in the new debris-covered glacier land cover category, this has been left unchanged as 'land ice'. The effects of varying debris cover thickness are beyond the scope of this study, so here the four soil layers are all land ice, and the surface parameters are given by the other three tables (LANDUSE.TBL, VEGPARM.TBL and MPTABLE.TBL), representing the properties of debris cover. The three tables all contain 24 rows (one for each of the 24 land cover categories shown in Fig. 4.1), with values for the various parameters (albedo, surface roughness etc). As such, all three tables representing the surface parameters have been altered to include the new debris-covered glacier land cover category. For the purposes of this study, the debris cover is assumed to be entirely barren of vegetation (debris-covered glaciers can have a very small amount of vegetation, near the glacier terminus, but the majority of the debris-covered area is barren). As such, all the values

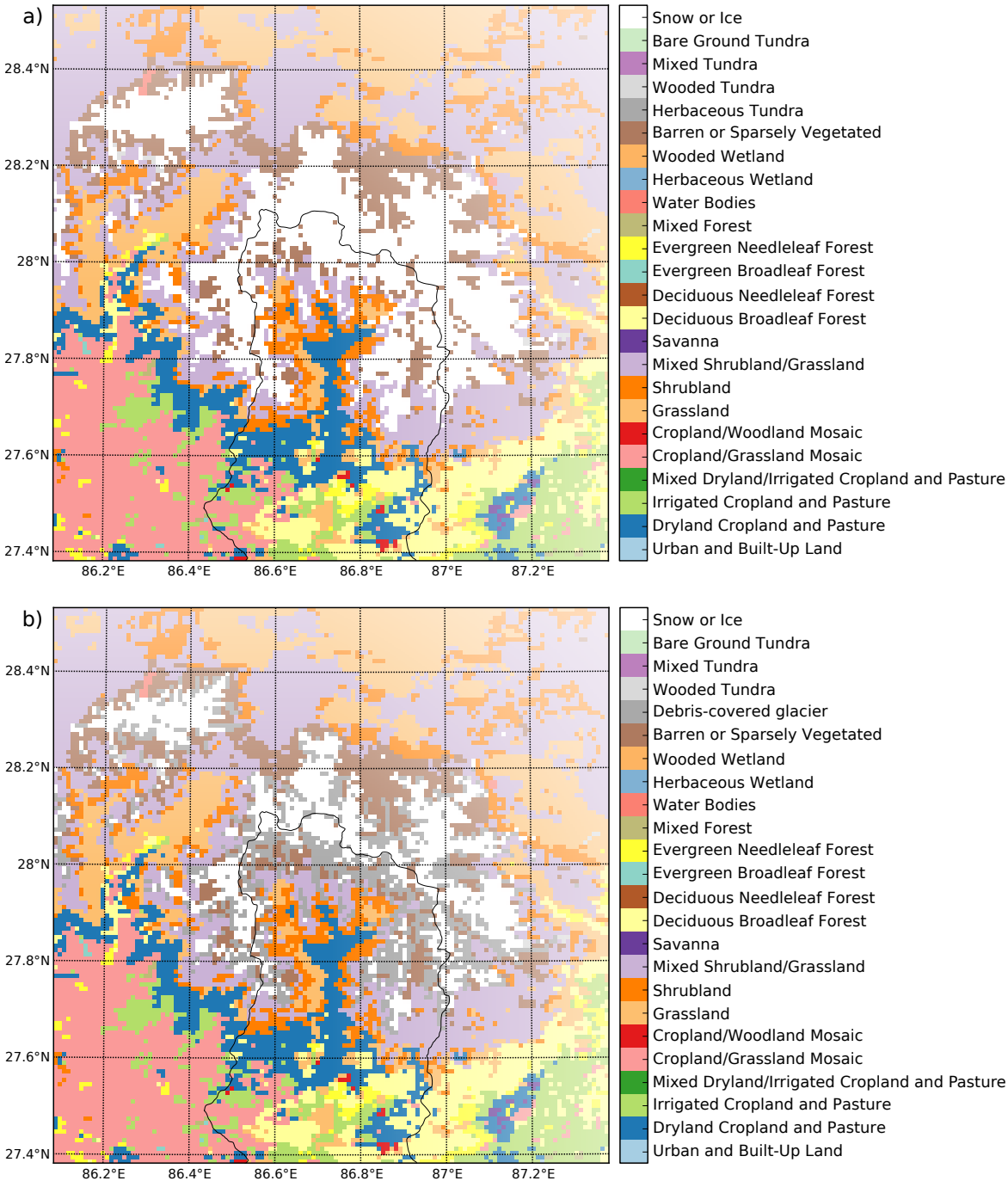

Fig. 4.1 The landuse index (LU_INDEX) showing the 24 land cover categories, used by the default WRF configuration (a) and with debris cover added (b), in the inner model domain. The outline of the Dudh Koshi River Basin is shown as a black line.

for the debris-covered glacier land cover category in MPTABLE.TBL have been copied to match the values for snow and ice. Similarly, those values in VEGPARM.TBL which refer to

vegetation parameters are also taken, in the debris-covered glacier land cover category, to be the same as those for snow and ice. The other values used in VEGPARM.TBL, and all those used in LANDUSE.TBL, and the justification for these values, are shown in Table 4.1.

LANDUSE.TBL has different values for summer and winter, which reflect changes in vegetation growth. As such, for the debris-covered glacier land cover category all values are kept the same for summer and winter. Note that where comparisons are available, the values used in this study are similar to those used by Collier et al. (2015), namely albedo=0.2 (0.2 in Collier et al. (2015)), surface emissivity=0.95 (0.94 in Collier et al. (2015)), roughness length=0.02 m (0.016 m in Collier et al. (2015)).

The modified LANDUSE.TBL, VEGPARM.TBL and MPTABLE.TBL tables are given in full in Appendix C.

Limitations of the new debris-covered glacier land cover category

There are various limitations of representing debris cover in the WRF model in this way, compared to the coupled model used by Collier et al. (2015). Most notably, the properties described above are constant over the glacier, and therefore do not take into account the varying debris-thickness that Collier et al. (2015) include. For example, Reid et al. (2012) found that thermal conductivity (and therefore surface thermal inertia) varied considerably with only a 1 cm difference in debris thickness. The surface moisture availability also varies with debris thickness Collier et al. (2014). As mentioned in Section

Model experiments with the new debris-covered glacier land cover category

In this chapter, three WRF model runs are compared, all for July 2013. These consist of the two summer runs from Chapter 3, with the default WRF model clean-ice land cover category (‘clean-ice run’), and with all the permanent snow and ice removed (‘bare ground run’). The WRF model is rerun in exactly the same setup as for the clean-ice run and the bare ground run, but with the new debris-covered glacier land cover category added (‘debris-cover run’). The observations from the AWS at Changri Nup, which were analysed in Section 3.2.1, are compared to all three runs to assess whether using the debris-covered glacier land cover category is an improvement over using either clean-ice or bare ground.

Table 4.1 The new debris-covered glacier category values. The default WRF clean-ice glacier values are also shown.

Variable	Original clean-ice value	New debris-cover value	Value taken from	Used in	Reasoning
Surface emissivity	0.95	0.95 (fraction 0 to 1)	Nicholson and Benn (2006)	LANDUSE.TBL, VEGPARM.TBL	This was assumed for Larsbreen Glacier, Svalbard, but a similar value of 0.94 was found on Miage glacier, Italy (Brock et al., 2010)
Surface albedo	0.55 (min), 0.7 (max)	0.2 (fraction 0 to 1)	Inoue and Yoshida (1980) Takeuchi et al. (2000) Kayastha et al. (2000) Nicholson and Benn (2013)	LANDUSE.TBL, VEGPARM.TBL	The albedo over debris covered glaciers varies hugely. The studies cited here are all taken from glaciers in the Dudh Koshi Valley and all include 0.2 in the measured albedo range.
Factor for albedo modification with snow	0	1.6		LANDUSE.TBL	Taken to be the same as the value for Tundra
Upper bound on maximum albedo over deep snow	82	70 (%)	Brock et al. (2010)	VEGPARM.TBL	
Roughness length	0.001	0.02 (m)	Quincey et al. (2017)	LANDUSE.TBL, VEGPARM.TBL	This was found to be 0.0184 at one site on Khumbu Glacier and 0.0243 at another.
Surface moisture availability	0.95	0.02 (fraction 0 to 1)		LANDUSE.TBL,	Taken to be the same as barren ground in LANDUSE.TBL
Surface thermal inertia	0.05	0.03 (cal cm^{-2} K^{-1} $s^{-\frac{1}{2}}$)	Calculated from Reid and Brock (2010)	LANDUSE.TBL	Calculated as $\sqrt{\text{volumetric heat capacity} \times \text{ thermal conductivity}}$, using the equation from Wang et al. (2010), where the volumetric heat capacity is equal to specific heat capacity $\times$ density
Surface heat capacity	9.00	8.10×10^5 (J m^{-3} K^{-1})	Reid and Brock (2010)	LANDUSE.TBL	Average of the values for Miage glacier, Italy and Villarrica glacier, Chile. Not used but included for completeness
Threshold water-equivalent snow depth that implies 100% snow cover	0.02	0.03 (m)		VEGPARM.TBL	Taken to be the same as the value for scrubland.

To compare the model output against the data at Changri Nup, the nearest model grid point to the AWS is taken, as described in Section 3.1.4. The observed wind is adjusted to the model height of 10 m, and the model air temperature at 2 m is adjusted to account for the difference in elevation between the model and observations, as described in Section 3.1.4.

To test for significant differences between the model runs, a paired t-test and a bootstrap method are used, similar to that used to calculate the significance of the glacier removal experiment in Section 3.1.4, and fully described in Appendix A.

In this chapter, the output of the column-integrated water vapour and hydrometeors are also examined. The WRF microphysics scheme used throughout this thesis (Morrison double-moment, as described in Section 3.1.1) computes water vapour and five hydrometeors: cloud droplets, rain particles, ice crystals, snow particles and graupel particles, all given as mixing ratios, $\mathrm{kg\,kg^{-1}}$ (Orr et al., 2017). Water vapour represents uncondensed water in the atmosphere, the five hydrometeors represent condensed water in the atmosphere (Cossu and Hocke, 2014). Note that these do not include precipitated water on the ground, which is represented by different variables. The column-integrated hydrometeors for each mixing ratio are calculated to give a quantity of the water (of that type) in the model column (from the ground to the model top at 50 hPa, for each grid cell) in $\mathrm{kg\,m^{-2}}$, or mm. The column integrated water vapour, for example, is calculated by:

$$\sum_{k=1}^{N} \mathrm{QVAPOR}_k \cdot \rho_k \cdot \Delta z_k \tag{4.1}$$

Where N is the number of vertical levels in the model, QVAPOR is the water vapour mixing ratio ($\mathrm{kg\,kg^{-1}}$), ρ is the air density ($\mathrm{kg\,m^{-3}}$), and Δz is the thickness of the vertical levels (m) (Cossu and Hocke, 2014). The column integrated hydrometeors are calculated in the same way, and summed to give their total.

4.2 Results

4.2.1 Comparison with observations

In order to fully investigate the new debris-covered glacier land cover category, the model is compared against all the available observations at the Changri Nup AWS, which are air temperature at 2 m, wind speed at 10 m, and relative humidity at 2 m (Fig. 4.2), and incoming and outgoing shortwave and longwave radiation at the surface (Fig. 4.3).

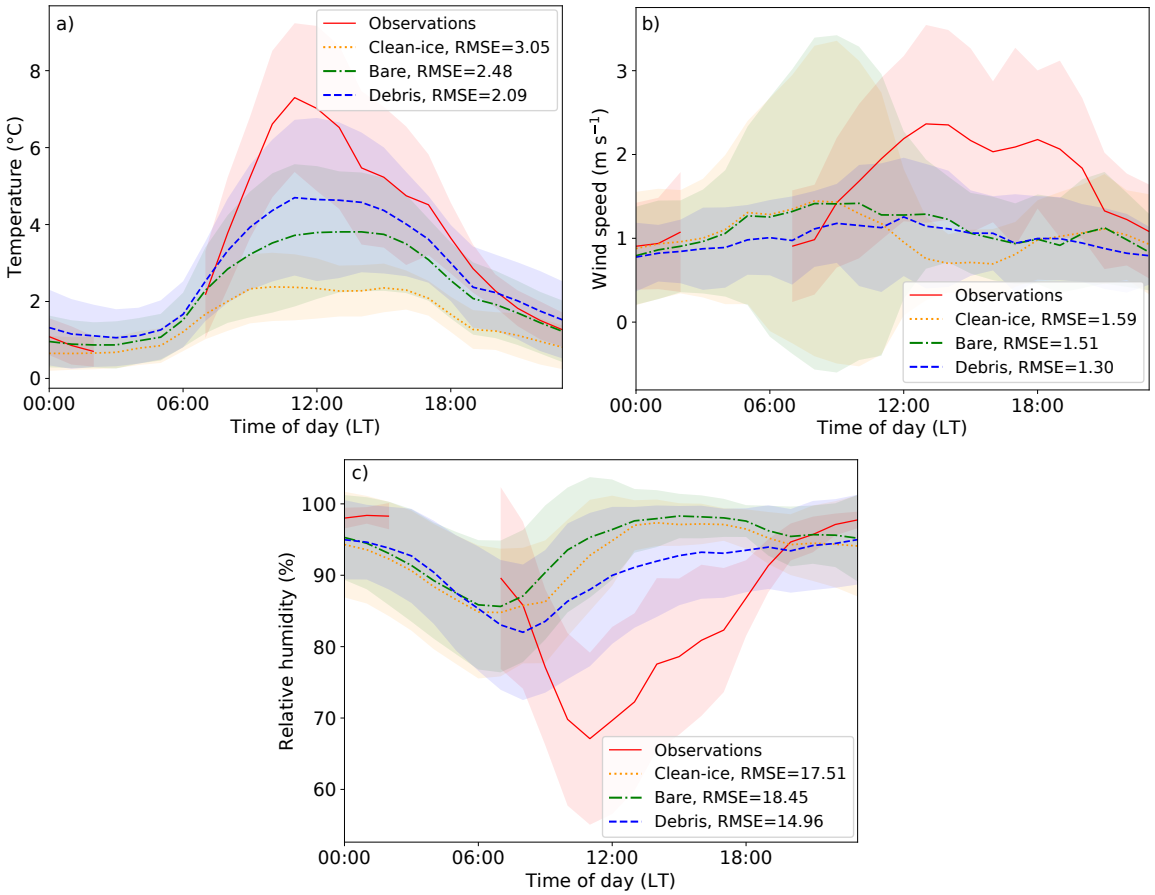

Fig. 4.2 The average diurnal air temperature at 2 m (a), wind speed at 10 m (b) and relative humidity at 2 m (c) for July 2013 at the Changri Nup AWS. The observations are shown (red solid line), along with the three model runs: the original clean-ice category (clean-ice; orange dotted line), the bare ground category (bare; green dash-dot line), the new debris-cover category (debris; blue dashed line). Shading indicates one standard deviation from the mean. The root mean square error (RMSE) between each model run and the observations is also shown.

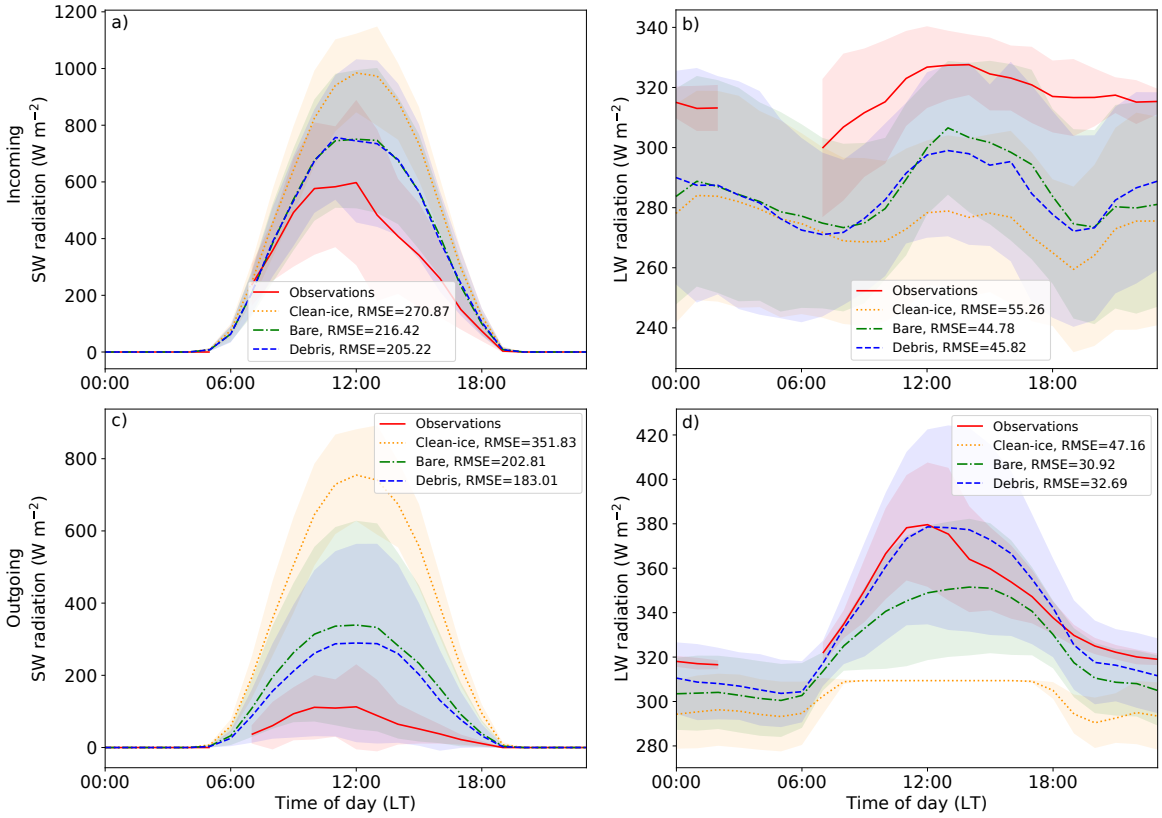

Fig. 4.3 As for Fig. 4.2, but for the incoming shortwave radiation (a), incoming longwave radiation (b), outgoing shortwave radiation (c), and outgoing longwave radiation (d).

All three of the model runs show a cold bias in the daytime average air temperature at 2 m compared to the observations, but the debris-cover run shows an improvement over both the clean-ice run and the bare ground run (maximum daytime temperatures are just over 7 °C in the observations, just over 4 °C and 3 °C in the debris-cover run and bare ground run respectively, and about 2 °C in the clean-ice run) (Fig. 4.2 (a)). The improvement can also be seen in the RMSEs (RMSE of 2.09 °C for the debris-cover run, compared to an RMSE of 2.48 °C and 3.05 °C for the bare ground and clean-ice run, respectively). The nighttime air temperature at 2 m is well captured by all three model runs (Fig. 4.2 (a)). There is a statistically significant difference between the debris-cover run and the clean-ice run during both the day and at night, but no significant difference between the debris-cover run and the bare ground run (Table 4.2).

All three model runs fail to capture the diurnal cycle in wind speed at 10 m. However, the debris-cover run has the lowest RMSE when compared with observations (1.30 m s^{-1}, compared to 1.51 m s^{-1} and 1.59 m s^{-1} for the bare ground and clean-ice runs, respectively) (Fig. 4.2 (b)). Both the clean-ice and the bare ground runs show occasional high wind speeds

Table 4.2 The debris-cover run is tested for statistically significant differences against the clean-ice run and bare ground run at Changri Nup (Figs. 4.2 and 4.3). This table shows whether the difference between the runs is significant at 5 % for the average daytime values (06:00-18:00 LT) and the average nighttime values (19:00-05:00 LT), using a *t*-test with autocorrelation, and a bootstrap test, as described in Appendix A.

	Clean-ice run		Bare ground run	
	Day	Night	Day	Night
Air temperature at 2 m (Fig. 4.2 (a))	yes	yes	no	no
Wind speed at 10 m (Fig. 4.2 (b))	no	no	no	no
Relative humidity at 2 m (Fig. 4.2 (c))	no	no	yes	yes
Incoming shortwave radiation (Fig. 4.3 (a))	yes	yes	no	no
Incoming longwave radiation (Fig. 4.3 (b))	yes	no	no	no
Outgoing shortwave radiation (Fig. 4.3 (c))	yes	yes	no	no
Outgoing longwave radiation (Fig. 4.3 (d))	yes	yes	yes	yes

in the early morning (as can be seen by the shading in Fig. 4.2 (b)), which are not present in the debris-cover run or the observations. There is no significant difference between the debris-cover run and the clean-ice and bare ground run, in either the day or night (Table 4.2).

At night, where observations are available for comparison, the relative humidity at 2 m is well represented in all three model runs (Fig. 4.2 (c)). However the minimum daytime relative humidity is approximately three hours early in all three model runs, compared to the observations, and is overestimated. The debris-cover run has the lowest RMSE of 14.96 % (compared to 17.51 % for the clean-ice run and 18.45 % for the bare ground run) (Fig. 4.2 (c)). There is no significant difference between the debris-cover run and the clean-ice run in either the day or night, but there is a statistically significant difference between the debris-cover run and the bare ground run for both the day and night (Table 4.2).

In the radiation comparisons, the debris-cover run and the bare ground run perform similarly well (Fig. 4.3). This is likely due to the similar albedos, of 0.2 and 0.25 for debris cover and bare ground, respectively. Both runs show a substantial improvement over the clean-ice run in all four radiation terms. Comparison of both the incoming shortwave and longwave radiation terms (Fig. 4.3 (a) and (b)) suggest that the debris-cover and bare ground runs cause more cloud during the day, compared to the clean-ice run. This is confirmed by examining the average cloud fraction in the model column above Changri Nup in the three model runs, where the clean-ice run shows a slightly smaller amount of cloud than the debris-cover and bare ground runs. The incoming shortwave radiation is decreased in

the debris-cover and bare ground runs, compared to the clean-ice run, during the day (at the daytime maximum, it is 1000 W m^{-2} in the clean-ice run and just under 800 W m^{-2} in both the debris-cover and bare ground runs, compared to 600 W m^{-2} in the observations) (Fig. 4.3 (a)). There is a corresponding increase in incoming longwave radiation (Fig. 4.3 (b)), in the debris-cover and bare ground runs compared to the clean-ice run, during the day. However, the bare ground and debris-cover runs still overestimate the incoming shortwave radiation and underestimate the incoming longwave radiation, compared with observations (Figs. 4.3 (a) and (b), respectively). There is a significant difference in the incoming shortwave radiation between the debris-cover run and the clean-ice run, but no significant difference between the debris-cover run and the bare ground run (Table 4.2). Moreover, there is a significant difference in the incoming longwave radiation between the debris-cover run and the clean-ice run during the day, but not at night (and no significant difference between the debris-cover run and the bare ground run, during either the day or the night) (Table 4.2). The effect of the debris-cover addition on cloud cover will be further investigated in Section 4.2.2.

The outgoing shortwave radiation is overestimated during the day in all three runs. While the maximum average outgoing radiation is about 100 W m^{-1} in the observations, it is just under (over) 300 W m^{-1} in the debris-cover run (bare ground run), and almost 800 W m^{-1} in the clean-ice run. Again, the bare ground and debris-cover runs show a substantial improvement over the clean-ice run (Fig. 4.3 (c)), with an RMSE for the debris-cover run of 183.01 W m^{-1} compared to an RMSE of 351.85 W m^{-1} for the clean-ice run. The overestimation of outgoing shortwave radiation may be due, in part, to the overestimation of incoming shortwave radiation (as more incoming shortwave radiation means there is more shortwave radiation to be reflected) (Fig. 4.3 (a)). There is a significant difference in the outgoing shortwave radiation between the debris-cover run and the clean-ice run, but not between the debris-cover and bare ground runs.

Lastly, the debris-cover run captures, on average, the timing and amplitude of the diurnal cycle in outgoing longwave radiation (Fig. 4.3 (d)), although the bare ground run has a slightly lower RMSE (30.92 W m^{-2} and 32.69 W m^{-2} for the bare ground run and the debris-cover run, respectively). Both the bare ground and debris-cover runs show a substantial improvement over the clean-ice run. There is a significant difference between the debris-cover run and both the clean-ice and bare ground runs, for both the day and the night, for outgoing longwave radiation (Table 4.2).

4.2.2 Effects of adding debris cover to the WRF model

To establish more generally the effects of using the debris-covered glacier land cover category compared to the original clean-ice land cover category, the output from the debris-cover run and the clean-ice run are compared across the Dudh Koshi River Basin. Note that the bare ground run is not compared, and all figures in this section show only significant differences, and are cropped to focus on the glacierised area. All the surface energy balance terms discussed in this section are taken with a positive term being towards the surface, i.e. all the incoming and outgoing shortwave and longwave radiation terms, as well as the sensible and latent heat fluxes, are calculated with positive values denoting fluxes from the atmosphere to the ground. The ground heat flux is denoted with positive values denoting a flux from below the ground to the surface.

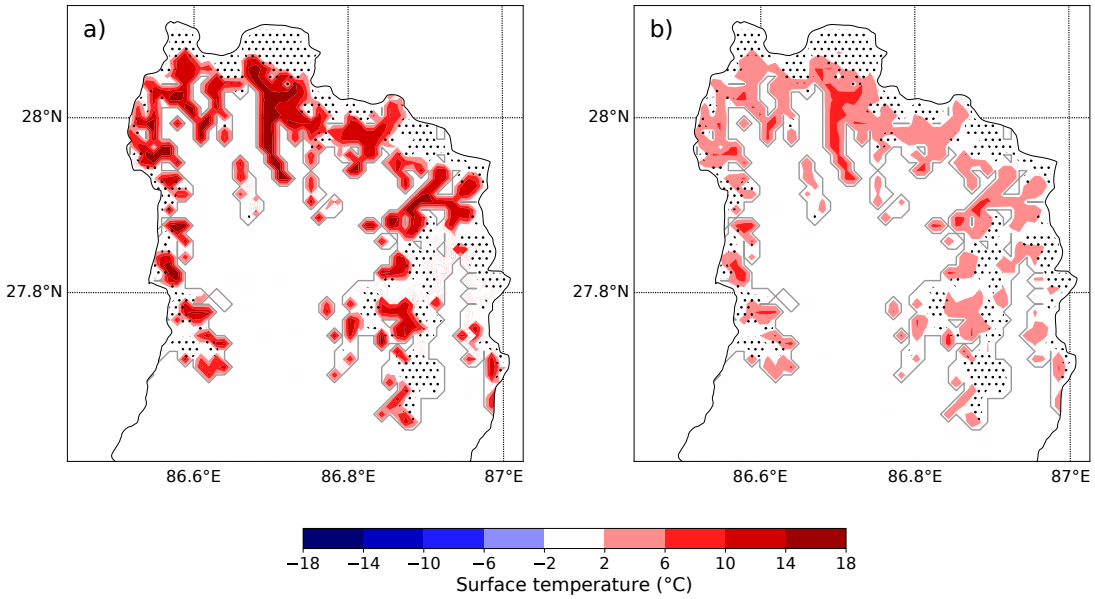

Fig. 4.4 The significant differences in surface temperature between the debris-cover run and the clean-ice run (i.e. debris-cover run minus clean-ice run). The grey outline shows the edge of the glacier in the model, and the stippling shows the clean-ice areas of the glaciers. The average daytime (06:00-18:00 LT) values over July 2013 are shown in (a), average nighttime (19:00-05:00 LT) values are shown in (b). Note that the domain has been cropped to show only the areas surrounding the glaciers, where almost all the differences are.

The debris-cover run substantially increases the surface temperature compared to the clean-ice run over the debris-covered areas of the glacier (Fig. 4.4). The largest increases occur during the day, where the surface temperature is increased by over 14 °C over some of

the debris-covered parts of the glaciers (Fig. 4.4 (a)). On average, the surface temperature increases from −0.47 °C in the clean-ice run to 8.41 °C in the debris-cover run, over the debris-covered glaciers during the day (Table 4.3). Given that clean-ice glaciers can only reach a maximum of temperature of 0 °C, the increase in surface temperature during the day is to be expected. There is also a smaller increase in temperature over the debris-covered glaciers at night, suggesting that the debris-cover retains heat during the night (Fig. 4.4 (b)).

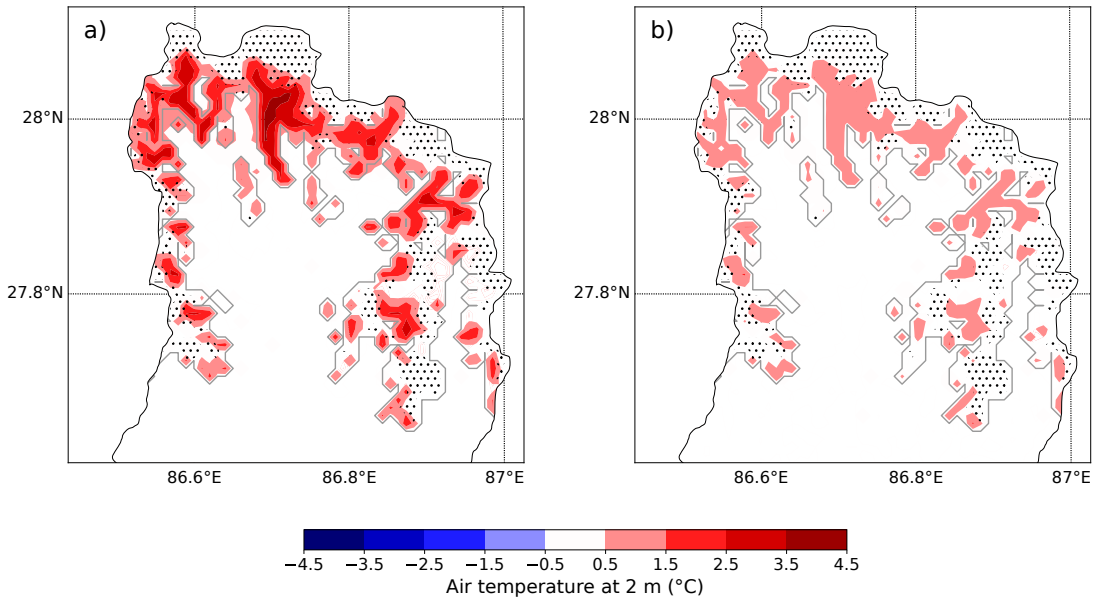

Fig. 4.5 As for Fig. 4.4, but for the air temperature at 2 m.

The increase in surface temperature over the debris-covered glaciers leads to an increase in air temperature at 2 m in the debris-cover run compared to the clean-ice run, of up to 3.5 °C over some parts of the debris-covered glaciers during the day, and a smaller increase of 0.5 °C to 1.5 °C at night (Figs. 4.5 (a) and (b)). On average, over the debris-covered parts of the glaciers, the air temperature at 2 m increases from 1.57 °C in the clean-ice run to 3.13 °C in the debris-cover run (Table 4.3).

In Chapter 3, it was shown that when the glaciers are removed from the model, the wind continues further up the valley, especially over the northern regions. Figure 4.6 demonstrates that a similar effect is obtained by adding debris-cover to the WRF model. The increases in temperature seen in Figs. 4.4 and 4.5 cause a temperature gradient between the surface temperature and the air temperature away from the surface, leading to a horizontal pressure difference and therefore an increase in upslope winds over the debris-covered ice. The

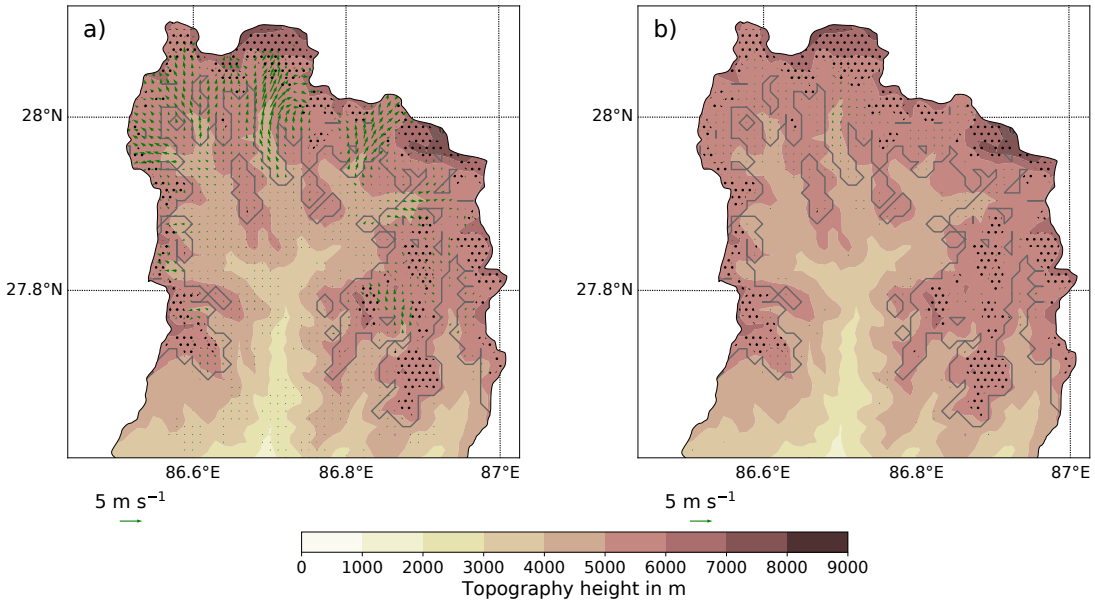

Fig. 4.6 The change in wind velocity (vectors) (debris-cover run minus clean-ice run). Only vectors which show a significant difference in either the meridional or zonal velocities are shown. The grey outline shows the edge of the glacier in the model, and the stippling shows the clean-ice parts of the glaciers. The average daytime (06:00-18:00 LT) values over July 2013 are shown in (a), average nighttime (19:00-05:00 LT) values are shown in (b). Note that the domain has been cropped to show only the glacierised areas, where almost all the differences are.

increase in upslope winds is much more evident during the day (Fig. 4.6 (a)), where the increase in surface temperature is greatest, but there is also a very small increase in upslope winds at night (Fig. 4.6 (b)).

In addition to the change in surface temperature (and subsequent effects on air temperature at 2 m and wind at 10 m), the debris-cover has a much lower soil moisture content than the clean-ice. This leads to a decrease in relative humidity at 2 m in the debris-cover run compared to the clean-ice run, during the day over the debris-covered areas (from 91.72 % in the clean-ice run to 88.59 % in the debris-cover run (Table 4.3)), as there is less moisture at the surface for evaporation (Fig. 4.7 (a)). This decrease in relative humidity in the debris-cover run could also be due to the higher temperatures at 2 m. Recall that the debris-covered glacier still has 'land ice' as the underlying soil type, however the glaciers in the WRF model are fixed, i.e. they cannot melt during the model run, so the soil moisture is not changed due to melting glacier. There is also an increase in the relative humidity at 2 m over the (unchanged) clean-ice areas of the glacier during the day (from 91.97 % in the clean-ice run to 93.97 %

Table 4.3 Average daytime values over the debris-covered glacier area and the clean-ice glacier area, for the clean-ice run and the debris-cover run for July 2013. All surface energy budget terms have been calculated with positive values denoting fluxes from the atmosphere to the ground. Note that all values are used in the averages shown here, regardless of significance.

	Clean-ice glacier area (stippling in Fig. 4.4)		Debris-covered glacier area (non-stippling inside glacier outline in Fig. 4.4)	
	Clean-ice run	Debris-cover run	Clean-ice run	Debris-cover run
Surface temperature (°C)	-1.00	-0.90	-0.47	8.41
Air temperature at 2 m (°C)	-0.72	-0.65	1.57	3.13
Relative humidity at 2 m (%)	91.97	93.97	91.72	88.59
Column integrated water vapour ($kg\,m^{-2}$)	8.76	8.93	10.79	10.97
Total column integrated hydrometeors (ice+snow+grapel+rain+cloud) ($kg\,m^{-2}$)	0.30	0.31	0.30	0.30
Vertical velocity at lowest model level ($m\,s^{-2}$)	-0.18	0.01	-0.11	0.11
Incoming shortwave radiation ($W\,m^{-2}$)	584.21	557.91	561.41	439.74
Outgoing shortwave radiation ($W\,m^{-2}$)	-457.70	-434.25	-422.19	-175.12
Incoming longwave radiation ($W\,m^{-2}$)	268.78	277.42	276.98	292.00
Outgoing longwave radiation ($W\,m^{-2}$)	-304.62	-305.02	-307.01	-350.28
Total net radiation ($W\,m^{-2}$) (incoming radiation positive)	90.67	96.06	109.18	206.34
Sensible heat flux ($W\,m^{-2}$)	-0.70	-0.52	8.32	-83.10
Latent heat flux ($W\,m^{-2}$)	-9.18	-6.97	3.94	-52.98
Ground heat flux ($W\,m^{-2}$)	-75.41	-82.96	-116.20	-64.05
Snow height (m)	0.38	0.37	0.19	0.13

in the debris-cover run (Fig. 4.7 (a) and Table 4.3)), suggesting that the increased up-valley winds over the debris-cover glacier seen in Fig. 4.6 are transporting water vapour further up the valley.

This theory that the increase in up-valley winds transports water vapour further up the valley is confirmed by examining the column-integrated water vapour, which is increased over parts of both the debris-covered and clean ice glaciers, in the debris-cover run compared to the clean-ice run during the day (Fig. 4.8 (a) and Table 4.3). As discussed, the relative humidity is decreased over the debris-covered glaciers in the debris-cover run compared to the clean-ice run. Thus, the increase in water vapour over the glaciers in the debris-cover run must be due to the increase in near-surface winds transporting water vapour further up the valley (rather than evaporation from the surface). There is also an increase in water vapour at night at the lower elevations in the valley (Fig. 4.8 (b)). It is not clear what is causing this increase, or whether it represents a physical phenomenon, however it should be noted

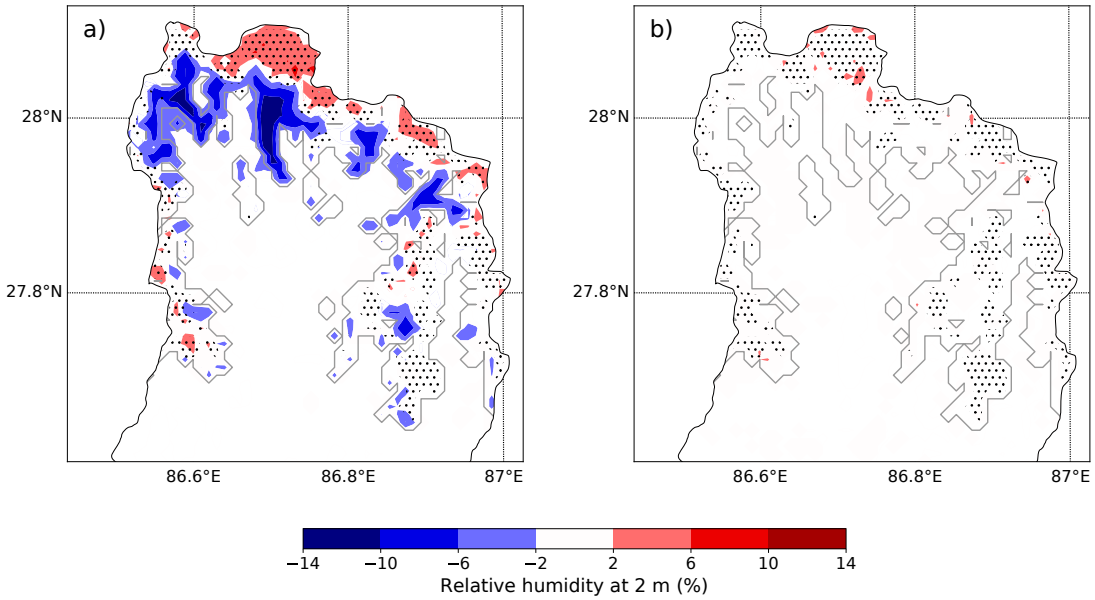

Fig. 4.7 As for Fig. 4.4, but for the relative humidity at 2 m. Note that this refers to the absolute change in relative humidity (measured as a percentage), not the percentage change in relative humidity.

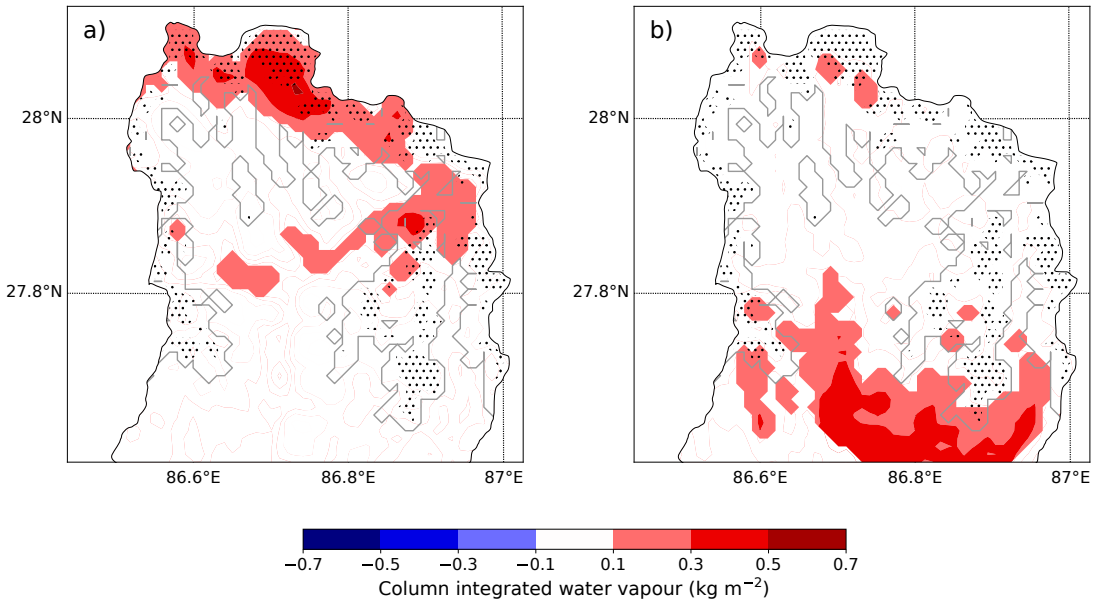

Fig. 4.8 As for Fig. 4.4, but for the column integrated water vapour.

that (during both the day and night, and in both the debris-cover and clean-ice runs) the column-integrated water vapour is substantially higher at the lower elevations in the valley than over the glacierised regions (not shown). As such, the daytime increase in water vapour

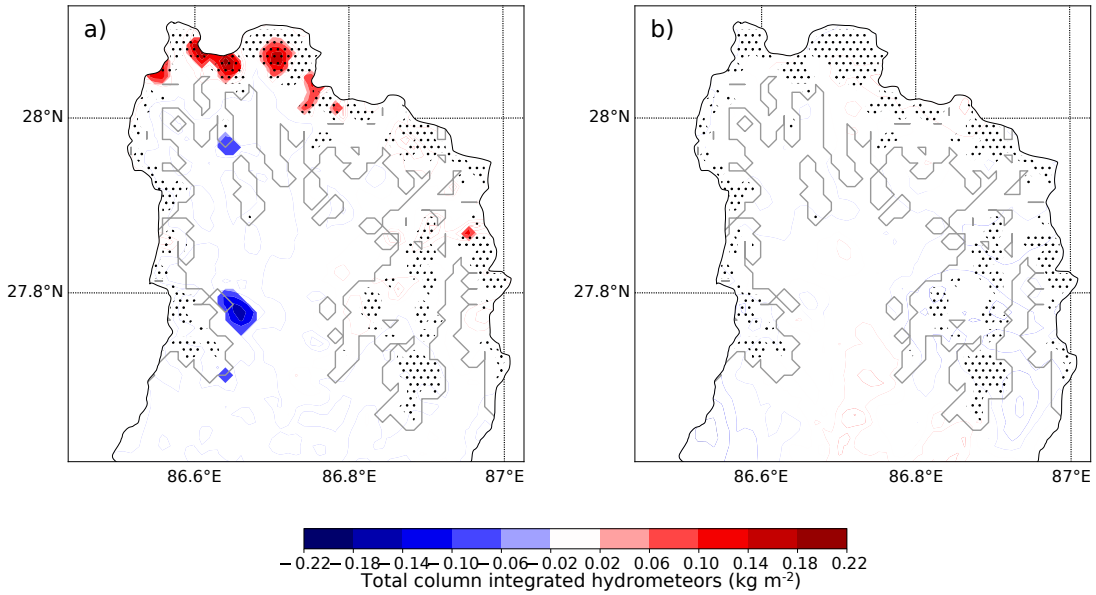

Fig. 4.9 As for Fig. 4.4, but for total column integrated mass for all hydrometeors, i.e. cloud droplets + rain particles + ice crystals + snow particles + graupel particles.

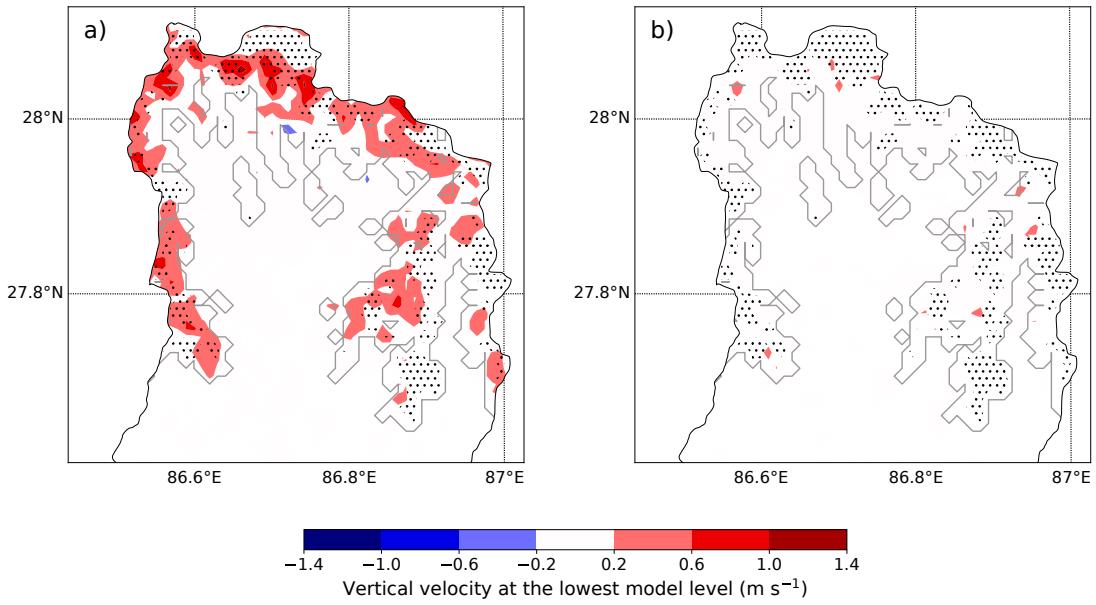

Fig. 4.10 As for Fig. 4.4, but for vertical velocity at the lowest model level.

over the glaciers is, relatively, a much larger increase than the nighttime increase at lower elevations.

There is an increase in total column integrated mass for all hydrometeors (cloud droplets + rain particles + ice crystals + snow particles + graupel particles) in the debris-cover run compared to the clean-ice run, over some of the glacierised areas during the day (Fig. 4.9 (a)). Overall, there is a very small increase over the clean-ice areas of the glacier, from 0.30 kg m^{-2} in the clean-ice run to 0.31 kg m^{-2} in the debris-cover run (Table 4.3), but in a few places the increase is over 0.18 kg m^{-2} (Fig. 4.9 (a)). There are two likely causes of this increase. First, as just discussed, there is an increase in water vapour over the glaciers during the day in the debris-cover run compared to the clean-ice run. Second, there is an increase in vertical velocity at low altitudes, especially at the boundary between the debris-covered parts of the glaciers and the clean-ice parts of the glacier, during the day in the debris-cover run compared to the clean-ice run (Fig. 4.10 (a)). Where the upslope winds meet the clean-ice glaciers, there is convergence of the wind, leading to increased vertical wind velocities and lifting the water vapour to higher altitudes. The water vapour condenses into cloud at high altitudes, so the mass of the hydrometeors is increased (Fig. 4.9 (a)). In the clean-ice run, the convergence of the wind occurs at the edge of the glacier, whereas in the debris-cover run it occurs over boundary between the debris-covered and clean-ice glaciers (Fig. 4.6). There is very little change in total mass of column integrated hydrometeors seen at night (Fig. 4.9 (b)).

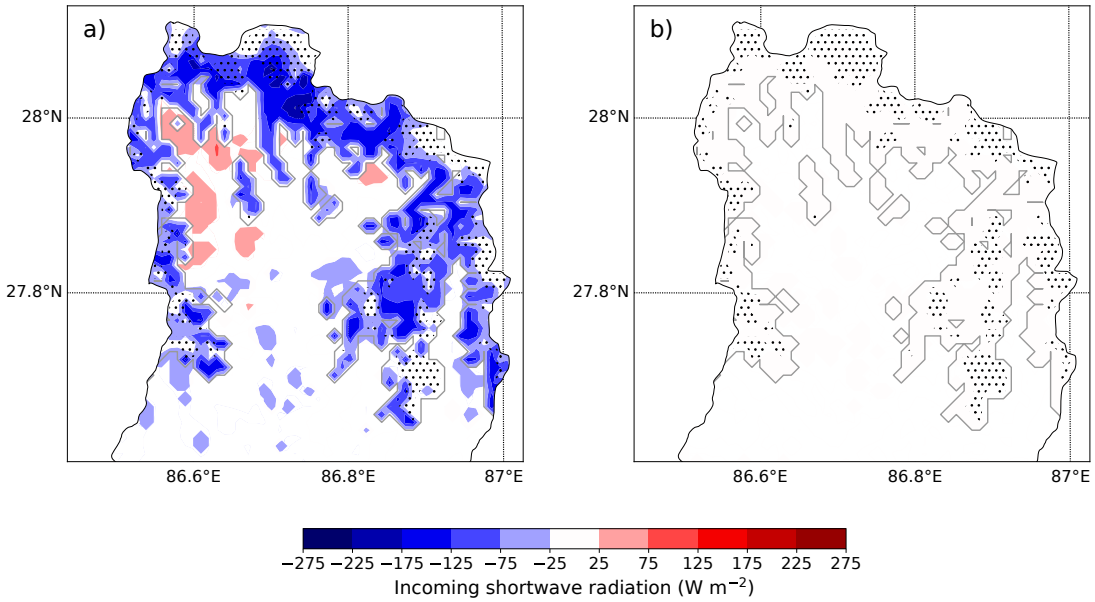

Fig. 4.11 As for Fig. 4.4, but for incoming shortwave radiation.

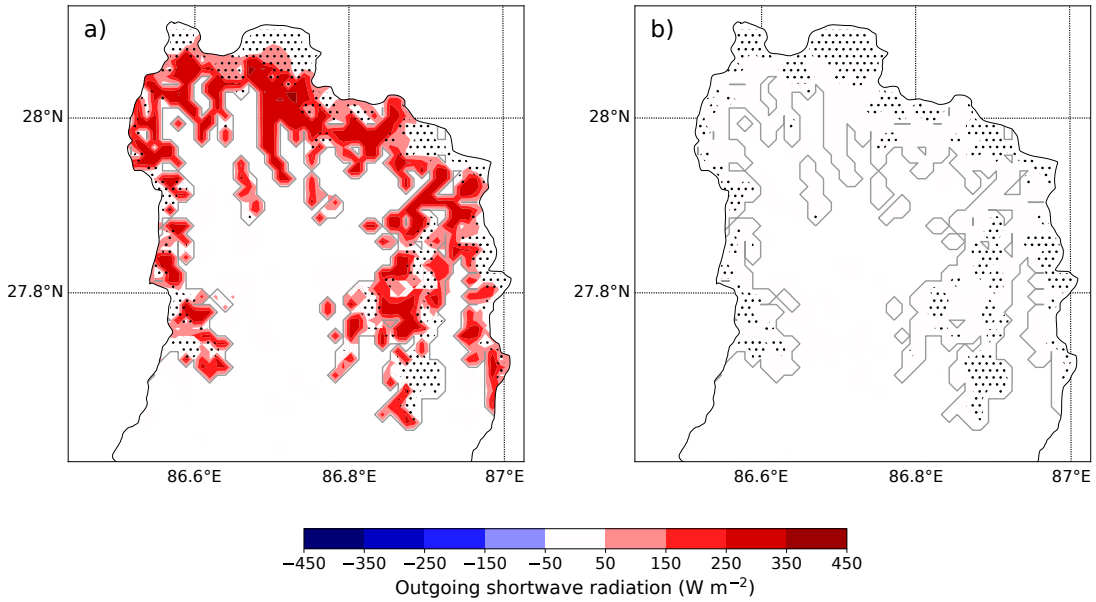

Fig. 4.12 As for Fig. 4.4, but for outgoing shortwave radiation.

The land cover parameter choice for the debris-covered glaciers setup, and the subsequent effects on total mass of hydrometeors, cause changes to the surface energy balance. Note that for Figs. 4.11 to 4.17, positive values denote a flux from the atmosphere to the ground. Over the clean-ice areas of the glaciers where there is the largest increase in mass of total hydrometeors during the day (Fig. 4.9), the incoming shortwave radiation is reduced in the debris-cover run compared to the clean-ice run (Fig. 4.11 (a)). There is also a general decrease in incoming shortwave radiation over the debris-covered areas (from 561.41 W m^{-2} in the clean-ice run to 439.74 W m^{-2} in the debris-cover run (Table 4.3 and Fig. 4.11 (a)). This is at least partially due to the increase in the total column integrated water vapour over the debris-covered areas, which absorbs the shortwave radiation before it reaches the surface (Fig. 4.8 (a)).

The outgoing shortwave radiation becomes much less negative (from −422.19 W m^{-2} in the clean-ice run to −175.12 W m^{-2} in the debris-cover run (Table 4.3 and Fig. 4.12(a))) over the debris-cover areas of the glacier during the day, as would be expected from the lower albedo of debris-covered ice compared to clean ice. There is also a small reduction in outgoing shortwave radiation over the clean-ice parts of the glaciers in the debris-cover run compared to the clean-ice run (Fig. 4.12 (a)), due to the reduction in incoming radiation. Overall, there is a net increase in energy transferred from the atmosphere to the ground from shortwave radiation during the day over the debris-covered parts of the glaciers, in the

debris-cover run compared to the clean-ice run, of 124.41 W m^{-2}, and a net decrease over the clean-ice parts of the glacier, of 2.86 W m^{-2}.

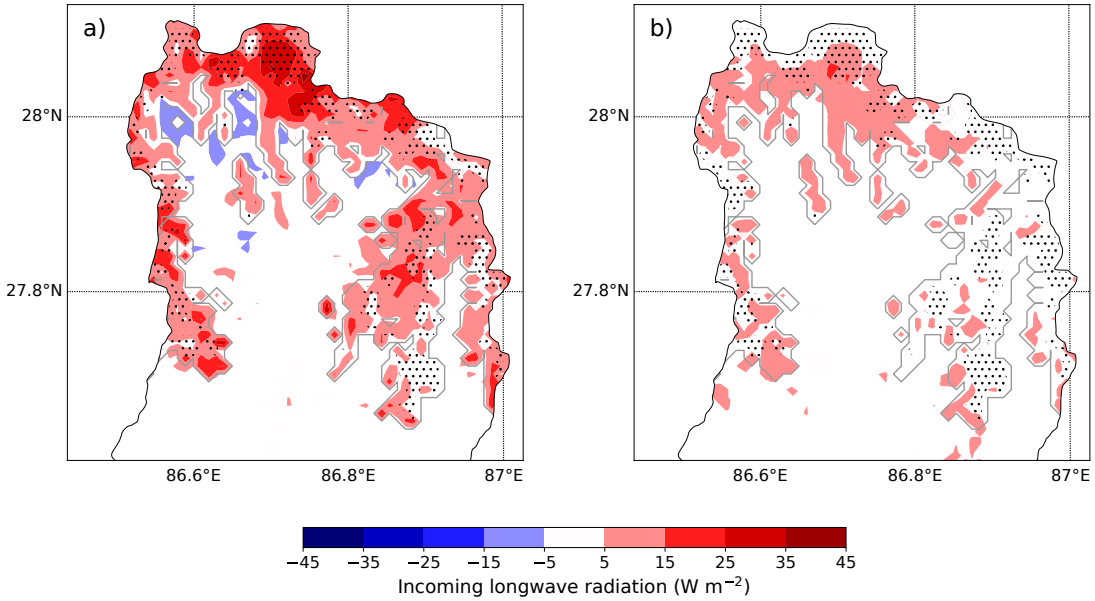

Fig. 4.13 As for Fig. 4.4, but for incoming longwave radiation.

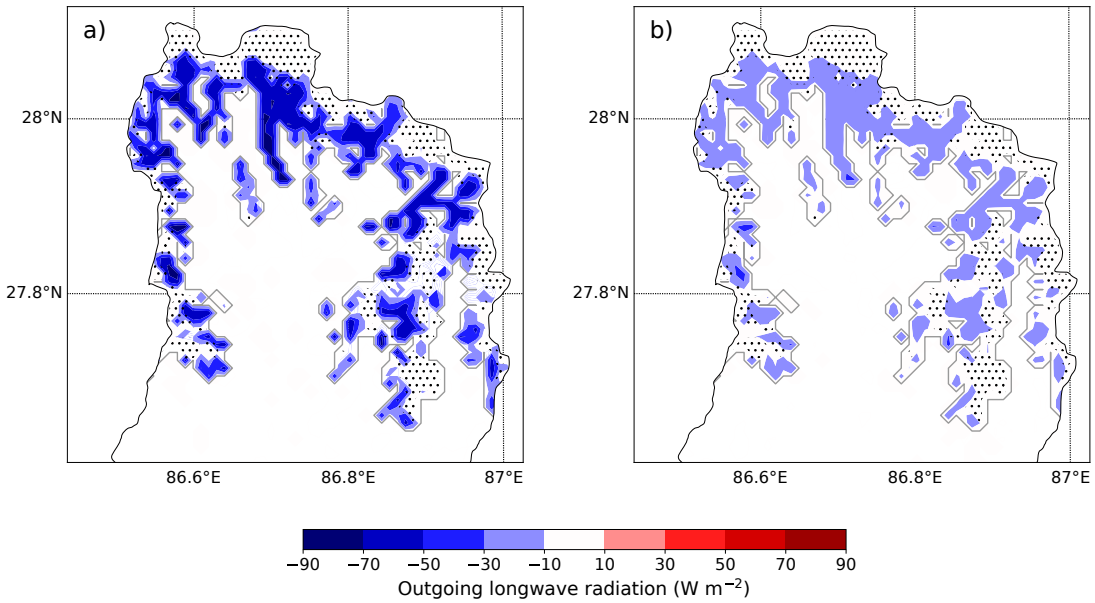

Fig. 4.14 As for Fig. 4.4, but for outgoing longwave radiation.

The change in albedo over the debris-covered glaciers, and the increase in hydrometeors and water vapour, also have an impact on longwave radiation. There is an increase in the incoming longwave radiation during the day in the debris-cover run compared to the clean-ice run, over the areas of increased hydrometeors and water vapour (Fig. 4.13 (a) and Table 4.3) due to the increased emissivity of the atmosphere. There is also a small increase in incoming LW radiation at night, from 280.71 W m^{-2} in the clean-ice run to 287.54 W m^{-2} in the debris-cover run over the debris-covered parts of the glacier (Fig. 4.13 (b)). This is probably due to a small increase in water vapour at night (Fig. 4.8).

There is an increase in the outgoing longwave radiation over the debris-cover areas of the glacier in the debris-cover run (−350.28 W m^{-2}) compared to the clean-ice run (−307.01 W m^{-2}) during the day (Fig. 4.14 (a) and Table 4.3). This is also seen at night to a smaller extent, as the debris-cover retains heat into the night (Fig. 4.14 (b)). Overall, there is a net decrease in energy at the surface during the day from longwave radiation over the debris-covered parts of the glaciers in the debris-cover run compared to the clean-ice run, of −28.25 W m^{-2}, and a net increase over the clean-ice parts of the glacier, of 8.25 W m^{-2}. At night there is a smaller decrease over the debris-covered parts of the glacier of −10.49 W m^{-2}.

Overall, there is a small increase in the net radiation over the clean-ice areas of the glacier in the debris-cover run (96.06 W m^{-2}) compared to the clean-ice run (90.67 W m^{-2}) during the day (Table 4.3), due to the increase in incoming longwave radiation. Over the debris-covered areas, there is a large increase in the net radiation in the debris-cover run (206.34 W m^{-2}) compared to the clean-ice run (109.18 W m^{-2}) during the day (Table 4.3).

The sensible heat flux shows a decrease and a change of sign over the debris-covered areas of the glacier during the day, from 8.32 W m^{-2} in the clean-ice run to −83.10 W m^{-2} in the debris-cover run (Fig. 4.15 (a) and Table 4.3), with no change at night. The decrease in sensible heat during the day shows very similar patterns to the increase in surface temperature during the day, as the increase in surface temperature causes more convection, transferring heat away from the surface (Fig. 4.15 (a) cf. 4.4 (a)).

The latent heat flux also shows a decrease, and a change of sign, over the debris-covered parts of the glacier during the day (from 3.92 W m^{-2} in the clean-ice run to −52.98 W m^{-2} in the debris-cover run) (Fig. 4.15 (a) and Table 4.3). Recall that positive values denote a flux of energy from the atmosphere to the surface, i.e. condensation or freezing. In the clean-ice run,

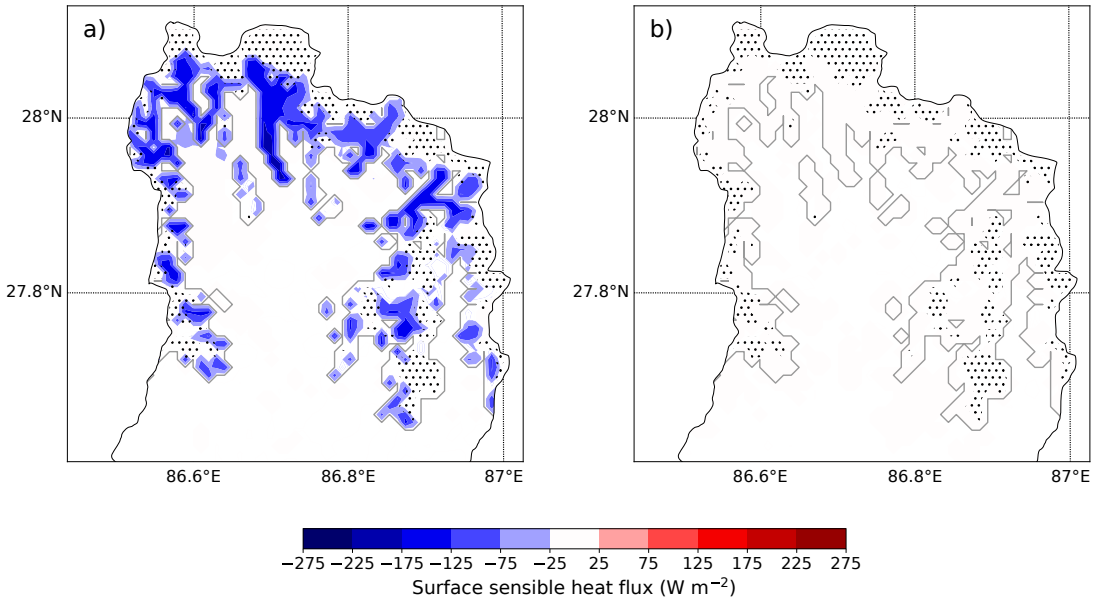

Fig. 4.15 As for Fig. 4.4, but for the sensible heat flux.

the small positive latent heat flux during the day is due to condensation and freezing on the ice surface. In the debris-cover run the large negative latent heat flux during the day is probably due to evaporation or snow melt at the surface. There is no change at night (Fig. 4.16 (b)).

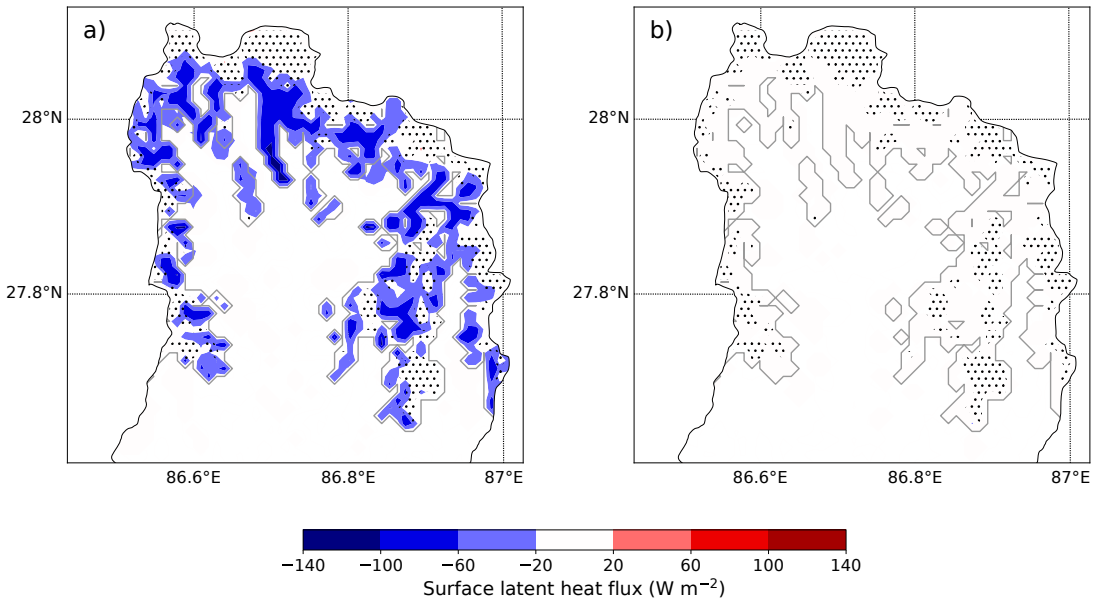

Fig. 4.16 As for Fig. 4.4, but for the latent heat flux.

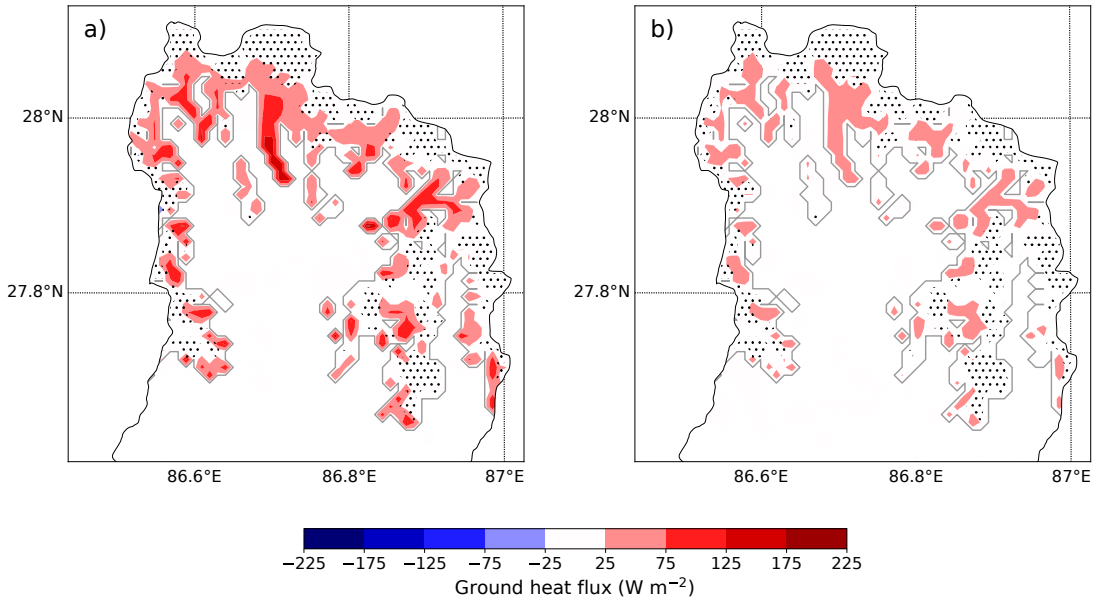

Fig. 4.17 As for Fig. 4.4, but for the ground heat flux.

The ground heat flux is also affected by the debris-cover addition, changing over the debris-covered glacier areas from −116.20 W m^{-2} in the clean-ice run to −64.05 W m^{-2} in the debris-cover run (i.e. in both cases the ground is absorbing energy from the surface during the day). The increase suggests that the clean-ice requires more energy to warm it to the same degree as the debris-cover during the day (Fig. 4.17 (a)). At night over the debris-covered parts of the glaciers the ground heat flux is positive in both runs (not show), and greater in the debris-cover run than the clean-ice run (Fig. 4.17 (b)), i.e. the debris-cover warms the surface more than the clean-ice at night, as might be expected given the debris-cover remains warm into the night.

Lastly, the increased hydrometeors over the clean-ice parts of the glaciers (Fig. 4.9 (a)), and the changes to the surface energy balance terms, have a subsequent effect on the snow depth on the ground (Fig. 4.18). Where the increase in total column integrated hydrometeors is greatest, there is an increase in snow depth in the debris-cover run compared to the clean-ice run (Fig. 4.18). Overall, the increase in hydrometeors is likely to cause more snow through direct precipitation, and also affect the total radiation reaching the surface. The increase in snow depth is seen in both the day and the night, as might be expected given that there is little snow melt at night. There are also some areas where snow depth is reduced in the debris-cover run compared to the clean-ice run, which may be due to changes in either precipitation or in the surface energy balance. As the snow cover alters the surface albedo,

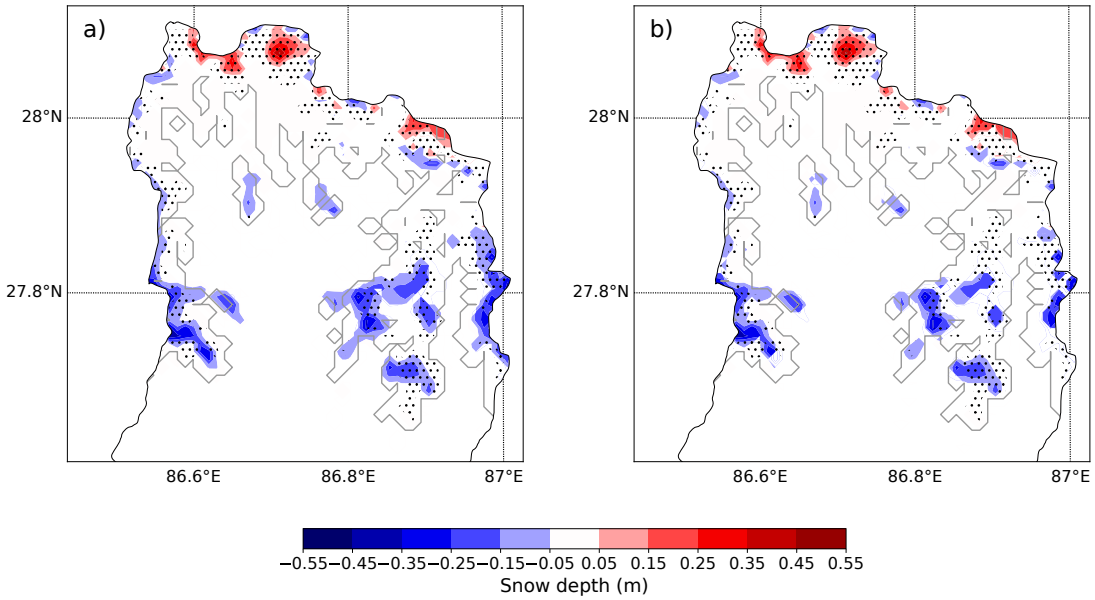

Fig. 4.18 As for Fig. 4.4, but for snow depth.

there are feedbacks between the snow depth and the surface energy balance, making it difficult to assess the energy available for melt at the surface on the days of increased snow depth.

4.3 Discussion and Conclusions

In this chapter, the WRF model was run with a new debris-covered glacier land cover category added (debris-cover run), and compared to both a model run with all the snow and ice removed (bare ground run) and to a model run with the original clean-ice land cover category (clean-ice run), for July 2013. The debris-cover run improves the WRF model compared to the clean-ice run, with a smaller RMSE between model output and observations at Changri Nup, for all variables measured (air temperature at 2 m, wind speed at 10 m, relative humidity at 2 m, and incoming and outgoing shortwave and longwave radiation at the surface). There is a significant difference between the model output in the debris-cover run and clean-ice run at Changri Nup during the day for air temperature at 2 m and all four radiation terms.

Some of the near-surface meteorological variables and surface fluxes of debris-cover might be expected to be more similar to bare ground than to clean-ice. As such, the debris-cover run was also compared against the bare ground run, to ensure that the new debris-cover category provides a real improvement to the WRF model over other surface types. The debris-cover run is only significantly different to the bare ground run for relative humidity and outgoing longwave radiation for the month tested. However, as measured by the RMSEs between model outputs and observations, the debris-cover run shows a substantial improvement over the bare ground run for air temperature at 2 m, wind speed at 10 m and relative humidity at 2 m, and a small improvement for incoming and outgoing shortwave radiation. There are no variables for which the model output from the debris-cover run is markedly worse than that from the bare ground run, when compared to observations. To fully test the debris-cover category, the model should be tested over a range of different areas, and over a longer time period (in particularly for all seasons), which was not possible for this study. However, the experiment results presented suggest that the debris-cover category improves the accuracy of the WRF model over debris-covered glaciers.

Next, output from the debris-cover run was compared to the clean-ice run over the whole of the Dudh Koshi Valley. The addition of the debris-cover has an effect not just over the debris-cover glacier areas, but also over some of the clean-ice areas (where the land cover category is unchanged). The results from this study are compared below to those previous studies, particularly that of Collier et al. (2015), who compared debris-covered and clean-ice versions of the WRF model, as part of a coupled atmosphere-glacier model, over a river basin

in the Karakoram region.

Surface temperature and air temperature at 2 m are both increased over the debris-cover areas in the debris-cover run, particularly during the day. These findings agree with those of Collier et al. (2015), in both sign and magnitude. Both the present study and the study by Collier et al. (2015) find an increase in surface temperature of almost 20 °C in some locations, between clean-ice and debris-cover runs, and an increase in air temperature at 2 m of 3 °C to 4 °C. An increase in surface temperature was also found by Reid et al. (2012), who examined the effects of adding debris-cover to a glacier model over a glacier in Switzerland.

In this study, the increase in surface and near-surface air temperature leads to an increase in the wind speed at 10 m over the debris-covered areas, in the debris-cover run compared to the clean-ice run, due to an increase in the upslope winds. This agrees with a short observational study on the Khumbu Glacier by Takeuchi et al. (2000), who found that wind speeds were slightly higher at an AWS on debris-covered ice compared to one on clean ice. However, it is in contrast to the findings of Collier et al. (2015), who found that the increase in roughness length over the debris-cover slowed the wind speed at 10 m. The roughness length used in this study is slightly higher than that used in Collier et al. (2015). It should be noted that Collier et al. (2015) found sustained katabatic winds in the clean-ice run, which are not present in this study. As such, this suggests that glaciers in different regions, particularly with different topographies or climatic regimes, may react differently to the addition of debris-cover, in terms of near-surface wind speed.

The increase in upslope wind with the addition of debris-cover observed in this study has consequent effects on other meteorological variables, by driving water vapour further up the valley. This, in turn, leads to an increase in total mass of column-integrated hydrometeors over the clean ice areas to the north of the valley, and consequent effects on the surface energy balance terms. The net shortwave radiation is increased over the debris-covered areas of the glacier, due predominantly to the lower albedo of debris-cover leading to a much smaller outgoing shortwave radiation term, compared with clean ice. There is also less incoming shortwave radiation, especially over the clean-ice areas where there is an increase in hydrometeors. Collier et al. (2015) also found an increase in net shortwave radiation in the debris-cover run compared to the clean-ice run, however the increase found in that study (of approximately 30 W m^{-2} in the areas of most exposed debris-covered grid cells) is much smaller than the increase found in this study, which averages over 125 W m^{-2} over the

debris-covered areas, despite both studies using the same albedo of 0.2.

Net longwave radiation (incoming minus outgoing) is decreased in this study, as the debris cover emits more longwave radiation than the clean ice. This agrees with the studies of Collier et al. (2015) and Reid et al. (2012). The magnitude of the change is similar in the present study and that of Reid et al. (2012), both of which suggest outgoing longwave radiation is around $-310\,\mathrm{W\,m^{-2}}$ in the clean-ice run and around $-350\,\mathrm{W\,m^{-2}}$ in the debris-cover run (for a debris thickness of 6 cm in the Reid et al. (2012) study) during the day. This study also suggests that incoming longwave radiation is increased (although by less than the reduction in outgoing longwave radiation over debris-covered parts of the glaciers) due to the increased hydrometeors and water vapour emitting longwave radiation toward the ground. Overall, there is a net increase in longwave radiation over the clean-ice parts of the glaciers in this study, due to the increased hydrometeors and water vapour. Note that Collier et al. (2015) does not present the incoming and outgoing radiation terms individually, and does not comment on hydrometeors or water vapour changes.

Both the sensible and latent heat fluxes are reduced over debris cover compared to clean ice, both in this study and in Collier et al. (2015). Similar effects on the sensible heat flux were also found by Reid et al. (2012). The reduction in sensible heat is due to the heating of the debris-covered surface during the day, leading to convection of heat away from the surface, and snowmelt or evaporation of moisture from the debris-covered surface leads to the reduction in latent heat flux. The results from this study into the effects of debris cover on the surface energy balance terms also agree with the observational results of Inoue and Yoshida (1980), who found that debris cover reflects much less solar radiation than clean ice, but causes a larger negative sensible and latent heat flux.

As highlighted above, the effects of adding debris cover on the surface and near-surface meteorological variables differ between this study and the study of Collier et al. (2015). This highlights the need for further study into the effects of adding debris cover to atmospheric models, over a range of different glaciers and valleys in the HKKH region, with their varying large-scale climatic regimes, glacier aspects and topographies.

Chapter 5

Lapse rate variation in the Dudh Koshi Valley and over the Khumbu Glacier

Glaciers in the HKKH are often in locations which are difficult to access. Consequently, the meteorological inputs to glacier models sometimes have to be extrapolated from measurements taken at lower elevations. One particularly important input to glacier models is the near-surface air temperature. As such, a good understanding of how the near-surface air temperature varies with elevation, i.e. the lapse rate, is essential to accurately model glacier and snow melt in the region. This chapter investigates the variability of the lapse rate both off-glacier in the Dudh Koshi Valley and over the debris-covered tongue of the Khumbu Glacier by means of a field campaign and using the WRF model. Note that, as discussed in Section 2.3, the term 'lapse rate' will here refer to the variation of near-surface air temperature with elevation as you move up a slope, rather than the variation in air temperature above a fixed point on the ground.

First, this chapter describes and analyses the data collected during the fieldwork campaign, which lasted for 18 days in May 2017 (i.e. the pre-monsoon period) and 116 days between June and October 2017 (i.e the monsoon period). Other meteorological variables, beside air temperature, were also measured (wind speed and direction, air pressure, incoming shortwave radiation, relative humidity and cloud cover), to investigate their relationship with lapse rate. Second, it reports and analyses the results of the WRF model output, which includes the use of the new debris-covered glacier land cover category detailed in Chapter 4. The WRF model is used to analyse the near-surface potential temperature budget off-glacier and on the glacier with and without the debris cover.

5.1 Fieldwork, model and methods

5.1.1 Fieldwork campaign

Instrumentation was installed at a total of 19 locations in the Dudh Koshi Valley and on the Khumbu Glacier in early May 2017. These locations will be referred to as 'stations' for the remainder of this chapter. There were nine off-glacier stations situated in the valley (labelled TV1 to TV9), and ten on-glacier stations on the Khumbu Glacier, nine of which were located on the debris-covered glacier tongue (numbered TG1 to TG9), with one on the clean ice (TG10). See Fig. 5.1 for their locations. All stations had an iButton temperature sensor, set approximately 2 m above the ground. Five of the stations also measured relative humidity, with two situated off-glacier (TV1 and TV7), two on the debris-covered portion of the glacier

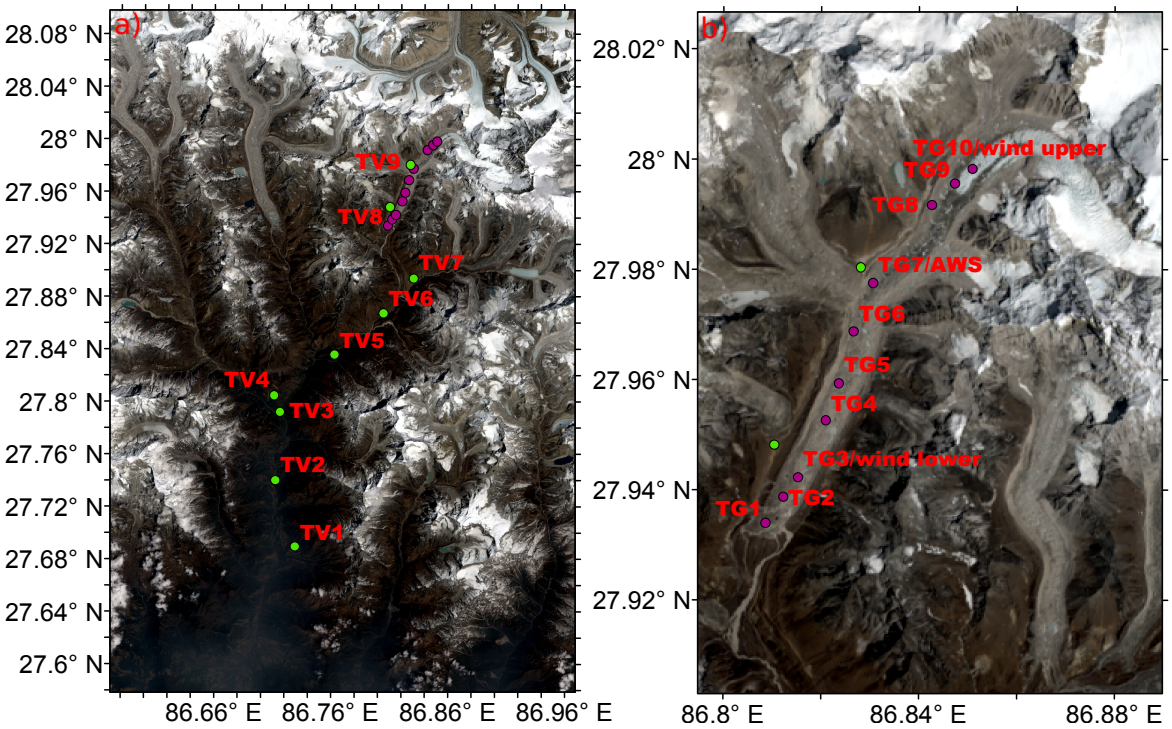

Fig. 5.1 Map showing the locations of the nine off-glacier stations (a; green circles) labelled TV1 to TV9, and the ten on-glacier stations (b; purple circles) labelled TG1 to TG10, set up from 5th May to the 22nd May. Also shown are the location of the AWS (labelled AWS in panel (b)) and the two anemometers (labelled wind lower and wind upper in panel (b)). Stations at TV1, TV7, TG3, TG7 and TG10 measured relative humidity. Off-glacier stations at TV1, TV3, TV5 and TV6 were left over the monsoon season (TV3 was missing when the stations were collected), from the 12th June to the 6th October, along with on-glacier stations TG1 to TG9. All stations left over the monsoon period measured temperature only. The underlying image is from Landsat 8, 2017.

(TG3 and TG7), and one on the clean ice (TG10). Note that it was not possible to install any stations further up the glacier, as TG10 was only slightly below the Khumbu Icefall, and thus higher elevations were inaccessible.

Table 5.1 Details of the fieldwork set-up for May, showing the location, elevation and variables measured at each of the stations. Off-glacier stations TV1, TV3, TV5 and TV6 were left over the monsoon season (TV3 was missing when the stations were collected), along with on-glacier stations TG1 to TG9. The locations of some on-glacier stations were adjusted when they were left over the monsoon period, to move them away from ice cliffs.

Off-glacier stations	Latitude	Longitude	Elevation (m asl)	Measurements
TV1	27.68934	86.72919	2810	Temperature, Relative humidity
TV2	27.73985	86.7123	2595	Temperature
TV3	27.79203	86.71628	3035	Temperature
TV4	27.80463	86.71139	3405	Temperature
TV5	27.83578	86.76279	3836	Temperature
TV6	27.86732	86.80484	4021	Temperature
TV7	27.89368	86.83076	4309	Temperature, Relative humidity
TV8	27.94814	86.81046	4886	Temperature
TV9	27.98036	86.82812	5136	Temperature
On-glacier stations				
TG1	27.93396	86.8087	4881	Temperature
TG2	27.9387	86.81233	4903	Temperature
TG3/wind lower	27.94221	86.81533	4923	Temperature, Relative humidity, Wind speed and direction
TG4	27.95258	86.82101	4912	Temperature
TG5	27.9593	86.82366	4942	Temperature
TG6	27.96869	86.82667	4984	Temperature
TG7/AWS	27.97754	86.83062	5039	5 × Temperature, 3 × Relative humidity, Wind speed and direction, Atmospheric pressure, Incoming shortwave radiation
TG8	27.99168	86.84264	5176	Temperature
TG9	27.99557	86.84732	5209	Temperature
TG10/wind upper	27.99825	86.85095	5230	Temperature, Relative humidity, Wind speed and direction

In addition, an AWS was set up on the debris-covered portion of the glacier, measuring wind speed and direction, pressure, incoming shortwave radiation, air temperature and rela-

tive humidity (labelled AWS in Fig. 5.1, at TG7). For calibration purposes, three iButtons were also set up in this location. There were also two further sensors, of different makes, measuring temperature and relative humidity, to check the accuracy of the iButton results (Table 5.1). Two anemometers (in addition to the anemometer on the AWS) were also set-up on the glacier, one on the debris-covered portion of the glacier ('wind lower', at TG3) and one on the clean ice ('wind upper', at TG10) (Fig. 5.1). Full details of all the instrumentation is given in Table 5.1. All the instrumentation was in place between the 5th May 00:00 LT and 23rd May 00:00 LT (referred to as the 5th to the 22nd throughout this chapter, as all averages are taken up until the final measurement on the 22nd). However the battery on the 'wind upper' anemometer failed on the 19th May. Lastly, cloud cover was measured by eye (in oktas), every three hours between 09:00 and 18:00 LT, from the 5th May to the 22nd May.

A reduced number of the iButtons were left in place during the monsoon season (after I had returned to the UK). This comprised four of the stations situated off-glacier (TV1, TV3, TV5 and TV6), and nine situated on the debris-covered portion of the glacier (TG1-TG9). When the stations were collected in October, TV3 was missing. Note that the on-glacier stations were slightly adjusted in some cases (compared to their locations in May), where they were located too close to ice cliffs. The elevations used for the monsoon season results in this chapter are for the adjusted positions. All of the temperature sensors for the monsoon period were set up by the 30th May, and taken down between the 6th and 13th October by Evan Miles (University of Leeds) and Katie Miles (Aberystwyth University). The monsoon onset and withdrawal dates for Nepal in 2017 were 12th June to 16th October (taken from http://www.dhm.gov.np/climate/), so the monsoon period data is taken from 12th June 00:00 LT to 6th October 23:00 LT. This period will be referred to as the monsoon season throughout this chapter.

Due to difficulties obtaining accurate elevation measurements using a hand-held Global Positioning System (GPS), the elevation of each station was calculated from a digital elevation model (DEM) with a horizontal resolution of 8 m (based on high-resolution satellite imagery, from 16th July 2017, and available at https://nsidc.org/data/HMA_DEM8m_CT) (Shean, 2017). These were calculated using the latitude and longitude coordinates from the GPS.

Details of all the instrumentation and their accuracies are given in Table 5.2. All the stations had an iButton temperature sensor. Those measuring temperature only had the

Table 5.2 Manufacturer reported instrument accuracy

Instrument	Reported accuracy
CS215 Temperature	Temperature: ±0.3 °C (at 25 °C); ±0.4 °C (5 °C to 40 °C);
& Relative Humidity Sensor	±0.9 °C (−40 °C to 70 °C)
	Relative humidity: ±2 % (10 % to 90 % range) at 25 °C;
	±4 % (0 % to 100 % range) at 25 °C
RM Young 05103	Wind Speed: ±0.3 m s^{-1} or 1 % of reading
	Wind Direction: ±3°
Vaisala BAROCAP Barometer PTB110 series	±0.3 hPa at 20 °C
CS300 Pyranometer	±5 % for daily total radiation
Gill WindSonic (1405-PK-100)	±2 % at 12 m s^{-1} (for wind speed and direction)
iButton DS1922L	±0.5 °C from −10 °C to 65 °C
iButton DS1923	Temp: ±0.5 °C from −10 °C to 65 °C
	Relative humidity: ±5 %
HOBO U23 Pro v2 Temperature	Temperature: ±0.21 °C from 0 °C to 50 °C
/Relative Humidity Data Logger	Relative humidity: ±2.5 % (10 % to 90 % range);
	±5 % (0 % to 100 % range)

iButton DS1922L; those measuring both temperature and relative humidity had the iButton DS1923. The iButtons were suspended in a plastic mesh inside a plastic drainpipe wrapped in silver foil, which acted as a naturally-aspirating radiation shield, located at 2 m above the ground (Fig. 5.2). A similar construction was used in Steiner and Pellicciotti (2016). The plastic set-up was chosen because it is cheap, light, and could be easily constructed in the field. To ensure they were aspirated, the stations were set up with the radiation shield aligned roughly in-line with the dominant wind direction (i.e. along the valley axis). This direction was approximately north-south, and thus also avoided the low morning and evening sun shining into the shield.

The AWS measured temperature using five instruments of three different makes. Three of the temperature sensors also measured relative humidity. There were three iButtons; two iButtons measuring only temperature, and one iButton measuring temperature and relative humidity. There was also a HOBO U23 Pro v2 temperature and relative humidity data logger, and a CS215 temperature and relative humidity sensor, both measuring temperature and relative humidity. As discussed, these were set up to test the accuracy of the iButton temperature sensors. The AWS also measured wind speed and direction using an RM Young 05103 anemometer, air pressure using a Vaisala BAROCAP barometer PTB110 series, and incoming shortwave radiation using a CS300 pyranometer. All instruments were installed at approximately 2 m above the ground, with the exception of the barometer, which was installed in a watertight plastic box at approximately 0.3 m above the ground. A battery and

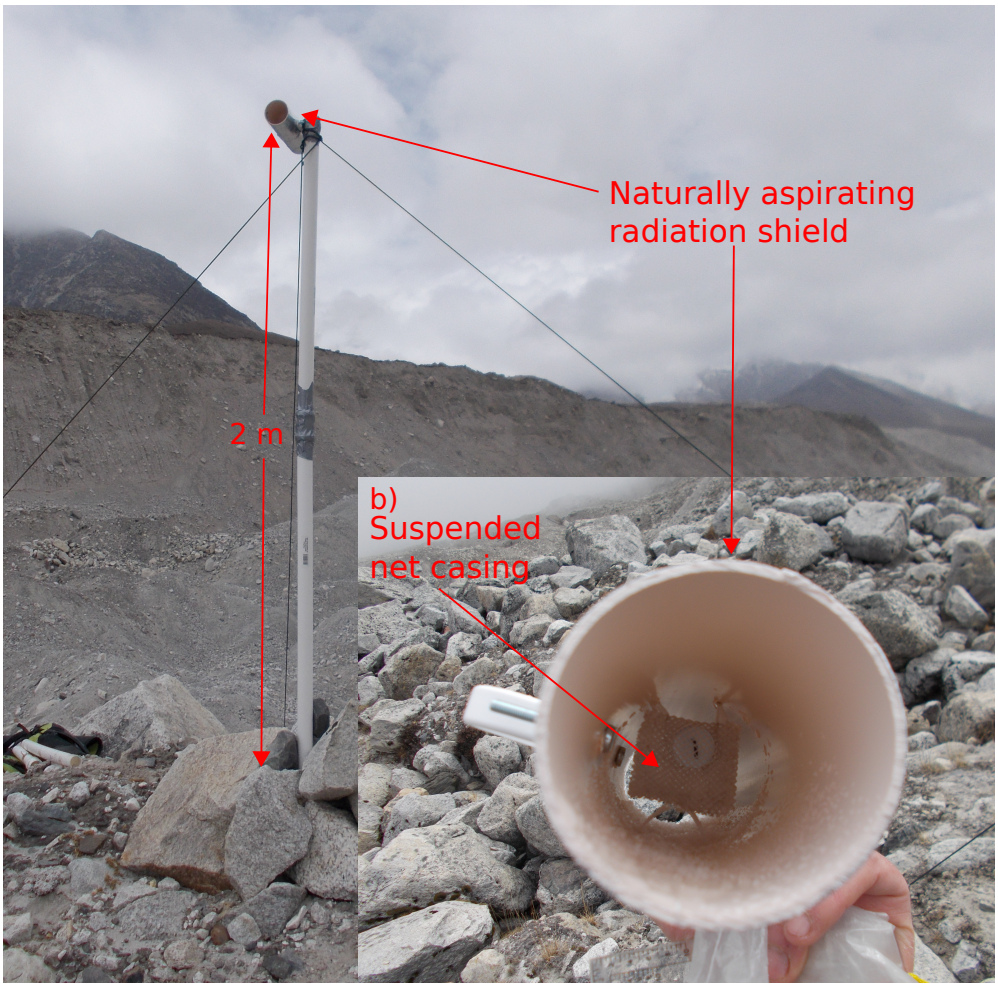

Fig. 5.2 The set-up of the temperature stations on the glacier (a). The insert (b) shows a close-up of the inside of the radiation shield, and an iButton suspended in a mesh pouch.

CS 1000 data logger were also in the watertight box. The AWS set-up can be seen in Fig. 5.3.

The two anemometers at wind lower and wind upper measured wind speed and direction using a Gill WindSonic (1405-PK-100). They were mounted on metal poles, at approximately 2 m above the ground. The poles for both the iButtons and anemometers were either buried into the rock (on the debris-covered glacier), drilled into the ice (over the clean-ice section of the glacier), or attached to existing structures (off-glacier, where possible). All free-standing structures were secured with guylines.

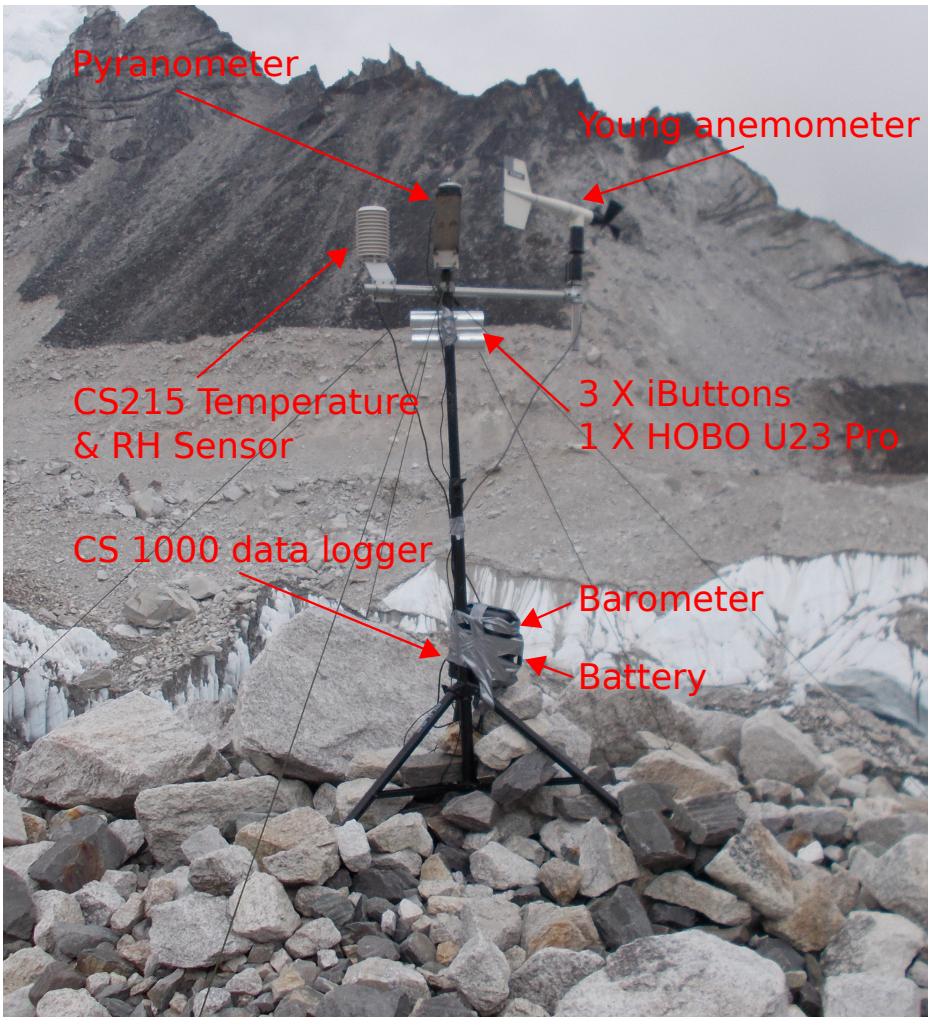

Fig. 5.3 The set-up of the AWS, and the location of the CS 1000 data logger, battery, barometer, CS215 temperature and relative humidity (RH) sensor, HOBO U23 Pro temperature and humidity sensor, pyranometer, anemometer and the three iButtons.

Calibration and data checking

The iButtons were tested both indoors and in the field, to ensure consistency. Initially, the iButtons (both the DS1922L and DS1923 makes) were tested indoors over a 12 hour period (recording every minute). The average standard deviation between the iButtons (at approximately 20 °C) was found to be 0.13 °C, and the average range between the iButtons was found to be 0.42 °C. As such, the iButtons were found to be well within the manufacturer accuracy of 0.5 °C in a controlled environment (Table 5.2).

In addition, as discussed, three iButtons, a HOBO U23 Pro temperature and relative humidity logger, and a CS215 temperature and relative humidity sensor were set up on the AWS in the field, to check the agreement in temperature and relative humidity measurements between the three different instruments. These were left for the full 18 days measured in May 2017. Although the iButtons measured slightly higher temperatures than the other two instruments (Fig. 5.4 (a)), there was a high degree of consistency between the three iButtons. Additionally, the relative humidity measured by the iButton shows a good agreement with the CS215 relative humidity, suggesting these measurements are accurate (Fig. 5.4 (b)). The temperature and relative humidity measurements at the AWS location were subsequently taken from the iButton measuring both temperature and relative humidity, for consistency with the iButton measurements made elsewhere.

A quality control check was applied to the temperature station data by checking for anomalies. For example, in May, station TG10 on the clean ice recorded maximum temperatures 2 °C higher than the two nearest stations on the debris-covered ice (located approximately 1 km and 2 km away). This could be due to particularly high temperatures over the clean-ice glacier due to a reversal in the lapse rate, however it is thought to be due to ice sails surrounding the clean-ice station reflecting the sun into the radiation shield, making the results unreliable. The temperature measurements from station TG10 are therefore excluded in the subsequent analysis. The data collected during the monsoon season were also checked for anomalies. Data from two of the on-glacier stations (TG7 and TG9) were discarded, as one had almost entirely fallen over during the season, leaving the radiation shield vertical and the iButton inside exposed to direct sunlight, while the other had twisted to face east-west, leaving the iButton exposed to the early morning and late evening sun.

The two WindSonic anemometers were calibrated in the factory shortly before the fieldwork. In addition, the data from the three anemometers set up in the field were checked against each other for consistency. One of the WindSonic anemometers (wind lower) produced some unrealistic values (wind speeds of up to 999 $\mathrm{m\,s^{-1}}$). As such, data are discarded from this station for any instances when the wind speed measured at the lower wind site was more than 6 $\mathrm{m\,s^{-1}}$ greater than the wind speed measured at the AWS. When the AWS was retrieved, its anemometer was found to be approximately 20° off. This has subsequently been corrected in the results, by adding 20° to each of the measurements recorded. The pressure sensor was also calibrated in the factory shortly before the fieldwork.

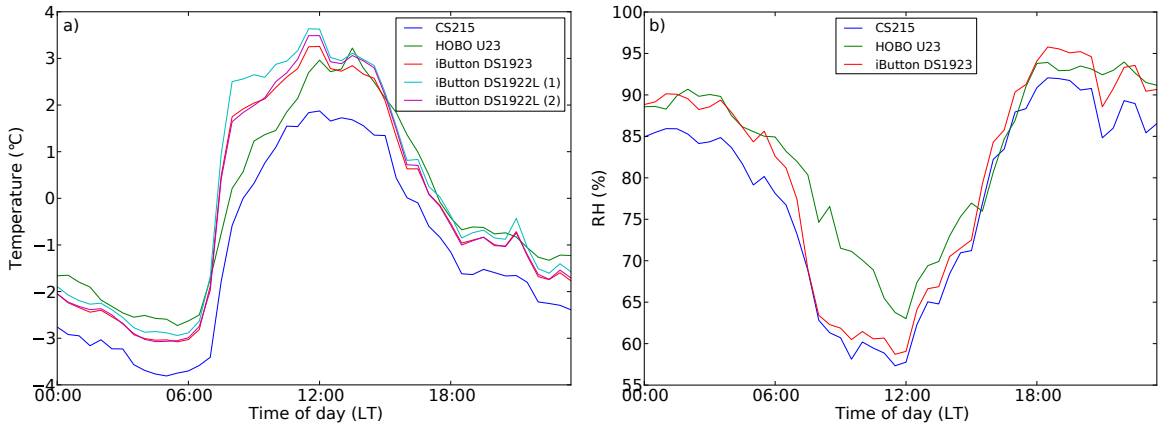

Fig. 5.4 Comparison of the diurnal average of the CS215 (blue line), HOBO U23 (green line), and three iButtons (red, cyan and magenta lines) temperature sensors at the AWS (a), between 5th May and 22nd May. The relatively humidity (measured by the CS215, HOBO U23 and one iButton) is shown in panel (b). The AWS and HOBO U23 measurements are subsampled to a half-hour resolution.

5.1.2 Atmospheric model description

The WRF model set-up is identical to that described in Section 3.1.1, except for the addition of a debris-covered glacier land cover category, as described in Section 4.1.1. The WRF model is run for the 18 days in May and 116 days of the monsoon as described in Section 5.1. Both runs had at least two weeks spinup period. The addition of the debris cover in the model allows the model results to be compared to observations on the debris-covered tongue of the Khumbu Glacier. It should be noted that the debris-covered portion of Khumbu Glacier covers approximately fifteen 1 km by 1 km model grid squares. As the glacier is only about 1 km wide at the widest points, and does not run directly north-south or east-west, defining the glacier at a 1 km resolution in the WRF model is difficult. Ideally, the model would be run at a higher resolution to more accurately capture the glacier and the meteorological variables above it, however computational demands at 1 km are already very high. For the pre-monsoon period, the model is also run with the original WRF land cover category, of clean-ice (rather than debris-covered ice) on the Khumbu Glacier, for comparison. These runs will be described analogously to those in Chapter 4, as the 'debris-cover run' and the 'clean-ice run'.

5.1.3 Potential temperature budget

The WRF model was modified to output the individual terms of the potential temperature (θ) budget, in an analogous way to the momentum budget methodology described in Section 3.1.3. The potential temperature budget is given by:

$$\partial_t \Theta + (\nabla \cdot \mathbf{V}\theta) = F_\Theta \tag{5.1}$$

Here the change in time of mass coupled potential temperature is given by $\partial_t \Theta$, where Θ is the mass coupled potential temperature, $\Theta = \mu_d \theta$, and θ is the uncoupled potential temperature. As described in Section 3.1.3, $\mu_d(x,y)$ is the mass of dry air in the column. The coupled wind velocity $\mathbf{V} = (U,V,W) = \mu_d \mathbf{v}$, where U and V are the mass coupled zonal and meridional velocities and W is the mass coupled vertical velocity, and $\mathbf{v} = (u,v,w)$ is the uncoupled velocity. The advection term is given by $\nabla \cdot \mathbf{V}\theta$. The term F_Θ represents forcing from horizontal and numerical diffusion and the contribution from model physics due to turbulent vertical mixing, radiation and latent heating.

The potential temperature and components of the potential temperature budget used for analysis in this chapter are all taken from the lowest model level, which is approximately 25 m above the ground. The advection term describes the effects of the larger-scale wind on the potential temperature. The radiation term represents the total incoming and outgoing longwave and shortwave radiation contributions. Horizontal diffusion and turbulent vertical mixing represent, respectively, the horizontal and vertical transportation of potential temperature from sub-grid scale turbulent processes. Turbulent vertical mixing is driven predominantly by the sensible heat flux at the surface (Lehner and Whiteman, 2014). Numerical diffusion is added for numerical stability. Latent heating arises from the model microphysics parametrisation. All terms in Eq. 5.1 are subsequently divided by μ_d, in order to describe the components of change in uncoupled potential temperature, (i.e. $\partial_t \theta$).

5.1.4 Methods

In this chapter, the observed temperature measurements are used to calculate lapse rates. The lapse rates are calculated by taking a linear regression between the air temperature at 2 m at each station and the elevation of each station. The gradient of the line of best fit is taken to represent the lapse rate. The model lapse rate is calculated in the same way as the observed lapse rate (using the model air temperature at 2 m and elevation data from the nearest model

grid point to each station). As in Chapter 3, where comparisons are made between the model and observations, the nearest model grid point is taken. Note that for two pairs stations on the glacier, the associated nearest model grid point is the same within each pair. As cloud cover was observed over the entire visible sky, to compare with the model, the maximum cloud fraction in the model vertical column was averaged over a horizontal 8 km by 8 km patch of model grid points. To compare the model and observed temperature and wind speed, the observed temperature and model wind speed variables were adjusted as described in Section 3.1.4. In addition, the model pressure has been adjusted to the height of the observations by calculating the change of surface pressure with elevation over the model domain for every time step, and adjusting the model pressure accordingly. All the off-glacier model output is taken from the debris-cover run.

For all comparisons between different instruments, or between the instruments and the model, data were first subsampled to the lowest temporal resolution (by only using the data points which fell on the hour/half hour). In May the station observational data were recorded every half-hour, while the AWS and anemometer data were recorded every 15 minutes. The model data and the station data for the monsoon season both have a resolution of 1 hour. Where a comparison is made between the observed cloud cover and observational lapse rate, the cloud measurements have a three-hourly resolution, whilst the resolution of the lapse rate is half an hour.

5.2 Pre-monsoon season results

5.2.1 Evaluation of a linear lapse rate in the observations

Figures 5.5 (a) and (b) demonstrate that in the pre-monsoon, the variation of measured air temperature at 2 m with elevation obeys a linear relationship (i.e. a linear lapse rate) off-glacier, during the day (–4.9 °C km^{-1}; correlation coefficient R=-0.997) and at night (–5.4 °C km^{-1}; correlation coefficient R=-0.999). Given that the off-glacier stations are spaced over an elevation range of over 2500 m, the strength of this relationship is to be expected. Here, the daytime lapse rate is shallower than the nighttime lapse rate (Fig. 5.5 (a) and (b) re-

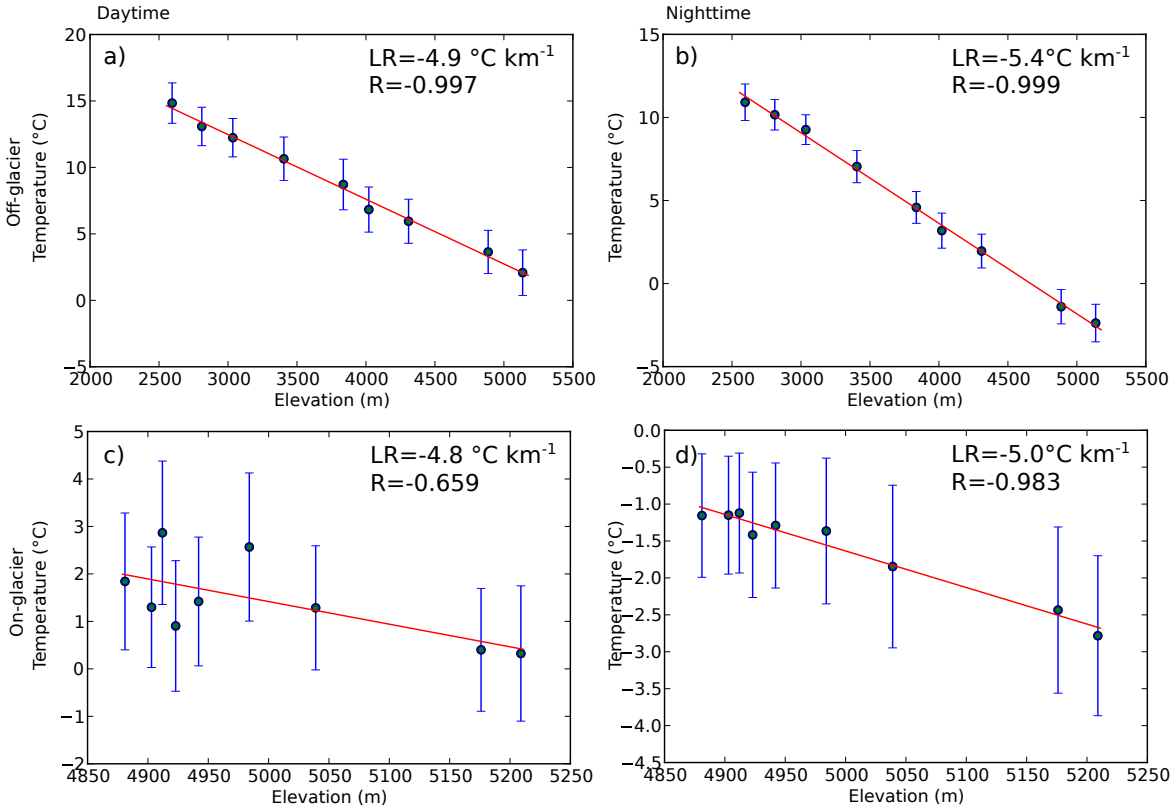

Fig. 5.5 The average daytime (06:00-18:00 LT; a) and nighttime (18:30-05:30 LT; b) temperatures and elevations for the nine off-glacier stations from 5th May to 22nd May. Panels (c-d) show the equivalent for the nine on-glacier stations. The gradient of the line of best fit gives the near-surface temperature lapse rate (LR). The correlation coefficient is also shown (R); panels (a), (b) and (d) are significant at the 5 % level and panel (c) is significant at the 10 % level. Blue bars show the standard deviation of the daytime averaged or nighttime averaged measurements at each station over the 18 days. The nighttime averages are taken over 17 days to ensure each nighttime value is taken over the same timespan. Note that the temperature ranges are different for each panel.

spectively), and the variation in air temperature at 2 m over the 18 days is greater in the day than in the night, due to the influence of differential heating by the sun during the daytime.

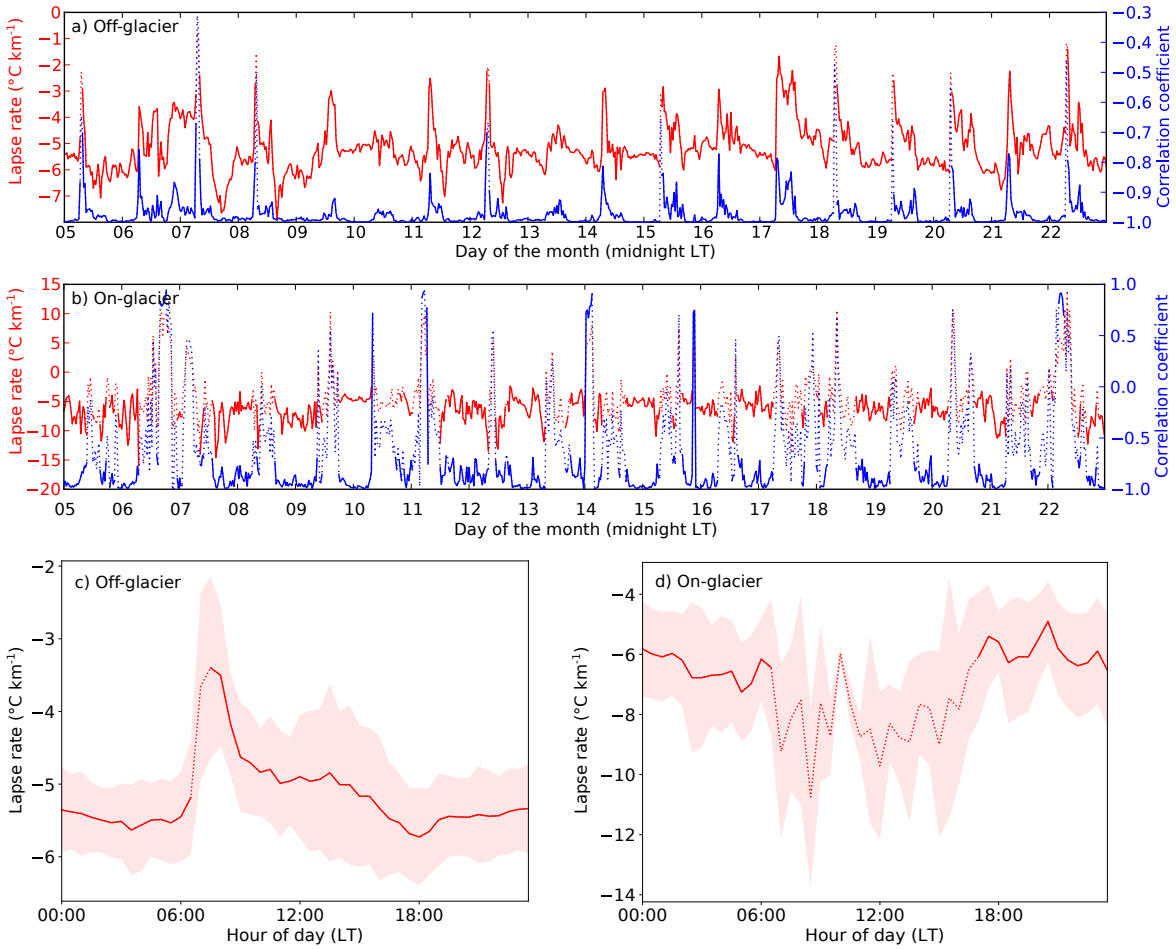

Fig. 5.6 The lapse rate derived from the nine stations off-glacier, every half-hour from 5th May to 22nd May (a). The lapse rate is shown in red, and the correlation coefficient in blue. Dotted lines indicate times where the linear regression model is not statistically significant at 5 %. Panel (b) is the equivalent of panel (a) for the nine on-glacier stations. Panels (c) and (d) shown the average diurnal cycle in lapse rate for the off-glacier and on-glacier stations, respectively, for the same period as considered in (a) and (b). Shading indicates one standard deviation from the mean. Only significant times are included in the average and standard deviation, and times of the day for which less than 75 % of the days have a statistically significant lapse rate are shown as a dotted red line.

On-glacier, it is more difficult to determine whether the linear lapse rate provides an accurate fit for 2 m air temperature variation in the pre-monsoon (Fig. 5.5 (c) and (d)), as the debris-covered section of the Khumbu Glacier is relatively flat, with an elevation range

of only about 350 m. However, Fig. 5.5 (d) demonstrates that, during the night, a linear lapse rate does provide a reasonable model for near-surface air temperature, with a lapse rate of -5.0 °C km^{-1} (correlation coefficient R=-0.983), which is slightly shallower than the nighttime off-glacier lapse rate of -5.4 °C km^{-1}. However, on-glacier in the daytime, the small elevation range and differential heating of the sun means that a statistically significant linear relationship (at 5 % significance) cannot be determined. As with the off-glacier stations, the day-to-day variation in air temperature at 2 m on the glacier is larger during the day (standard deviation of just over 1 °C at most stations) than at night (standard deviation of just under 1 °C at most stations).

Figures 5.6 (a) and (b) show the variation in lapse rate over the 18 day pre-monsoon period, along with the associated correlation coefficient at each half-hour. The lapse rate varies considerably over the 18 days, both off- and on-glacier. For example, during the day on 7th May there is an extremely steep lapse rate off-glacier, which is greater than -7.5 °C km^{-1} (Fig. 5.6 (a)). Reasons for this steep lapse rate will be discussed in Section 5.2.2. As discussed above, the large elevation range off-glacier leads to a statistically significant lapse rate at almost every time interval. In addition to the variability over the 18 days, there is some diurnal variability, with spikes in the off-glacier lapse rate most mornings of about 1.5 °C, at about 07:00-08:00 LT (Figs. 5.6 (a) and (c)). These early morning spikes are due to the air surrounding the stations at high elevations (off-glacier) heating up earlier than the air surrounding the stations at low elevations (Fig. 5.7), likely due to the steep topography leading to the sunlight hitting the ground around the higher-elevation stations before the ground around the lower-elevation stations. Air surrounding the on-glacier stations, at similar elevations to the high-elevation off-glacier stations, does not heat up earlier (Fig. 5.7). This could be due to small-scale topographic differences (for example, the lateral moraine is high and steep on the glacier, and could cause shadows in the early morning).

As discussed above, on-glacier during the day, the differential heating effects from the sun eclipse the effects of the small elevation range between the stations. As such, during the day there are few significant linear lapse rates (Fig. 5.6 (b) and (c)). There is some evidence of the early morning spikes seen in the off-glacier lapse rate in the on-glacier lapse rate, but more data would be needed to confirm these (Fig. 5.6 (b)).

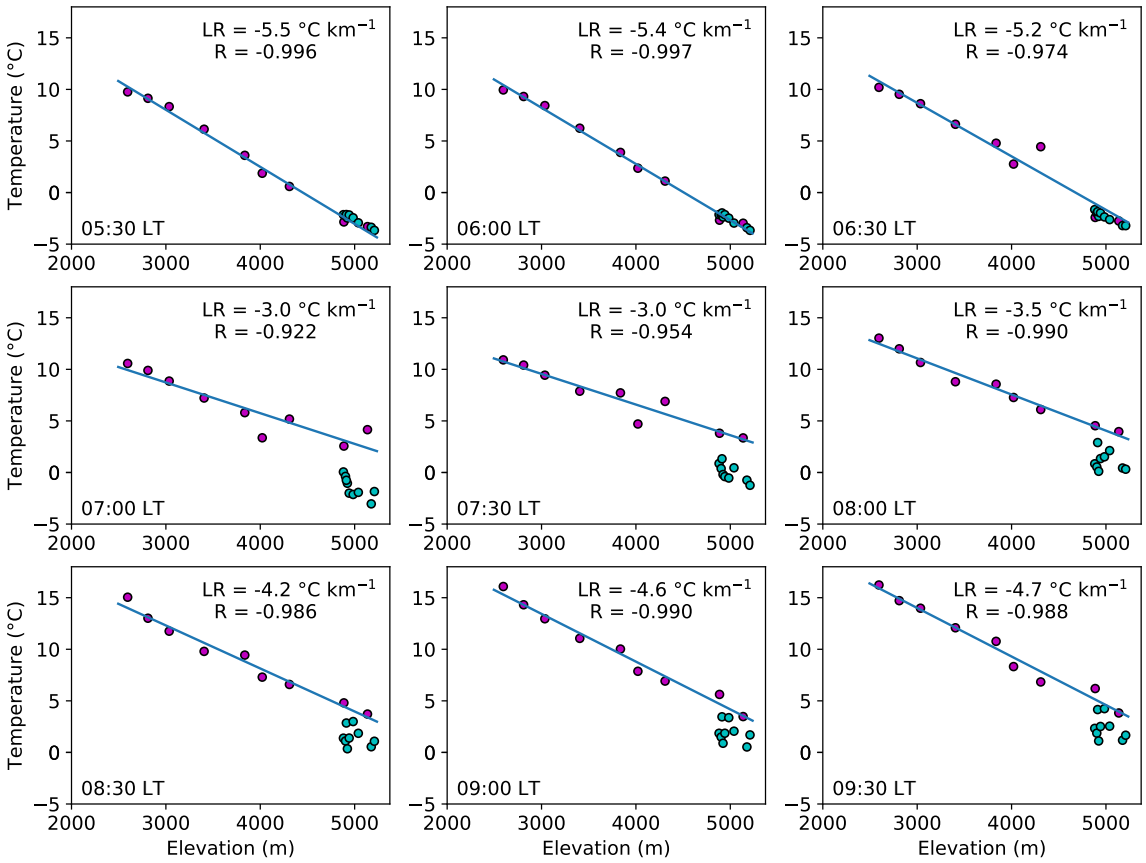

Fig. 5.7 The average temperatures and elevations for the nine off-glacier stations (purple points) from 5th May to 22nd May, every half-hour between 05:30 LT and 09:30 LT (averaged over the instantaneous temperature measurements taken every half-hour). Note that the lapse rate (LR) and correlation coefficient (R) for the off-glacier stations are also shown. The on-glacier stations are also shown for comparison (cyan points).

5.2.2 How do other meteorological variables affect the lapse rate in the observations?

To examine possible controls on the lapse rate, the variation in the observed lapse rate is compared to the corresponding variation in measured pressure, cloud cover, shortwave incoming radiation, relative humidity, and wind speed and direction (Fig. 5.8). Note that the wind speed is averaged over the three anemometers on-glacier, and the relative humidity is averaged over the five sensors off- and on-glacier (see Section 5.1.4). All variables except wind direction are shown as the anomaly from the average diurnal cycle, calculated by taking the average values at each half-hour over 18 days, and subtracting this from each corresponding measurement. Anomaly values were taken because there is a clear diurnal cycle in variables such as wind speed and incoming shortwave radiation, and the aim is to compare changes in these values with variability in the lapse rate.

All 18 off- and on-glacier stations are used to calculate the lapse rate. Both sets of data were combined in order to maximise the number of data points used to calculate lapse rate, as (except in the early morning) there is no substantial difference between lapse rates or temperatures on- and off-glacier (Figs. 5.5 and 5.7).

Figures. 5.8 (a), (b) and (c) demonstrate that there is no direct association between pressure and lapse rate, cloud and lapse rate, or shortwave incoming radiation and lapse rate in the data collected. However, both the relative humidity (Fig. 5.8 (d)) and the wind speed (Fig. 5.8 (e)) appear in some instances to be relate to lapse rate. This is particularly apparent during 6^{th} to 8^{th} May, when there is large variation in the lapse rate. During this period, it appears that higher than average wind speeds and drier than average relative humidities occur at the same time as shallower than average lapse rates, and vice versa. As such, this period is chosen for closer examination.

Figures 5.9 (a) and (b) show a case study version of Figs. 5.8 (d) and (e) for the 6^{th}, 7^{th} and 8^{th} days of the month. The variation in the temperature at every site over the three days is also shown (Fig. 5.9 (c)). The nighttime of the 6^{th}-7^{th} shows a much shallower (a positive anomaly of over 2 °C km^{-1}) lapse rate compared to the rest of the period examined. This is due to the on-glacier stations, as well as the two highest-elevation off-glacier stations (TV8 and TV9), being much warmer than average, while the lower elevation stations are slightly cooler than average for this period (Fig. 5.9 (c)). This further corroborates the idea that

the temperature variation at the stations is not primarily dictated by whether they are on- or off-glacier. Hereafter, the stations TV8-9 and TG1-9 will be referred to as the 'high-elevation stations, and the stations TV1-7 as the 'low-elevation' stations. The nighttime of the 6^{th}-7^{th} also shows the strongest (and one of only a few instances of) nighttime downslope winds at all three anemometers on the glacier (Fig. 5.9 (a)), with wind speeds over $3\,m\,s^{-1}$ stronger than the diurnal average, as well as 40 % lower than average relative humidities (Fig. 5.9 (b)).

The increased wind speed on-glacier during the nighttime of the 6^{th}-7^{th} (Fig. 5.9 (a)) is likely to cause more mixing, both between the surface and the air, and within the boundary layer, which could act to warm the air at 2 m. As the anemometers are on the glacier, it is not possible to say whether the katabatic winds continue further down the valley during this period. If they do not, it would explain the difference in temperature variation between the high- and low-elevation stations. There are also two periods of steeper than average lapse rates (more negative anomalies), where the lapse rate is over $2\,°C\,km^{-1}$ steeper than average, during the evenings of the 7^{th} and 8^{th}. These are associated with very low wind speeds, more than $2\,m\,s^{-1}$ lower than average, and with average relative humidity. This suggests that the lack of mixing during the day from up-valley winds over the glacier, due to the lower than average wind speed, may cause the steeper than average lapse rate. These possible mechanisms will be explored further using the WRF model in Section 5.2.7.

The association between drier than average relative humidities and shallower than average lapse rates is surprising, as when considering environmental lapse rates (i.e. the change in temperature with altitude directly above a point), in general higher relative humidities are associated with shallower lapse rates, due to air rising and condensing into clouds at high altitudes, leading to latent heating at high altitudes (Whiteman, 2000). This would also be the case for the near-surface lapse rate, if clouds were forming at ground level at high-elevations. The change in relative humidity during this three-day period is due to both changes in the absolute humidity and changes in temperature (i.e. where the relative humidity is lower, the absolute humidity is lower and the temperature is higher (not shown)). In addition to the changing temperautre, Fig. 5.9 (b) suggests that for this three day period, the effects of the wind may be stronger than those of relative humidity. The unusual nighttime katabatic wind could be drawing drier air down from the tops of the mountains, causing the lower relative humidity during the night of the 7^{th} May.

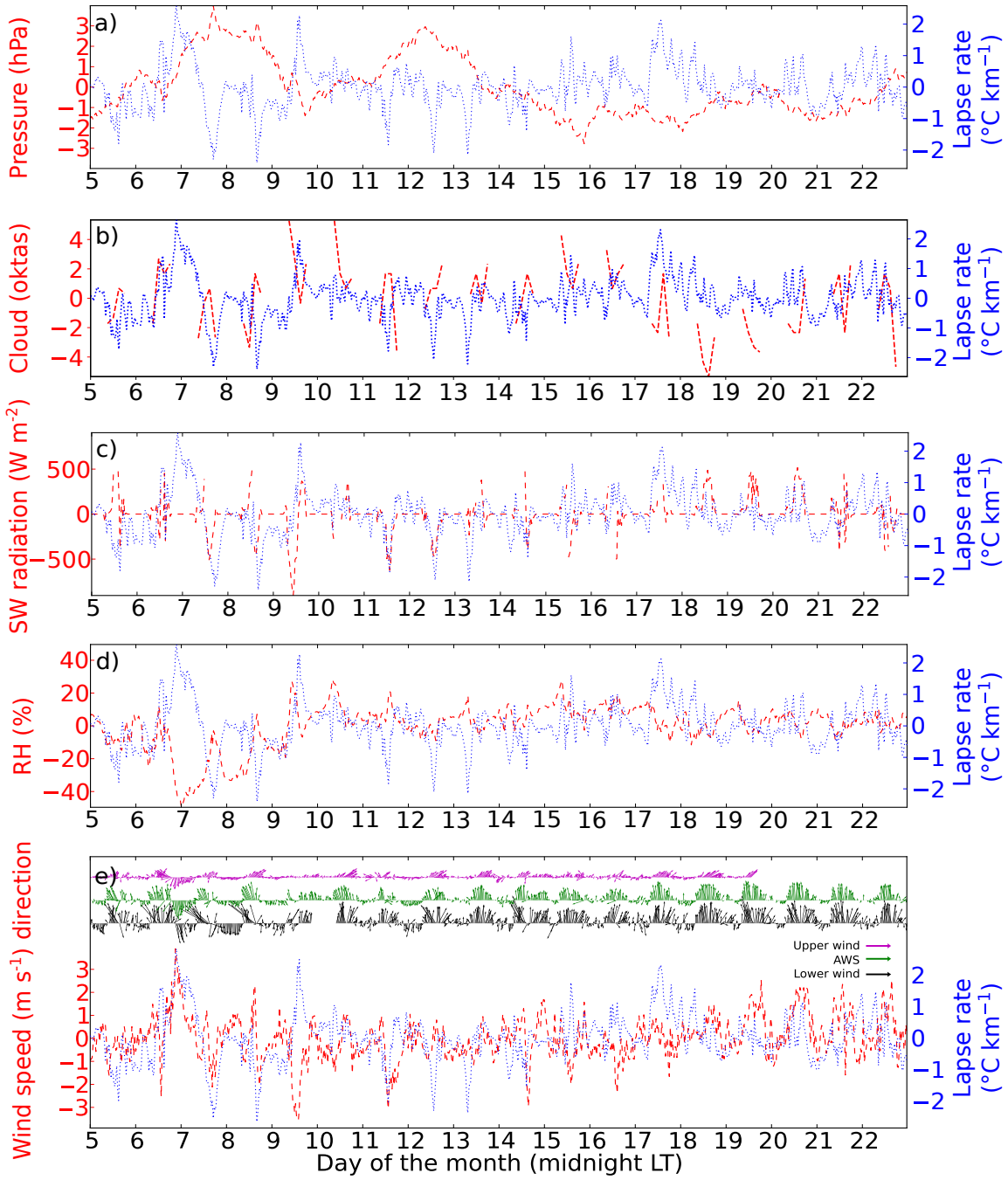

Fig. 5.8 The anomaly in lapse rate from 5th May to 22nd May, versus the anomaly in air pressure (a), cloud cover (b), shortwave incoming radiation (c), average relative humidity at 2 m (over the five relative humidity loggers) (d) and average wind speed at 10 m (over the three anemometers) and wind direction at each anemometer (e). The lapse rate shown on each plot is taken over all the loggers off- and on-glacier. The wind vectors in panel (e) are shown with southerly winds as arrows pointing north, and the lengths of the vectors represent the wind speeds. The anomalies are calculated by subtracting the average diurnal cycle for the 18 days of May.

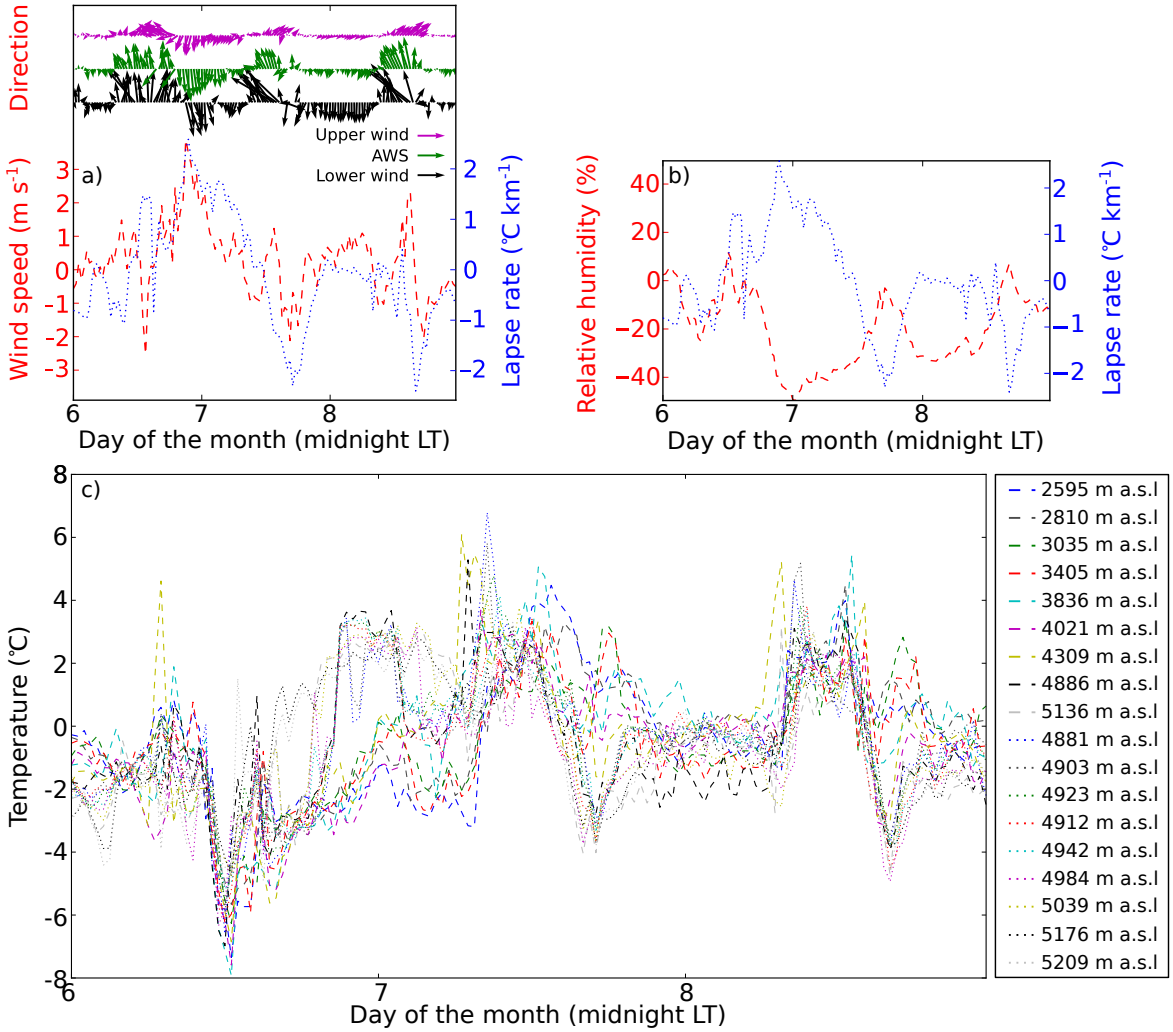

Fig. 5.9 Panels (a) and (b) are as for Fig. 5.8 (e) and (d), respectively, but for 6th May to 9th May only (with diurnal cycle from which the anomaly is taken still taken over the full 18 days). Panel (c) shows the anomaly in air temperature at 2 m at each of the 18 stations over the three day period. Dotted lines indicate on-glacier stations, and dashed lines indicate off-glacier stations. The elevation of each of the stations is also shown.

5.2.3 Comparison of the WRF simulated and observed air temperatures at 2 m

In order to use the WRF model to investigate the mechanisms affecting lapse rate variability, it is first necessary to assess how good the model is at representing the measured temperature during the pre-monsoon period. This section also serves to further validate the new debris-covered glacier land cover category added to the model in Chapter 4.

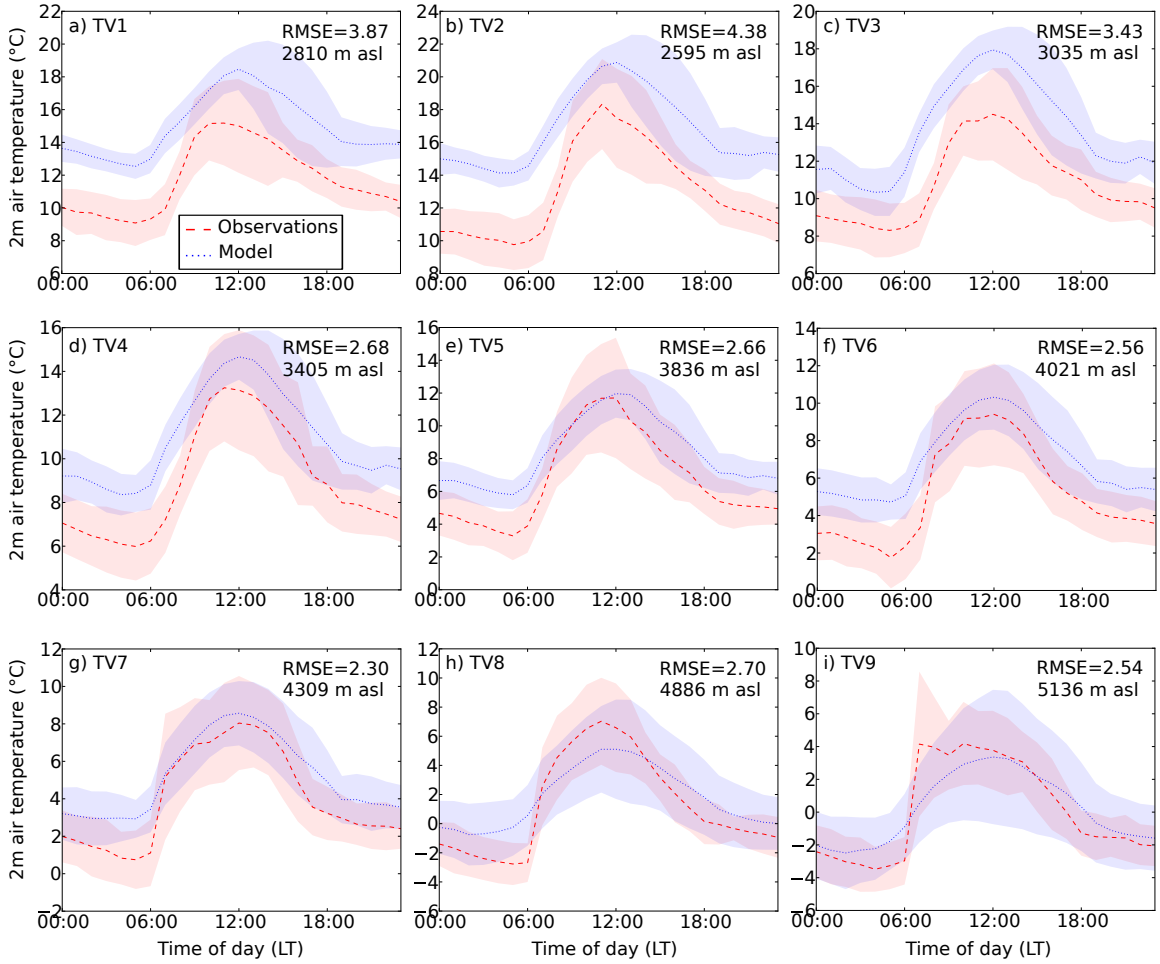

Fig. 5.10 The average off-glacier diurnal cycle of air temperature at 2 m from 5th May to 22nd May at TV1-TV9 (a-i), in the debris-cover run (blue, dotted) and observations (red, dashed). Shading represents one standard deviation from the mean. The root mean square error (RMSE) and the elevation of each station are also shown. Note the change of scale for each panel.

At the off-glacier stations TV1-TV4, the model captures the amplitude and timing of the diurnal cycle in the air temperature at 2 m, but has a systematic warm bias of 2 °C to 4 °C (Fig.

5.10 (a), (b), (c) and (d)) (RMSEs of 3.87 °C, 4.38 °C, 3.43 °C and 2.68 °C respectively). At TV5, TV6 and TV7, the model captures the maximum daytime temperature accurately, but overestimates the nighttime temperature by about 2 °C (Fig. 5.10 (e), (f) and (g)) (RMSEs of 2.66 °C, 2.56 °C and 2.30 °C respectively). At the high-elevation stations off-glacier, TV8 and TV9, the model underestimates the maximum daytime temperature by 1 °C to 2 °C, and overestimates the minimum nighttime temperature by 0.5 °C to 2 °C (Fig. 5.10 (h) and (i)) (RMSEs of 2.70 °C and 2.54 °C respectively).

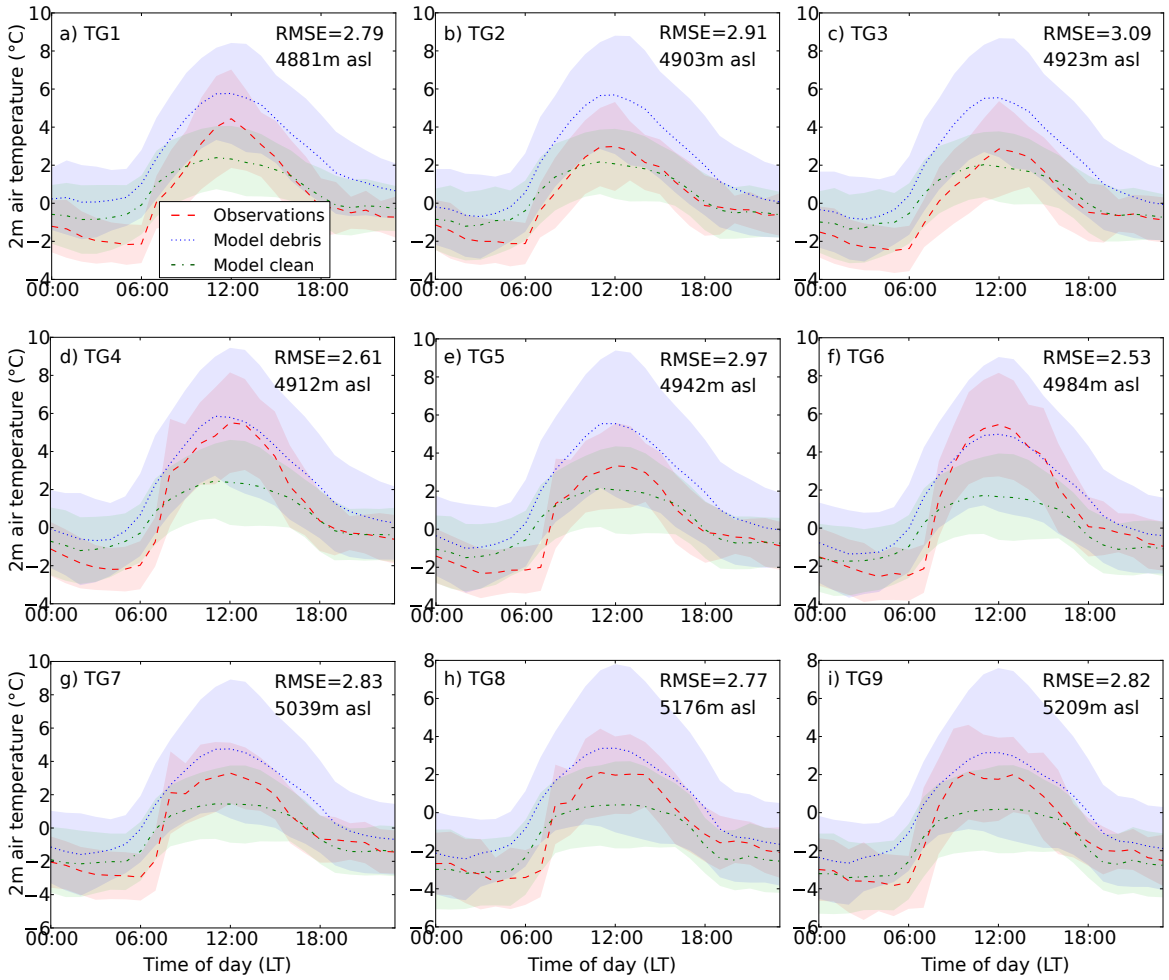

Fig. 5.11 As for Fig. 5.10, but for the on-glacier stations. Panels (a-i) show the stations TG1-TG9 respectively. The observations are shown as a red dashed line and the model with the new debris-covered glacier land cover category as a blue dotted line, as before. The default WRF model clean-ice land cover category is shown as a green dash-dot line. The root mean square errors (RMSE) are only shown between the observations and the model with the new debris-covered glacier land cover category.

Figure 5.11 shows the diurnal cycle in 2 m air temperature on the glacier in the observations and in the model, both with the new debris-covered glacier land cover category (hereafter called the 'debris-cover run') and with the default representation of glacier in WRF (representing a clean-ice glacier; hereafter called the 'clean-ice run'). The new debris-covered glacier land cover category substantially improves the representation of air temperature at 2 m over the glacier, compared to the default WRF clean-ice glacier land cover category. In the debris-cover run, the model represents the air temperature at 2 m relatively well, with RMSEs of between 2.53 °C to 3.09 °C at every station. There is a warm bias at most of the stations in the debris-cover run, which is largest at TG1-TG3 and TG5, where it is about 2 °C (Fig. 5.11 (a), (b), (c) and (e)), and mostly under 1 °C at the other stations (Fig. 5.11 (d), (f), (g), (h) and (i)). As there is a warm bias at many of the off-glacier stations, the warm bias on-glacier in the debris-cover run is expected. The debris-cover run captures the amplitude of the diurnal cycle at every on-glacier station, and both the debris-cover run and observations show a difference of about 6 °C between the minimum nighttime and maximum daytime temperatures at most stations (Fig. 5.11). By contrast, the amplitude of the diurnal cycle in the clean-ice run is about 3 °C, with maximum daytime temperatures too cold in the model at all stations (Fig. 5.11). As such, the new debris-covered glacier land cover category proves to be a substantial improvement over the default WRF model clean-ice in the pre-monsoon, confirming the results of Chapter 4.

5.2.4 Comparison between the WRF model and observations in the other meteorological variables

To explain the differences between the model and observed air temperature at 2 m, and also to validate the new debris-covered glacier land cover category using the other variables, the model and observed pressure, cloud cover, shortwave incoming radiation, average relative humidity and average wind speed are compared (Fig. 5.12). As noted earlier, these variables are predominantly measured on the debris-covered glacier, so any differences between the model and observations are more likely to explain temperature differences at the stations on or close to the glacier.

The model has particularly high cloud cover, and subsequently low incoming shortwave radiation at the surface between the 5th and 9th May. This persistent cloud is not seen in the observations (Fig. 5.12 (b) and (c)). Over this four day period, the model underestimates the maximum daytime temperature over the on-glacier stations, and some of the high-elevation off-glacier stations (not shown). After the 12th May, the model mostly captures well the diurnal cycle in cloud cover, and therefore also incoming shortwave radiation, with clear mornings and cloudy afternoons (Fig. 5.12 (b) and (c)).

The model captures well the amplitude of the diurnal cycle in relative humidity. However where the model shows a peak in the early evening of each day, the observations show a more sustained maximum in relative humidity into the night (Fig. 5.12 (d)). In addition, the model underestimates the relative humidity for much of the month. This is consistent with the model warm bias.

Lastly, the model represents the average wind speed well from the 16th to the 22nd May, when there is a clear diurnal cycle in the wind (due to the clearer days and therefore enhancement of the valley wind regime) (Fig. 5.12 (e)). From the 5th to the 12th May, the model captures the range of wind speeds, but not the timings of the diurnal cycle. From the 12th to the 16th May the model overestimates the wind speed, especially at night, and does not capture the daytime maximum in wind speed seen in the observations, particularly between the 12th to the 14th (Fig. 5.12 (e)).

The model represents the wind direction during the day well at the lower wind station and the upper wind station, but is slightly too westerly at the AWS (Fig. 5.13 (a), (c) and

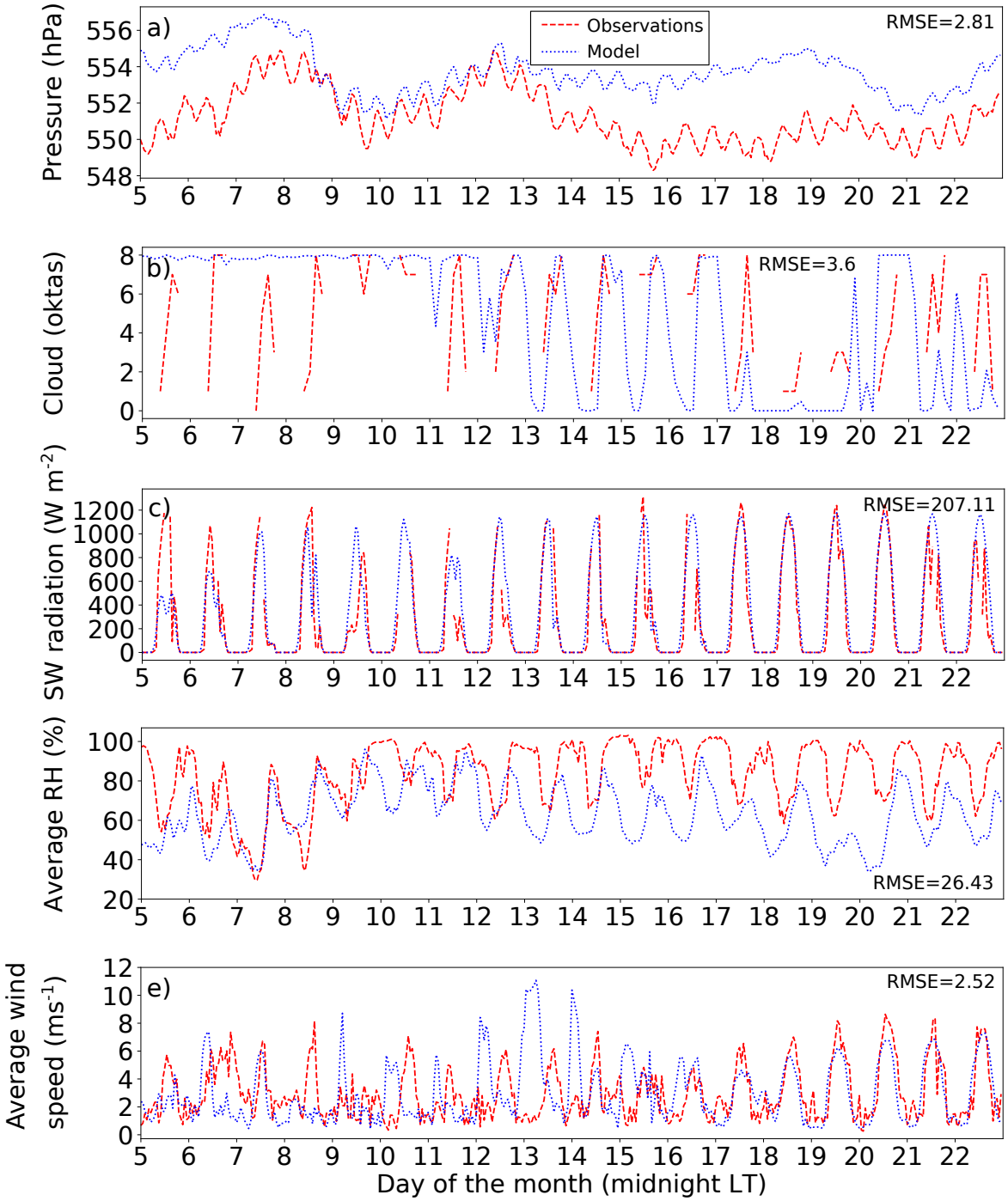

Fig. 5.12 Comparison between the model (blue, dotted) and observations (red, dashed) for the pressure (a), cloud (b), incoming short-wave radiation (c), average relative humidity (d) and average wind speed (e), every hour from 5th May to 22nd May. The root mean square error for each variable is also shown.

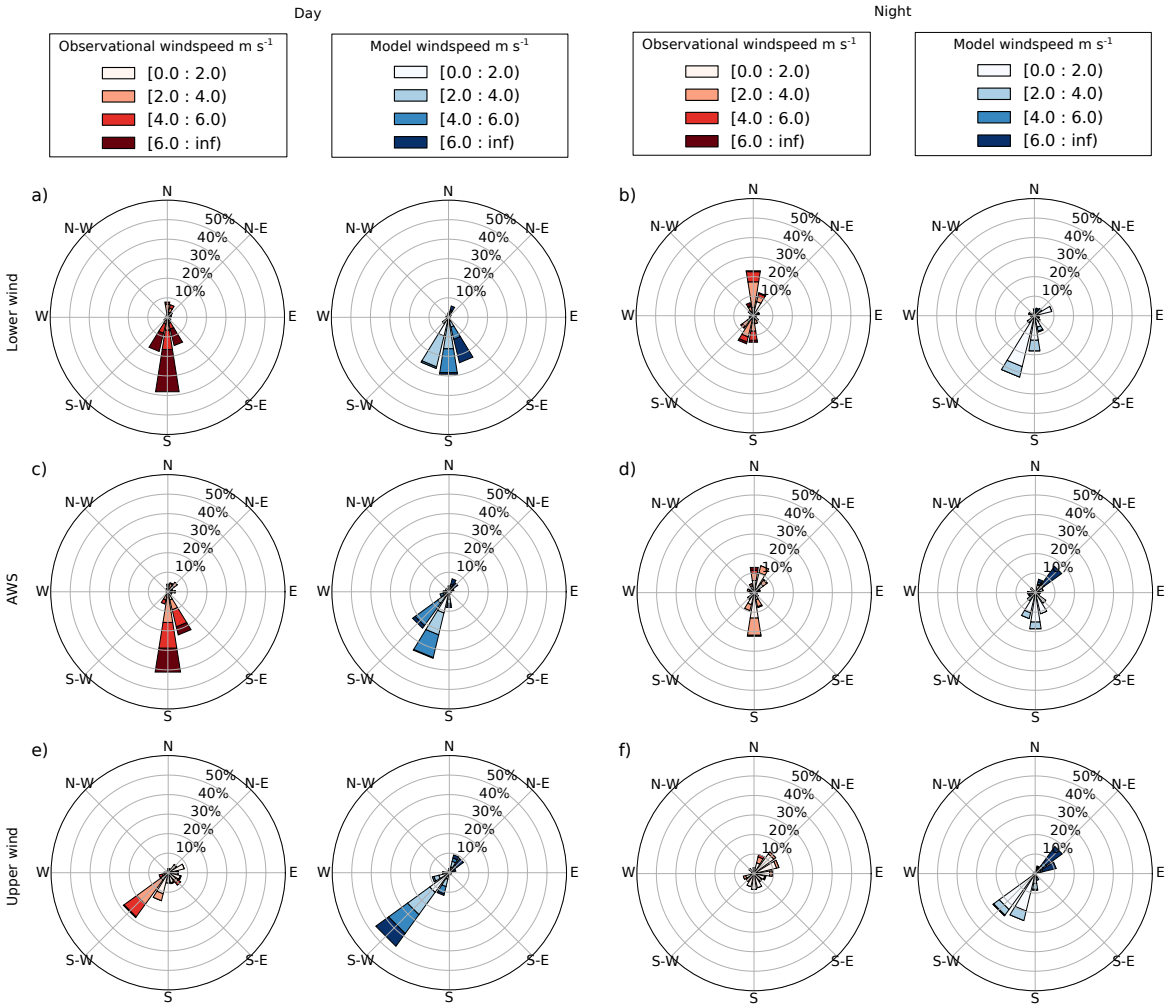

Fig. 5.13 Wind roses showing the observed (red, left) and model (blue, right) wind speed and direction at the lower wind site during the day (06:00-18:00 LT; a) and at night (19:00-05:00 LT; b), from 5th May to 22nd May. Panels (c-d) and (e-f) show the equivalent at the AWS site and the upper wind site.

(e)). As the AWS is between the lower and upper wind stations, this difference in direction is probably due to small topographic differences between the model and observations, rather than a difference in larger-scale wind direction. At night the wind is, on average, much weaker than during the day in both the model and observations, and although the model and observations both still show wind travelling along the length of the glacier, the model does not always capture the right proportion of up-glacier and down-glacier winds (Fig. 5.13 (b), (d) and (f)).

5.2.5 Comparison of the WRF simulated and observed lapse rates

As discussed in Section 5.2.3, in general the model represents the temperature of the higher elevation off-glacier stations more accurately than the temperature of the lower elevation stations, where the model has a distinct warm bias. As such, the model lapse rate (of 6.4 °C km^{-1} during the day and 6.5 °C km^{-1} at night) is steeper than the observed lapse rate off-glacier for both the day and night during the pre-monsoon (Fig. 5.14 (a) and (b)). On-glacier in the debris-cover run, the model lapse rate is also steeper than the observed lapse rate, due to a larger warm bias at the lower elevation on-glacier stations. In addition, on the glacier the variation in the model air temperature at 2 m is greater than the variation in the observations, in both the daytime and nighttime (Fig. 5.14 (c) and (d)).

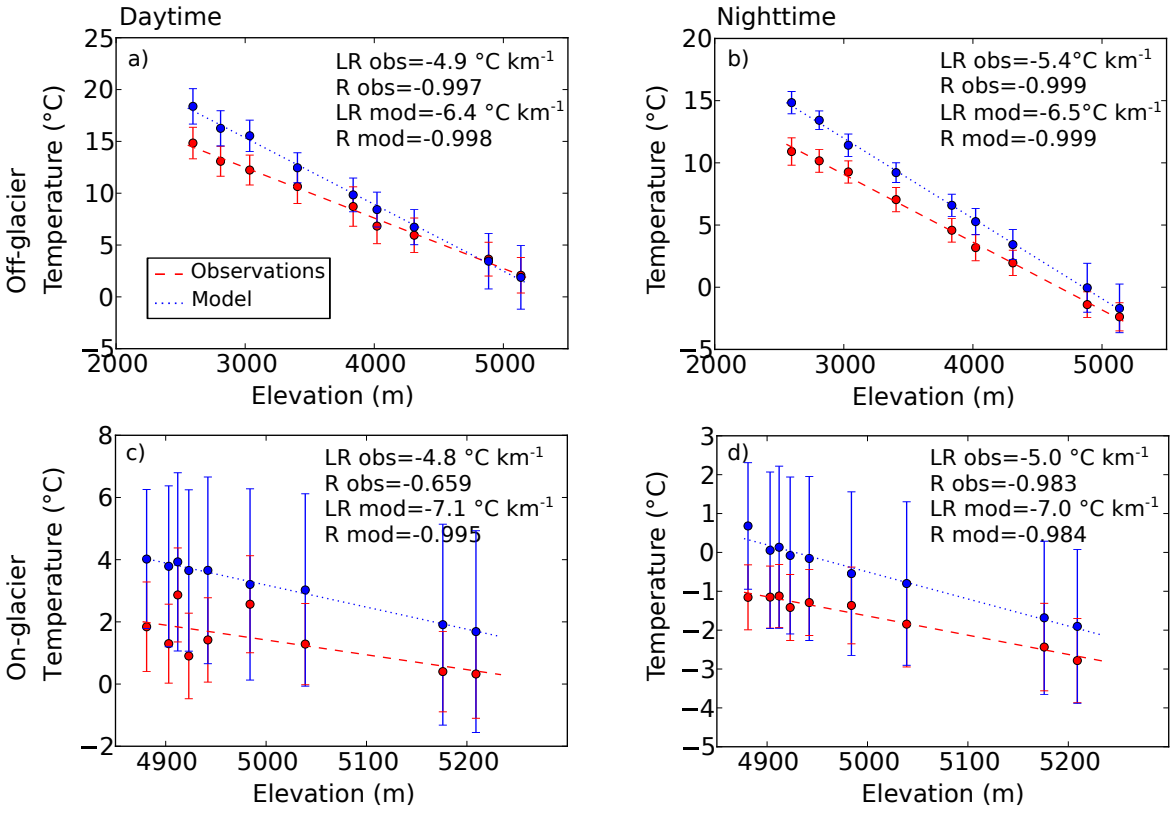

Fig. 5.14 As for Fig. 5.5, for the debris-cover model run (mod, blue dotted) and observations (obs, red dashed).

Off-glacier, the model lapse rate is much steeper than the observed lapse rate from the 5th to 8th May, but improves slightly afterwards, and particularly after the 12th May (Fig. 5.15 (a)). This is because the warm bias in the model at low elevations is particularly bad for the first few days of the period (not shown). This may be related to the poor representation of

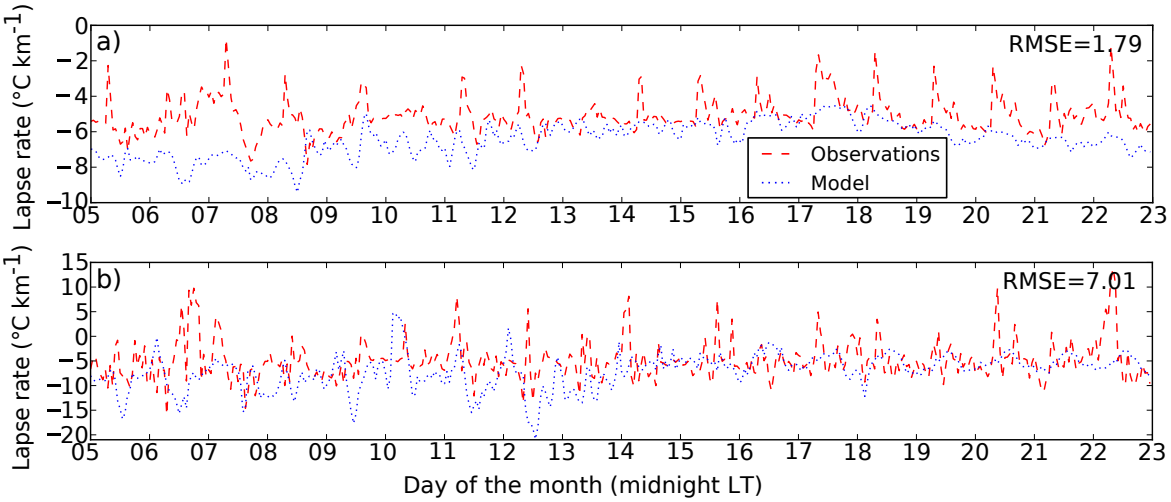

Fig. 5.15 The lapse rate derived from the nine off-glacier stations, every half-hour from 5th May to 22nd May in the observations (red, dashed), and model (blue, dotted) (a). All lapse rates are shown, even if not statistically significant. Panel (b) is the equivalent for the nine on-glacier stations.

cloud from the 5th to 8th May, as discussed in Section 5.2.4. The effect of cloud cover on the model lapse rate is further examined in Section 5.2.6. In addition, the model does not capture the amplitude of the morning spike in the off-glacier lapse rate seen in the observations (Fig. 5.15 (a)). On-glacier (in the debris-cover run), the model lapse rate is more variable, but appears to improve after the 14th May (Fig. 5.15 (b)).

5.2.6 How do other meteorological variables affect the lapse rate in the model simulation?

To examine the variations in model lapse rate, Fig. 5.16 shows the equivalent of Fig. 5.8 for the model output, i.e. the variation in lapse rate versus the variation in model pressure, cloud, shortwave incoming radiation, relative humidity and wind speed and direction, all from the model simulation.

There appears to be some association between the model lapse rate and the model cloud cover and incoming shortwave radiation, as suggested in Section 5.2.5. Three case studies are chosen to further examine the cloud cover, as follows: the 5th to the 8th May represents a period of steeper than average model lapse rates and high model cloud cover at high elevations; the 9th to the 12th May represents a period of approximately average model lapse rates, but still high model cloud cover at high elevations; and the 17th to the 20th May represents a period of shallower than average model lapse rates and low model cloud cover at high elevations (Fig. 5.16 (b) and (c)).

From the 5th to the 8th May, there is complete cloud over the higher elevations of the valley, whereas at lower elevations in the valley the maximum cloud fraction is between about 0.5 and 0.7 (Fig. 5.17 (a)). This leads to more incoming shortwave radiation and therefore warmer temperatures at lower elevations, in comparison to high elevations in the valley. As such, this may be the cause of the steeper lapse rates from the 5th to the 8th May, which are particularly steep during the day (Fig. 5.16 (b)). The pattern of cloud cover at higher elevations is similar from the 9th to the 12th May as that for the 5th to the 8th May (Fig. 5.17 (b) cf. Fig. 5.17 (a)), and therefore appears similar in Fig. 5.16 (b) (as the cloud cover is taken as an 8 km by 8 km area over the glacier, to match observations). However at lower elevations there is more cloud cover from the 9th to the 12th May than the 5th to the 8th May (Fig. 5.17 (b) and (a) respectively), and consequently the lapse rate is shallower (Fig. 5.16 (b)). This explains the jump to a shallower lapse rate on the 8th May, as the difference in cloud between lower and higher elevations is reduced. In contrast, the shallow lapse rate from the 17th to the 20th is associated with very little cloud (maximum cloud fraction between 0 and 0.3) over the entire valley (Fig. 5.17 (c)).

To further explore the relationship between nighttime katabatic winds and lapse rates identified in Section 5.2.2, Fig. 5.18 shows the equivalent of Fig. 5.9 for the model output,

but for the period where nighttime katabatic winds are seen in the model, from 12th to 14th May. Although the relationship between nighttime katabatic winds and shallow lapse rates is not quite as clear in the model as in the observations, similar relationships are still evident (Fig. 5.18 (a) cf. Fig. 5.9 (a)). This mechanism is particularly clear around midnight on both the 13th and 14th May, where the nighttime katabatic winds on the glacier are 8 m s^{-1} stronger than the average for the rest of the period (Fig. 5.18 (a)). This downslope wind corresponds with an increase in the temperature of the high-elevation stations (whilst the lower elevation stations are no warmer than average) (Fig. 5.18 (c)), and therefore a shallower than average lapse rate. The relative humidity is also slightly lower than average during the periods of nighttime katabatic winds, however the variation is much less substantial than in the observations. Although overall it appears that the changing cloud cover in the model has the clearest impact on the model lapse rates, the mechanism of high-elevation warming from nighttime katabatic winds also contributes to the changing lapse rate during this three day period.

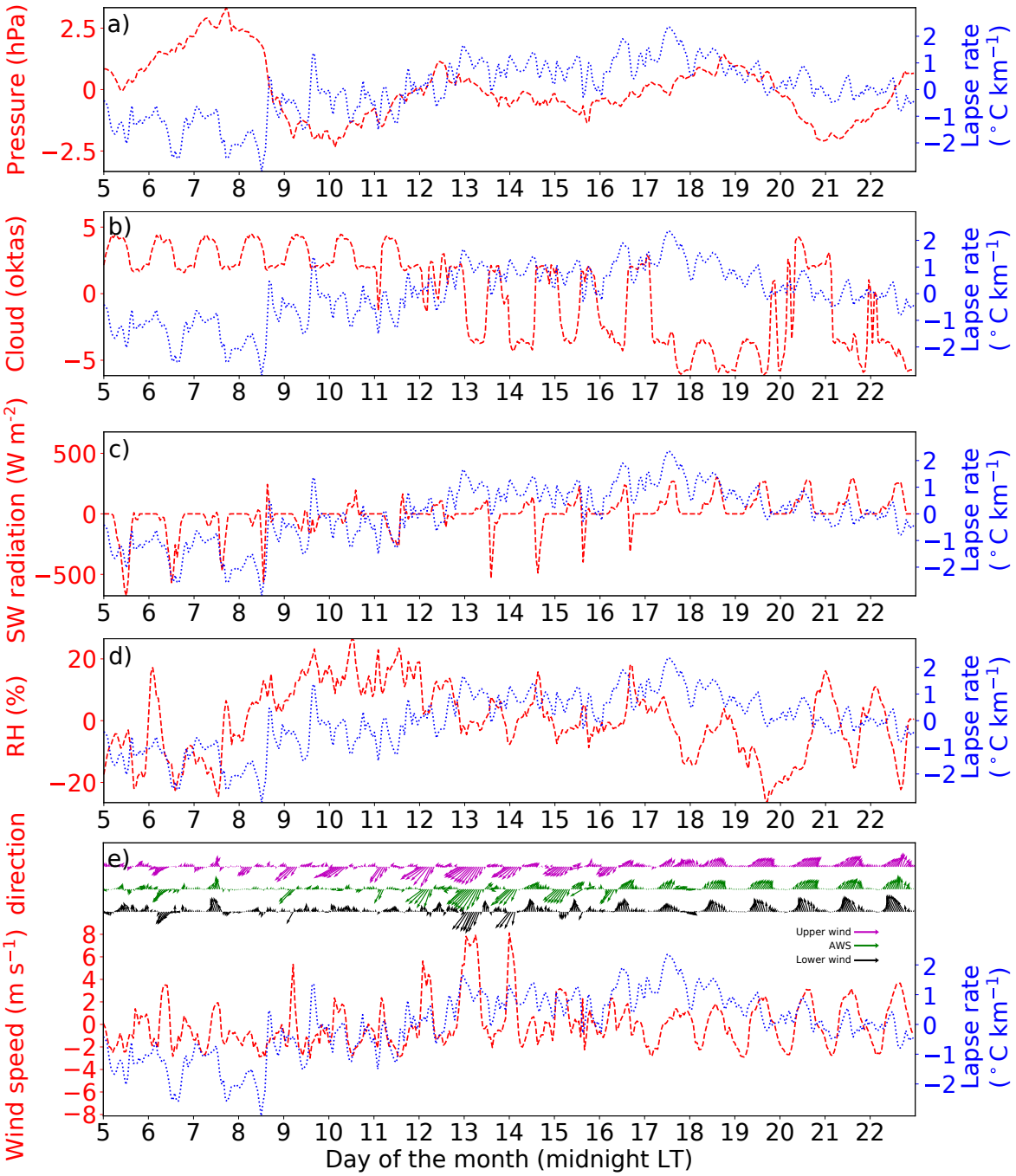

Fig. 5.16 As for Fig. 5.8, but for the model output. Note that the pressure and incoming shortwave radiation are taken from the nearest model grid point to the location of the AWS (on the glacier), the cloud is averaged over an 8 km by 8 km patch of model grid points (centred on the AWS), the relative humidity is averaged over the nearest model grid points to the two off-glacier and three on-glacier stations measuring relative humidity, and the wind speed is averaged over the nearest model grid points to the three on-glacier anemometers. As for Fig. 5.8, all values are anomalies, calculated by subtracting the average diurnal cycle for the 18 days of May.

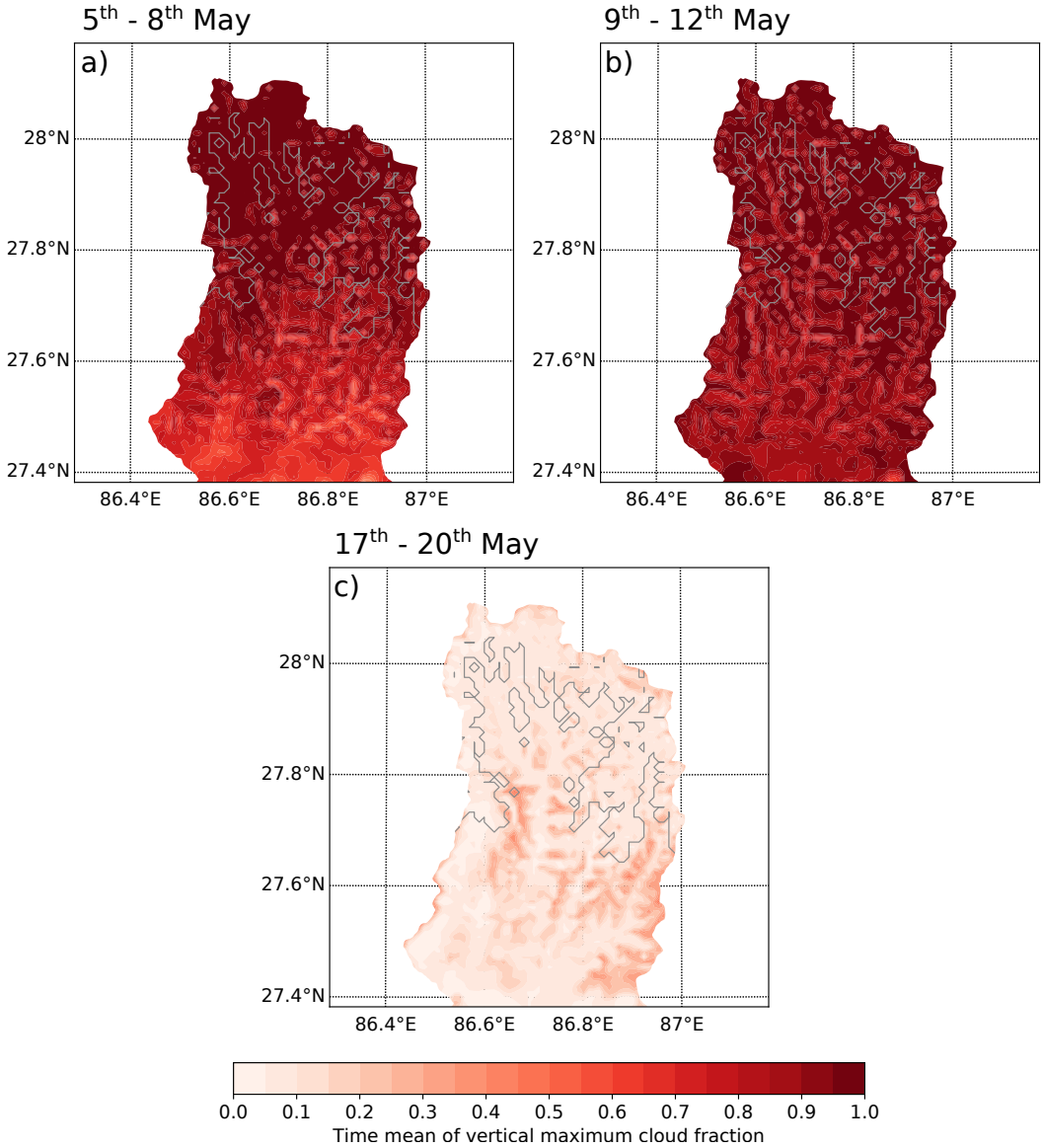

Fig. 5.17 The time averaged vertical maximum of cloud fraction from the model output (red shading) for three three-day periods, from 5th May to 8th May (a), 9th May to 12th May (b), and 17th May to 20th May (c). The cloud fraction gives the fraction of each model grid box which is cloud covered, so the vertical maximum of cloud fraction gives an approximate measure of the fraction of sky which is cloud covered when observed from the ground, in that model column. The glacier outline is shown in grey.

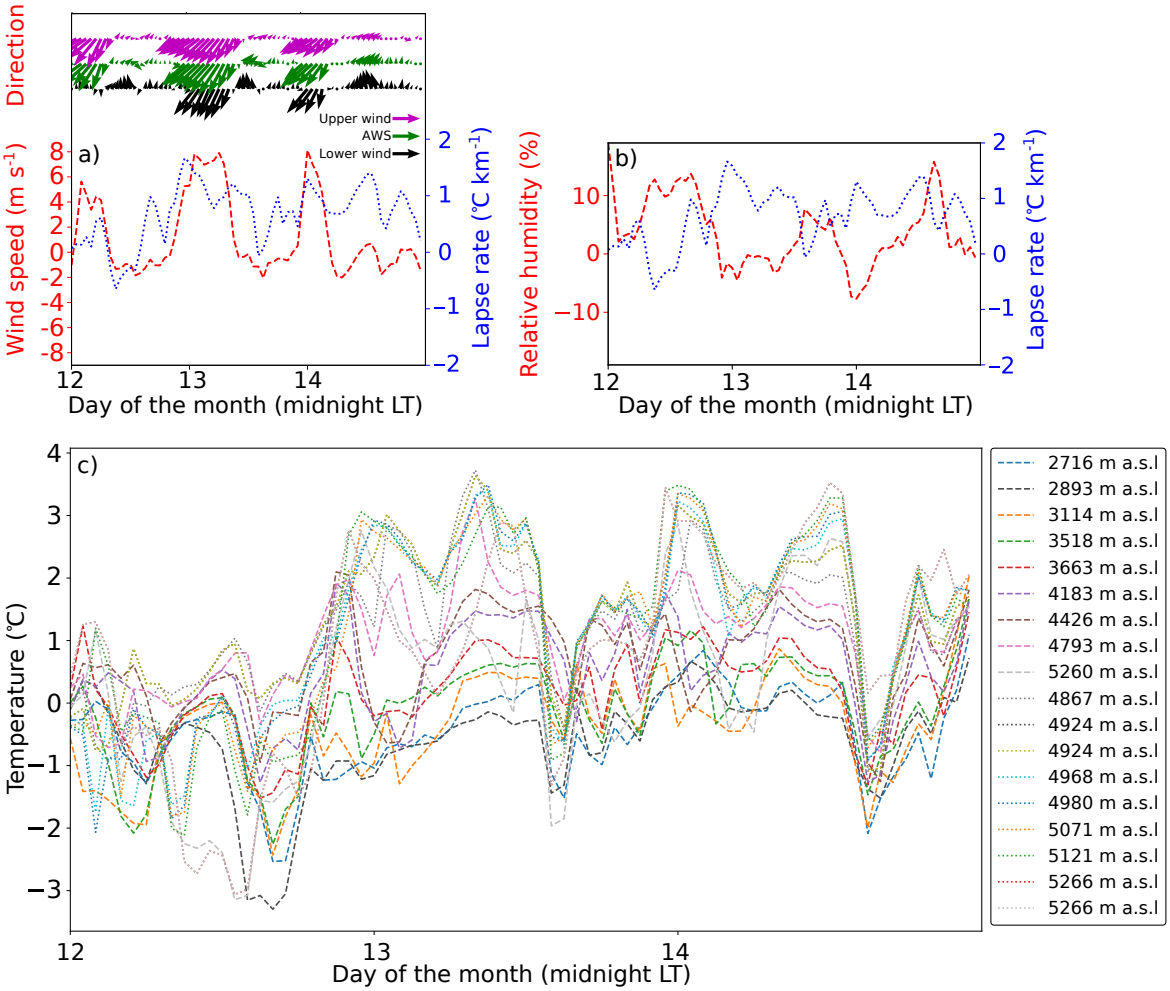

Fig. 5.18 As for Fig. 5.9, but for the model air temperatures and relative humidities at 2 m, and wind speed at 10 m. The case study is taken over the 12th to the 14th May. Note that only seven of the on-glacier points are visible, as for two pairs of stations, the nearest model grid point is the same.

5.2.7 Model potential temperature budget

As shown in Section 5.2.3, the model represents the timing and amplitude of the diurnal cycle in air temperature at 2 m well, both in the Dudh Koshi Valley and on the Khumbu Glacier. As such, it provides a useful tool for examining the components of change in potential temperature. Figure 5.19 shows the average diurnal cycle in potential temperature and corresponding potential temperature budget components at the lowest model level for the 18 days in May. These are shown as an average for all the off-glacier stations (Fig. 5.19 (a) and (d)), and the on-glacier stations for both the debris-cover run (Fig. 5.19 (b) and (e)) and for the clean-ice run (Fig. 5.19 (c) and (f)). This analysis is analogous to the momentum budget presented in Chapter 3.

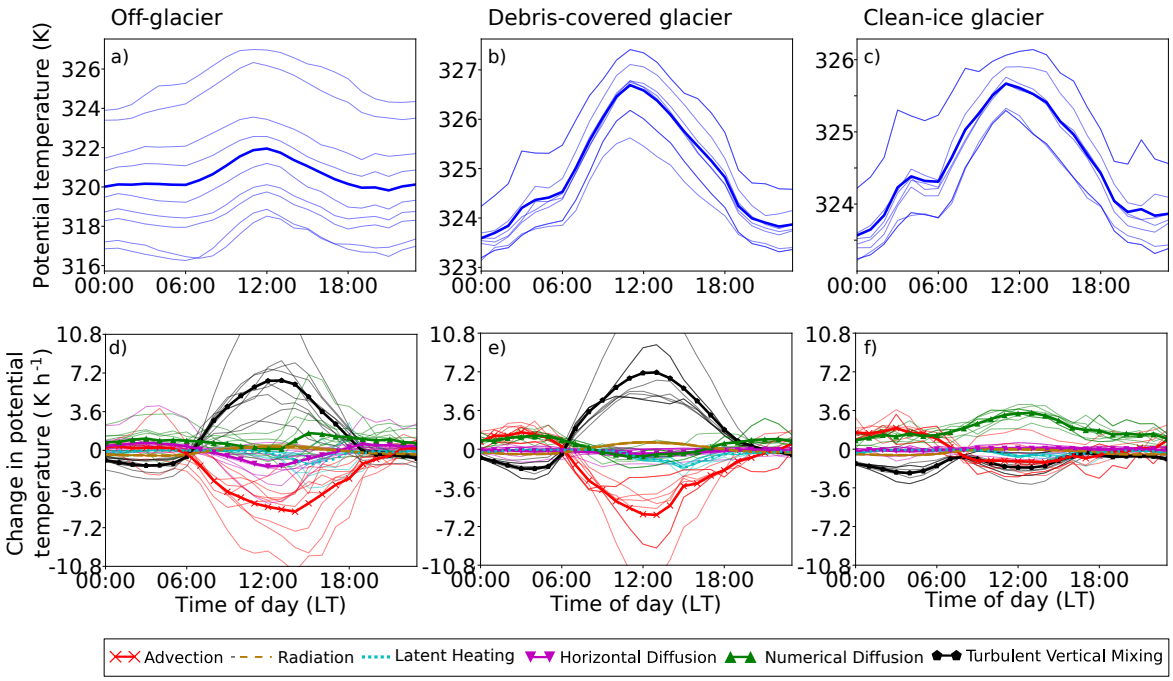

Fig. 5.19 Model derived averaged potential temperature over the 18 days of May, for each of the points representing the off-glacier stations (a), on-glacier stations in the debris-cover run (b) and on-glacier stations in the clean-ice run (c). The individual terms are shown as thin lines and the averages as thick lines with markers (or dashed/dotted lines). Lower potential temperatures correspond approximately to the lower elevation stations for both the off-glacier and on-glacier stations. The individual potential temperature budget terms for the three regions are shown in (d), (e) and (f) respectively.

The model representation of potential temperature at the lowest model level at both the off-glacier stations and the on-glacier stations (in both the debris-cover and clean-ice runs)

shows a clear diurnal cycle over the day (Fig. 5.19 (a), (b) and (c)), as would be expected from the plots for air temperature at 2 m (Figs. 5.10 and 5.11). At the on-glacier stations in the debris-cover run, there is an average range of approximately 3 K between the maximum daytime and minimum nighttime potential temperature (Fig. 5.19 (b)). At the off-glacier stations, and the on-glacier stations in the clean-ice run, this difference is slightly smaller, approximately 2 K (Fig. 5.19 (a) and (c)).

First, the potential temperature budget terms for the off-glacier stations, and the on-glacier stations in the debris-cover run, are discussed (Fig. 5.19 (d) and (e)). The clear diurnal cycle seen in the potential temperature (Fig. 5.19 (a) and (b)) is also seen in the potential temperature budget terms (Fig. 5.19 (d) and (e)). At both the off-glacier stations and the on-glacier stations in the debris-cover run, the largest contributions to change in potential temperature come from the advection term and the turbulent vertical mixing term. Both of these terms show a much larger contribution during the day than at night. Advection is wind driven, and for most of the month, the daytime wind speeds (averaging around $6\,\mathrm{m\,s^{-1}}$) are much larger than the nighttime wind speeds (averaging around $1\,\mathrm{m\,s^{-1}}$ to $2\,\mathrm{m\,s^{-1}}$) (Fig. 5.12 (e)). Turbulent vertical mixing is driven by the vertical gradient in potential temperature between the surface and the lowest model level, which in this case is larger during the day, when the sun is heating the ground, than at night. Turbulent vertical mixing increases the near-surface potential temperature during the day by up to $7\,\mathrm{K\,h^{-1}}$ and advection decreases the near-surface potential temperature during the day by just under $7\,\mathrm{K\,h^{-1}}$ (Fig. 5.19 (a) and (b)). At night, the sign of the advection and turbulent vertical mixing terms switches, and the magnitude of both terms is much smaller. Although there is variation between the different stations, all of the stations off-glacier and on-glacier in the debris-cover run have this same pattern of positive turbulent vertical mixing and negative advection during the day (Fig. 5.19 (d) and (e)).

The latent heating term has a small cooling effect (under $1.5\,\mathrm{K\,h^{-1}}$) in the afternoon at most stations off-glacier and on-glacier in the debris-cover run, due to evaporation, snow melt or sublimation. As seen in Fig. 5.12 (d), relative humidity increases in the afternoon from about 70 % to 100 %, and it often snowed in the afternoon, leading to more moisture to be evaporated. Radiation has a small heating effect during the day at all stations. There is a small negative contribution from horizontal diffusion (under $1.5\,\mathrm{K\,h^{-1}}$) at the off-glacier stations (Fig. 5.19 (d)), which is even smaller at the on-glacier stations in the debris-cover run (Fig. 5.19 (e)). Numerical diffusion has a small positive effect in the afternoon at the

off-glacier stations (under $2\,\mathrm{K\,h^{-1}}$) (Fig. 5.19 (d)), and a small positive contribution through the night at the on-glacier stations in the debris-cover run (Fig. 5.19 (e)).

Second, the potential temperature budget terms for the on-glacier stations for the clean-ice run are discussed (Fig. 5.19 (f)). Note that the on-glacier stations for the clean-ice and debris-cover runs are in the same locations (on the debris-covered portion of the Khumbu Glacier), as discussed in Section 5.2.3. The on-glacier stations in the clean-ice run show a different pattern in the components of the potential temperature budget, compared to the on-glacier stations in the debris-cover run (Fig. 5.19 (f) cf. Fig. 5.19 (e)). The average potential temperature budget for the on-glacier stations in the clean-ice run shows a positive contribution from numerical diffusion during the day of about $3.6\,\mathrm{K\,h^{-1}}$ at the maximum, with a small negative contribution from advection and turbulent vertical mixing of about $1\,\mathrm{K\,h^{-1}}$ to $1.5\,\mathrm{K\,h^{-1}}$ each (Fig. 5.19 (f)). The negative contribution from turbulent vertical mixing during the day is expected, as the near-surface air temperature is above $0\,^{\circ}\mathrm{C}$ and the glacier has a maximum temperature of $0\,^{\circ}\mathrm{C}$, so there must be a transfer of heat from the air to the glacier. At night, the temperature budget contributions are very similar for the on-glacier stations in the clean-ice and debris-cover runs (Fig. 5.19 (f) cf. Fig. 5.19 (e)).

The model temperature budget can be used to investigate the relationship between wind and lapse rate discussed in Section 5.2.6, which indicated a possible connection between increased downslope nighttime winds and a change in lapse rate, whereby downslope nighttime winds warmed the higher-elevation stations (but not the lower-elevation stations), causing a shallower lapse rate. The potential temperature terms from the case study determined in Section 5.2.6, from the 12$^{\mathrm{th}}$ to the 14$^{\mathrm{th}}$ May, are examined for the high-elevation (TV8 and TV9, and TG1-TG9) and low-elevation (TV1-TV7) stations (Fig. 5.18).

Around midnight of the 13$^{\mathrm{th}}$ and 14$^{\mathrm{th}}$ May (when there are strong nighttime katabatic winds and shallow lapse rates in the model), the potential temperature budget shows a large negative contribution from turbulent vertical mixing and a large positive contribution from advection at the high-elevation stations (Fig. 5.20 (b)). At the low-elevation stations, the nighttime contributions from advection and turbulent vertical mixing are small (Fig. 5.20 (a)), as they are for the rest of the period (Fig. 5.19). This is because the nighttime downslope winds only continue as far as the high-elevation stations (not shown). The pattern of strong nighttime katabatic winds and subsequent positive advection and negative turbulent mixing at night is also seen in the early hours of the 12$^{\mathrm{th}}$ May (Fig. 5.20 (b)), however here the katabatic

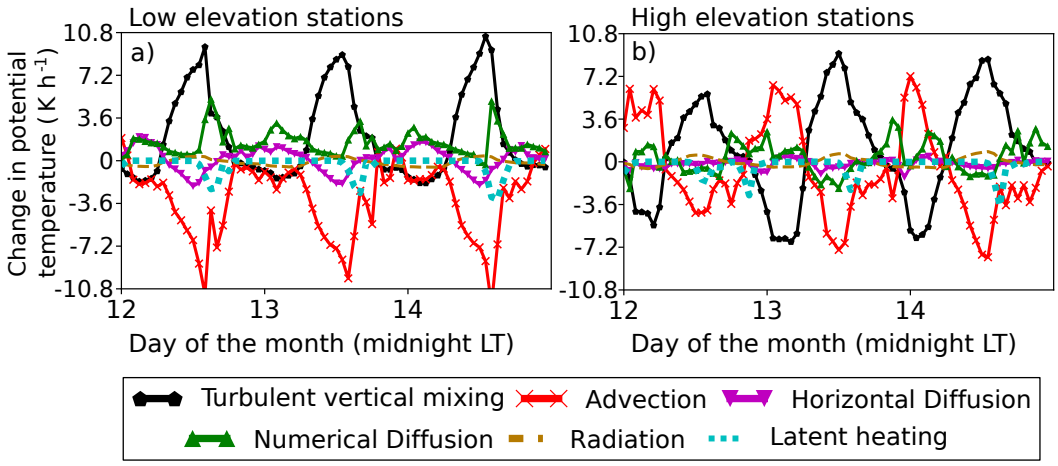

Fig. 5.20 Average potential temperature budget terms for the low-elevation stations (all off-glacier stations except TV8 and TV9; a) and the high-elevation stations (TV8, TV9, and all the on-glacier stations; b), from 12th to 14th May.

winds do not continue to the bottom of the glacier and there is a smaller change in lapse rate (Fig. 5.18 a). The large positive advection term, and large negative turbulent vertical mixing term evident at high elevations at night during this three day period is not typical of the rest of the period (Figs. 5.19 (d) and (e)), where there are very weak down-glacier winds at night (Fig. 5.16 (e)).

5.3 Monsoon season results

5.3.1 Evaluation of a linear lapse rate in the observations

In the monsoon season, the daytime off-glacier lapse rate is $-4.7\,^{\circ}\mathrm{C\,km^{-1}}$ (although this linear fit is not significant at the 5 % level, due to the small number of stations left in place off-glacier) (Fig. 5.21 (a)). At night, the lapse rate is $-5.1\,^{\circ}\mathrm{C\,km^{-1}}$, which is significant at the 5 % level (Fig. 5.21 (b)). As such, the lapse rate off-glacier is slightly shallower in the monsoon season than for the 18 days in May (equivalent pre-monsoon values off-glacier are $-4.9\,^{\circ}\mathrm{C\,km^{-1}}$ and $-5.4\,^{\circ}\mathrm{C\,km^{-1}}$ for the day and night, respectively (Fig. 5.5 (a) and (b)). As such, off-glacier the diurnal variation in lapse rates is reduced in the monsoon season compared to the pre-monsoon season. The monsoon season on-glacier lapse rates are $-3.7\,^{\circ}\mathrm{C\,km^{-1}}$ during the day and $-5.0\,^{\circ}\mathrm{C\,km^{-1}}$ at night (Fig. 5.21 (c) and (d)). Although these are both statistically significant at the 5 % level, there are large daily variations at each station.

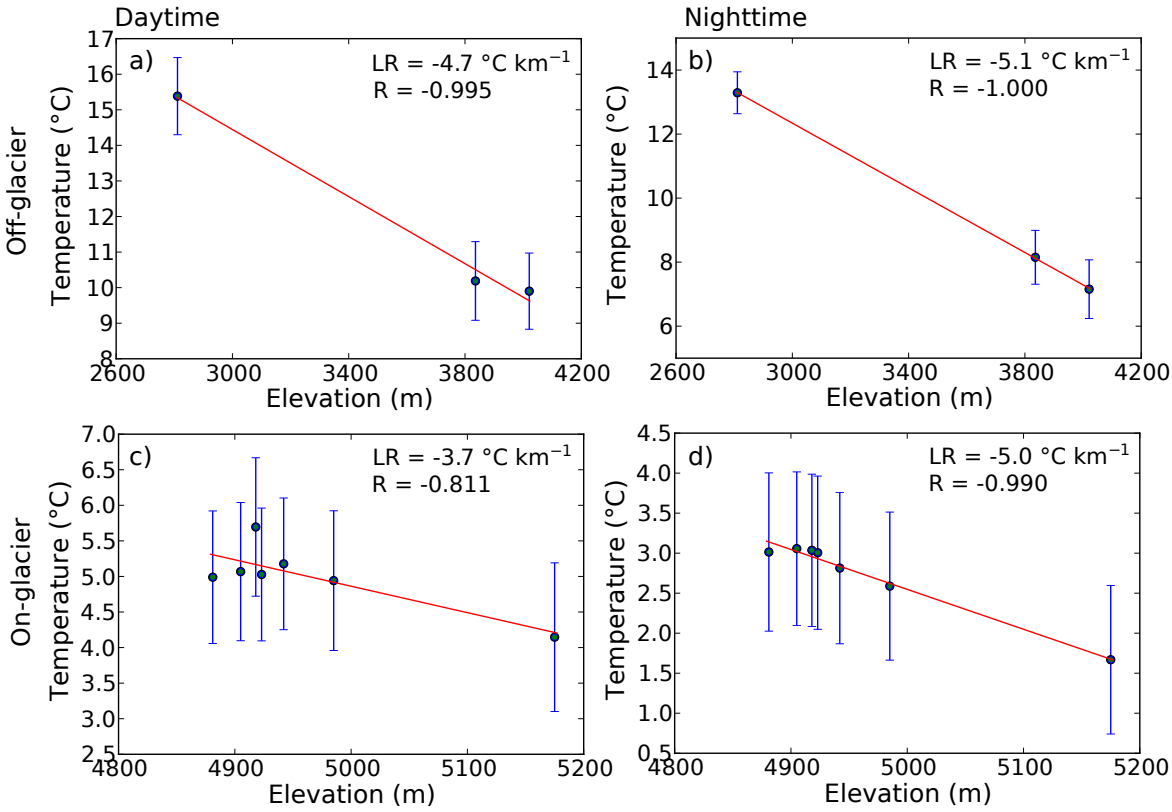

Fig. 5.21 As for Fig. 5.5, but for the three off-glacier stations and seven on-glacier stations left over the monsoon season, from 12$^{\mathrm{th}}$ June to 6$^{\mathrm{th}}$ October. Daytime is taken as 06:00-18:00 LT and nighttime as 19:00-05:00 LT. Panels (b), (c) and (d) are statistically significant at the 5% level. Note the different scales in each panel.

In addition, as data from two of the highest three stations on the glacier had to be discarded, the distribution of station elevations is quite uneven on-glacier in the monsoon season. No statistically significant on-glacier daytime lapse rate was found in the pre-monsoon, but the on-glacier nighttime lapse rates of $-5.0\,^{\circ}\mathrm{C\,km^{-1}}$ are the same for both the pre-monsoon and monsoon seasons.

5.3.2 Comparison of the WRF simulated and observed air temperatures at 2 m

One reason for leaving a series of stations up over the monsoon season (in addition to comparing the pre-monsoon and monsoon lapse rates) was to provide a longer period of measurements with which to evaluate the new glacier debris-covered glacier land cover category. For the monsoon season, there is no comparison to the default WRF model land cover category, so all on-glacier model run results are for a debris-cover run. In general, the WRF model performs better during the monsoon season than over the pre-monsoon (Fig. 5.22 cf. Fig. 5.10). At the off-glacier stations, the RMSE over the season ranges from 1.6 °C to 1.91 °C at the three stations, although the model underestimates the amplitude of the diurnal cycle.

On-glacier, the WRF model also performs better than in May, with RMSEs ranging from 1.67 °C to 2.0 °C at the seven stations (Fig. 5.23 cf. Fig. 5.11). During the monsoon, the model captures the amplitude of the diurnal cycle, and the maximum and minimum temperatures well at all on-glacier stations, except at TG8 where there is a slight cold bias in the model during the day.

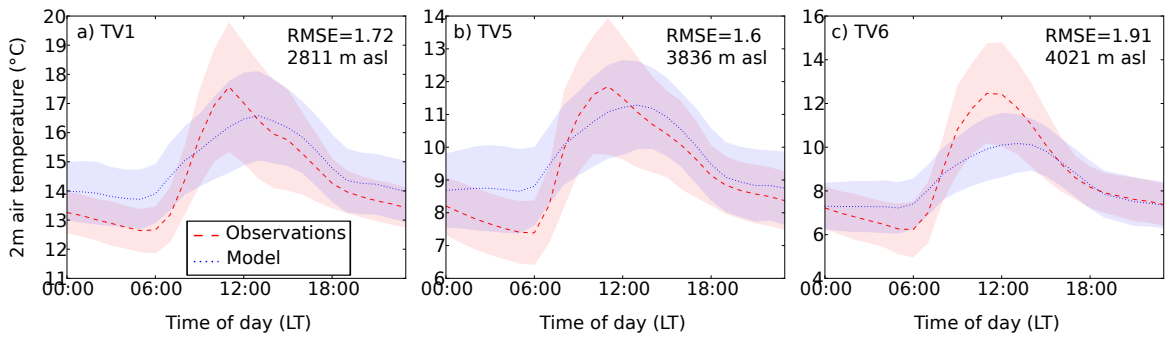

Fig. 5.22 As for Fig. 5.10, but for the three temperature loggers left over the monsoon season, from 12th June to 6th October, at TV1, TV5 and TV6 (a-c).

As the model represents the air temperature at 2 m more accurately in the monsoon season than in the pre-monsoon, there is a corresponding improvement in the model representation of the lapse rate off-glacier, and on-glacier at night (not shown). The model (and observational) lapse rates are −5.2 °C km^{-1} (−4.7 °C km^{-1}) for the daytime off-glacier averages, −5.3 °C km^{-1} (−5.1 °C km^{-1}) for the nighttime off-glacier averages, −7.1 °C km^{-1} (−3.7 °C km^{-1}) for the daytime on-glacier averages and −6.4 °C km^{-1} (−5.0 °C km^{-1}) for the nighttime on-glacier averages. The overly steep model lapse rate of −7.1 °C km^{-1} in the

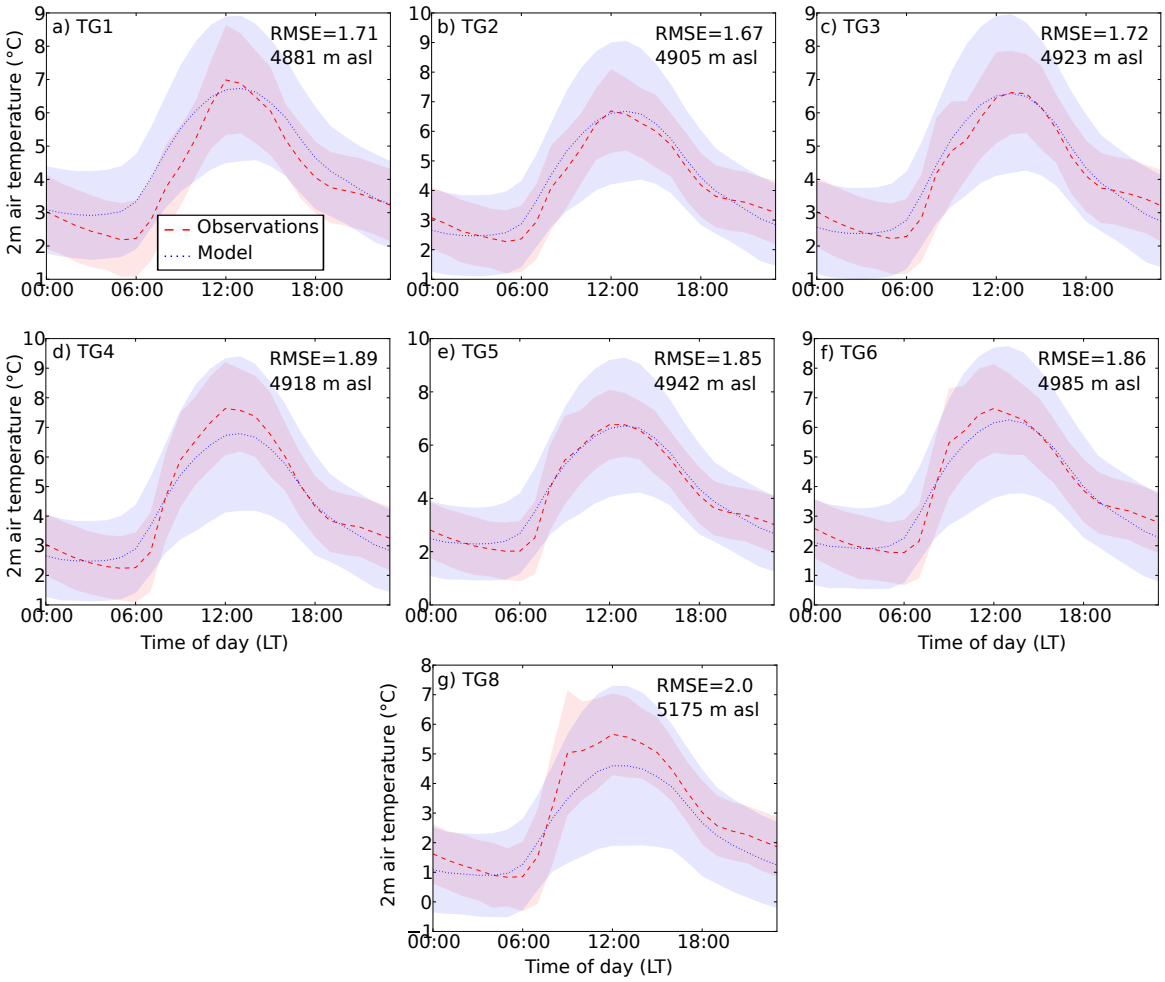

Fig. 5.23 As for Fig. 5.22, but for the on-glacier stations. Panels (a-g) show the glacier stations TG1-TG6 and TG8, respectively.

daytime on-glacier is reflective of the cold bias in the daytime seen at the highest station (Fig. 5.23 (g)), and the uneven spread of the stations on the glacier.

5.3.3 Model potential temperature budget

Overall, the pattern of potential temperature and the associated budget terms in the monsoon season is similar to that in the pre-monsoon. Off-glacier and on-glacier, there is a clear diurnal cycle in potential temperature, although off-glacier the amplitude of the diurnal cycle is only about 1 K (Fig. 5.24 (a)). By comparison, on-glacier the maximum daytime temperature is about 2.5 K higher than the minimum nighttime temperature (Fig. 5.24 (b)). Both of these increases are smaller than the pre-monsoon equivalents (Fig. 5.19 (a) and (b)).

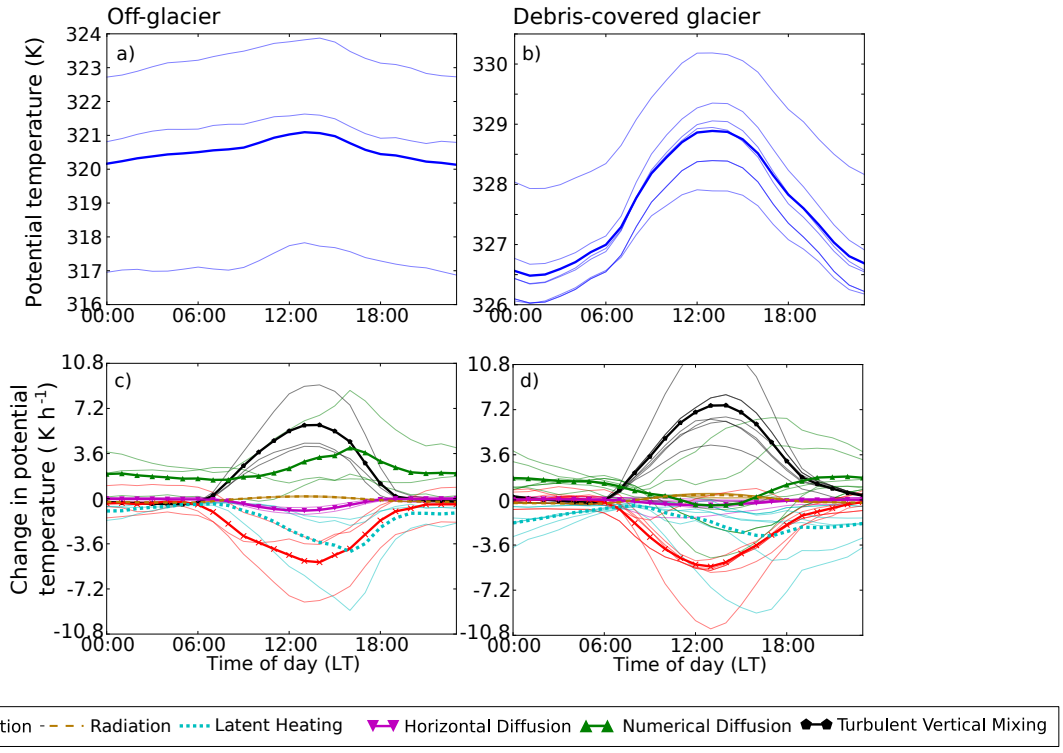

Fig. 5.24 As for Fig. 5.19, but diurnally averaged over the monsoon season, from 12th June to 6th October. The off-glacier average is taken over model grid points representing the three off-glacier stations (a and c) and the on-glacier average is taken over the model grid points representing the seven on-glacier stations (b and d). Note that the WRF model with clean ice was not run for the monsoon season. As was the case in Fig. 5.19, lower potential temperatures generally correspond to lower elevation stations.

The contributions from turbulent vertical mixing and advection are very similar in the monsoon period to the pre-monsoon, both off- and on-glacier. That is, both have a positive contribution from turbulent vertical mixing and a negative contribution from advection during the day, which become very small at night (Fig. 5.24 (c) and (d)). The magnitude of these terms is similar to the magnitudes in the pre-monsoon, 5 K h^{-1} to 6 K h^{-1} in the early

afternoon. As might be expected due to the increased precipitation in the monsoon season, there is a much larger negative contribution from latent heating during the monsoon season (of over $4\,\mathrm{K\,h^{-1}}$ in the late afternoon) than in the pre-monsoon, both off- and on-glacier (Fig. 5.24 (c) and (d)). There is also a cooling effect of about $1\,\mathrm{K\,h^{-1}}$ from latent heating throughout the night, especially on-glacier, indicating that evaporation or melting at the surface continues through the night. The nighttime increases in latent cooling are somewhat balanced by an increase in the numerical diffusion term.

5.4 Discussion

In the 18 days analysed in this chapter for the pre-monsoon period, the off-glacier lapse rates are similar to those found in other studies, and show similar diurnal patterns. Table 5.3 shows the a comparison of the off- and on-glacier lapse rates found in this chapter and previous studies. In this chapter, there is an average pre-monsoon off-glacier lapse rate of $-4.9\,^{\circ}\mathrm{C\,km^{-1}}$ during the day, and $-5.4\,^{\circ}\mathrm{C\,km^{-1}}$ at night. Yang et al. (2017) also analysed near-surface lapse rates in the Dudh Koshi Valley, finding an average lapse rate for 2007-2011 of $-5.8\,^{\circ}\mathrm{C\,km^{-1}}$ in May during the day (Table 5.3). As such, the pre-monsoon lapse rate found in this study is slightly shallower than the May average found by Yang et al. (2017). Given the large variation in lapse rate over the 18 days, this difference is unsurprising. Yang et al. (2017) also found steeper lapse rates in the lower elevations of the valley than the higher elevations in the pre-monsoon. Off-glacier, the high correlation coefficient of the lapse rate for the 18 days analysed in this study suggests that there is no difference in lapse rates between the low and high elevations of the valley (except in the morning). In the Langtang Valley, about 100 km to the west of the Dudh Koshi Valley, Heynen et al. (2016) also found a steeper lapse rate in the pre-monsoon (between 2012 and 2014) than is found in this study, of about $-6.0\,^{\circ}\mathrm{C\,km^{-1}}$ (Table 5.3). Heynen et al. (2016) also found an early morning peak in off-glacier lapse rates, of a similar magnitude to that found in this study. These early morning peaks are attributed to the sun hitting different sites at different times in the early morning (Heynen et al., 2016).

A comparison has also been made between the lapse rates on the debris-covered Lirung Glacier tongue, in the Langtang Valley, and those off-glacier (Steiner and Pellicciotti, 2016). Steiner and Pellicciotti (2016) find a nighttime lapse rate of $-4.3\,^{\circ}\mathrm{C\,km^{-1}}$ on the debris-covered glacier in the pre-monsoon, slightly shallower than the nighttime lapse rate on the debris-covered section of the Khumbu Glacier in this study, of $-5.0\,^{\circ}\mathrm{C\,km^{-1}}$ (Table 5.3). Similarly to this study, Steiner and Pellicciotti (2016) found that a value for the daytime on-glacier lapse rate was difficult to ascertain. Note that over the short period measured during May in this study, on-glacier stations were slightly cooler than off-glacier stations at same elevation, which is the opposite to what was found on Lirung Glacier (Steiner and Pellicciotti, 2016). However given the difficulties of obtaining on-glacier lapse rate values, more investigations may be needed to ascertain this relationship.

Table 5.3 A comparison of the lapse rates found in this study and previous literature. Note that on-glacier values refer to debris-covered glacier tongues. Note that Yang et al. (2017) and Heynen et al. (2016) do not explicitly split the results into day and night.

	May/pre-monsoon		Monsoon	
Off-glacier	Day	Night	Day	Night
This study	$-4.9\,^{\circ}\mathrm{C\,km^{-1}}$	$-5.4\,^{\circ}\mathrm{C\,km^{-1}}$	$-4.7\,^{\circ}\mathrm{C\,km^{-1}}$	$-5.1\,^{\circ}\mathrm{C\,km^{-1}}$
Yang et al. (2017)	$-5.8\,^{\circ}\mathrm{C\,km^{-1}}$		$-4.9\,^{\circ}\mathrm{C\,km^{-1}}$ to $-5.3\,^{\circ}\mathrm{C\,km^{-1}}$	
Heynen et al. (2016)	$-6.0\,^{\circ}\mathrm{C\,km^{-1}}$ to $-6.4\,^{\circ}\mathrm{C\,km^{-1}}$		$-4.2\,^{\circ}\mathrm{C\,km^{-1}}$ to $-4.5\,^{\circ}\mathrm{C\,km^{-1}}$	
On-glacier				
This study	$-4.8\,^{\circ}\mathrm{C\,km^{-1}}$	$-5.0\,^{\circ}\mathrm{C\,km^{-1}}$	$-3.7\,^{\circ}\mathrm{C\,km^{-1}}$	$-5.0\,^{\circ}\mathrm{C\,km^{-1}}$
Steiner and Pellicciotti (2016)	$-5.7\,^{\circ}\mathrm{C\,km^{-1}}$	$-4.3\,^{\circ}\mathrm{C\,km^{-1}}$	$-8.3\,^{\circ}\mathrm{C\,km^{-1}}$	$-4.9\,^{\circ}\mathrm{C\,km^{-1}}$

In the monsoon season, this study agrees with previous literature, that the lapse rate in the Nepalese Himalaya is generally shallower in the monsoon season than in the pre-monsoon season (Table 5.3). The contrast between the monsoon and pre-monsoon seasons is less stark in this study than in previous work in Himalayan valleys (Table 5.3), suggesting that the 18 days measured in May might have had a particularly shallow lapse rate compared to previous years. The measurements from this study agree with previous literature, that the strength of the diurnal cycle is reduced in the monsoon season. However where this study finds a slightly shallower lapse rate during the day than at night, in the Langtang Valley there is a slightly steeper lapse rate during the day (Heynen et al., 2016). The differences may arise from topographic variations between the two valleys, or from differences in surface type.

On-glacier in the monsoon season, Steiner and Pellicciotti (2016) found a nighttime lapse rate of $-4.9\,^{\circ}\mathrm{C\,km^{-1}}$ on Lirung Glacier, where the equivalent for the Khumbu Glacier is found to be $-5.1\,^{\circ}\mathrm{C\,km^{-1}}$ in this study (Table 5.3).

Both the observational and modelled lapse rates were compared against variations in pressure, cloud cover, incoming shortwave radiation, relative humidity and wind speed and direction. The observational lapse rate appears to show some association with wind speed and direction (with higher wind speeds corresponding to shallower lapse rates), and relative humidity (with drier humidity corresponding to shallower lapse rates), for some of the period measured. In particular, there appears in the observations to be an association between periods of strong nighttime katabatic winds and warmer temperatures at high elevations, and therefore a shallower lapse rate. This agrees with findings over the debris-covered Miage Glacier in Italy, where higher wind speeds were associated with higher temperatures over the debris-covered glacier, particularly when the wind was flowing down-glacier (Shaw et al.,

2016). There may also be a more complicated relationship between lapse rate and pressure, cloud cover and incoming shortwave radiation, but it was not obvious from the observations taken in May in this study. The model lapse rate appears to be associated with cloud cover (and therefore incoming shortwave radiation), with some association to wind speed and direction.

In an idealised (unglacierised) valley, it has been found that during the day the turbulent heat flux acts to warm the air near the surface, due to the heat exchange with the ground (Schmidli, 2013). In addition, valley circulations are driven by the equalising of temperatures in a valley, and as such, advection acts to cool the air immediately next to the surface (as this is warmer than the air away from the surface) (Schmidli, 2013). As such, both off-glacier and on-glacier in the debris cover run, the present study, which also shows daytime heating from vertical turbulent mixing and cooling from advection, agrees well with results from an idealised valley. The similarity of the potential temperature budget terms off-glacier and on the debris-covered glacier suggests that when representing near-surface air temperature, debris-covered glaciers should be treated more like unglacierised regions than clean-ice glaciers, in terms of mechanisms of heat exchange.

Idealised studies on heat exchange in valleys often use a dry atmosphere (Schmidli, 2013), which are often suitable over mid-latitude mountain ranges, such as the Alps. The present study highlights the importance of latent heat exchange in monsoon-dominated Himalayan valleys. Even in the pre-monsoon, both off- and on-glacier in the debris-cover run, there was a small but noticeable negative contribution to the near-surface potential temperature budget from latent heating in the afternoon (Fig. 5.19). Precipitation often fell during the afternoon in this period, and the early afternoon was one of the warmest times of the day, leading to evaporation, and therefore latent cooling through phase change. The cooling effects of latent phase change have been seen in previous studies to be large at the surface of debris-covered glaciers after precipitation events (Brock et al., 2010), and the results presented here suggest that this effect is similar in the near-surface air.

In the monsoon season, the effects of latent heating are much more substantial, with a longer period of latent cooling during the daytime off-glacier and on the debris-covered glacier (Fig. 5.24 (e)). It is often assumed that the effects of latent heating follow a simple mechanism, which is that in the monsoon the up-valley daytime winds drive moist air up the valley, which cools as it rises leading to condensation and heating at high elevations

(Kattel et al., 2013; Yang et al., 2017). However this study finds that as the warm moist air is driven up the valley, the potential temperature is in fact reduced by latent cooling, due to phase changes in the atmosphere. This suggests that there may be differences in some cases between the mechanisms controlling the environmental lapse rate (i.e. the variation of temperature with altitude above a point) and the near-surface lapse rate. The importance of latent heating in the potential temperature budget demonstrates that care is needed when translating knowledge of heat exchange from drier mountain ranges and dry idealised mountain studies to the Himalaya.

In addition to the findings associated with the general temperature budget discussed above, this chapter also uses the potential temperature budget to investigate the effects of (occasional) stronger than average nighttime katabatic winds on lapse rate in the pre-monsoon season, which act to warm high-elevation locations over the debris-covered glacier and just beside it, leading to unusually shallow lapse rates. This was due to a positive contribution from advection, and a negative contribution from turbulent vertical mixing during the nights with high-elevation katabatic winds. As the advection warms the near-surface air temperature, the temperature gradient between the cold nighttime surface and the warmer near-surface air is increased, thus increasing the sensible heat flux at the surface, and turbulent vertical mixing.

Over melting clean-ice glaciers (i.e. where the air above the glacier is above 0 °C), katabatic winds increase the sensible heat flux exchange from the glacier surface to the air at 2 m through turbulent vertical mixing (Greuell and Böhm, 1998; Shea and Moore, 2010). This turbulent vertical mixing acts to lower the potential temperature at 2 m. In the nighttime katabatic winds found during the pre-monsoon in this study, the cooling effect on the near-surface air from turbulent vertical mixing suggests that the debris-cover cools faster than the surrounding air, leading to a similar cooling effect through turbulent heat exchange to that previously found over clean-ice glaciers. Note that if the air is cooling as it flows down the glacier due to turbulent heat exchange, this suggests that parcels of air up-wind of the point being measured have a greater potential temperature than parcels of air down-wind, therefore the advection term would be positive in this instance. Here, the overall combination of the drivers is to increase the potential temperature.

5.5 Conclusions

In this chapter, data collected during a fieldwork campaign to investigate the temperature lapse rates in the Dudh Koshi Valley and on the Khumbu Glacier were analysed, and compared with output from the WRF model. In addition, the model potential temperature budget was analysed to investigate the mechanisms affecting variation in near-surface temperature lapse rates, especially the effects of wind on temperature variation. These variations were investigated both diurnally, and over the course of 18 days during the pre-monsoon season, and 116 days over the monsoon season. The main findings are as follows:

- For the 18 days measured in May 2017, the off-glacier near surface temperature lapse rate was $-4.9\,^{\circ}\mathrm{C\,km^{-1}}$ in the daytime and $-5.4\,^{\circ}\mathrm{C\,km^{-1}}$ at night. On the debris-covered tongue of the Khumbu Glacier, the near surface temperature lapse rate was $-4.8\,^{\circ}\mathrm{C\,km^{-1}}$ in the daytime and $-5.0\,^{\circ}\mathrm{C\,km^{-1}}$ at night. As such, there is no substantial difference between the near surface lapse rate on- and off-glacier. However, the lapse rate does vary considerably over the 18 days measured. Particularly shallow lapse rates at night are associated with periods of unusually strong nighttime katabatic winds at high elevations.

- In the monsoon season, similar lapse rates to those found in the pre-monsoon are found at night, of $-5.1\,^{\circ}\mathrm{C\,km^{-1}}$ off-glacier and $-5.0\,^{\circ}\mathrm{C\,km^{-1}}$ on-glacier. The smaller set of temperature loggers left over the monsoon season meant it was not possible to calculate statistically significant near-surface temperature lapse rates in the daytime off-glacier.

- The new glacier debris-covered glacier land cover addition to the WRF model, introduced in Chapter 4, is further analysed, and found to match observations of air temperatures at 2 m as well on-glacier as it does off-glacier. In the pre-monsoon, it improves the modelled air temperatures at 2 m in comparison to the default WRF clean-ice land cover category. Overall, the model performs better over the monsoon season than in the pre-monsoon, when compared with observations of air temperature at 2 m.

- The lapse rate is compared to air pressure, cloud cover, incoming shortwave radiation, relative humidity and wind speed and direction during the pre-monsoon, for both the model and observations. In the observations, there appears to be an association between periods of strong nighttime katabatic winds and shallower than average lapse rates. In the model, steeper lapse rates are associated with cloud cover over high elevations, and shallower lapse rates with clear skies.

- During both the pre-monsoon and the monsoon periods and both off-glacier and over the debris-covered glacier, the main terms to affect near-surface potential air temperature variation during the day are the turbulent vertical mixing, linked to the sensible heat flux, and the advection of potential temperature by the wind. During the monsoon season there is a much larger negative contribution from latent heating compared to the pre-monsoon season, in addition to a larger contribution from numerical diffusion.
- In the pre-monsoon, the near-surface potential temperature budget is analysed over the period of unusually strong nighttime katabatic winds. Due to the increased wind, there is a large contribution from the advection and turbulent vertical mixing terms not generally seen at night in the 18 day period. At night, the debris-cover is generally colder than the air at 2 m, so the turbulent vertical mixing term acts to cool the near-surface temperature, whereas the advection term acts to heat it.

Near-surface temperature lapse rates are often used to interpolate air temperature from lower elevation stations to the glacier elevations, where they are used as input to glacier mass balance models (Immerzeel et al., 2014). As such, understanding the temperature variation in Himalayan valleys, and over debris-covered and clean-ice glaciers, is vital for accurate glacier mass balance modelling. This chapter highlights the variability of the near surface temperature lapse rate, suggesting that a time-varying lapse rate should be used as a glacier model input. In addition, the temperature above the debris-covered portion of the glacier has similar drivers to that of the off-glacier temperature, in contrast to the drivers of the temperature above an equivalent clean-ice glacier model run. This highlights the need for debris-covered glacier representation in regional climate modelling. Lastly, the substantial contribution from latent heating to the near-surface potential temperature budget emphasises the difficulties in translating knowledge from other, drier mountain ranges, or dry idealised studies, to Himalayan valleys, especially during the monsoon season.

Chapter 6

Conclusions

Understanding the processes of wind and temperature variation in glacierised valleys worldwide is of vital importance for accurate parametrisations in climate models, as inputs to glaciological models, and for fundamental understanding of the glacio-hydro-meteorological system. It is particularly important in the HKKH region, which holds the third largest quantity of snow and ice in the world. The meltwater from the snow and ice contributes to rivers which provide water resources for 240 million people living in the mountainous regions of the HKKH, and almost 2 billion people living downstream (Wester et al., 2019). This thesis uses a high-resolution regional climate model with a new debris-covered glacier representation, as well as results from a fieldwork campaign, to define and illuminate some of the processes controlling wind and temperature variation in the Dudh Koshi Valley and over the Khumbu Glacier. In addition, it highlights the importance of including debris-cover in high-resolution regional climate models over debris-covered glaciers.

6.1 Achievement of thesis aims

6.1.1 Aim 1: To establish the patterns of the local wind regime and the dominant mechanisms controlling it

Local valley wind regimes, whereby wind travels up-valley and upslope during the day, and in some cases down-valley and downslope at night, have already been observed in valleys in the HKKH region, including in the Dudh Koshi Valley (Bollasina et al., 2002; Inoue, 1976; Ohata et al., 1981; Shea et al., 2015a; Ueno et al., 2001; Yang et al., 2017). However, these studies are based on only a handful of in-situ observations, and also typically lack

the added insight gained by an accompanying model-based study. Chapter 3 illustrates the advantages that come from using high-resolution regional climate models in conjunction with observational studies. Here, the WRF model was shown to accurately represent the diurnal cycle of winds in the Dudh Koshi Valley, with strong up-valley winds during the day and weak up-valley winds at night. The model was used to examine the winds over a much wider area than observations. For example, where some observational studies have recorded down-valley winds at night in winter in the Dudh Koshi Valley (Bollasina et al., 2002; Ueno et al., 2008; Yang et al., 2017), this thesis finds that the down-valley winds are only present in small regions of the valley in January 2014, and that the dominant nighttime wind pattern is of weak up-valley winds in the valley.

In addition, Chapter 3 uses the WRF model to determine the dominant drivers of the wind acceleration in the Dudh Koshi Valley. Of the few studies that have sought to understand the dynamical drivers of the local valley wind regime in the HKKH region, focus has generally been on the role of the pressure gradient (Sun et al., 2018; Zängl et al., 2001). Chapter 3 uses a momentum budget analysis to determine the drivers of the near-surface wind, finding that while the pressure gradient and advection terms are the dominant drivers of winds in the valley, they are extremely spatially variable, and in some regions the effects of turbulent vertical mixing can make an equally large contribution to the acceleration of the wind. This momentum budget analysis has been successfully used in other regions of the world to understand various wind regimes (Lehner and Whiteman, 2014; Moisseeva and Steyn, 2014; Renfrew, 2004; van Angelen et al., 2011; Van den Broeke et al., 2002), but this is the first use of a momentum budget analysis in a valley in the HKKH. The results of Chapter 3 suggest that this method could profitably be employed over other valleys in the HKKH to examine how the drivers of the wind acceleration vary across the region. As the wind affects temperature, the transport (blowing) of snow, moisture flux convergence and cloud cover (Immerzeel et al., 2014; Shea et al., 2015a), these results have implications for our understanding not only of local winds, but also the wider glacio-hydro-meteorological system, including glacier mass balance and river runoff, in valleys over the HKKH region.

6.1.2 Aim 2: To identify temperature lapse rates, the controls on this temperature variation, and the ways in which lapse rates vary in relation to other meteorological variables

The second aim of this thesis is investigated in Chapter 5, using a combination of the WRF model and measurements from a fieldwork campaign to investigate temperature lapse rates in the Dudh Koshi Valley, and over the Khumbu Glacier. The fieldwork campaign conducted for this thesis builds on previous studies observing near-surface temperature lapse rates in the HKKH region (Heynen et al., 2016; Immerzeel et al., 2014; Steiner and Pellicciotti, 2016; Yang et al., 2017). High-resolution observational studies, such as this and the work of Immerzeel et al. (2014), Heynen et al. (2016) and Steiner and Pellicciotti (2016) help to build understanding of how lapse rates vary across the region, as well as with season, time of day, elevation, and in response to other meteorological variables. However, the complexity of the topography and climatology of the HKKH region leads to considerable variation in the lapse rates between studies (Yadav et al., 2018) and, as such, additional observational campaigns are much needed. This study finds slightly shallower off-glacier lapse rates during the monsoon period compared to the pre-monsoon period, although the differences were not as large as those found by Yang et al. (2017), also in the Dudh Koshi Valley. In addition, whilst Heynen et al. (2016) found steeper lapse rates during the day than at night in the pre-monsoon period, the observations from this study showed slightly shallower lapse rates during the day (compared to the night) off-glacier.

Chapter 5 also investigates controls on the lapse rates. In particular, Brock et al. (2010) notes the need for a study investigating the effects of wind speed and direction on temperature lapse rates. Data from the fieldwork campaign that Chapter 5 is based on suggested an association between nighttime katabatic winds and shallower lapse rates, whereby nighttime katabatic winds warmed the higher-elevation areas on- and off-glacier. Down-glacier winds causing warming of the air above a debris-covered glacier has also been observed by Shaw et al. (2016), who investigated the controls on temperature variation above the debris-covered Miage Glacier, Italy. Chapter 5 investigates this mechanism further, finding that occasional strong nighttime katabatic winds cause warming from advection and cooling from turbulent vertical mixing. In general, in both the pre-monsoon and monsoon seasons, the air is warmed by turbulent vertical mixing and cooled by advection and latent cooling during the day, both off-glacier and over the debris-covered glacier. The latent cooling demonstrates the importance of including latent processes in atmospheric and idealised models representing

the HKKH region.

This study provides an important contribution to the growing body of work relating to near-surface temperature lapse rates in the HKKH. This is of fundamental importance for calculating inputs to glaciological models, where near-surface air temperature over high-elevation glacierised regions is often estimated from observations at lower elevations. Near-surface air temperature is one of the most important controls in determining glacier melt rates (Hodgkins et al., 2012; Immerzeel et al., 2014), so understanding the controls on lapse rates is essential for accurate predictions of current and future glacier melt, and ultimately hydrological change in the HKKH.

6.1.3 Aim 3: To investigate the effects of glaciers (particularly the difference between clean-ice glaciers and debris-covered glaciers) on wind variability and temperature lapse rates, and the subsequent effects on other meteorological variables

Aim 3 of this thesis is investigated over Chapters 3, 4 and 5. Chapter 3 conducts a sensitivity study to investigate the effects of removing all the glaciers in the Dudh Koshi Valley on the local wind regime. This study finds that when the glaciers are removed from the region, the up-valley winds during the day, which were previously weakened by the glaciers, continue further up-valley. This has implications for the transport of moisture and aerosols (such as black carbon from cooking stoves) up the valley as the glaciers in the region melt due to climate change, and may lead to feedbacks between changes in precipitation and clouds, and changes to the albedo of the glaciers due to deposits of black carbon.

Chapter 4 introduces a new debris-covered glacier land cover addition into the WRF model. Approximately 25 % of the glaciers in the Dudh Koshi Valley are debris-covered (Salerno et al., 2017; Shea et al., 2015a). Debris cover has previously been included in the WRF model, as part of a coupled atmosphere-glacier model, and was found to have a substantial impact on the surface and near-surface meteorological variables (Collier et al., 2015). Chapters 4 and 5 demonstrate that a simple representation of debris-cover in the (atmosphere only) WRF model is also capable of improving the representation of meteorological variables when compared against observations, in comparison to the default clean-ice WRF land cover. In particular, the amplitude of the diurnal cycle in air temperature at 2 m is much larger, and more representative of observations, in the model using the debris-covered

glacier land cover compared to the default clean-ice glacier land cover. Furthermore, Chapter 4 indicates that the addition of debris-cover into the WRF model markedly changes the simulated surface temperature and near-surface air temperature, and this has consequential effects on the near-surface wind, water vapour and hydrometeors, the terms of the surface energy budget, and ultimately on snow cover. As such, it is strongly recommended that debris cover is included in high-resolution modelling studies of glacierised regions, where a large proportion of the glaciers are debris covered.

Chapter 5 also compares the off-glacier and on-glacier (over the debris-covered glacier) lapse rates. In the pre-monsoon, the nighttime on-glacier lapse rate is slightly shallower than the nighttime off-glacier lapse rates. During the day, the small elevation range of the debris-covered glacier tongue, along with the differential heating of the debris, makes it difficult to ascertain a daytime on-glacier lapse rate. This difficulty was also found by Steiner and Pellicciotti (2016). In the monsoon season, the nighttime on- and off-glacier lapse rates are very similar. More investigation, over a range of glaciers in the HKKH, is needed to ascertain the exact effects of debris-covered glaciers on near-surface temperature lapse rates.

6.1.4 Limitations

There are some limitations to the methods used in this thesis. As seen in chapter 3, the WRF model cannot accurately represent the wind speed and direction at the peaks of the mountains. In addition, the highest spatial modelling resolution used in this thesis, of 1 km, only coarsely represent the glaciers in the region. A resolution of 500 m would have more accurately represented the shape of the glaciers in the region, and in particular the debris-covered regions, but this was not possible due to the computational expense. The WRF model is run with one-way nesting throughout this thesis, and this could have an impact on the coarser-resolution nests, as they are not receiving the detailed information from the inner domains. In this case, one-way nesting was necessary in order to test the effects of glacier removal in chapter 3 and the addition of debris cover in chapter 4, which were only changed in the inner domain.

The representation of debris-covered glaciers introduced in chapter 4 included a number of simplifications. In the model used in this thesis, the debris-cover properties are constant across the glacier. As such, variations in debris-cover thickness and the varying particle size of the debris are not taken into account. This would affect, for example, the roughness length

and specific heat capacity of the debris, and may have subsequent effects on the near-surface wind and temperature.

6.2 Future work

There are many possible directions in which this research could be extended, for both understanding the meteorological processes in valleys in the HKKH, and for understanding glacier mass balance in the region. Four possible avenues for future work are discussed below.

6.2.1 Extending the new debris-covered glacier land cover

The results of Chapter 4 suggest that adding debris-cover to the WRF model has a considerable impact on the near-surface meteorology. However, comparison with a previous study by Collier et al. (2015), who investigated the impact of adding debris cover to the WRF model over the Karakoram region, suggests that debris cover affects near-surface meteorological variables differently in different regions of the HKKH. For example, whilst in this study the wind speed is increased by the addition of debris cover, in the Karakoram the debris-cover is found to decrease the wind speeds. As such, the effects of adding debris cover to a regional climate model should be investigated over multiple areas in the HKKH region, in order to fully understand how the impacts of adding debris-cover vary. In addition, it would be useful to test the debris-covered glacier land cover addition over a longer period (particularly over the winter and post-monsoon seasons), ideally in comparison to a high-resolution observational dataset.

6.2.2 Idealised modelling

Due to the complexity of the topography of the HKKH region and the complex climatic regimes, idealised modelling could be used to simplify the valley topography and isolate dominant mechanisms of meteorological variation. The simplification of the complex topography allows the model to be run at much higher resolution than is possible over real topography. Idealised modelling also allows for simplified atmospheric processes. For example most previous idealised studies use a dry atmosphere, so microphysical processes need not be considered. This allows for isolation of individual atmospheric mechanisms. Idealised modelling of meteorological processes in valleys has been demonstrated, in recent years, to be a useful tool in understanding the fundamental meteorological processes in valleys around

the world. This method has been successfully employed to examine both the controlling mechanisms on the local wind regimes in valleys (Lang et al., 2015; O'Steen, 2000; Wagner et al., 2015a,b), and the effects of the local valley wind regime on the transport of heat within a valley (Schmidli, 2013; Serafin and Zardi, 2010).

While the studies above do not use real topography, they are generally more representative of mountain ranges such as the Alps, with smaller valleys than are typical for valleys in the HKKH region, and use a dry atmosphere. As such, they do not include the impacts of moisture on wind and temperature, which is shown through this thesis to be an important factor in the Dudh Koshi Valley. It would therefore be profitable to conduct some high-resolution idealised modelling studies on larger valleys, with moisture included. This idealised modelling could be used to further illuminate some of the processes discussed in this thesis. First, the effects of changing land cover could be examined more closely. The higher resolution of an idealised model would lead to a larger number of model grid cells over glaciers, which could thus be used to more accurately examine the effects of debris-covered glaciers on the near-surface atmospheric processes. Second, an idealised modelling framework would be extremely useful for further investigations of the mechanism by which katabatic winds cause shallower lapse rates. Due to the short length of the pre-monsoon fieldwork study in this thesis, it was only possible to identify strong nighttime katabatic winds over a period of a few days. With an idealised study, it would be possible to test the impacts of strong nighttime katabatic winds more precisely, by eliminating other meteorological variation.

6.2.3 Impact on glacier accumulation and melt

Ultimately, improved understanding of wind and temperature variation in the HKKH is necessary, primarily, to better predict glacier melt and differences to water resources. One interesting avenue for future work would be to use the high-resolution regional climate model as input to a glacier mass balance model. In general, glacier mass balance models need climatic input data on a spatial scale of tens or hundreds of meters. Reanalysis data, and global climate models, generally have a spatial scale of tens of kilometres. As such, the climatic input needs to be downscaled. The high-resolution climate modelling from this thesis is much closer to the resolution needed by glacier models than, say, ERA-Interim data. As such, using this dynamically downscaled data should improve the accuracy of the glacier mass blance model. The mass balance model forced by dynamically downscaled data

could then be compared to a mass balance model forced by statistically downscaled climate inputs (or gridded observational data, as used by Marzeion et al. (2015)), to determine the added value of dynamical downscaling. The model run for the monsoon period analysed in Chapter 5 might be long enough for a sensitivity study, as it covers the main melt season. This sensitivity experiment may help to bound uncertainty in terms of glacier melt, or allow for a bias correction of the glacier melt models, leading to more accurate future predictions of glacier mass change.

6.2.4 Future climate projections

Another important avenue for future work would be to use the WRF model, with the new debris-covered glacier land cover, to examine how valley-scale meteorological processes may change in the future. Given the high computational cost of running the WRF model at the 1 km resolution used in this study, it would be very difficult to run the model for a period of decades (or more), but it might be possible to run it at a lower resolution, perhaps 5 km, to investigate future climate in valleys in the HKKH. The WRF model would be forced using output from global climate models. This would be useful to determine whether any valley-scale processes might change in the future. Future climate projections could also then be used to run short glacier mass balance studies in the future, to better determine patterns in the rates of glacier mass balance change in the future.

6.3 Final remarks

This thesis adds to a growing body of work investigating the meteorological processes occurring in glacierised valleys in the HKKH region. It highlights the usefulness of combining fieldwork campaigns with high-resolution numerical modelling studies. Observations are of vital importance, both to validate numerical models and to identify patterns and associations between meteorological variables. High-resolution regional climate models give a broader understanding of the distribution of meteorological variables over valleys, as well as being a useful tool to examine the meteorological processes taking place.

This thesis, and the studies preceding it, highlight the complexity of wind and temperature in valleys in the HKKH region. It is hoped that the work contained in this thesis will inspire others to combine field measurements and high-resolution modelling to investigate wind,

temperature and other meteorological variables in valleys in the HKKH, and that this work will ultimately be of use to glaciological modelling and to predicting future water resources in the HKKH. Furthermore, the improved understanding of the mechanisms controlling wind and temperature variation, as well as the new debris-covered glacier category, will hopefully be of use, ultimately, to improving parametrisations of glacierised valleys in weather and climate models in the future.

Appendix A

Calculating significance for the snow removal experiment

In Chapter 3, two model outputs are compared, one with the currently glacierised area (the summer run) and one with the glacierised area removed (the perturbation experiment). The difference in the near-surface winds is calculated over the valley. To test whether the difference in the wind is significant, a Student's t-test is used with autocorrelation taken into account. In addition, a bootstrapping method is used to check the significance, and points are only shown as significant if they are significant according to both of these tests. Both tests use a paired test, i.e. the difference between the perturbation run and the summer run is calculated, and tested for a significant difference from 0. The t-test and bootstrapping methods are described below. The same method is used for assessing whether the difference between the debris-cover run and the bare ground and clean-ice runs is significant, in Chapter 4.

A.1 Student's t-test

Every 1 km grid point in the domain is considered separately, so the model output at each point for both the summer run and the perturbation experiment is a time series of U and V wind velocities, every hour for the month. These model outputs are sample datasets. When the 'distribution' is referred to, this refers to the distribution of the underlying population data set.

The t-test relies on three assumptions (von Storch and Zwiers, 1999):

1. Each data point comes from the same distribution (i.e. if the population has a normal distribution, each data point much be generated from the same normal distribution).

2. The distribution is normal.

3. Each data point in the model output occurs independently of all other data points.

First consider assumption 1, that each data point comes from the same distribution. The differences in meridional velocity V from one location is used as an example. The assumption amounts to the assumption that each hour is equally likely to have same differences in velocity. The results of Chapter 3 show that the winds have a diurnal cycle and are likely to be stronger in the daytime than at night, and therefore that the difference between the runs is likely to be larger during the day, therefore the dataset needs modification for assumption 1 to hold. The differences in meridional wind velocities are averaged for each day and night of the month, and the significances are considered separately for the day and night. The summer run and summer perturbation experiment in Chapter 3 run from 00:00 01/07/2013 to 23:00 31/07/2013. The first and last half a night in the month are ignored, leaving a dataset of 31 daytime meridional velocity differences and 30 nighttime meridional velocity differences. It is now reasonable to assume that each of the 31 daytime meridional velocity differences (and the 30 nighttime velocity differences) are drawn from the same distribution (indeed, the wind has been shown in Chapter 3 to be very consistent over the month). Thus assumption 1 holds.

For assumption 2 it is assumed that the distribution is normal, i.e. that the differences in the daytime (or nighttime) averaged meridional velocity V over the month of July are normally distributed.

The third assumption is that each data point is independent of all other data points. If the daytime meridional wind velocity difference is large on one day of the month, it might be expected to also be large the following day, and so this assumption may not hold. This is known as autocorrelation, and can be tested by calculating the autocorrelation function. Let $\{v_1 ... v_{31}\}$ be the sample dataset of the differences in daytime meridional velocity between the summer run and the summer perturbation experiment. Then the autocorrelation function ρ is calculated using the formula given in Chandler and Scott (2011):

$$\rho(k) = \frac{\sum_{t=k+1}^{n}(v_t - \bar{v})(v_{t-k} - \bar{v})}{\sum_{t=1}^{T}(v_t - \bar{v})^2} \tag{A.1}$$

Where k is the lag (day of the month, so $\rho(5)$ represents the autocorrelation between the original time series and the time series shifted forward five days), and the sample mean is given by $\bar{v}$. An example of the autocorrelation function is shown in Fig. A.1. The confidence intervals are given by $\pm 1.96/\sqrt{31}$, as suggested in Chandler and Scott (2011). Any points where the autocorrelation function lies outside of the confidence interval is taken as a significant autocorrelation. The autocorrelation function at a test point in the domain is given in Fig. A.1.

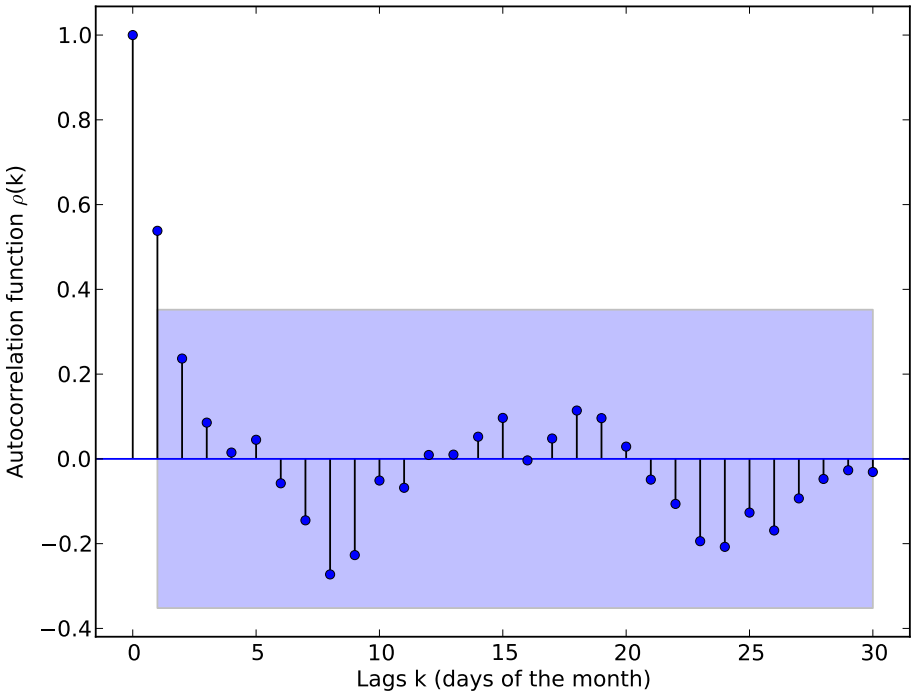

Fig. A.1 The autocorrelation function for a sample point in the domain, showing the autocorrelation of the daytime 10 m meridional velocity difference. Shading indicates the 95% confidence intervals that indicate significant difference from 0.

In almost all points in the domain, where there is a significant autocorrelation it occurs in the lag 1 autocorrelation. As such, the process is assumed to be a first-order autoregressive process (AR(1)). Approximately half of the points in the domain show lag 1 autocorrelation in the daytime meridional velocity.

To account for the autocorrelation, an effective sample size n_e must be calculated. Assuming that the process is AR(1) as discussed above, Chandler and Scott (2011) and von

Storch and Zwiers (1999) suggest that an effective sample size can be calculated using the formula:

$$n_e = n\frac{1-\rho(1)}{1+\rho(1)} \tag{A.2}$$

Where n is the length of the sample (31 in this case) and $\rho(1)$ is the autocorrelation function evaluated at lag 1. This gives an effective sample size at each point in the domain where there is autocorrelation (where there is no autocorrelation the sample size is left as 31). For the daytime meridional velocity case, the average n_e is 10.5 for the locations with autocorrelation. The equivalent sample sizes for the perturbation run are calculated in the same way. The t statistic (t') is then calculated using the equation from von Storch and Zwiers (1999):

$$t' = \frac{\bar{v}}{\sqrt{\frac{S^2}{n_e}}} \tag{A.3}$$

Where $\bar{v}$ is the sample mean of the difference in meridional wind velocity, and S is the sample variance. This t' statistic was then checked for significance at the 5% level.

A.2 Bootstrapping

To check the reliability of the statistics from the t-test, and to account for the fact that at 5% of the points in the domain, the null hypothesis (of no change in the wind) may have been incorrectly rejected, a bootstrapping method is also employed. This method is described in von Storch and Zwiers (1999), and the code used was based on code provided by Christine McKenna at the British Antarctic Survey. Again, each point in the domain is considered separately.

The bootstrapping method does not have any assumptions, except that the sample can be represented by random variables ($\{v_1 ... v_{31}\}$ in this case). A new sample is created by randomly picking (with replacement) 31 of these random variables. As they are picked with replacement, this sample can contain repeat variables (so, for example, it might contain 10 copies of v_4, 6 copies of v_{25} and 15 copies of v_{31}). The mean of the sample is then calculated. This process of finding mean of a randomly picked sample is repeated a large number of times (in this case, 10000 times). The sample means are then ordered. As the random variables represent differences between the two runs on each day, the null hypothesis is that the means

of the samples will be centred on 0. If fewer than 2.5% (or the chosen significance level $\alpha/2$) of the sample means are 0 or less, this suggests that there has been a significant increase in the winds at that point. An example of the histogram produced by the 10000 samples and the confidence intervals is shown in Fig. A.2.

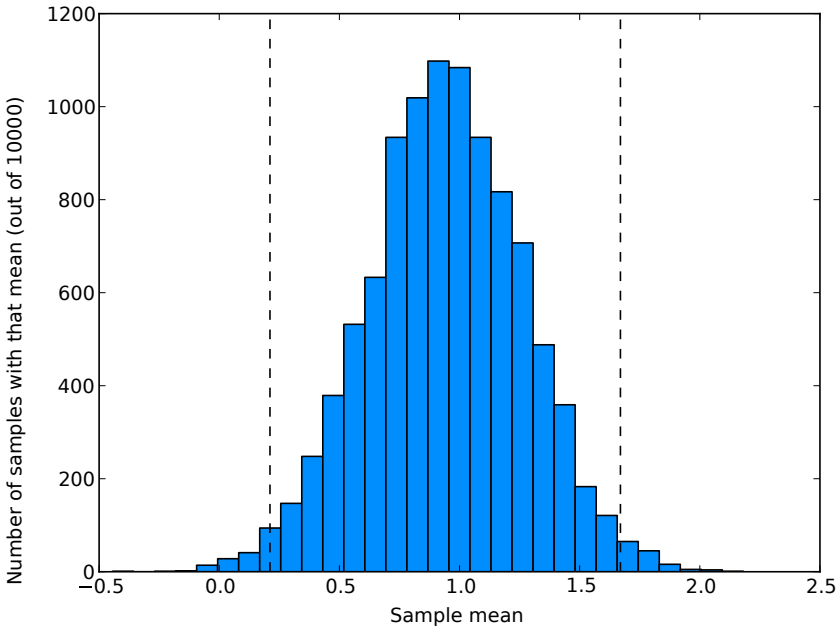

Fig. A.2 Histogram showing the distribution of the sample means from the bootstrapping method. The vertical dashed lines show the confidence intervals between which $1-\alpha$ of the data lie, where α is the chosen confidence level.

A.3 Final significance

As the significance is being carried out on wind vectors, it is assessed in both the zonal (U) and meridional (V) directions. If either direction is significant, the wind change is deemed to be significant. A significance level of 5% in either direction suggests that there is a 5% chance of incorrectly rejecting the null hypothesis (n_V: there is no change in the mean wind velocity in the meridional direction). As significance is being assessed in both direction, this leads to a greater than 5% chance of incorrectly rejecting the null hypothesis. Let x be the probability of incorrectly rejecting the null hypothesis in either direction. Then the possibility for incorrectly rejecting either or both of the null hypotheses is $x^2+2x(1-x)$, i.e. the probability of incorrectly rejecting both null hypothesis, plus the probability of

incorrectly rejecting one or the other of the null hypothesis. Solving $x^2 + 2x(1-x) = 0.05$ gives the probability that should be used in either direction to ensure a confidence interval at 5% overall. Hence the significance level in either direction is set to 2.53%. This is applied in both the *t*-test and the bootstrapping. For the variables considered in Chapter 4, such as surface temperature, the significance is kept at 5 %.

Lastly, the significance from the *t*-test and from the bootstrapping were compared against each other. These two methods showed very similar patterns in the significance of wind change in over the domain. Only the points which were significant in both methods were taken as significant.

Appendix B

WRF model and extracting tendency terms

B.1 WRF dynamics and physics

As described in Sections 3.1.3 and 5.1.3, the horizontal momentum budget and potential temperature budget are given by

$$\partial_t U = -\nabla \cdot \mathbf{V}u - (\mu_d \alpha \partial_x p + (\alpha/\alpha_d)\partial_\eta p \partial_x \phi) + F_U \tag{B.1}$$

$$\partial_t V = -\nabla \cdot \mathbf{V}v - (\mu_d \alpha \partial_y p + (\alpha/\alpha_d)\partial_\eta p \partial_y \phi) + F_V \tag{B.2}$$

and

$$\partial_t \Theta = -(\nabla \cdot \mathbf{V}\theta) + F_\Theta \tag{B.3}$$

respectively, where $\mu_d(x,y)$ is the mass of dry air in the column and p is the pressure. The coupled wind velocity $\mathbf{V} = (U,V,W) = \mu_d \mathbf{v}$, where U and V are the mass coupled zonal and meridional velocities and W is the mass coupled vertical velocity, and $\mathbf{v} = (u,v,w)$ is the uncoupled velocity. The vertical coordinate used by WRF is given by $\eta = (p_{dh} - p_{dht})/\mu_d$ where p_{dh} is the hydrostatic pressure of the dry atmosphere and p_{dht} represents this value at the top of the model. ϕ is the geopotential and $\nabla\cdot$ is the divergence. The inverse density of dry air is given by α_d, with $\alpha = \alpha_d(1 + q_v + q_c ...)^{-1}$ where q_v, q_c are the mixing ratios of vapour and cloud, respectively. The ∂_* sign denotes partial differentiation with respect to subscript *. See Skamarock et al. (2008) for further details.

To transform the equations from those described on the sphere above to the x-y grid, the WRF model uses projections. In the setup used here, a Lambert conformal projection is used, with $\Delta x = \Delta y$ over the grid, where Δx and Δy are the grid spacings in the x and y directions respectively. The map scale factors in WRF are given by m_x and m_y. They are defined as 'the ratio of the distance in computational space to the corresponding distance on the earth's surface' (Skamarock et al., 2008). As the inner domain in the model setup used here is 130 km by 130 km, and therefore small (and relatively near the equator), in the inner domain of the model setup used here m_x and m_y are both very close to 1 (they vary from 0.997 to 1.003).

The right hand side of Eqs. B.1-B.3 contain the terms arising from the model physics, curvature, Coriolis and mixing terms. In the setup here, in Eq. B.1 these are $F_U = F_{UCOR} + F_{UCURV} + F_{UHDIFF} + F_{UNDIFF} + F_{UVDIFF} + F_{URAY}$, where F_{UCOR} and F_{UCURV} represent the forcing from Coriolis and curvature respectively, F_{UHDIFF} and F_{UNDIFF} are the horizontal and numerical diffusion terms, and F_{UVDIFF} is the vertical diffusion (turbulent vertical mixing) term, which in this setup arises through parametrization in the boundary layer scheme. F_{URAY} represents the effects of Rayleigh damping, used to avoid reflection of waves off the top boundary. This damping only affects the stratosphere, so is ignored in the method used here. The F_V terms are the same as the F_U terms and the F_T terms are as follows $F_T = F_{THDIFF} + F_{TNDIFF} + F_{TVDIFF} + F_{TRAY} + F_{HDIABATIC} + F_{RAD}$. The first four terms are the horizontal, numerical and vertical diffusion and Rayleigh damping (ignored), as in the F_U equation. $F_{HDIABATIC}$ is a physics parametrization of the effects of latent heating from the microphysics scheme, and F_{RAD} is the radiation from the radiation parametrization. Lastly, Eqs. B.1-B.3 are written in perturbation form to reduce numerical errors.

B.1.1 Model discretization

The WRF model uses a third-order Runge-Kutta (RK3) to integrate the low-frequency modes using the model time step Δt. High-frequency acoustic modes require a smaller time step to maintain stability, so to improve model performance these modes are integrated using an acoustic time step. Using Eq. B.1 as an example and defining it as $\partial_t U = R(U)$, the RK3 advances from $U(t)$ to $U(t+\Delta t)$ as follows

$$U^* = U^t + \frac{\Delta t}{3} R(U^t) \tag{B.4}$$

$$U^{**} = U^t + \frac{\Delta t}{2} R(U^*) \tag{B.5}$$

$$U^{t+\Delta t} = U^t + \Delta t R(U^{**}) \tag{B.6}$$

The acoustic variables are written as perturbations from the most recent RK3 step variables. So defining U^{t^*} to represent either U^t, U^* or U^{**}, the acoustic variable is given by $U'' = U - U^{t^*}$. These variables are substituted into the governing equations and the resulting equations are solved on the smaller acoustic time-step ($\Delta t/3$). For full details see Skamarock et al. (2008) pg. 16.

B.2 Code and extraction

The dynamics in the WRF model are contained in the script `WRF>dyn_em>module_em.F`. Within this, the large time step changes are contained in the subroutine `rk_tendency`. This calls functions to add the effects of advection, pressure gradient, Coriolis, curvature and numerical diffusion to the tendency term. These variables were outputted by recording the tendency term before and after each function is called, and taking the difference to calculate the effect of each function at each time step. The horizontal diffusion term is outputted similarly from the subroutine `horizontal_diffusion_2` in the script `WRF>dyn_em>module_diffusion_em.F`. The acoustic term is similarly extracted from the script `WRF>solve_em.F`, where the `advance_uv` function adds the large-time step tendency to the small time step pressure gradient tendency. Lastly, the physics options (for turbulent vertical mixing in both the momentum and temperature budgets, and radiation in the temperature budget) are contained in the script `WRF>phys>module_physics_addtendc.F` in the subroutine `update_phy_ten`. The microphysics latent heating term in the temperature budget is already recorded in WRF, so just needs to be added to the registry to output it.

An example of the additions to record the Θ advection tendency is shown below:

```
  t_tend_old = t_tend                                    !!EP: added line to
record current t_tendency
  CALL advect_scalar ( t, t, t_tend, ru, rv, ww,      &
                       mut, time_step, config_flags, &
                       msfux, msfuy, msfvx, msfvy,    &
                       msftx, msfty, fnm, fnp,        &
                       rdx, rdy, rdnw,                &
                       ids, ide, jds, jde, kds, kde, &
```

```
                          ims, ime, jms, jme, kms, kme, &
                          its, ite, jts, jte, kts, kte )
  t_tend_adv = t_tend - t_tend_old              !!EP: added line for
t_adv
```

Where `t_tend_adv` is then output as the Θ advection term. All the altered model code was based on the instructions and code provided in Moisseeva (2014), and the temperature budget additions were based on the work in Lehner (2012). The complete model code needed to output the momentum and temperature budget terms can be found at https://github.com/Empott/WRF-momentum-and-temperature-budget-variables.

B.3 Checking the code changes

To check that the code edits have output the correct momentum budget terms, the momentum budget sums were checked at a few locations for every time step. There is an option in WRF to output a time series at a few chosen locations of certain variables at every time step and every vertical level for the run. The WRF code script `wrf_timeseries.F` is altered to include the new momentum terms (and also to only output timeseries for domain 4). The altered tslist code can be found at https://github.com/Empott/tslist_code.

B.3.1 Checking the U and V terms

The acceleration is approximated by $\frac{\partial u}{\partial t} = \frac{u_{t+1}-u_t}{\Delta t}$. The final terms outputted from WRF are the advection (`RU_TEND_ADV`), pressure gradient (`RU_TEND_PGF`), Coriolis (`RU_TEND_COR`), curvature (`RU_TEND_CURV`), horizontal diffusion (`RU_TEND_HDIFF`), numerical diffusion (`RU_TEND_6THDIFF`), physics contribution (`RU_TEND_PHYS`) and acoustic (`UTEND_SOUND`) terms (the acoustic term is added to the pressure gradient term in the analysis in Chapter 3). All the variables are coupled, meaning that they are divided by the mass of dry air in the column (`MUU`) to give an acceleration term. In addition, the term `UTEND_SOUND` is divided by Δt. These momentum budget terms are summed, and the result is compared to the calculated acceleration. An example (of 5000 time steps) of the results at Namche at the lowest model level and the 10^{th} model level is shown in Fig. B.1. This shows that for the momentum equations there is no error in the model output.

The terms in the V direction are calculated in an identical way to the terms in the U direction described above.

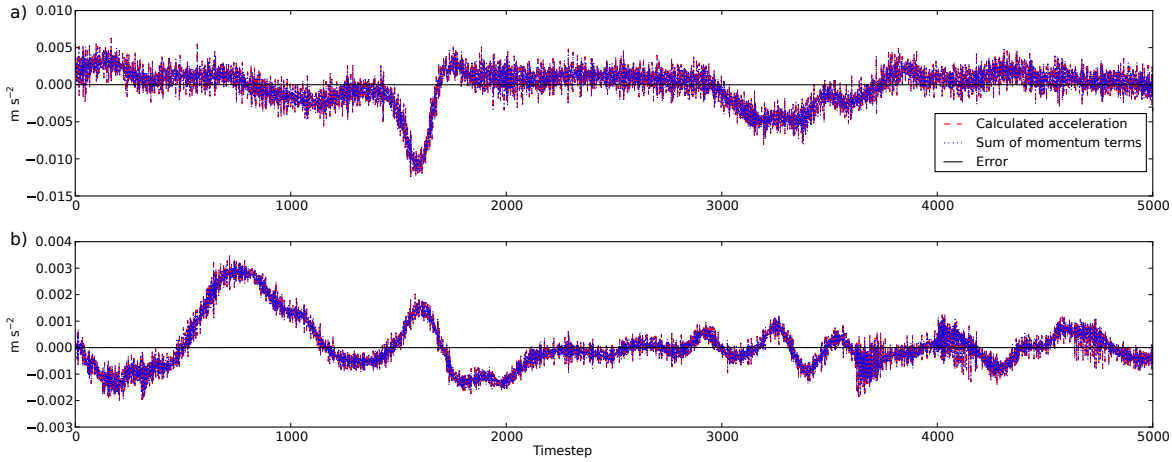

Fig. B.1 A 5000 time step sample from the time series for Namche in the July 2013 run at the lowest model level (a) and the 10th model level (b), demonstrating the error in the calculated zonal u acceleration and the sum of the momentum budget terms. The calculated acceleration is shown as a red dashed line, the sum of the terms in a blue dotted line and the error between the two as a black solid line.

B.3.2 Checking the Θ terms

The change in potential temperature is approximated by $\frac{\partial \theta}{\partial t} = \frac{\theta_{t+1} - \theta_t}{\Delta t}$. The final terms outputted from WRF are the advection (`T_TEND_ADV`), horizontal diffusion (`T_TEND_HDIFF`), numerical diffusion (`T_TEND_6THDIFF`), physics contribution from the boundary layer scheme (vertical mixing) (`T_TEND_PHYS_BL`), physics contribution from radiation (`T_TEND_PHYS_RAD`), latent heating (`H_DIABATIC`), and acoustic (`TTEND_SOUND`) terms. All the terms are coupled except for `H_DIABATIC`, and the term `TTEND_SOUND` must be divided by Δt. There is some error in the model output, but as can be seen in Fig. B.2, the error is very small compared to the change in Θ. These outputs have also been checked at Pheriche.

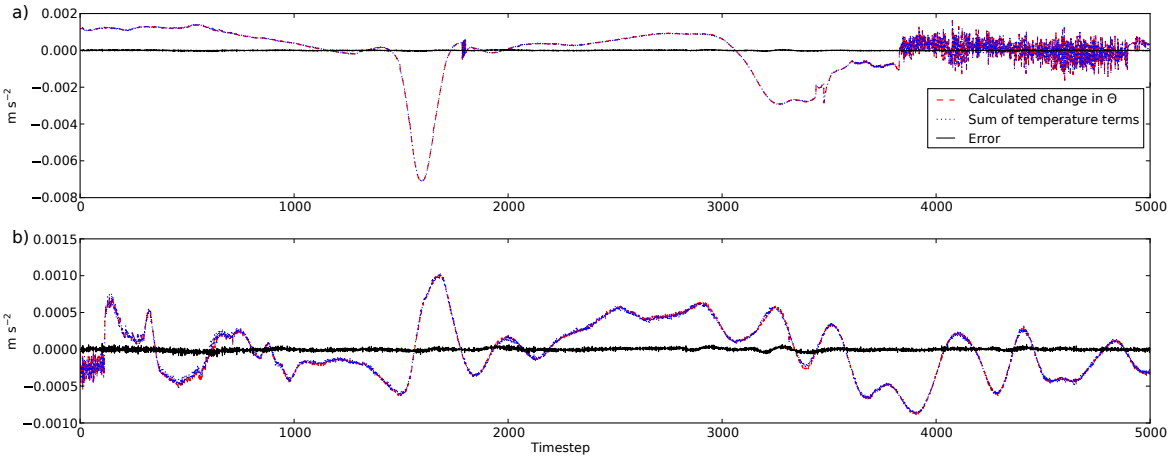

Fig. B.2 A 5000 time step sample from the time series for Namche in the July 2013 run at the lowest model level (a) and the 10th model level (b), demonstrating the error in the calculated change in potential temperature (θ) and the sum of the temperature budget terms. The calculated acceleration is shown as a red dashed line, the sum of the terms in a blue dotted line and the error between the two as a black solid line.

Appendix C

The altered LANDUSE.TBL, VEGPARM.TBL and MPTABLE.TBL tables.

C.1 The USGS section of the LANDUSE.TBL table is given below. Alterations are marked by !EP

```
!EP: Definitions and units are taken from
    http://diposit.ub.edu/dspace/bitstream/2445/105800/1/TFM_Bernat_Jimenez.pdf,
    http://www2.mmm.ucar.edu/mm5/documents/MM5_tut_Web_notes/TERRAIN/terrain.htm
    and http://mailman.ucar.edu/pipermail/wrf-users/2009/001098.html
!ALBD: surface albedo (%)
!SLMO: soil moisture availability (fraction 0 to 1)
!SFEM: surface emissivity (fraction 0 to 1)
!SFZ0: roughness length (cm)
!THERIN: thermal inertia (cal cm^(-2) K^(-1) s^-(1/2))
!SCFX: factor for albedo modificaiton with snow
!SFHC: surface heat capacity (J m^(-3) K^(-1))

USGS
33,2, 'ALBD    SLMO    SFEM    SFZ0 THERIN    SCFX    SFHC    '
SUMMER
1,      15.,    .10,    .88,    80.,     3.,   1.67, 18.9e5,'Urban and
    Built-Up Land'
2,      17.,    .30,   .985,    15.,     4.,   2.71, 25.0e5,'Dryland
    Cropland and Pasture'
3,      18.,    .50,   .985,    10.,     4.,   2.20, 25.0e5,'Irrigated
    Cropland and Pasture'
4,      18.,    .25,   .985,    15.,     4.,   2.56, 25.0e5,'Mixed
    Dryland/Irrigated Cropland and Pasture'
```

```
5,      18.,    .25,    .98,    14.,     4.,   2.56,
    25.0e5,'Cropland/Grassland Mosaic'
6,      16.,    .35,   .985,    20.,     4.,   3.19,
    25.0e5,'Cropland/Woodland Mosaic'
7,      19.,    .15,    .96,    12.,     3.,   2.37, 20.8e5,'Grassland'
8,      22.,    .10,    .93,     5.,     3.,   1.56, 20.8e5,'Shrubland'
9,      20.,    .15,    .95,     6.,     3.,   2.14, 20.8e5,'Mixed
    Shrubland/Grassland'
10,     20.,    .15,    .92,    15.,     3.,   2.00, 25.0e5,'Savanna'
11,     16.,    .30,    .93,    50.,     4.,   2.63, 25.0e5,'Deciduous
    Broadleaf Forest'
12,     14.,    .30,    .94,    50.,     4.,   2.86, 25.0e5,'Deciduous
    Needleleaf Forest'
13,     12.,    .50,    .95,    50.,     5.,   1.67, 29.2e5,'Evergreen
    Broadleaf Forest'
14,     12.,    .30,    .95,    50.,     4.,   3.33, 29.2e5,'Evergreen
    Needleleaf Forest'
15,     13.,    .30,    .97,    50.,     4.,   2.11, 41.8e5,'Mixed Forest'
16,      8.,    1.0,    .98,    0.01,    6.,     0., 9.0e25,'Water Bodies'
17,     14.,    .60,    .95,    20.,     6.,   1.50, 29.2e5,'Herbaceous
    Wetland'
18,     14.,    .35,    .95,    40.,     5.,   1.14, 41.8e5,'Wooded Wetland'
19,     25.,    .02,    .90,     1.,     2.,   0.81, 12.0e5,'Barren or
    Sparsely Vegetated'
20,     20.,    .02,    .95,     2.,     3.,    1.6,  8.1e5,'Debris Cover'
    !EP
21,     15.,    .50,    .93,    30.,     5.,   2.67, 9.0e25,'Wooded Tundra'
22,     15.,    .50,    .92,    15.,     5.,   2.67, 9.0e25,'Mixed Tundra'
23,     25.,    .02,    .90,    10.,     2.,   1.60, 12.0e5,'Bare Ground
    Tundra'
24,     55.,    .95,    .95,    0.1,     5.,     0., 9.0e25,'Snow or Ice'
25,     30.,    .40,    .90,     1.,     5.,    .62, 12.0E5,'Playa'
26,     18.,    .50,    .95,    15.,     6.,    .62, 12.0E5,'Lava'
27,     70.,    .40,    .90,     1.,     5.,     0., 12.0E5,'White Sand'
28,     15.,    .50,    .92,    10.,     5.,   2.87, 9.0e25,'Herbaceous
    Tundra'
29,     15.,    .02,    .88,    80.,     3.,   1.67, 18.9e5,'Unassigned'
30,     15.,    .10,    .88,    80.,     3.,   1.67, 18.9e5,'Unassigned'
31,     10.,    .10,    .97,    80.,     3.,   1.67, 18.9e5,'Low Intensity
    Residential '
32,     10.,    .10,    .97,    80.,     3.,   1.67, 18.9e5,'High Intensity
    Residential'
33,     10.,    .10,    .97,    80.,     3.,   1.67, 18.9e5,'Industrial or
    Commercial'
WINTER
1,      15.,    .10,    .88,    80.,     3.,   1.67, 18.9e5,'Urban and
    Built-Up Land'
2,      20.,    .60,    .92,     5.,     4.,   2.00, 25.0e5,'Dryland
    Cropland and Pasture'
3,      20.,    .50,    .93,     2.,     4.,   1.76, 25.0e5,'Irrigated
    Cropland and Pasture'
```

```
4,      20.,    .50,    .92,     5.,     4.,  2.00, 25.0e5,'Mixed
    Dryland/Irrigated Cropland and Pasture'
5,      20.,    .40,    .92,     5.,     4.,  2.00,
    25.0e5,'Cropland/Grassland Mosaic'
6,      20.,    .60,    .93,    20.,     4.,  2.00,
    25.0e5,'Cropland/Woodland Mosaic'
7,      23.,    .30,    .92,    10.,     4.,  2.00, 20.8e5,'Grassland'
8,      22.,    .20,    .93,     1.,     4.,  1.30, 20.8e5,'Shrubland'
9,      22.,    .25,    .93,     1.,     4.,  1.24, 20.8e5,'Mixed
    Shrubland/Grassland'
10,     20.,    .15,    .92,    15.,     3.,  2.00, 25.0e5,'Savanna'
11,     17.,    .60,    .93,    50.,     5.,  2.40, 25.0e5,'Deciduous
    Broadleaf Forest'
12,     15.,    .60,    .93,    50.,     5.,  2.60, 25.0e5,'Deciduous
    Needleleaf Forest'
13,     12.,    .50,    .95,    50.,     5.,  1.67, 29.2e5,'Evergreen
    Broadleaf Forest'
14,     12.,    .60,    .95,    50.,     5.,  3.00, 29.2e5,'Evergreen
    Needleleaf Forest'
15,     14.,    .60,    .93,    20.,     6.,  1.12, 41.8e5,'Mixed Forest'
16,      8.,    1.0,    .98,    0.01,    6.,    0., 9.0e25,'Water Bodies'
17,     14.,    .75,    .95,    20.,     6.,  1.50, 29.2e5,'Herbaceous
    Wetland'
18,     14.,    .70,    .95,    40.,     6.,  1.14, 41.8e5,'Wooded Wetland'
19,     23.,    .05,    .90,     1.,     2.,  0.81, 12.0e5,'Barren or
    Sparsely Vegetated'
20,     20.,    .02,    .95,     2.,     3.,   1.6,  8.135,'Debris Cover'
    !EP
21,     15.,    .60,    .93,    30.,     5.,  1.75, 9.0e25,'Wooded Tundra'
22,     15.,    .60,    .92,    15.,     5.,  1.75, 9.0e25,'Mixed Tundra'
23,     25.,    .05,    .90,     5.,     5.,  1.80, 12.0e5,'Bare Ground
    Tundra'
24,     70.,    .95,    .95,    0.1,     5.,    0., 9.0e25,'Snow or Ice'
25,     40.,    .40,    .90,     1.,     5.,   .62, 12.0E5,'Playa'
26,     18.,    .40,    .95,    15.,     5.,   .62, 12.0E5,'Lava'
27,     70.,    .40,    .90,     1.,     5.,    0., 12.0E5,'White Sand'
28,     15.,    .60,    .92,    10.,     5.,  2.00, 9.0e25,'Herbaceous
    Tundra'
29,     15.,    .02,    .88,    80.,     3.,  1.67, 18.9e5,'Unassigned'
30,     15.,    .10,    .88,    80.,     3.,  1.67, 18.9e5,'Unassigned'
31,     10.,    .10,    .97,    80.,     3.,  1.67, 18.9e5,'Low Intensity
    Residential '
32,     10.,    .10,    .97,    80.,     3.,  1.67, 18.9e5,'High Intensity
    Residential'
33,     10.,    .10,    .97,    80.,     3.,  1.67, 18.9e5,'Industrial or
    Commercial'
```

C.2 The USGS section of the VEGPARM.TBL table is given below. Alterations are marked by !EP

```
!EP: definitions taken from the wrf code in
   WRF3.8>phys>module_sf_noahmplsm.F,
!and https://ral.ucar.edu/sites/default/files/public/product-tool/noah-
   multiparameterization-land-surface-model-noah-mp-lsm/vegparm.html
!SHDFAC: green vegetation fraction (0.0-1.0)
!NROOT: number of soil layers with root present
!RS: leaf stomatal resistance (s/m)
!RGL: Parameter used in radiation stress function
!HS: Parameter used in vapor pressure deficit function
!SNUP: Threshold water-equivalent snow depth (m) that implies 100% snow
   cover
!MAXALB: Upper bound on maximum albedo over deep snow (%)
!LAIMIN/LAIMAX: minumum/maximum leaf area index through the year (m2/m2)
!EMISSMIN/EMISSMAX: minumum/maximum background emissivity through the
   year fraction (0.0 to 1.0)
!ALBEDOMIN/ALBEDOMAX: minumum/maximum background albedo through the
   year fraction (0.0 to 1.0)
!Z0MIN/Z0MAX: minumum/maximum background roughness length through the
   year (m)
!ZTOPV/ZBOTV: height of canopy top/bottom

Vegetation Parameters
USGS
27,1, 'SHDFAC NROOT   RS      RGL      HS      SNUP  MAXALB   LAIMIN
   LAIMAX  EMISSMIN EMISSMAX ALBEDOMIN ALBEDOMAX  Z0MIN     Z0MAX
   ZTOPV    ZBOTV'
1,     .10,   1,    200.,   999.,   999.0,   0.04,   46.,     1.00,
   1.00,   .880,    .880,     .15,      .15,      .50,     .50,
   0.00,    0.00,    'Urban and Built-Up Land'
2,     .80,   3,     40.,   100.,   36.25,   0.04,   66.,     1.56,
   5.68,   .920,    .985,     .17,      .23,      .05,     .15,
   0.50,    0.01,    'Dryland Cropland and Pasture'
3,     .80,   3,     40.,   100.,   36.25,   0.04,   66.,     1.56,
   5.68,   .930,    .985,     .20,      .25,      .02,     .10,
   0.50,    0.01,    'Irrigated Cropland and Pasture'
4,     .80,   3,     40.,   100.,   36.25,   0.04,   66.,     1.00,
   4.50,   .920,    .985,     .18,      .23,      .05,     .15,
   0.50,    0.01,    'Mixed Dryland/Irrigated Cropland and Pasture'
5,     .80,   3,     40.,   100.,   36.25,   0.04,   68.,     2.29,
   4.29,   .920,    .980,     .18,      .23,      .05,     .14,
   0.50,    0.01,    'Cropland/Grassland Mosaic'
6,     .80,   3,     70.,    65.,   44.14,   0.04,   60.,     2.00,
   4.00,   .930,    .985,     .16,      .20,      .20,     .20,
   0.50,    0.01,    'Cropland/Woodland Mosaic'
7,     .80,   3,     40.,   100.,   36.35,   0.04,   70.,     0.52,
   2.90,   .920,    .960,     .19,      .23,      .10,     .12,
   0.50,    0.01,    'Grassland'
```

```
8,      .70,   3,    300.,   100.,   42.00,   0.03,    60.,    0.50,
    3.66,   .930,    .930,     .25,      .30,      .01,     .05,
    0.50,    0.10,    'Shrubland'
9,      .70,   3,    170.,   100.,   39.18,  0.035,    65.,    0.60,
    2.60,   .930,    .950,     .22,      .30,      .01,     .06,
    0.50,    0.10,    'Mixed Shrubland/Grassland'
10,     .50,   3,     70.,    65.,   54.53,   0.04,    50.,    0.50,
    3.66,   .920,    .920,     .20,      .20,      .15,     .15,
    5.00,    0.10,    'Savanna'
11,     .80,   4,    100.,    30.,   54.53,   0.08,    58.,    1.85,
    3.31,   .930,    .930,     .16,      .17,      .50,     .50,
    20.0,    11.5,    'Deciduous Broadleaf Forest'
12,     .70,   4,    150.,    30.,   47.35,   0.08,    54.,    1.00,
    5.16,   .930,    .940,     .14,      .15,      .50,     .50,
    14.0,     7.0,    'Deciduous Needleleaf Forest'
13,     .95,   4,    150.,    30.,   41.69,   0.08,    35.,    3.08,
    6.48,   .950,    .950,     .12,      .12,      .50,     .50,
    35.0,     1.0,    'Evergreen Broadleaf Forest'
14,     .70,   4,    125.,    30.,   47.35,   0.08,    52.,    5.00,
    6.40,   .950,    .950,     .12,      .12,      .50,     .50,
    17.0,     8.5,    'Evergreen Needleleaf Forest'
15,     .80,   4,    125.,    30.,   51.93,   0.08,    53.,    2.80,
    5.50,   .930,    .970,     .17,      .25,      .20,     .50,
    18.0,    10.0,    'Mixed Forest'
16,     .00,   0,    100.,    30.,   51.75,   0.01,    70.,    0.01,
    0.01,   .980,    .980,     .08,      .08,    0.0001,  0.0001,
    0.00,    0.00,    'Water Bodies'
17,     .60,   2,     40.,   100.,   60.00,   0.01,    68.,    1.50,
    5.65,   .950,    .950,     .14,      .14,      .20,     .20,
    0.50,    0.01,    'Herbaceous Wetland'
18,     .60,   2,    100.,    30.,   51.93,   0.02,    50.,    2.00,
    5.80,   .950,    .950,     .14,      .14,      .40,     .40,
    20.0,    11.5,    'Wooded Wetland'
19,     .01,   1,    999.,   999.,   999.0,   0.02,    75.,    0.10,
    0.75,   .900,    .900,     .38,      .38,      .01,     .01,
    0.02,    0.01,    'Barren or Sparsely Vegetated'
20,     .00,   1,    999.,   999.,   999.0,   0.03,    70.,    0.01,
    0.01,   .950,    .950,     .2,       .2,       .02,     .02,
    0.00,    0.00,    'Debris Cover' !EP
21,     .60,   3,    150.,   100.,   42.00,  0.025,    55.,    0.41,
    3.35,   .930,    .930,     .15,      .20,      .30,     .30,
    10.0,    0.10,    'Wooded Tundra'
22,     .60,   3,    150.,   100.,   42.00,  0.025,    60.,    0.41,
    3.35,   .920,    .920,     .15,      .20,      .15,     .15,
    5.00,    0.10,    'Mixed Tundra'
23,     .30,   2,    200.,   100.,   42.00,   0.02,    75.,    0.41,
    3.35,   .900,    .900,     .25,      .25,      .05,     .10,
    0.02,    0.01,    'Bare Ground Tundra'
24,     .00,   1,    999.,   999.,   999.0,   0.02,    82.,    0.01,
    0.01,   .950,    .950,     .55,      .70,     0.001,   0.001,
    0.00,    0.00,    'Snow or Ice'
```

```
25,      .50,    1,      40.,    100.,    36.25,    0.02,     75.,      0.01,
    0.01,    .890,     .890,      .30,       .30,       .01,      .01,
    0.00,     0.00,      'Playa'
26,      .00,    0,     999.,    999.,    999.0,    0.02,     75.,      0.01,
    0.01,    .880,     .880,      .16,       .16,       .15,      .15,
    0.00,     0.00,      'Lava'
27,      .00,    0,     999.,    999.,    999.0,    0.02,     75.,      0.01,
    0.01,    .830,     .830,      .60,       .60,       .01,      .01,
    0.00,     0.00,      'White Sand'

TOPT_DATA
 298.0
CMCMAX_DATA
 0.5E-3
CFACTR_DATA
 0.5
RSMAX_DATA
 5000.0
BARE
 19
NATURAL
 5
CROP
 3
LOW_DENSITY_RESIDENTIAL
 31
HIGH_DENSITY_RESIDENTIAL
 32
HIGH_INTENSITY_INDUSTRIAL
 33
```

C.3 The USGS section of the MPTABLE.TBL table is given below. Alterations (columns) are marked by !EP

```
! EP: definitions can be found at
    http://www.rap.ucar.edu/~barlage/Noah-MP/documentation/MPTABLE.html
&noahmp_usgs_veg_categories
 VEG_DATASET_DESCRIPTION = "USGS"
 NVEG = 27
/
&noahmp_usgs_parameters
 ! NVEG = 27
 !  1: Urban and Built-Up Land
 !  2: Dryland Cropland and Pasture
 !  3: Irrigated Cropland and Pasture
 !  4: Mixed Dryland/Irrigated Cropland and Pasture
 !  5: Cropland/Grassland Mosaic
 !  6: Cropland/Woodland Mosaic
 !  7: Grassland
 !  8: Shrubland
 !  9: Mixed Shrubland/Grassland
 ! 10: Savanna
 ! 11: Deciduous Broadleaf Forest
 ! 12: Deciduous Needleleaf Forest
 ! 13: Evergreen Broadleaf Forest
 ! 14: Evergreen Needleleaf Forest
 ! 15: Mixed Forest
 ! 16: Water Bodies
 ! 17: Herbaceous Wetland
 ! 18: Wooded Wetland
 ! 19: Barren or Sparsely Vegetated
 ! 20: Debris cover !EP
 ! 21: Wooded Tundra
 ! 22: Mixed Tundra
 ! 23: Bare Ground Tundra
 ! 24: Snow or Ice
 ! 25: Playa
 ! 26: Lava
 ! 27: White Sand


 ISURBAN                       =  1
 ISWATER                       = 16
 ISBARREN                      = 19
 ISICE                         = 24
 EBLFOREST                     = 13
 LOW_DENSITY_RESIDENTIAL       = 31
 HIGH_DENSITY_RESIDENTIAL      = 32
 HIGH_INTENSITY_INDUSTRIAL     = 33
```

```
!------------------------------------------------------------------------------
!             1       2       3       4       5       6       7       8       9
      10      11      12      13      14      15      16      17      18      19
      20  !EP  21      22      23      24      25      26      27

   !------------------------------------------------------------------------------
CH2OP =   0.1,    0.1,    0.1,    0.1,    0.1,    0.1,    0.1,    0.1,    0.1,
     0.1,    0.1,    0.1,    0.1,    0.1,    0.1,    0.1,    0.1,    0.1,
   0.1,    0.1,    0.1,    0.1,    0.1,    0.1,    0.1,    0.1,    0.1,
DLEAF =   0.04,   0.04,   0.04,   0.04,   0.04,   0.04,   0.04,   0.04,   0.04,
    0.04,   0.04,   0.04,   0.04,   0.04,   0.04,   0.04,   0.04,   0.04,
   0.04,   0.04,   0.04,   0.04,   0.04,   0.04,   0.04,   0.04,   0.04,
Z0MVT =   1.00,   0.15,   0.15,   0.15,   0.14,   0.50,   0.12,   0.06,   0.09,
    0.50,   0.80,   0.85,   1.10,   1.09,   0.80,   0.00,   0.12,   0.50,
   0.00,   0.00,   0.30,   0.20,   0.03,   0.00,   0.01,   0.00,   0.00,
HVT    =  15.0,   2.00,   2.00,   2.00,   1.50,   8.00,   1.00,   1.10,   1.10,
    10.0,   16.0,   18.0,   20.0,   20.0,   16.0,   0.00,   0.50,   10.0,
   0.00,   0.00,   4.00,   2.00,   0.50,   0.00,   0.10,   0.00,   0.00,
HVB    =  1.00,   0.10,   0.10,   0.10,   0.10,   0.15,   0.05,   0.10,   0.10,
    0.10,   11.5,   7.00,   8.00,   8.50,   10.0,   0.00,   0.05,   0.10,
   0.00,   0.00,   0.10,   0.10,   0.10,   0.00,   0.10,   0.00,   0.00,
DEN    =  0.01,   25.0,   25.0,   25.0,   25.0,   25.0,   100.,   10.0,   10.0,
    0.02,   0.10,   0.28,   0.02,   0.28,   0.10,   0.01,   10.0,   0.10,
   0.01,   0.00,   1.00,   1.00,   1.00,   0.00,   0.01,   0.01,   0.01,
RC     =  1.00,   0.08,   0.08,   0.08,   0.08,   0.08,   0.03,   0.12,   0.12,
    3.00,   1.40,   1.20,   3.60,   1.20,   1.40,   0.01,   0.10,   1.40,
   0.01,   0.00,   0.30,   0.30,   0.30,   0.00,   0.01,   0.01,   0.01,
MFSNO =   2.50,   2.50,   2.50,   2.50,   2.50,   2.50,   2.50,   2.50,   2.50,
    2.50,   2.50,   2.50,   2.50,   2.50,   2.50,   2.50,   2.50,   2.50,
   2.50,   2.50,   2.50,   2.50,   2.50,   2.50,   2.50,   2.50,   2.50,

! Row 1:  Vis
! Row 2:  Near IR
RHOL_VIS=0.00,   0.11,   0.11,   0.11,   0.11,   0.11,   0.11,   0.07,   0.10,
    0.10,   0.10,   0.07,   0.10,   0.07,   0.10,   0.00,   0.11,   0.10,
   0.00,   0.00,   0.10,   0.10,   0.10,   0.00,   0.10,   0.00,   0.00,
RHOL_NIR=0.00,   0.58,   0.58,   0.58,   0.58,   0.58,   0.58,   0.35,   0.45,
    0.45,   0.45,   0.35,   0.45,   0.35,   0.45,   0.00,   0.58,   0.45,
   0.00,   0.00,   0.45,   0.45,   0.45,   0.00,   0.45,   0.00,   0.00,

! Row 1:  Vis
! Row 2:  Near IR
RHOS_VIS=0.00,   0.36,   0.36,   0.36,   0.36,   0.36,   0.36,   0.16,   0.16,
    0.16,   0.16,   0.16,   0.16,   0.16,   0.16,   0.00,   0.36,   0.16,
   0.00,   0.00,   0.16,   0.16,   0.16,   0.00,   0.16,   0.00,   0.00,
RHOS_NIR=0.00,   0.58,   0.58,   0.58,   0.58,   0.58,   0.58,   0.39,   0.39,
    0.39,   0.39,   0.39,   0.39,   0.39,   0.39,   0.00,   0.58,   0.39,
   0.00,   0.00,   0.39,   0.39,   0.39,   0.00,   0.39,   0.00,   0.00,

! Row 1:  Vis
! Row 2:  Near IR
```

```
 TAUL_VIS=0.00,  0.07,  0.07,  0.07,  0.07,  0.07,  0.07,  0.05,  0.05,
     0.05,  0.05,  0.05,  0.05,  0.05,  0.05,  0.00,  0.07,  0.05,
    0.00,  0.00,  0.00,  0.05,  0.05,  0.00,  0.05,  0.00,  0.00,
 TAUL_NIR=0.00,  0.25,  0.25,  0.25,  0.25,  0.25,  0.25,  0.10,  0.10,
     0.25,  0.25,  0.10,  0.25,  0.10,  0.25,  0.00,  0.25,  0.25,
    0.00,  0.00,  0.00,  0.25,  0.25,  0.00,  0.25,  0.00,  0.00,

 ! Row 1:  Vis
 ! Row 2:  Near IRv
 TAUS_VIS=0.00, 0.220, 0.220, 0.220, 0.220, 0.220, 0.220, 0.001, 0.001,
    0.001, 0.001, 0.001, 0.001, 0.001, 0.001, 0.000, 0.220, 0.001,
    0.000, 0.000, 0.001, 0.001, 0.001, 0.000, 0.001, 0.000, 0.000,
 TAUS_NIR=0.00, 0.380, 0.380, 0.380, 0.380, 0.380, 0.380, 0.001, 0.001,
    0.001, 0.001, 0.001, 0.001, 0.001, 0.001, 0.000, 0.380, 0.001,
    0.000, 0.000, 0.001, 0.001, 0.001, 0.000, 0.001, 0.000, 0.000,

 XL     = 0.000, -0.30, -0.30, -0.30, -0.30, -0.30, -0.30, 0.010, 0.250,
    0.010, 0.250, 0.010, 0.010, 0.010, 0.250, 0.000, -0.30, 0.250,
    0.000, 0.000, 0.250, 0.250, 0.250, 0.000, 0.250, 0.000, 0.000,
! CWPVT =   3.0,   3.0,   3.0,   3.0,   3.0,   3.0,   3.0,   3.0,
    3.0,   3.0,   3.0,   3.0,   3.0,   3.0,   3.0,   3.0,   3.0,   3.0,
    3.0,   3.0,   3.0,   3.0,   3.0,   3.0,   3.0,   3.0,   3.0,
 CWPVT =  0.18,   0.18,   0.18,   0.18,   0.18,   0.18,   0.18,   0.18,
      0.18,   0.18,   0.18,   0.18,   0.18,   0.18,   0.18,   0.18,
    0.18,  0.18,  0.18,  0.18,  0.18,  0.18,  0.18,  0.18,  0.18,
 C3PSN =   1.0,   1.0,   1.0,   1.0,   1.0,   1.0,   1.0,   1.0,   1.0,
      1.0,   1.0,   1.0,   1.0,   1.0,   1.0,   1.0,   1.0,   1.0,
    1.0,   1.0,   1.0,   1.0,   1.0,   1.0,   1.0,   1.0,   1.0,
 KC25 =  30.0,  30.0,  30.0,  30.0,  30.0,  30.0,  30.0,  30.0,  30.0,
     30.0,  30.0,  30.0,  30.0,  30.0,  30.0,  30.0,  30.0,  30.0,
    30.0,  30.0,  30.0,  30.0,  30.0,  30.0,  30.0,  30.0,  30.0,
 AKC    =  2.1,   2.1,   2.1,   2.1,   2.1,   2.1,   2.1,   2.1,   2.1,
      2.1,   2.1,   2.1,   2.1,   2.1,   2.1,   2.1,   2.1,   2.1,
    2.1,   2.1,   2.1,   2.1,   2.1,   2.1,   2.1,   2.1,   2.1,
 KO25 =  3.E4,  3.E4,  3.E4,  3.E4,  3.E4,  3.E4,  3.E4,  3.E4,  3.E4,
     3.E4,  3.E4,  3.E4,  3.E4,  3.E4,  3.E4,  3.E4,  3.E4,  3.E4,
    3.E4,  3.E4,  3.E4,  3.E4,  3.E4,  3.E4,  3.E4,  3.E4,  3.E4,
 AKO    =  1.2,   1.2,   1.2,   1.2,   1.2,   1.2,   1.2,   1.2,   1.2,
      1.2,   1.2,   1.2,   1.2,   1.2,   1.2,   1.2,   1.2,   1.2,
    1.2,   1.2,   1.2,   1.2,   1.2,   1.2,   1.2,   1.2,   1.2,
 AVCMX =  2.4,   2.4,   2.4,   2.4,   2.4,   2.4,   2.4,   2.4,   2.4,
      2.4,   2.4,   2.4,   2.4,   2.4,   2.4,   2.4,   2.4,   2.4,
    2.4,   2.4,   2.4,   2.4,   2.4,   2.4,   2.4,   2.4,   2.4,
 AQE    =  1.0,   1.0,   1.0,   1.0,   1.0,   1.0,   1.0,   1.0,   1.0,
      1.0,   1.0,   1.0,   1.0,   1.0,   1.0,   1.0,   1.0,   1.0,
    1.0,   1.0,   1.0,   1.0,   1.0,   1.0,   1.0,   1.0,   1.0,

 LTOVRC=   0.0,   1.2,   1.2,   1.2,   1.2,  1.30,  0.50,  0.65,  0.70,
     0.65,  0.55,   0.2,  0.55,   0.5,   0.5,   0.0,   1.4,   1.4,
    0.0,   0.0,   1.3,   1.4,   1.0,   0.0,   1.0,   0.0,   0.0,
```

```
DILEFC=  0.00,  0.50,  0.50,  0.50,  0.35,  0.20,  0.20,  0.20,  0.50,
    0.50,  0.60,  1.80,  0.50,  1.20,  0.80,  0.00,  0.40,  0.40,
   0.00,  0.00,  0.30,  0.40,  0.30,  0.00,  0.30,  0.00,  0.00,
DILEFW=  0.00,  0.20,  0.20,  0.20,  0.20,  0.20,  0.10,  0.20,  0.20,
    0.50,  0.20,  0.20,  4.00,  0.20,  0.20,  0.00,  0.20,  0.20,
   0.00,  0.00,  0.20,  0.20,  0.20,  0.00,  0.20,  0.00,  0.00,
RMF25 =  0.00,  1.00,  1.40,  1.45,  1.45,  1.45,  1.80,  0.26,  0.26,
    0.80,  3.00,  4.00,  0.65,  3.00,  3.00,  0.00,  3.20,  3.20,
   0.00,  0.00,  3.00,  3.00,  3.00,  0.00,  3.00,  0.00,  0.00,
SLA   =    60,    80,    80,    80,    80,    80,    60,    60,    60,
     50,    80,    80,    80,    80,    80,     0,    80,    80,
    0,     0,    80,    80,    80,     0,    80,     0,     0,
FRAGR =  0.00,  0.20,  0.20,  0.20,  0.20,  0.20,  0.20,  0.20,  0.20,
    0.20,  0.20,  0.10,  0.20,  0.10,  0.10,  0.00,  0.10,  0.10,
   0.10,  0.00,  0.10,  0.10,  0.10,  0.00,  0.10,  0.00,  0.00,
TMIN  =     0,   273,   273,   273,   273,   273,   273,   273,   273,
    273,   273,   268,   273,   265,   268,     0,   268,   268,
    0,     0,   268,   268,   268,     0,   268,     0,     0,
VCMX25=  0.00,  80.0,  80.0,  80.0,  60.0,  70.0,  40.0,  40.0,  40.0,
    40.0,  60.0,  60.0,  60.0,  50.0,  55.0,  0.00,  50.0,  50.0,
   0.00,  0.00,  50.0,  50.0,  50.0,  0.00,  50.0,  0.00,  0.00,
TDLEF =   278,   278,   278,   278,   278,   278,   278,   278,   278,
    278,   278,   268,   278,   278,   268,     0,   268,   268,
    0,     0,   268,   268,   268,     0,   268,     0,     0,
BP    = 1.E15,  2.E3,  2.E3,  2.E3,  2.E3,  2.E3,  2.E3,  2.E3,  2.E3,
    2.E3,  2.E3,  2.E3,  2.E3,  2.E3,  2.E3, 1.E15,  2.E3,  2.E3,
   2.E3, 1.E15,  2.E3,  2.E3,  2.E3, 1.E15,  2.E3, 1.E15, 1.E15,
MP    =    9.,    9.,    9.,    9.,    9.,    9.,    9.,    9.,    9.,
     9.,    9.,    6.,    9.,    6.,    9.,    9.,    9.,    9.,
    9.,    9.,    9.,    9.,    9.,    9.,    9.,    9.,    9.,
QE25  =    0.,  0.06,  0.06,  0.06,  0.06,  0.06,  0.06,  0.06,  0.06,
    0.06,  0.06,  0.06,  0.06,  0.06,  0.06,  0.00,  0.06,  0.06,
   0.06,  0.00,  0.06,  0.06,  0.06,  0.00,  0.06,  0.00,  0.00,
RMS25 =  0.00,  0.10,  0.10,  0.10,  0.10,  0.10,  0.10,  0.10,  0.10,
    0.32,  0.10,  0.64,  0.30,  0.90,  0.80,  0.00,  0.10,  0.10,
   0.00,  0.00,  0.10,  0.10,  0.00,  0.00,  0.00,  0.00,  0.00,
RMR25 =  0.00,  0.00,  0.00,  0.00,  0.00,  0.00,  1.20,  0.00,  0.00,
    0.01,  0.01,  0.05,  0.05,  0.36,  0.03,  0.00,  0.00,  0.00,
   0.00,  0.00,  2.11,  2.11,  0.00,  0.00,  0.00,  0.00,  0.00,
ARM   =    2.0,   2.0,   2.0,   2.0,   2.0,   2.0,   2.0,   2.0,   2.0,
     2.0,   2.0,   2.0,   2.0,   2.0,   2.0,   2.0,   2.0,   2.0,
    2.0,   2.0,   2.0,   2.0,   2.0,   2.0,   2.0,   2.0,   2.0,
FOLNMX=  0.00,   1.5,   1.5,   1.5,   1.5,   1.5,   1.5,   1.5,   1.5,
     1.5,   1.5,   1.5,   1.5,   1.5,   1.5,  0.00,   1.5,   1.5,
    1.5,  0.00,   1.5,   1.5,   1.5,  0.00,   1.5,  0.00,  0.00,
WDPOOL=  0.00,  0.00,  0.00,  0.00,  0.00,  0.00,  0.00,  1.00,  1.00,
    1.00,  1.00,  1.00,  1.00,  1.00,  1.00,  0.00,  0.00,  1.00,
   0.00,  0.00,  1.00,  1.00,  0.00,  0.00,  0.00,  0.00,  0.00,
WRRAT =  0.00,  0.00,  0.00,  0.00,  0.00,  0.00,  0.00,  3.00,  3.00,
    3.00,  30.0,  30.0,  30.0,  30.0,  30.0,  0.00,  0.00,  30.0,
   0.00,  0.00,  3.00,  3.00,  0.00,  0.00,  0.00,  0.00,  0.00,
```

```
MRP   = 0.00,  0.23,  0.23,  0.23,  0.23,  0.23,  0.17,  0.19,  0.19,
    0.40,  0.40,  0.37,  0.23,  0.37,  0.30,  0.00,  0.17,  0.40,
   0.00,  0.00,  0.23,  0.20,  0.00,  0.00,  0.20,  0.00,  0.00,
NROOT =     1,     3,     3,     3,     3,     3,     3,     3,     3,
       3,     4,     4,     4,     4,     4,     0,     2,     2,
   1,     1,     3,     3,     2,     1,     1,     0,     0,
RGL   = 999.0, 100.0, 100.0, 100.0, 100.0,  65.0, 100.0, 100.0, 100.0,
    65.0,  30.0,  30.0,  30.0,  30.0,  30.0,  30.0, 100.0,  30.0,
   999.0, 999.0, 100.0, 100.0, 100.0, 999.0, 100.0, 999.0, 999.0,
RS    = 200.0,  40.0,  40.0,  40.0,  40.0,  70.0,  40.0, 300.0, 170.0,
    70.0, 100.0, 150.0, 150.0, 125.0, 125.0, 100.0,  40.0, 100.0,
   999.0, 999.0, 150.0, 150.0, 200.0, 999.0,  40.0, 999.0, 999.0,
HS    = 999.0, 36.25, 36.25, 36.25, 36.25, 44.14, 36.35, 42.00, 39.18,
   54.53, 54.53, 47.35, 41.69, 47.35, 51.93, 51.75, 60.00, 51.93,
   999.0, 999.0, 42.00, 42.00, 42.00, 999.0, 36.25, 999.0, 999.0,
TOPT  = 298.0, 298.0, 298.0, 298.0, 298.0, 298.0, 298.0, 298.0, 298.0,
   298.0, 298.0, 298.0, 298.0, 298.0, 298.0, 298.0, 298.0, 298.0,
   298.0, 298.0, 298.0, 298.0, 298.0, 298.0, 298.0, 298.0, 298.0,
RSMAX = 5000., 5000., 5000., 5000., 5000., 5000., 5000., 5000., 5000.,
   5000., 5000., 5000., 5000., 5000., 5000., 5000., 5000., 5000.,
   5000., 5000., 5000., 5000., 5000., 5000., 5000., 5000., 5000.,

SAI_FEB = 0.0,   0.3,   0.3,   0.3,   0.3,   0.3,   0.3,   0.2,   0.2,
     0.3,   0.4,   0.3,   0.5,   0.4,   0.4,   0.0,   0.2,   0.3,
   0.0,   0.0,   0.2,   0.1,   0.0,   0.0,   0.0,   0.0,   0.0,
SAI_MAR = 0.0,   0.3,   0.3,   0.3,   0.3,   0.3,   0.3,   0.2,   0.2,
     0.3,   0.4,   0.3,   0.5,   0.4,   0.4,   0.0,   0.2,   0.3,
   0.0,   0.0,   0.2,   0.1,   0.0,   0.0,   0.0,   0.0,   0.0,
SAI_APR = 0.0,   0.3,   0.3,   0.3,   0.3,   0.3,   0.3,   0.2,   0.2,
     0.3,   0.4,   0.4,   0.5,   0.3,   0.4,   0.0,   0.2,   0.3,
   0.0,   0.0,   0.2,   0.1,   0.0,   0.0,   0.0,   0.0,   0.0,
SAI_MAY = 0.0,   0.2,   0.2,   0.2,   0.3,   0.3,   0.3,   0.2,   0.2,
     0.3,   0.4,   0.4,   0.5,   0.4,   0.4,   0.0,   0.3,   0.3,
   0.0,   0.0,   0.2,   0.1,   0.0,   0.0,   0.0,   0.0,   0.0,
SAI_JUN = 0.0,   0.3,   0.3,   0.3,   0.4,   0.4,   0.4,   0.2,   0.3,
     0.4,   0.4,   0.7,   0.5,   0.5,   0.4,   0.0,   0.4,   0.4,
   0.0,   0.0,   0.2,   0.2,   0.0,   0.0,   0.0,   0.0,   0.0,
SAI_JUL = 0.0,   0.4,   0.4,   0.4,   0.6,   0.6,   0.8,   0.4,   0.6,
     0.8,   0.9,   1.3,   0.5,   0.5,   0.7,   0.0,   0.6,   0.6,
   0.0,   0.0,   0.4,   0.4,   0.0,   0.0,   0.0,   0.0,   0.0,
SAI_AUG = 0.0,   0.5,   0.5,   0.5,   0.9,   0.9,   1.3,   0.6,   0.9,
     1.2,   1.2,   1.2,   0.5,   0.6,   0.8,   0.0,   0.9,   0.9,
   0.0,   0.0,   0.6,   0.6,   0.0,   0.0,   0.0,   0.0,   0.0,
SAI_SEP = 0.0,   0.4,   0.4,   0.4,   0.7,   1.0,   1.1,   0.8,   1.0,
     1.3,   1.6,   1.0,   0.5,   0.6,   1.0,   0.0,   0.7,   1.0,
   0.0,   0.0,   0.8,   0.7,   0.0,   0.0,   0.0,   0.0,   0.0,
SAI_OCT = 0.0,   0.3,   0.3,   0.3,   0.3,   0.8,   0.4,   0.7,   0.6,
     0.7,   1.4,   0.8,   0.5,   0.7,   1.0,   0.0,   0.3,   0.8,
   0.0,   0.0,   0.7,   0.5,   0.0,   0.0,   0.0,   0.0,   0.0,
SAI_NOV = 0.0,   0.3,   0.3,   0.3,   0.3,   0.4,   0.4,   0.3,   0.3,
     0.4,   0.6,   0.6,   0.5,   0.6,   0.5,   0.0,   0.3,   0.4,
   0.0,   0.0,   0.3,   0.3,   0.0,   0.0,   0.0,   0.0,   0.0,
```

```
 SAI_DEC = 0.0,    0.3,    0.3,    0.3,    0.3,    0.3,    0.4,    0.2,    0.3,
      0.4,    0.4,    0.5,    0.5,    0.5,    0.4,    0.0,    0.3,    0.4,
    0.0,    0.0,    0.2,    0.2,    0.0,    0.0,    0.0,    0.0,    0.0,

 LAI_JAN = 0.0,    0.0,    0.0,    0.0,    0.2,    0.0,    0.4,    0.0,    0.2,
      0.3,    0.0,    0.0,    4.5,    4.0,    2.0,    0.0,    0.2,    0.2,
    0.0,    0.0,    1.0,    0.6,    0.0,    0.0,    0.0,    0.0,    0.0,
 LAI_FEB = 0.0,    0.0,    0.0,    0.0,    0.3,    0.0,    0.5,    0.0,    0.3,
      0.3,    0.0,    0.0,    4.5,    4.0,    2.0,    0.0,    0.3,    0.3,
    0.0,    0.0,    1.0,    0.6,    0.0,    0.0,    0.0,    0.0,    0.0,
 LAI_MAR = 0.0,    0.0,    0.0,    0.0,    0.3,    0.2,    0.6,    0.2,    0.4,
      0.5,    0.3,    0.0,    4.5,    4.0,    2.2,    0.0,    0.3,    0.3,
    0.0,    0.0,    1.1,    0.7,    0.0,    0.0,    0.0,    0.0,    0.0,
 LAI_APR = 0.0,    0.0,    0.0,    0.0,    0.4,    0.6,    0.7,    0.6,    0.7,
      0.8,    1.2,    0.6,    4.5,    4.0,    2.6,    0.0,    0.4,    0.6,
    0.0,    0.0,    1.3,    0.8,    0.0,    0.0,    0.0,    0.0,    0.0,
 LAI_MAY = 0.0,    1.0,    1.0,    1.0,    1.1,    2.0,    1.2,    1.5,    1.4,
      1.8,    3.0,    1.2,    4.5,    4.0,    3.5,    0.0,    1.1,    2.0,
    0.0,    0.0,    1.7,    1.2,    0.0,    0.0,    0.0,    0.0,    0.0,
 LAI_JUN = 0.0,    2.0,    2.0,    2.0,    2.5,    3.3,    3.0,    2.3,    2.6,
      3.6,    4.7,    2.0,    4.5,    4.0,    4.3,    0.0,    2.5,    3.3,
    0.0,    0.0,    2.1,    1.8,    0.0,    0.0,    0.0,    0.0,    0.0,
 LAI_JUL = 0.0,    3.0,    3.0,    3.0,    3.2,    3.7,    3.5,    2.3,    2.9,
      3.8,    4.5,    2.6,    4.5,    4.0,    4.3,    0.0,    3.2,    3.7,
    0.0,    0.0,    2.1,    1.8,    0.0,    0.0,    0.0,    0.0,    0.0,
 LAI_AUG = 0.0,    3.0,    3.0,    3.0,    2.2,    3.2,    1.5,    1.7,    1.6,
      2.1,    3.4,    1.7,    4.5,    4.0,    3.7,    0.0,    2.2,    3.2,
    0.0,    0.0,    1.8,    1.3,    0.0,    0.0,    0.0,    0.0,    0.0,
 LAI_SEP = 0.0,    1.5,    1.5,    1.5,    1.1,    1.3,    0.7,    0.6,    0.7,
      0.9,    1.2,    1.0,    4.5,    4.0,    2.6,    0.0,    1.1,    1.3,
    0.0,    0.0,    1.3,    0.8,    0.0,    0.0,    0.0,    0.0,    0.0,
 LAI_OCT = 0.0,    0.0,    0.0,    0.0,    0.3,    0.2,    0.6,    0.2,    0.4,
      0.5,    0.3,    0.5,    4.5,    4.0,    2.2,    0.0,    0.3,    0.3,
    0.0,    0.0,    1.1,    0.7,    0.0,    0.0,    0.0,    0.0,    0.0,
 LAI_NOV = 0.0,    0.0,    0.0,    0.0,    0.3,    0.0,    0.5,    0.0,    0.3,
      0.3,    0.0,    0.2,    4.5,    4.0,    2.0,    0.0,    0.3,    0.3,
    0.0,    0.0,    1.0,    0.6,    0.0,    0.0,    0.0,    0.0,    0.0,
 LAI_DEC = 0.0,    0.0,    0.0,    0.0,    0.2,    0.0,    0.4,    0.0,    0.2,
      0.3,    0.0,    0.0,    4.5,    4.0,    2.0,    0.0,    0.2,    0.2,
    0.0,    0.0,    1.0,    0.6,    0.0,    0.0,    0.0,    0.0,    0.0,

 SLAREA=0.0228,0.0200,0.0200,0.0295,0.0223,0.0277,0.0060,0.0227,0.0188,
    0.0236,0.0258,0.0200,0.0200,0.0090,0.0223,0.0422,0.0390,  0.02,
    0.02,    0.02,    0.02,    0.02,    0.02,    0.02,    0.02,    0.02,

! Five types, one row for each type (BVOC currently not active).
 EPS1    = 41.87,  0.00,  0.00,  2.52,  0.04, 17.11,  0.02, 21.62,
    0.11, 22.80, 46.86,  0.00,  0.00,  0.46, 30.98,  2.31,  1.63,   0.0,
      0.0,    0.0,    0.0,    0.0,    0.0,    0.0,    0.0,    0.0,
 EPS2    =  0.98,  0.00,  0.00,  0.16,  0.09,  0.28,  0.05,  0.92,
    0.22,  0.59,  0.38,  0.00,  0.00,  3.34,  0.96,  1.47,  1.07,   0.0,
      0.0,    0.0,    0.0,    0.0,    0.0,    0.0,    0.0,    0.0,
```

```
 EPS3    =  1.82,   0.00,   0.00,   0.23,   0.05,   0.81,   0.03,   1.73,
    1.26,   1.37,   1.84,   0.00,   0.00,   1.85,   1.84,   1.70,   1.21,    0.0,
     0.0,    0.0,    0.0,    0.0,    0.0,    0.0,    0.0,    0.0,    0.0,
 EPS4    =   0.0,    0.0,    0.0,    0.0,    0.0,    0.0,    0.0,    0.0,
    0.0,    0.0,    0.0,    0.0,    0.0,    0.0,    0.0,    0.0,    0.0,    0.0,
     0.0,    0.0,    0.0,    0.0,    0.0,    0.0,    0.0,    0.0,    0.0,
 EPS5    =   0.0,    0.0,    0.0,    0.0,    0.0,    0.0,    0.0,    0.0,
    0.0,    0.0,    0.0,    0.0,    0.0,    0.0,    0.0,    0.0,    0.0,    0.0,
     0.0,    0.0,    0.0,    0.0,    0.0,    0.0,    0.0,    0.0,    0.0,
/
```

References

Alexander, S., Orr, A., Webster, S., and Murphy, D. (2017). Observations and fine-scale model simulations of gravity waves over Davis, East Antarctica (69° S, 78° E). *Journal of Geophysical Research: Atmospheres*, 122(14):7355–7370.

Anderson, R. S. and Anderson, L. S. (2016). Modeling debris-covered glaciers: response to steady debris deposition. *The Cryosphere*, 10(3):1105.

Arnold, N. S., Rees, W. G., Hodson, A. J., and Kohler, J. (2006). Topographic controls on the surface energy balance of a high Arctic valley glacier. *Journal of Geophysical Research: Earth Surface*, 111(F2).

Ayala, A., Pellicciotti, F., and Shea, J. (2015). Modeling 2 m air temperatures over mountain glaciers: Exploring the influence of katabatic cooling and external warming. *Journal of Geophysical Research: Atmospheres*, 120(8):3139–3157.

Barnett, T. P., Adam, J. C., and Lettenmaier, D. P. (2005). Potential impacts of a warming climate on water availability in snow-dominated regions. *Nature*, 438(7066):303.

Barry, R. G. (2008). *Mountain weather and climate*. Cambridge University Press.

Bolch, T., Kulkarni, A., Kääb, A., Huggel, C., Paul, F., Cogley, J. G., Frey, H., Kargel, J. S., Fujita, K., Scheel, M., et al. (2012). The state and fate of Himalayan glaciers. *Science*, 336(6079):310–314.

Bollasina, M., Bertolani, L., and Tartari, G. (2002). Meteorological observations at high altitude in the Khumbu Valley, Nepal Himalayas, 1994-1999. *Bulletin of Glaciological Research*, 19:1–12.

Bonasoni, P., Cristofanelli, P., Marinoni, A., Vuillermoz, E., and Adhikary, B. (2012). Atmospheric pollution in the Hindu Kush–Himalaya region: Evidence and implications for the regional climate. *Mountain Research and Development*, 32(4):468–479.

Bonekamp, P., Collier, E., and Immerzeel, W. (2018). The Impact of Spatial Resolution, Land Use, and Spinup Time on Resolving Spatial Precipitation Patterns in the Himalayas. *Journal of Hydrometeorology*, 19(10):1565–1581.

Bookhagen, B. and Burbank, D. W. (2006). Topography, relief, and TRMM-derived rainfall variations along the Himalaya. *Geophysical Research Letters*, 33(8).

Bookhagen, B. and Burbank, D. W. (2010). Toward a complete Himalayan hydrological budget: Spatiotemporal distribution of snowmelt and rainfall and their impact on river discharge. *Journal of Geophysical Research: Earth Surface*, 115(F3).

Brock, B., Rivera, A., Casassa, G., Bown, F., and Acuña, C. (2007). The surface energy balance of an active ice-covered volcano: Villarrica Volcano, southern Chile. *Annals of Glaciology*, 45:104–114.

Brock, B. W., Mihalcea, C., Kirkbride, M. P., Diolaiuti, G., Cutler, M. E., and Smiraglia, C. (2010). Meteorology and surface energy fluxes in the 2005–2007 ablation seasons at the Miage debris-covered glacier, Mont Blanc Massif, Italian Alps. *Journal of Geophysical Research: Atmospheres*, 115(D9).

Brun, F., Berthier, E., Wagnon, P., Kääb, A., and Treichler, D. (2017). A spatially resolved estimate of High Mountain Asia glacier mass balances from 2000 to 2016. *Nature geoscience*, 10(9):668.

Cai, X., Song, Y., Zhu, T., Lin, W., and Kang, L. (2007). Glacier winds in the Rongbuk Valley, north of Mount Everest: 2. Their role in vertical exchange processes. *Journal of Geophysical Research: Atmospheres*, 112(D11).

Carturan, L., Cazorzi, F., Blasi, F. D., and Dalla Fontana, G. (2015). Air temperature variability over three glaciers in the Ortles–Cevedale (Italian Alps): effects of glacier fragmentation, comparison of calculation methods, and impacts on mass balance modeling. *The Cryosphere*, 9(3):1129–1146.

Chandler, R. and Scott, M. (2011). *Statistical methods for trend detection and analysis in the environmental sciences*. John Wiley & Sons.

Collier, E. and Immerzeel, W. W. (2015). High-resolution modeling of atmospheric dynamics in the Nepalese Himalaya. *Journal of Geophysical Research: Atmospheres*, 120(19):9882–9896.

Collier, E., Maussion, F., Nicholson, L., Mölg, T., Immerzeel, W., and Bush, A. (2015). Impact of debris cover on glacier ablation and atmosphere-glacier feedbacks in the Karakoram. *Cryosphere*, 9(4):1617–1632.

Collier, E., Mölg, T., Maussion, F., Scherer, D., Mayer, C., and Bush, A. (2013). High-resolution interactive modelling of the mountain glacier–atmosphere interface: an application over the Karakoram. *The Cryosphere*, 7(3):779–795.

Collier, E., Nicholson, L., Brock, B., Maussion, F., Essery, R., and Bush, A. (2014). Representing moisture fluxes and phase changes in glacier debris cover using a reservoir approach. *The Cryosphere*, 8(4):1429–1444.

Collins, W. D., Rasch, P. J., Boville, B. A., Hack, J. J., McCaa, J. R., Williamson, D. L., Kiehl, J. T., Briegleb, B., Bitz, C., Lin, S., et al. (2004). Description of the NCAR community atmosphere model (CAM 3.0). Technical report, NCAR.

Cossu, F. and Hocke, K. (2014). Influence of microphysical schemes on atmospheric water in the Weather Research and Forecasting model. *Geoscientific Model Development*, 7(1):147–160.

Dadson, S. J. and Church, M. (2005). Postglacial topographic evolution of glaciated valleys: a stochastic landscape evolution model. *Earth Surface Processes and Landforms*, 30(11):1387–1403.

Dee, D. P., Uppala, S., Simmons, A., Berrisford, P., Poli, P., Kobayashi, S., Andrae, U., Balmaseda, M., Balsamo, G., Bauer, P., et al. (2011). The ERA-Interim reanalysis: Configuration and performance of the data assimilation system. *Quarterly Journal of the royal meteorological society*, 137(656):553–597.

Dimri, A., Niyogi, D., Barros, A., Ridley, J., Mohanty, U., Yasunari, T., and Sikka, D. (2015). Western disturbances: a review. *Reviews of Geophysics*, 53(2):225–246.

Duan, A., Wu, G., Zhang, Q., and Liu, Y. (2006). New proofs of the recent climate warming over the Tibetan Plateau as a result of the increasing greenhouse gases emissions. *Chinese Science Bulletin*, 51(11):1396–1400.

Egger, J., Bajrachaya, S., Heinrich, R., Kolb, P., Lämmlein, S., Mech, M., Reuder, J., Schäper, W., Shakya, P., Schween, J., et al. (2002). Diurnal winds in the Himalayan Kali Gandaki valley. Part III: Remotely piloted aircraft soundings. *Monthly weather review*, 130(8):2042–2058.

Eriksson, M., Xu, J., Shrestha, A. B., Vaidya, R. A., Santosh, N., Sandström, K., et al. (2009). *The changing Himalayas: impact of climate change on water resources and livelihoods in the greater Himalayas.* International centre for integrated mountain development (ICIMOD).

Foster, L., Brock, B., Cutler, M., and Diotri, F. (2012). A physically based method for estimating supraglacial debris thickness from thermal band remote-sensing data. *Journal of Glaciology*, 58(210):677–691.

Fujita, K. and Sakai, A. (2000). Air temperature environment on the debris-covered area of Lirung Glacier, Langtang Valley, Nepal Himalayas. *IAHS PUBLICATION*, pages 83–88.

Gardner, A. S., Sharp, M. J., Koerner, R. M., Labine, C., Boon, S., Marshall, S. J., Burgess, D. O., and Lewis, D. (2009). Near-surface temperature lapse rates over Arctic glaciers and their implications for temperature downscaling. *Journal of Climate*, 22(16):4281–4298.

Glasser, N., Goodsell, B., Copland, L., and Lawson, W. (2006). Debris characteristics and ice-shelf dynamics in the ablation region of the McMurdo Ice Shelf, Antarctica. *Journal of Glaciology*, 52(177):223–234.

Gobiet, A., Kotlarski, S., Beniston, M., Heinrich, G., Rajczak, J., and Stoffel, M. (2014). 21st century climate change in the European Alps—a review. *Science of the Total Environment*, 493:1138–1151.

Government of Nepal (2019). Monsoon Onset and Withdrawal date. http://www.dhm.gov.np/uploads/climatic/1622225684monsoon%20onset%20n%20withdrawal.pdf. Accessed: 2019-04-02.

Greuell, W. and Böhm, R. (1998). 2 m temperatures along melting mid-latitude glaciers, and implications for the sensitivity of the mass balance to variations in temperature. *Journal of Glaciology*, 44(146):9–20.

Guo-Yu, R. and Shrestha, A. B. (2017). Climate change in the Hindu Kush Himalaya. *Advances in Climate Change Research*, 8(3):137–140.

Hasson, S., Lucarini, V., Khan, M. R., Petitta, M., Bolch, T., and Gioli, G. (2014). Early 21st century snow cover state over the western river basins of the Indus River system. *Hydrology and Earth System Sciences*, 18(10):4077–4100.

Heikkilä, U., Sandvik, A., and Sorteberg, A. (2011). Dynamical downscaling of ERA-40 in complex terrain using the WRF regional climate model. *Climate dynamics*, 37(7-8):1551–1564.

Heynen, M., Miles, E., Ragettli, S., Buri, P., Immerzeel, W. W., and Pellicciotti, F. (2016). Air temperature variability in a high-elevation Himalayan catchment. *Annals of Glaciology*.

Hodgkins, R., Carr, S., Pálsson, F., Guðmundsson, S., and Björnsson, H. (2012). Sensitivity analysis of temperature-index melt simulations to near-surface lapse rates and degree-day factors at Vestari-Hagafellsjökull, Langjökull, Iceland. *Hydrological Processes*, 26(24):3736–3748.

Immerzeel, W., Pellicciotti, F., and Bierkens, M. (2013). Rising river flows throughout the twenty-first century in two Himalayan glacierized watersheds. *Nature geoscience*, 6(9):742.

Immerzeel, W., Petersen, L., Ragettli, S., and Pellicciotti, F. (2014). The importance of observed gradients of air temperature and precipitation for modeling runoff from a glacierized watershed in the Nepalese Himalayas. *Water Resources Research*, 50(3):2212–2226.

Immerzeel, W. W., Van Beek, L. P., and Bierkens, M. F. (2010). Climate change will affect the Asian water towers. *Science*, 328(5984):1382–1385.

Inoue, J. (1976). Climate of Khumbu Himal. *Journal of the Japanese Society of Snow and Ice*, 38(Special):66–73.

Inoue, J. and Yoshida, M. (1980). Ablation and heat exchange over the Khumbu Glacier. *Journal of the Japanese Society of Snow and Ice*, 41(Special):26–33.

Jackson, P., Mayr, G., and Vosper, S. (2013). Diurnal mountain wind systems. In *Mountain Weather Research and Forecasting*, pages 121–218. Springer.

Jacobi, H.-W., Lim, S., Ménégoz, M., Ginot, P., Laj, P., Bonasoni, P., Stocchi, P., Marinoni, A., and Arnaud, Y. (2015). Black carbon in snow in the upper Himalayan Khumbu Valley, Nepal: observations and modeling of the impact on snow albedo, melting, and radiative forcing. *The Cryosphere Discussions*, 9:1685–1699.

Jarvis, A., Reuter, H. I., Nelson, A., Guevara, E., et al. (2008). Hole-filled SRTM for the globe Version 4. *available from the CGIAR-CSI SRTM 90m Database (http://srtm. csi. cgiar. org)*, 15.

Jiménez, P. A., Dudhia, J., González-Rouco, J. F., Navarro, J., Montávez, J. P., and García-Bustamante, E. (2012). A revised scheme for the WRF surface layer formulation. *Monthly Weather Review*, 140(3):898–918.

Kääb, A., Berthier, E., Nuth, C., Gardelle, J., and Arnaud, Y. (2012). Contrasting patterns of early twenty-first-century glacier mass change in the Himalayas. *Nature*, 488(7412):495.

Karki, R., ul Hasson, S., Gerlitz, L., Schickhoff, U., Scholten, T., and Böhner, J. (2017). Quantifying the added value of convection-permitting climate simulations in complex terrain: a systematic evaluation of WRF over the Himalayas. *Earth System Dynamics*, 8(3):507–528.

Kaser, G., Großhauser, M., and Marzeion, B. (2010). Contribution potential of glaciers to water availability in different climate regimes. *Proceedings of the National Academy of Sciences*.

Kattel, D., Yao, T., Yang, K., Tian, L., Yang, G., and Joswiak, D. (2013). Temperature lapse rate in complex mountain terrain on the southern slope of the central Himalayas. *Theoretical and applied climatology*, 113(3-4):671–682.

Kattel, D. B., Yao, T., and Panday, P. K. (2018). Near-surface air temperature lapse rate in a humid mountainous terrain on the southern slopes of the eastern Himalayas. *Theoretical and Applied Climatology*, 132(3-4):1129–1141.

Kattel, D. B., Yao, T., Yang, W., Gao, Y., and Tian, L. (2015). Comparison of temperature lapse rates from the northern to the southern slopes of the Himalayas. *International Journal of Climatology*, 35(15):4431–4443.

Kayastha, R. B., Takeuchi, Y., Nakawo, M., and Ageta, Y. (2000). Practical prediction of ice melting beneath various thickness of debris cover on Khumbu Glacier, Nepal, using a positive degree-day factor. *IAHS PUBLICATION*, 7182.

Knievel, J. C., Bryan, G. H., and Hacker, J. P. (2007). Explicit numerical diffusion in the wrf model. *Monthly Weather Review*, 135(11):3808–3824.

Kraaijenbrink, P., Bierkens, M., Lutz, A., and Immerzeel, W. (2017). Impact of a global temperature rise of 1.5 degrees Celsius on Asia's glaciers. *Nature*, 549(7671):257.

Kulkarni, A., Patwardhan, S., Kumar, K. K., Ashok, K., and Krishnan, R. (2013). Projected climate change in the Hindu Kush-Himalayan region by using the high-resolution regional climate model PRECIS. *Mt Res Dev*, 33(2):142–151.

Laghari, A., Vanham, D., and Rauch, W. (2012). The Indus basin in the framework of current and future water resources management. *Hydrology and Earth System Sciences*, 16(4):1063.

Lang, M. N., Gohm, A., and Wagner, J. S. (2015). The impact of embedded valleys on daytime pollution transport over a mountain range. *Atmospheric Chemistry and Physics*, 15(20):11981–11998.

Lehner, M. (2012). *Observations and large-eddy simulations of the thermally driven cross-basin circulation in a small, closed basin*. PhD thesis, The University of Utah.

Lehner, M. and Whiteman, D. C. (2014). Physical mechanisms of the thermally driven cross-basin circulation. *Quarterly Journal of the Royal Meteorological Society*, 140(680):895–907.

Lejeune, Y., Bertrand, J.-M., Wagnon, P., and Morin, S. (2013). A physically based model of the year-round surface energy and mass balance of debris-covered glaciers. *Journal of Glaciology*, 59(214):327–344.

Loo, Y. Y., Billa, L., and Singh, A. (2015). Effect of climate change on seasonal monsoon in Asia and its impact on the variability of monsoon rainfall in Southeast Asia. *Geoscience Frontiers*, 6(6):817–823.

Loveland, T. R., Reed, B. C., Brown, J. F., Ohlen, D. O., Zhu, Z., Yang, L., and Merchant, J. W. (2000). Development of a global land cover characteristics database and IGBP DISCover from 1 km AVHRR data. *International Journal of Remote Sensing*, 21(6-7):1303–1330.

Lugauer, M. and Winkler, P. (2005). Thermal circulation in South Bavaria–climatology and synoptic aspects. *Meteorologische Zeitschrift*, 14(1):15–30.

Ma, L.-M. and Tan, Z.-M. (2009). Improving the behavior of the cumulus parameterization for tropical cyclone prediction: Convection trigger. *Atmospheric Research*, 92(2):190–211.

Ma, S., Zhou, L., Zou, H., Zhang, M., and Li, P. (2013). The role of snow/ice cover in the formation of a local Himalayan circulation. *Meteorology and Atmospheric Physics*, 120(1-2):45–51.

Madhura, R., Krishnan, R., Revadekar, J., Mujumdar, M., and Goswami, B. (2015). Changes in western disturbances over the Western Himalayas in a warming environment. *Climate dynamics*, 44(3-4):1157–1168.

Magnani, A., Ajmone-Marsan, F., D'Amico, M., Balestrini, R., Viviano, G., Salerno, F., and Freppaz, M. (2018). Soil properties and trace elements distribution along an altitudinal gradient on the southern slope of Mt. Everest, Nepal. *CATENA*, 162:61–71.

Marshall, S. J., Sharp, M. J., Burgess, D. O., and Anslow, F. S. (2007). Near-surface-temperature lapse rates on the Prince of Wales Icefield, Ellesmere Island, Canada: Implications for regional downscaling of temperature. *International Journal of Climatology*, 27(3):385–398.

Marzeion, B., Leclercq, P., Cogley, J., and Jarosch, A. (2015). Brief Communication: Global reconstructions of glacier mass change during the 20th century are consistent. *The Cryosphere*, 9(6):2399–2404.

McCarthy, M., Pritchard, H., Willis, I., and King, E. (2017). Ground-penetrating radar measurements of debris thickness on Lirung Glacier, Nepal. *Journal of Glaciology*, 63(239):543–555.

Ménégoz, M., Krinner, G., Balkanski, Y., Boucher, O., Cozic, A., Lim, S., Ginot, P., Laj, P., Gallée, H., Wagnon, P., et al. (2014). Snow cover sensitivity to black carbon deposition in the himalayas: from atmospheric and ice core measurements to regional climate simulations. *Atmospheric Chemistry and Physics*, 14(8):4237–4249.

Menon, A., Levermann, A., Schewe, J., Lehmann, J., and Frieler, K. (2013). Consistent increase in Indian monsoon rainfall and its variability across CMIP-5 models. *Earth System Dynamics*, 4:287–300.

Miles, E. S., Steiner, J. F., and Brun, F. (2017). Highly variable aerodynamic roughness length (z0) for a hummocky debris-covered glacier. *Journal of Geophysical Research: Atmospheres*, 122(16):8447–8466.

Minder, J. R., Mote, P. W., and Lundquist, J. D. (2010). Surface temperature lapse rates over complex terrain: Lessons from the Cascade Mountains. *Journal of Geophysical Research: Atmospheres*, 115(D14).

Moisseeva, N. (2014). Dynamical analysis of sea breeze hodograph rotation in Sardinia. Master's thesis, University of British Columbia.

Moisseeva, N. and Steyn, D. (2014). Dynamical analysis of sea-breeze hodograph rotation in Sardinia. *Atmospheric Chemistry and Physics*, 14(24):13471–13481.

Morrison, H., Thompson, G., and Tatarskii, V. (2009). Impact of cloud microphysics on the development of trailing stratiform precipitation in a simulated squall line: Comparison of one-and two-moment schemes. *Monthly Weather Review*, 137(3):991–1007.

Nakanishi, M. and Niino, H. (2004). An improved Mellor–Yamada level-3 model with condensation physics: Its design and verification. *Boundary-Layer Meteorology*, 112(1):1–31.

National Research Council (2012). *Himalayan glaciers: Climate change, water resources, and water security*. National Academies Press.

Nicholson, L. and Benn, D. I. (2006). Calculating ice melt beneath a debris layer using meteorological data. *Journal of Glaciology*, 52(178):463–470.

Nicholson, L. and Benn, D. I. (2013). Properties of natural supraglacial debris in relation to modelling sub-debris ice ablation. *Earth Surface Processes and Landforms*, 38(5):490–501.

Niu, G.-Y., Yang, Z.-L., Mitchell, K. E., Chen, F., Ek, M. B., Barlage, M., Kumar, A., Manning, K., Niyogi, D., Rosero, E., et al. (2011). The community Noah land surface model with multiparameterization options (Noah-MP): 1. Model description and evaluation with local-scale measurements. *Journal of Geophysical Research: Atmospheres*, 116(D12).

Nolin, A. W., Phillippe, J., Jefferson, A., and Lewis, S. L. (2010). Present-day and future contributions of glacier runoff to summertime flows in a Pacific Northwest watershed: Implications for water resources. *Water Resources Research*, 46(12).

Oerlemans, J. and Grisogono, B. (2002). Glacier winds and parameterisation of the related surface heat fluxes. *Tellus A: Dynamic Meteorology and Oceanography*, 54(5):440–452.

Ohata, T., Higuchi, K., and Ikegami, K. (1981). Mountain-valley wind system in the Khumbu Himal, East Nepal. *Journal of the Meteorological Society of Japan. Ser. II*, 59(5):753–762.

Oke, T. R. (2002). *Boundary layer climates*. Routledge.

Orr, A., Hosking, J., Hoffmann, L., Keeble, J., Dean, S., Roscoe, H., Abraham, N., Vosper, S., and Braesicke, P. (2015). Inclusion of mountain wave-induced cooling for the formation of PSCs over the Antarctic Peninsula in a chemistry-climate model. *Atmospheric chemistry and physics*, 15(2):1071–1086.

Orr, A., Listowski, C., Couttet, M., Collier, E., Immerzeel, W., Deb, P., and Bannister, D. (2017). Sensitivity of simulated summer monsoonal precipitation in Langtang Valley, Himalaya to cloud microphysics schemes in WRF. *Journal of Geophysical Research: Atmospheres*.

O'Steen, L. B. (2000). Numerical simulation of nocturnal drainage flows in idealized valley–tributary systems. *Journal of Applied Meteorology*, 39(11):1845–1860.

Palazzi, E., Von Hardenberg, J., and Provenzale, A. (2013). Precipitation in the Hindu-Kush Karakoram Himalaya: observations and future scenarios. *Journal of Geophysical Research: Atmospheres*, 118(1):85–100.

Pepin, N., Bradley, R., Diaz, H., Baraër, M., Caceres, E., Forsythe, N., Fowler, H., Greenwood, G., Hashmi, M., Liu, X., et al. (2015). Elevation-dependent warming in mountain regions of the world. *Nature Climate Change*, 5(5):424.

Petersen, L. and Pellicciotti, F. (2011). Spatial and temporal variability of air temperature on a melting glacier: atmospheric controls, extrapolation methods and their effect on melt modeling, Juncal Norte Glacier, Chile. *Journal of Geophysical Research: Atmospheres*, 116(D23).

Petersen, L., Pellicciotti, F., Juszak, I., Carenzo, M., and Brock, B. (2013). Suitability of a constant air temperature lapse rate over an Alpine glacier: testing the Greuell and Böhm model as an alternative. *Annals of glaciology*, 54(63):120–130.

Potter, E. R., Orr, A., Willis, I. C., Bannister, D., and Salerno, F. (2018). Dynamical drivers of the local wind regime in a Himalayan valley. *Journal of Geophysical Research: Atmospheres*.

Pratap, B., Dobhal, D., Bhambri, R., and Mehta, M. (2013). Near-surface temperature lapse rate in Dokriani Glacier catchment, Garhwal Himalaya, India. *Himalayan Geology*, 34:183–186.

Pritchard, H. D. (2017). Asia's glaciers are a regionally important buffer against drought. *Nature*, 545(7653):169.

Quincey, D., Smith, M., Rounce, D., Ross, A., King, O., and Watson, C. (2017). Evaluating morphological estimates of the aerodynamic roughness of debris covered glacier ice. *Earth Surface Processes and Landforms*, 42(15):2541–2553.

Rajbhandari, R., Shrestha, A. B., Nepal, S., Wahid, S., and Ren, G.-Y. (2017). Extreme climate projections over the transboundary Koshi River Basin using a high resolution regional climate model. *Advances in Climate Change Research*, 8(3):199–211.

Ramanathan, V. and Carmichael, G. (2008). Global and regional climate changes due to black carbon. *Nature geoscience*, 1(4):221.

Reid, T., Carenzo, M., Pellicciotti, F., and Brock, B. (2012). Including debris cover effects in a distributed model of glacier ablation. *Journal of Geophysical Research: Atmospheres*, 117(D18).

Reid, T. D. and Brock, B. W. (2010). An energy-balance model for debris-covered glaciers including heat conduction through the debris layer. *Journal of Glaciology*, 56(199):903–916.

Ren, Y.-Y., Ren, G.-Y., Sun, X.-B., Shrestha, A. B., You, Q.-L., Zhan, Y.-J., Rajbhandari, R., Zhang, P.-F., and Wen, K.-M. (2017). Observed changes in surface air temperature and precipitation in the Hindu Kush Himalayan region over the last 100-plus years. *Advances in Climate Change Research*, 8(3):148–156.

Renfrew, I. A. (2004). The dynamics of idealized katabatic flow over a moderate slope and ice shelf. *Quarterly Journal of the Royal Meteorological Society*, 130(598):1023–1045.

RGI Consortium (2015). Randolph Glacier Inventory – A Dataset of Global Glacier Outlines: Version 5.0. Technical report, Global Land Ice Measurements from Space, Colorado, USA.

Rounce, D., Quincey, D., and McKinney, D. (2015). Debris-covered glacier energy balance model for Imja–Lhotse Shar Glacier in the Everest region of Nepal. *The Cryosphere*, 9(6):2295–2310.

Salerno, F., Guyennon, N., Thakuri, S., Viviano, G., Romano, E., Vuillermoz, E., Cristofanelli, P., Stocchi, P., Agrillo, G., Ma, Y., et al. (2015). Weak precipitation, warm winters and springs impact glaciers of south slopes of Mt. Everest (central Himalaya) in the last 2 decades (1994–2013). *The Cryosphere*, 9(3):1229–1247.

Salerno, F., Thakuri, S., Tartari, G., Nuimura, T., Sunako, S., Sakai, A., and Fujita, K. (2017). Debris-covered glacier anomaly? Morphological factors controlling changes in the mass balance, surface area, terminus position, and snow line altitude of Himalayan glaciers. *Earth and Planetary Science Letters*, 471:19–31.

Sanjay, J., Krishnan, R., Shrestha, A. B., Rajbhandari, R., and Ren, G.-Y. (2017). Downscaled climate change projections for the Hindu Kush Himalayan region using CORDEX South Asia regional climate models. *Advances in Climate Change Research*, 8(3):185–198.

Schaner, N., Voisin, N., Nijssen, B., and Lettenmaier, D. P. (2012). The contribution of glacier melt to streamflow. *Environmental Research Letters*, 7(3):034029.

Scherler, D., Wulf, H., and Gorelick, N. (2018). Global Assessment of Supraglacial Debris-Cover Extents. *Geophysical Research Letters*, 45(21):11–798.

Schmidli, J. (2013). Daytime heat transfer processes over mountainous terrain. *Journal of the atmospheric sciences*, 70(12):4041–4066.

Serafin, S. and Zardi, D. (2010). Daytime heat transfer processes related to slope flows and turbulent convection in an idealized mountain valley. *Journal of the Atmospheric Sciences*, 67(11):3739–3756.

Shaw, T. E., Brock, B. W., Fyffe, C. L., Pellicciotti, F., Rutter, N., and Diotri, F. (2016). Air temperature distribution and energy-balance modelling of a debris-covered glacier. *Journal of Glaciology*, 62(231):185–198.

Shea, J., Immerzeel, W., Wagnon, P., Vincent, C., and Bajracharya, S. (2015a). Modelling glacier change in the Everest region, Nepal Himalaya. *The Cryosphere*, 9(3):1105–1128.

Shea, J. and Moore, R. (2010). Prediction of spatially distributed regional-scale fields of air temperature and vapor pressure over mountain glaciers. *Journal of Geophysical Research: Atmospheres*, 115(D23).

Shea, J. M., Wagnon, P., Immerzeel, W. W., Biron, R., Brun, F., and Pellicciotti, F. (2015b). A comparative high-altitude meteorological analysis from three catchments in the Nepalese Himalaya. *International journal of water resources development*, 31(2):174–200.

Shean, D. (2017). High Mountain Asia 8-meter DEM Mosaics Derived from Optical Imagery, Version 1.(tile 677). Boulder, Colorado USA. NASA National Snow and Ice Data Center Distributed Active Archive Center. doi: https://doi.org/10.5067/KXOVQ9L172S2.

Shrestha, A. B. and Aryal, R. (2011). Climate change in Nepal and its impact on Himalayan glaciers. *Regional Environmental Change*, 11(1):65–77.

Singh, N. and Ranade, A. A. (2010). *Determination of onset and withdrawal dates of summer monsoon across India using NCEP/NCAR re-analysis*. Citeseer.

Skamarock, W. C., Klemp, J. B., Dudhia, J., Gill, D. O., Barker, D. M., Duda, M. G., Huang, X.-Y., Wang, W., and Powers, J. G. (2008). A description of theadvanced research WRF version 3. Technical report, NCAR.

Soares, P. M., Cardoso, R. M., Miranda, P. M., de Medeiros, J., Belo-Pereira, M., and Espirito-Santo, F. (2012). WRF high resolution dynamical downscaling of ERA-Interim for Portugal. *Climate Dynamics*, 39(9-10):2497–2522.

Song, Y., Zhu, T., Cai, X., Lin, W., and Kang, L. (2007). Glacier winds in the Rongbuk Valley, north of Mount Everest: 1. Meteorological modeling with remote sensing data. *Journal of Geophysical Research: Atmospheres*, 112(D11).

Sperber, K. R., Annamalai, H., Kang, I.-S., Kitoh, A., Moise, A., Turner, A., Wang, B., and Zhou, T. (2013). The Asian summer monsoon: an intercomparison of CMIP5 vs. CMIP3 simulations of the late 20th century. *Climate Dynamics*, 41(9-10):2711–2744.

Steiner, J. F. and Pellicciotti, F. (2016). Variability of air temperature over a debris-covered glacier in the Nepalese Himalaya. *Annals of Glaciology*, 57(71):295–307.

Sun, F., Ma, Y., Hu, Z., Li, M., Tartari, G., Salerno, F., Gerken, T., Bonasoni, P., Cristofanelli, P., and Vuillermoz, E. (2018). Mechanism of Daytime Strong Winds on the Northern Slopes of Himalayas, near Mount Everest: Observation and Simulation. *Journal of Applied Meteorology and Climatology*, 57(2):255–272.

Sun, X.-B., Ren, G.-Y., Shrestha, A. B., Ren, Y.-Y., You, Q.-L., Zhan, Y.-J., Xu, Y., and Rajbhandari, R. (2017). Changes in extreme temperature events over the Hindu Kush Himalaya during 1961–2015. *Advances in Climate Change Research*, 8(3):157–165.

Takeuchi, Y., Kayastha, R. B., and Nakawo, M. (2000). Characteristics of ablation and heat balance in debris-free and debris-covered areas on Khumbu Glacier, Nepal Himalayas, in the pre-monsoon season. *IAHS PUBLICATION*, pages 53–62.

Tartari, G., Verza, G., and Bertolami, L. (1998). Meteorological data at the Pyramid Observatory Laboratory (Khumbu Valley, Sagarmatha National Park, Nepal). *Mem. Ist. Ital. Idrobiol*, 57:23–40.

Thayyen, R. and Dimri, A. (2014). Factors controlling Slope Environmental Lapse Rate (SELR) of temperature in the monsoon and cold-arid glacio-hydrological regimes of the Himalaya. *The Cryosphere Discussions*, (6):5645–5686.

Thayyen, R. J. and Dimri, A. P. (2018). Slope environmental lapse rate (SELR) of temperature in the monsoon regime of the western Himalaya. *Frontiers in Environmental Science*, 6:42.

Thayyen, R. J., Gergan, J., and Dobhal, D. (2005a). Monsoonal control on glacier discharge and hydrograph characteristics, a case study of Dokriani Glacier, Garhwal Himalaya, India. *Journal of hydrology*, 306(1-4):37–49.

Thayyen, R. J., Gergan, J., and Dobhal, D. (2005b). Slope lapse rates of temperature in Din Gad (Dokriani glacier) catchment, Garhwal Himalaya, India. *Bulletin of glaciological research*, 22:31–37.

Turner, A. G. and Annamalai, H. (2012). Climate change and the South Asian summer monsoon. *Nature Climate Change*, 2(8):587.

Ueno, K., Kayastha, R., Chitrakar, M., Bajracharya, O., Pokhrel, A., Fujinami, H., Kadota, T., Iida, H., Manandhar, D., Hattori, M., Yasunari, T., and Nakawo, M. (2001). Meteorological observations during 1994-2000 at the automatic weather station (GEN-AWS) in Khumbu region, Nepal Himalayas. *Bulletin of Glacier Research*, 18:23–30.

Ueno, K., Toyotsu, K., Bertolani, L., and Tartari, G. (2008). Stepwise onset of monsoon weather observed in the Nepal Himalaya. *Monthly Weather Review*, 136(7):2507–2522.

van Angelen, J. H., Van den Broeke, M., and Van de Berg, W. (2011). Momentum budget of the atmospheric boundary layer over the Greenland ice sheet and its surrounding seas. *Journal of Geophysical Research: Atmospheres*, 116(D10).

Van den Broeke, M., Van Lipzig, N., and Van Meijgaard, E. (2002). Momentum budget of the East Antarctic atmospheric boundary layer: Results of a regional climate model. *Journal of the Atmospheric Sciences*, 59(21):3117–3129.

von Storch, H. and Zwiers, F. W. (1999). *Statistical analysis in climate research*. Cambridge University Press.

Wagner, J., Gohm, A., and Rotach, M. (2015a). The impact of valley geometry on daytime thermally driven flows and vertical transport processes. *Quarterly Journal of the Royal Meteorological Society*, 141(690):1780–1794.

Wagner, J., Gohm, A., and Rotach, M. (2015b). Influence of along-valley terrain heterogeneity on exchange processes over idealized valleys. *Atmospheric Chemistry and Physics*, 15(12):6589–6603.

Wagnon, P., Vincent, C., Arnaud, Y., Berthier, E., Vuillermoz, E., Gruber, S., Ménégoz, M., Gilbert, A., Dumont, M., Shea, J., et al. (2013). Seasonal and annual mass balances of Mera and Pokalde glaciers (Nepal Himalaya) since 2007. *The Cryosphere*, 7(6):1769–1786.

Wahid, S., Shrestha, A., Murthy, M., Matin, M., Zhang, J., and Siddiqui, O. (2014). Regional water security in the Hindu Kush Himalayan region: Role of geospatial science and tools. *The International Archives of Photogrammetry, Remote Sensing and Spatial Information Sciences*, 40(8):1331.

Wang, J., Bras, R., Sivandran, G., and Knox, R. (2010). A simple method for the estimation of thermal inertia. *Geophysical Research Letters*, 37(5).

Wang, Y., Wang, L., Li, X., and Chen, D. (2018). Temporal and spatial changes in estimated near-surface air temperature lapse rates on Tibetan Plateau. *International Journal of Climatology*, 38(7):2907–2921.

Wester, P., Mishra, A., Mukherji, A., and Shrestha, B. (2019). *The Hindu Kush Himalaya Assessment–Mountains, Climate Change, Sustainability and People*. Springer.

Whiteman, C. D. (2000). *Mountain meteorology: fundamentals and applications*. Oxford University Press.

Widmann, M., Blake, R., Sooraj, K., Orr, A., Sanjay, J., Karumuri, A., Mitra, E., Rajagopal, A., Van Loon, D., Hannah, N. B., et al. (2017). Current Opportunities and Challenges in Developing Hydro-Climatic Services in the Himalayas. IUKWC report.

Xu, B., Cao, J., Hansen, J., Yao, T., Joswia, D. R., Wang, N., Wu, G., Wang, M., Zhao, H., Yang, W., et al. (2009). Black soot and the survival of Tibetan glaciers. *Proceedings of the National Academy of Sciences*, 106(52):22114–22118.

Yadav, J. S., Pratap, B., Gupta, A. K., Dobhal, D., Yadav, R., and Tiwari, S. K. (2018). Spatio-temporal variability of near-surface air temperature in the Dokriani glacier catchment (DGC), central Himalaya. *Theoretical and Applied Climatology*, pages 1–20.

Yang, K., Guyennon, N., Ouyang, L., Tian, L., Tartari, G., and Salerno, F. (2017). Impact of summer monsoon on the elevation-dependence of meteorological variables in the south of central Himalaya. *International Journal of Climatology*, pages 1748–1759.

Yao, T., Thompson, L., Yang, W., Yu, W., Gao, Y., Guo, X., Yang, X., Duan, K., Zhao, H., Xu, B., et al. (2012). Different glacier status with atmospheric circulations in Tibetan Plateau and surroundings. *Nature climate change*, 2(9):663.

Yasunari, T. (1976). Seasonal weather variations in Khumbu Himal. *Journal of the Japanese Society of Snow and Ice*, 38(Special):74–83.

Yasunari, T. and Inoue, J. (1978). Characteristics of monsoonal precipitation around peaks and ridges in Shorong and Khumbu Himal. *Journal of the Japanese Society of Snow and Ice*, 40(Special):26–32.

You, Q.-L., Ren, G.-Y., Zhang, Y.-Q., Ren, Y.-Y., Sun, X.-B., Zhan, Y.-J., Shrestha, A. B., and Krishnan, R. (2017). An overview of studies of observed climate change in the Hindu Kush Himalayan (HKH) region. *Advances in Climate Change Research*, 8(3):141–147.

Zängl, G., Egger, J., and Wirth, V. (2001). Diurnal winds in the Himalayan Kali Gandaki valley. Part II: Modeling. *Monthly weather review*, 129(5):1062–1080.

Zardi, D. and Whiteman, C. D. (2013). Diurnal mountain wind systems. In *Mountain Weather Research and Forecasting*, pages 35–119. Springer.

Zarfl, C., Lumsdon, A. E., Berlekamp, J., Tydecks, L., and Tockner, K. (2015). A global boom in hydropower dam construction. *Aquatic Sciences*, 77(1):161–170.

Zhan, Y.-J., Ren, G.-Y., Shrestha, A. B., Rajbhandari, R., Ren, Y.-Y., Sanjay, J., Xu, Y., Sun, X.-B., You, Q.-L., and Wang, S. (2017). Changes in extreme precipitation events over the Hindu Kush Himalayan region during 1961–2012. *Advances in Climate Change Research*, 8(3):166–175.

Zou, H., Zhou, L., Ma, S., Li, P., Wang, W., Li, A., Jia, J., and Gao, D. (2008). Local wind system in the Rongbuk Valley on the northern slope of Mt. Everest. *Geophysical Research Letters*, 35(13).